UNIVERSITÀ
DEGLI STUDI
FIRENZE

DOTTORATO DI RICERCA IN
SCIENZE CHIMICHE

CICLO XXX

COORDINATORE Prof. Baglioni Piero

Investigation of the structural properties of magnesium silicate hydrate cements and assessment of strategies for their development

Settore Scientifico Disciplinare CHIM/02

Dottorando	**Tutore**
Dott. Tonelli Monica	Dr. Ridi Francesca

Coordinatore
Prof. Baglioni Piero

Anni 2014/2017

Contents

Preface

This thesis concerns the study of magnesium silicate hydrate cement, obtained by hydration of reactive periclase (MgO) in the presence of silica sources (SiO_2). This cement can be produced with minimal CO_2 emissions, differently from traditional Portland cements, and nowadays it is attracting increasing interest because it has been demonstrated to be particularly important in nuclear waste encapsulation applications. In spite of its potential importance, there is still little knowledge about its structural features and formulation design. I focused my PhD on this class of cement, aiming to extent the knowledge on this material, which could pave the way for tailoring its macroscopic properties by means of a bottom-up approach, and a multi-technique approach has been used to accomplish this purpose.

In Chapter 1 an introduction of cements is given, starting from the traditional ones to the alternatives that are becoming more and more interesting in the last decades, including MgO/SiO_2 cement.

Chapter 2 refers to the details on the materials used and on the techniques applied for the experiments here reported.

Chapter 3 resumes the results obtained about the qualitative and quantitative structural characterization of magnesium silicate hydrate cements.

Chapter 4 concerns the combination of traditional Portland cement with MgO/SiO_2 cement.

In Chapter 5, 6 and 7 the evaluation of the effects of different additives on MgO/SiO_2 cement is reported: phosphate additives (Chapter 5), aluminate phases (Chapter 6) and halloysite nanoclays (Chapter 7).

In the Appendix the publications produced during this thesis are reprinted with permissions:

- **Paper I**: Tonelli, M.; Martini, F.; Calucci, L.; Fratini, E.; Geppi, M.; Ridi, F.; Borsacchi, S.; Baglioni, P. *Structural investigation of magnesium silicate hydrate.* **Dalton Transaction**, 2016, **45**, 3294-3304. DOI: 10.1039/c5dt03545g.

- **Paper II**: Martini, F.; Tonelli, M.; Calucci, L.; Geppi, M.; Ridi, F.; Borsacchi, S. *Hydration of MgO/SiO_2 and Portland cement mixtures: a structural investigation of the hydrated phases by means of X-ray diffraction* *and Solid State NMR spectroscopy.* **Cement** & **Concrete Research**, 2017, **102**, 60-67. DOI: 10.1016/j.cemconres.2017.08.029.

- **Paper III**: Tonelli, M.; Martini, F.; Calucci, L.; Geppi, M.; Borsacchi, S.; Ridi, F. *Traditional Portland cement and innovative MgO-based cement : a promising combination?.* **Physics and Chemistry of the Earth**, 2017, **99**, 158-167. DOI: 10.1016/j.pce.2017.01.011.

- **Paper IV**: Martini, F.; Calucci, L.; Geppi, M.; Tonelli, M.; Ridi, F.; Borsacchi, S. *Monitoring the hydration of MgO-based cement and its mixtures with Portland cement by* ^{1}*H NMR relaxometry.* **Microporous and Mesoporous Materials**, 2017. DOI: 10.1016/j.micromeso.2017.05.031.

- **Paper V**: Ridi, F.; Tonelli, M.; Fratini, E.; Chen, S.H; Baglioni, P. *Water as a probe of the colloidal properties of cement.* **Langmuir**, 2017. DOI: 10.1021/acs.langmuir.7b02304.

Abbreviations

List of abbreviations (in order of appearence)	
SCM	supplementary cementitious material
CAC	calcium aluminate cement
CSA	calcium solphoaluminate-based system
FA	fly ash
SGP	small gel pore
LGP	large gel pore
IGP	intraglobular pores
PCE	polycarboxylate
HMP	sodium hexametaphosphate
CNT	carbon nanotube
HNT	halloysite
IMO	imogolite
TMP	sodium trimetaphosphate
OP	sodium phosphate
w/s	water to solid weight ratio
DSC	differential scanning calorimetry
TGA	thermogravimetric analysis
FTIR	Fourier Transform IR
XRD	X-ray diffraction
SS-NMR	solid state NMR
SEM	scanning electron microscopy
AFM	atomic force microscopy
IC	isothermal calorimetry
FWI	Free Water Index
BNGM	Boundary Nucleation and Growth Model
LT-DSC	Low-temperature differential scanning calorimetry
CDF	Cumulative Distribution Functions
SSA	Solid State Adsorption
CPMG	Carr-Purcell-Meiboom-Gill
FID	Free Induction Decay
APTES	3-amminopropyltriethoxysilane

Name	**Chemical formula**	**Cement notation**
Lime, calcium oxide	CaO	C
Magnesia, periclase, magnesium oxide	MgO	M
Silica, silicon dioxide	SiO_2	S
Water	H_2O	H
Alumina, aluminum oxide	Al_2O_3	A
Iron or ferric oxide	Fe_2O_3	F
Potassium oxide	K_2O	K
Phosphorous hemi-pentoxide	P_2O_5	P
Titania, titanium dioxide	TiO_2	T
Sodium oxide	NaO_2	N
Sulfur trioxide	SO_3	$\overline{S}$
Carbon dioxide	CO_2	$\overline{C}$

Name	**Mineral phase**	**Chemical formula**	**Cement chemistry notation**
Tricalcium silicate	Alite	$3\,CaO \cdot SiO_2$	C_3S
Dicalcium silicate	Belite	$2\,CaO \cdot SiO_2$	C_2S
Tricalcium aluminate	Aluminate or Celite	$3\,CaO \cdot Al_2O_3$	C_3A
Calcium trisulfoaluminate hydrate	ettringite	$(CaO)_6(Al_2O_3)(SO_3)_3 \cdot 32\,H_2O$	AFt
Calcium monosolfoaluminate hydrate		$(CaO)_4(Al_2O_3)(SO_3) \cdot 12\,H_2O$	AFm
Hydrogarnet		$(CaO)_3(Al_2O_3) \cdot 6\,H_2O$	C_3AH_6
Tetracalcium alumino ferrite	Ferrite	$3\,CaO \cdot Al_2O_3 \cdot Fe_2O_3$	C_4AF
Calcium hydroxide	Portlandite	$Ca(OH)_2$	CH
Magnesium hydroxide	Brucite	$Mg(OH)_2$	MH
Calcium sulfate dihydrate	Gypsum	$CaSO_4 \cdot 2\,H_2O$	$C\overline{S}H_2$
Calcium silicate hydrate		$(CaO)_x(SiO_2)(H_2O)_y$	CSH
Magnesium silicate hydrate		$(MgO)_x(SiO_2)(H_2O)_y$	MSH

1 Introduction

1.1 Cement

The word cement can be traced back to the Roman term *opus caementicium*, used to describe concrete made of crushed rock and burnt lime (CaO).[1] Cement is one of the synthetic materials with the largest production and usage since Roman times. Between 30 and 15 BC, the engineer Vitruvius described in the books *De Architettura* a fascinating material able to increase its resistance along the time. That materials was called pozzolanic, from Pozzuoli, the place near Vesuvio where the ashes used to prepare cement were taken. Originally, a mixtures of lime and crushed volcanic ashes was used and it was able to set under water. According to the modern knowledge, the volcano made the calcination process that today is artificial, converting siliceous and aluminous material in an amorphous form.[2]
Today the term cement can be used for almost any type of binder or glue, with formulations ranging from totally organic to totally inorganic. It is commonly accepted that cement is a substance that sets, hardens and adheres to other materials, binding them together. Cements can be classified in non-hydraulic cements, when they do not set in presence of water, and hydraulic cements, when they hardens by hydration of the dry ingredients and they can set underwater. Thus, the water-activated cement used to make modern construction concretes are the so called hydraulic binders. When using fine aggregates cement produces mortar for masonry, when sands or gravel aggregates are chosen it produces concrete.[3]

Concrete is currently the material with the largest production: more than 11 billion metric of stones are consumed every year all over the world (see figure 1.1). The success of concrete comes from the availability and low cost of its components and from the ease with which it can be prepared. Anyway, cement remains one of the most complex inorganic system and despite the millenary history, several questions are still open in the cement research.[2, 5]

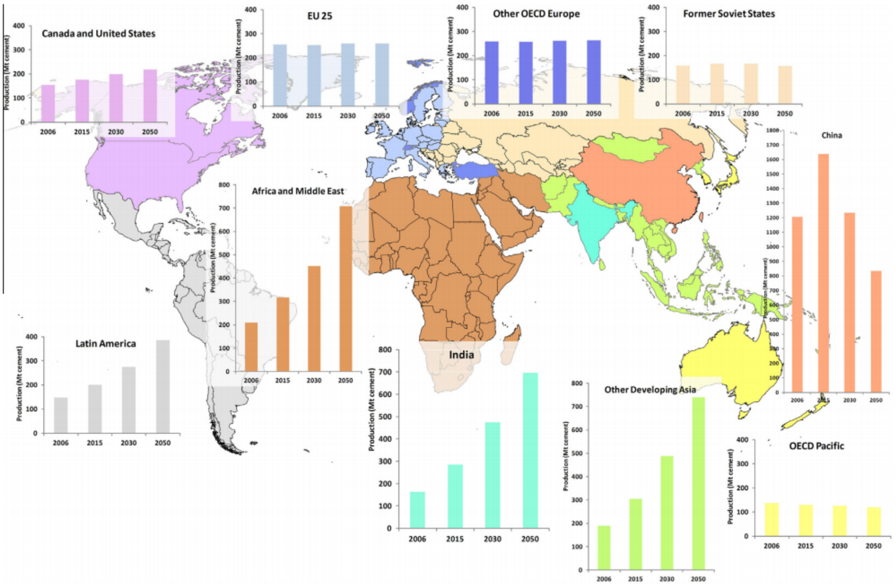

Figure 1.1: Expected growth in global cement production by region. Graphs are estimated levels of production for 2006, 2015, 2030 and 2050. Reproduced with permission from reference [4].

1.1.1 Portland cement

Portland cement (PC) is the most common type of cement in general use. Its name derives from its similarity to Portland stone, quarried in the island of Portland in Dorset, England. The development of modern PC (also called ordinary PC) began in the late 18th century. During the 19th century, Roman cement was refined and modern Portland cement was developed, quickly becoming popular.[6, 7] Nowadays PC is made by heating a mixture of crushed limestone rocks and clay to a temperature around 1400 °C.(see figure 1.2) In these conditions partial fusion occurs and nodules of clinker are produced. The principal reaction taking place during cement manufacture can be divided in three groups:

1. Reactions below 1300 °C (calcining), when the decomposition of clay minerals occur and the formed calcite or lime reacts with quartz and clay mineral decomposition products, to give belite ($2\,CaO \cdot SiO_2$, C_2S), aluminate ($3\,CaO \cdot Al_2O_3$, C_3A) and ferrite ($4\,CaO \cdot Al_2O_3 \cdot Fe_2O_3$, C_4AF).

2. Reactions at 1300-1450 °C (clinkering), when a melt is formed, mainly from the aluminate and ferrite phase, and belite and lime react to give alite ($3\,CaO \cdot SiO_2$,C_3S). The material nodulizes to form clinker.

3. Reactions during cooling, when the liquid crystallizes, giving mainly aluminate and ferrite, and polymorphic transitions of alite and belite occur.

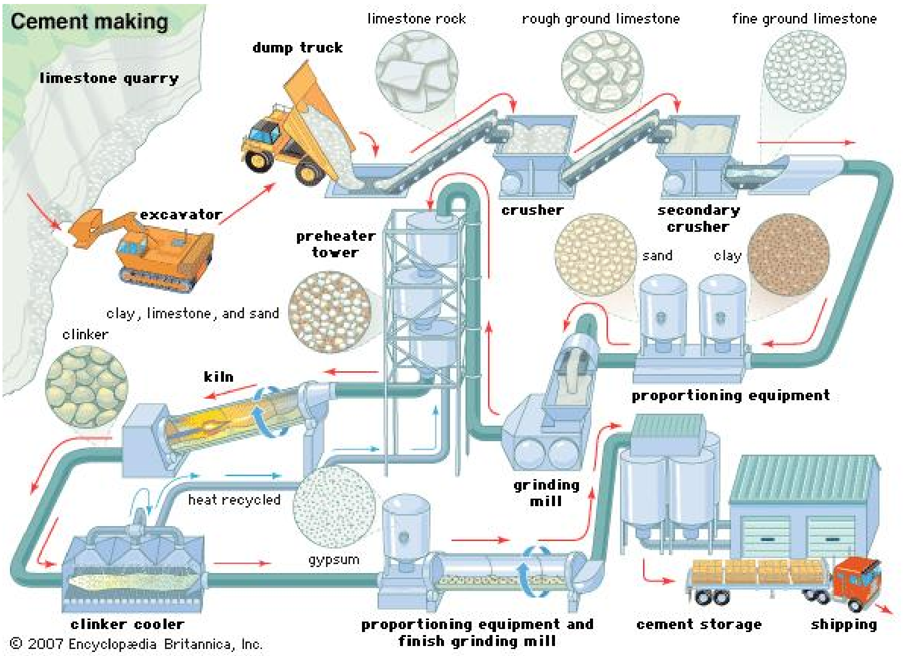

© 2007 Encyclopædia Britannica, Inc.

Figure 1.2: The cement making process, from crushing and grinding of raw materials, through roasting of the ground and mixed ingredients, to final cooling and storing of the finished product. Reproduced with permission from reference [8].

Then the clinker is finely ground and calcium sulfate is added, to control the rate of set and strength development. The great majority of PC are designed for construction purpose but, depending on the composition, physical properties and performance tests, different types of cement are classified. In a typical Portland cement the major phases are alite, belite, calcium aluminate and calcium ferrite. Alite generally constitutes 50-70% of the total mass and it is responsible for the setting time and short-term strength development. Belite constitutes 15-30% of the whole clinker and it substantially contributes to the long term strength developments. Aluminate and ferrite are respectively 5-10% and 5-15% of PC, they react very fast with water to form metastable species, that can evolve with time.[9] Hardening of PC results from reaction between the major phases and water:

$$\begin{aligned}(\mathrm{CaO})_3 \cdot \mathrm{SiO}_2 + (3 + \mathrm{x} + \mathrm{y})\mathrm{H}_2\mathrm{O} \longrightarrow \\ (\mathrm{CaO})_\mathrm{x} \cdot \mathrm{SiO}_2 \cdot (\mathrm{H}_2\mathrm{O})_\mathrm{y} + (3 - \mathrm{x})\mathrm{Ca(OH)}_2 \end{aligned} \tag{1.1}$$

$$\begin{aligned}&(\mathrm{CaO})_2 \cdot \mathrm{SiO_2} + (2 + \mathrm{x} + \mathrm{y})\mathrm{H_2O} \longrightarrow \\ &\qquad (\mathrm{CaO})_\mathrm{x} \cdot \mathrm{SiO_2} \cdot (\mathrm{H_2O})_\mathrm{y} + (3 - \mathrm{x})\mathrm{Ca(OH)_2}\end{aligned} \tag{1.2}$$

$$(\mathrm{CaO})_3 \cdot \mathrm{Al_2O_3} + 6\,\mathrm{H_2O} \longrightarrow (\mathrm{CaO})_3 \cdot \mathrm{Al_2O_3} \cdot (\mathrm{H_2O})_6 \tag{1.3}$$

$$\begin{aligned}&(\mathrm{CaO})_4 \cdot \mathrm{Al_2O_3} \cdot \mathrm{Fe_2O_3} + (\mathrm{n} + 6)\,\mathrm{H_2O} \longrightarrow \\ &\qquad (\mathrm{CaO})_3 \cdot \mathrm{Al_2O_3} \cdot (\mathrm{H_2O})_6 + \mathrm{CaO} \cdot \mathrm{Fe_2O_3} \cdot (\mathrm{H_2O})\mathrm{n}\end{aligned} \tag{1.4}$$

At the same time, it is important to use proper additives to control the reaction of hydration of the aluminate phases, which could lead to a rapid setting that generates a solid with very poor mechanical properties. Otherwise, the following reaction may compromise the characteristic excellent mechanical properties of calcium silicate hydrate (C-S-H), $(\mathrm{CaO})\mathrm{x} \cdot \mathrm{SiO_2} \cdot (\mathrm{H_2O})\mathrm{y}$:

$$(\mathrm{CaO})_3 \cdot \mathrm{Al_2O_3} + \mathrm{H_2O} \longrightarrow (\mathrm{CaO})_3 \cdot \mathrm{Al_2O_3} \cdot \mathrm{H_2O} \tag{1.5}$$

C-S-H is the main binding phase in hydrated cement. It consists of nanometer-scale solid particles that are packed or agglomerated into randomly oriented structures with gel pores.[10] In the last decades many studies investigated C-S-H structure. Jennings combined different previous works and obtain a hybrid model that is commonly accepted, the Colloidal Model, which basic idea is that the bulk microstructure is formed as a consequence of the packing of basic globules with peculiar shape and internal structure, as shown in figure 1.3.[11] Basic disk-like globules compose a structure with pores of different dimensions and two regions of different density can be distinguished in C-S-H (see also section 1.1.1).

1.1.2 CO_2 emissions

Cement production has undergone a tremendous development from its beginning. Today's annual global cement production has reached ~3 billion tonnes and it is expected to increase to 4 billion tonnes per year in 2050 (figure 1.4).[14] Cement is the key material to satisfy global housing and modern infrastructure needs. As a result of the large volumes of concrete used, the production of PC accounts for 5-8% of the global anthropocentric CO_2 emission. This is mainly due to limestone decarbonation and to the high temperatures required in the production process, preventing the use of alternative fuels. The production of each tonne of PC requires about 1.6 tonne of raw materials and releases approximately 0.9 tonne of carbon dioxide into the atmosphere. From the point of view of natural resources, ecology and economy, it seems to be impossible imaging a substitution of concrete by any other material. Thus, modifying

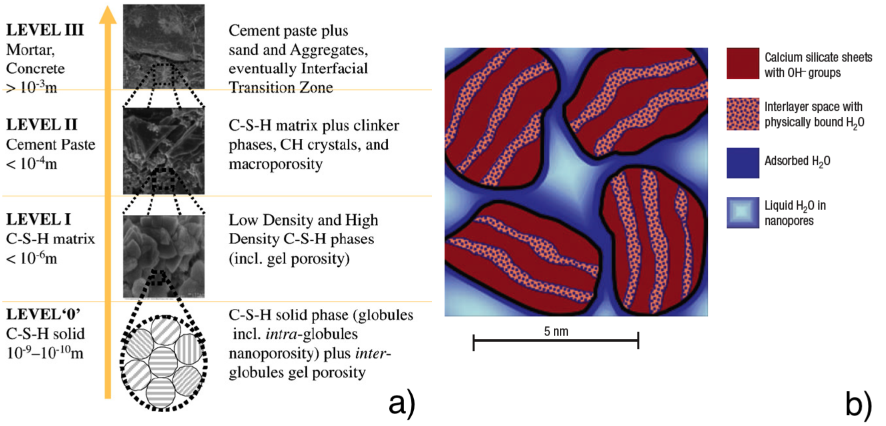

Figure 1.3: a) Definition of representative volume elements for a multiscale modeling approach; b) schematic diagram of the nanoscale C-S-H particles. Adapted with permissions from references [12] and [13].

the binder represents a major objective for an eco-sustainable development.[5, 12, 16] Recently, cement industry has assumed two important challenges to contribute: the first is to reduce particle and gas emission, the second involves the reduction of greenhouse gas emission, following the Kyoto Protocol.[17] Nowadays, developing an innovative alternative sustainable cement is one of the biggest challenges to reduce CO_2 emission and the consumption of energy and natural resources associated with traditional PC production.[12] For these reasons throughout the twentieth century the number of scientific papers on cements and derived materials raised both in terms of number and quality and, recently, the scientific community has began to work more and more on a design for new binders and a remarkable number of approaches toward low CO_2 cements was introduced.[18, 19]

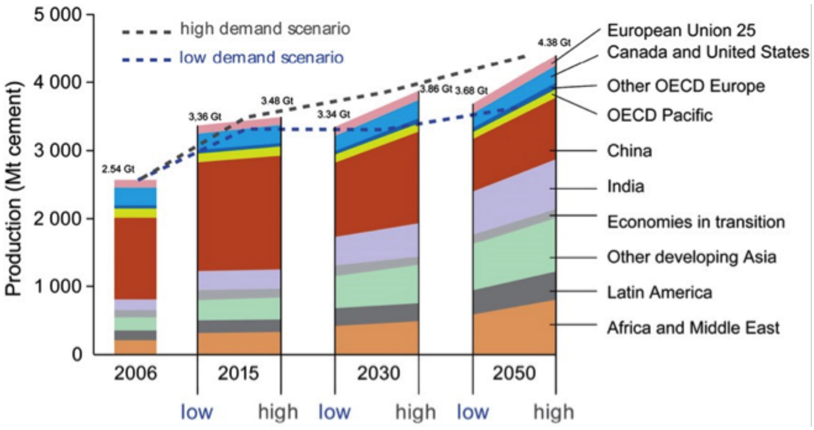

Figure 1.4: Annual world cement production and projection up to 2050. Reproduced with permission from reference [15].

1.2 Alternative cements

According to the International Energy Agency, some of the major objectives for cement producers are the increase in energy efficiency and the use of alternative materials, being them fuel or raw materials.[14] Cement production in its beginning only focused on PC, but later cements with several main constituents were produced by replacing parts of the clinker content with the so-called supplementary cementitious materials (SCMs), as shown in figure 1.5. Typical examples are fly ashes, slag cements and silica fume, that can reduce the permeability of the mixtures, increase strength or influence other properties. The drive towards sustainability in constructions is actually shaping

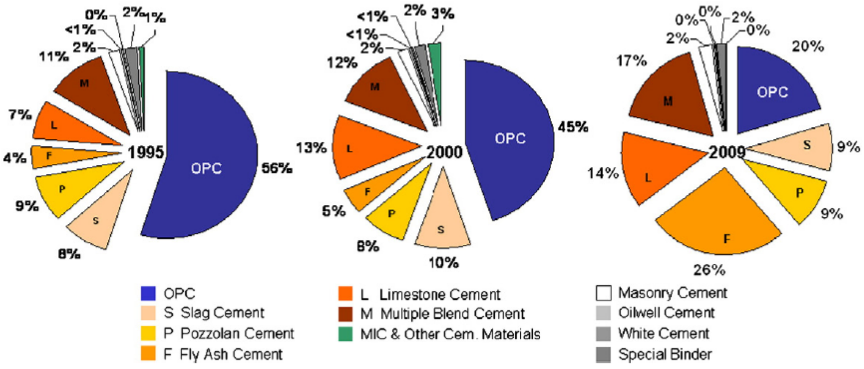

Figure 1.5: Types of cement produced by Holcim 1995-2000. Reproduced with permission from reference [14].

our attitudes towards alternatives to conventional PC hydraulic binders. In 2011 Juenger *et al.*[20] addressed four classes of sustainable alternative materials:

- **Calcium aluminate cements (CACs).** CACs contain primarily monocalcium aluminate ($CaO \cdot Al_2O_3$, CA). They have several distinct advantages over traditional Portland cement concrete, including rapid strength gain upon setting and enhanced resistance to abrasion, sulfate attack and alkali–silica reaction. Furthermore, production of CACs results in lower CO_2 emissions than Portland cement production. Currently, CACs are mainly used in refractory and building chemistry applications, such as floor screeds and rapid- hardening mortars. Despite the fact that they were developed over 100 years ago, they are not extensively used because of two main disadvantageous characteristics. First, a process called "conversion" can occur in hydrated CACs. In these conditions metastable hydrates convert to stable hydrates, leading to an increase in porosity and decrease in strength. Secondly, CACs are expensive compared to PC.

- **Calcium solphoaluminate-based systems (CSA).** CSA cements contain ye'elimite ($4\,CaO \cdot 3\,Al_2O_3 \cdot SO_3$, $C_4A_3\overline{S}$) as major constituent. CSA cements are not widely used in Europe and U.S., but in China they are known as "third cement series" and they have been used and standardized for about 30 years. They are receiving increasing attention because of the reduced CO_2 emissions, arising from the different starting material with respect to PC, and the firing temperature, that is 200 °C lower than in PC cements. Moreover the clinker is easier to grind than in PC and, due to their low pH, low porosity and ability to bind heavy metals, they are of interest in the field of hazardous waste encapsulation. Many types of CSAs have been developed in the past few decades and one of the most promising approach was to make combinations of belite, calcium sulphoaluminate (ye'elimite) and calcium aluminoferrite. Such "BCSAF" clinkers can produce cements with performances similar to PC and with 20-30% less CO_2 emissions, while in principle being manufactured in conventional plants.

- **Alkali-activated cements.** Alkali-activated binders are made by mixing solid aluminosilicate powders, such as fly ash, blast furnace slag or metakaolin with an alkaline activating solution. These binders are receiving increasing attention because of their high strength, durability and low environmental impact. Similarly to the other materials, the fundamental technology to make these cements is not new, but the sensitivity of the activation conditions to the amount of water added and the difficulties in handling concentrated caustic solutions, together with the cost of activators, are still limiting their use.

- **Supersulfated cements.** These binders are almost free of PC clinker. They are made of blast furnace slag, calcium sulfate and an alkaline activator, with eventually PC in small quantities. Supersulfated cements are attracting new attention due to their eco-sustainable composition, being made almost entirely from waste materials, due to their very low heat of hydration and to their good durability in chemical aggressive environments.[17, 20]

Additional motivation for exploring alternatives to PC can be derived from its shortcomings in certain applications and environments. For instance, rapid-repair applications demand a faster strength gain than PC cannot provide and environmental conditions with high acidity or high sulfate concentration can cause substantial degradation of traditional cements. Gartner *et al.*[3] further reviewed recent progresses in the development of alternative cement systems and two other important classes of alternative cements can be defined:

- **Partially prehydrated C-S-H based binders.** Researchers at the Karlsruhe Institute Technology recently developed this class of binders, avoiding the need of producing Portland clinkers and resulting in significant lower CO_2 emission, with excellent concrete performances. Their approach is to produce a coating of a C-S-H precursor phase on the surface of particles of a relatively unreactive substrate, as quartz. The manufacture of these binders requires three steps: limestone is first calcined to make quicklime; then lime, silica and water react at 200 °C to form α-C_2SH; finally, α-C_2SH is dried and intergrinded with a siliceous filler, like quartz.

- **Magnesia-based cements** Magnesia-based cements, by definition, use MgO as raw material, rather than CaO. Since the direct replacement of CaO with MgO in PC manufacture is precluded, different approaches are required and recently many different alternatives were proposed. MgO-based cements include reactive magnesia cements, oxy-chloride (Sorel) or oxy-sulfate cements, phosphate cements and silicate systems. In most cases, the reactivity of MgO is an important aspect to control the quality of such materials. In particular, higher calcination temperatures lead to reduced reactivity, since periclase crystals grow larger. Reactive magnesia cements consist of mixtures of a reactive MgO powder blended with a hydraulic cement and also a pozzolan. MgO contributes to the strengthening of the cement by reacting with water to form magnesium hydroxide. It is unclear in the literature if $Mg(OH)_2$ formed within the MgO/PC systems could undergo carbonation processes to a hydrated magnesium carbonate, $MgCO_3 \cdot H_2O$, over a time frame of several years under conditions of natural atmospheric exposure. If not, the overall environmental advantages of reactive MgO cements will be questionable.

Some papers also report the preparation of carbonated magnesia blocks. In this case, MgO/fly ash (MgO/FA) blends were mixed with sand and gravel to make blocks of sufficient porosity to enable their complete carbonation. However, conditions with both elevated CO_2 and elevated relative humidity are required for the production of a useful product, with limited strengths observed under atmospheric curing conditions. Sorel cements, invented over 140 years ago, are based on the hydration of MgO in concentrated solutions of magnesium chloride (or magnesium sulfate) to precipitate hydrated magnesium oxy-chloride (or oxy-sulfates). Despite their relatively high cost, they are good for some specialty applications, mainly for use in dry environments, as they are too water-sensitive for most outdoor applications. Another important class of MgO cements is based on magnesium phosphates. Since magnesium forms low soluble hexahydrated binary orthophosphates with either ammonium (struvite, $MgNH_4PO_4 \cdot 6H_2O$) or potassium, to prepare these cements MgO is added to a concentrated aqueous solution of the di-hydrogen phosphate salt of the monovalent cation, where it dissolves and then the double salt crystallizes. These cements can set and harden very quickly and can give high strength. Finally, the concept of using a magnesium silicate binder has existed for over 100 years. In 1889 Cummings reported the use of $MgCO_3$ and silica to form an hydraulic magnesium silicate hydrate cement, while in 1899 Steiger proposed the use of $MgCl_2$, MgO, potassium or sodium silicate with water. Other patents concerned the addition of soluble silicates to magnesium oxychloride cements or the fusion of talc/asbestos and silica, but the use of that cements remained relatively unresearched for over 50 years and they are still not well understood. Modern magnesium silicate hydrate (M-S-H) cements are formed from a source of magnesium (tipically MgO) and a source of highly reactive silica in situ. The possibility of substituting traditional PC with an eco-sustainable alternative based on an analogous binder, has sparked interest in these cements in recent years. On the other hand, one of the main problems in M-S-H cements is that they prevent the preparation of reinforcing concretes. As a matter of fact, MgO-based cementitious matrices buffer the pH of their pore solutions at values close to 10, too low for the passivation of steel.[3] Nowadays, M-S-H cements appears to be restricted to specific applications, but their knowledge is still lacking and not all the potentiality have been exploited yet.[3, 21]

1.2.1 MgO/SiO_2 cement

Magnesia binders are in the focus of attention since the last few years. As anticipated in the previous section, cements obtained by hydration of reactive periclase (MgO) in the presence of silica sources produce magnesium silicate hydrate (M-S-H), a binder gel phase analogous to C-S-H. M-S-H was initially considered one of the most interesting eco-sustainable alternatives to standard cementitious binders.[22] This product seemed to have the potentiality to even substitute CaO-based cements, but the latest literature underlined the limited mechanical properties and the low pH of these formulations (that prevents the use of steel reinforcing bars). Because of the low abudance of MgO, some processes have been recently proposed, based on magnesium silicate, brine or seawater. Novacem, a start-up company of the Imperial College of London, developed a process to obtain reactive periclase (MgO) from magnesium silicates, that is one of the main constituent of the Earth's crust (see figure 1.6 and 1.7).[23, 24] In 2010 the world economic forum named Novacem as one of its "Technology Pioneers" for 2011. Contemporary, *MIT Technology Review* featured Novacem on list of the 10 most important emerging technologies, while in 2012 Achternbosch and coworkers discussed about the real applicability of the MgO-based cementitous matrix previously proposed by Nikolas Vlasopolous in Novacem process.[22, 24] As a major component of the upper earth mantle, magnesium silicates are the most common rock forming silicates and minerals. However, its regional appearance differs great and its chemical and mineralogical composition can be very heterogeneous.[22] The lower temperature required by the Novacem process, compared to that commonly used in Portland cement production, allows the use of biomass as resources for the thermal and electrical energy. Nevertheless, this could be accepted only locally, in some specific situations. Another alternative, which is gaining renewed interest in the scientific community, is the production of reactive MgO from the treatment of brine or seawater.

As shown in figure 1.8, the formation of MgO-SiO_2-H_2O system from the reaction between MgO and SiO_2 in the presence of water can be schematized in four steps: dissolution of MgO, formation of brucite ($Mg(OH)_2$), dissolution of silica (SiO_2) and formation of M-S-H gel. [25] The hydration process of MgO has been extensively studied and two main mechanisms are reported in literature. According to Kitamura *et al.*, the mechanism starts with the formation of brucite on the surface and on the boundaries between single crystal

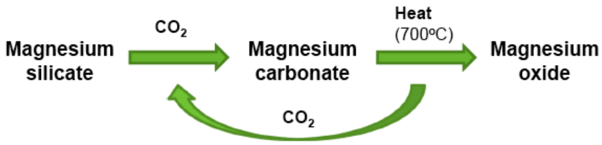

Figure 1.6: Scheme of the Novacem process for the preparation of MgO, starting from magnesium silicate. Reproduced with permission from reference [24].

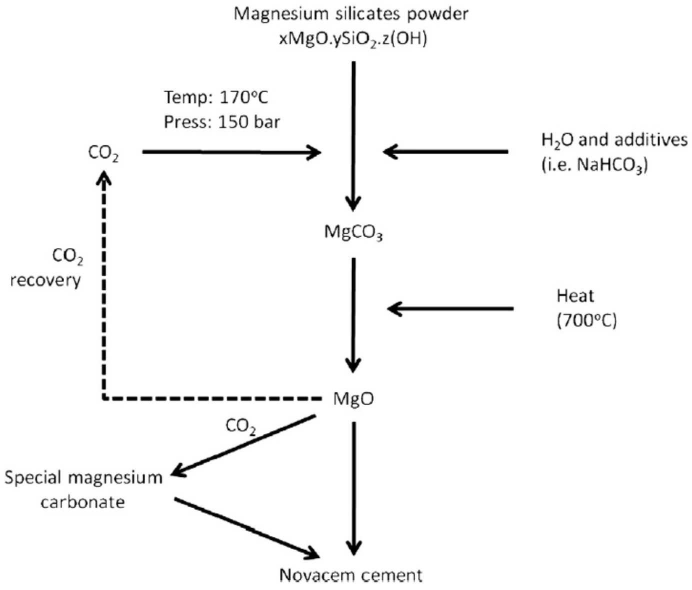

Figure 1.7: Outline of the Novacem process. Reproduced with permission from reference [3].

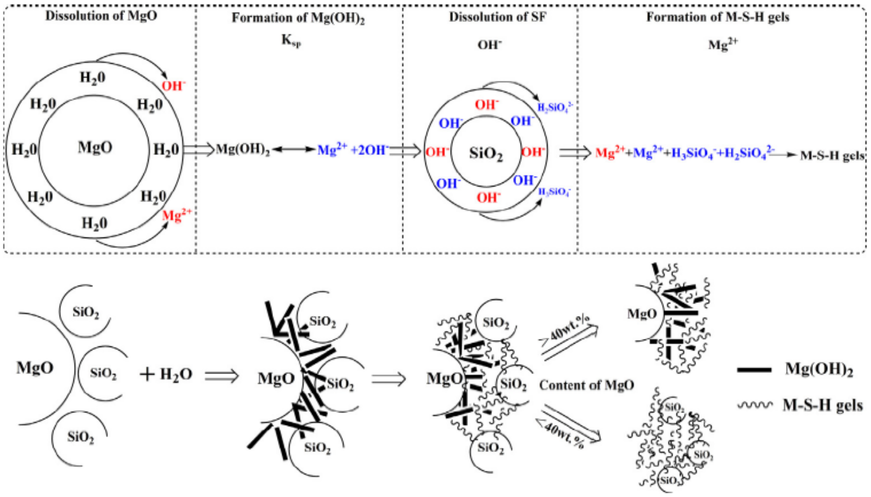

Figure 1.8: Schematic illustration of the reaction process of M-S-H system. Reproduced with permission from reference [26].

policrystalline grains are created. Brucite fills pores and free spaces causing tensions. Another mechanism, proposed by Szczerba *et al.*,[27] consists of the following stages:

$$\mathrm{MgO_{(S)} + H_2O \longrightarrow MgOH^{+}{}_{(surface)} + OH^{-}{}_{(aq)}} \tag{1.6}$$

$$\mathrm{MgOH^{+}{}_{(surface)} + OH^{-}{}_{(aq)} \longrightarrow MgOH^{+} \cdot OH^{-}{}_{(surface)}} \tag{1.7}$$

$$\mathrm{MgOH^{+} \cdot OH^{-}{}_{(surface)} \longrightarrow Mg^{2+}_{(aq)} + 2\,OH^{-}{}_{(aq)}} \tag{1.8}$$

When dissolved ions reach supersaturation in the solution, the precipitation of brucite starts on the surface of MgO, then the process become controlled by water diffusion by brucite layers. If microsilica is present in these conditions, it is partially dissolved and forms silicic acid ($HSiO_3^-$), that can be attracted by $Mg(OH)_2$ on the surface of MgO grains to form a layer and generate poorly crystalline M-S-H phase:[27]

$$\mathrm{HSiO_3^- + Mg(OH)_2 + H_2O \longrightarrow MgHSiO_4 \cdot 2\,H_2O} \tag{1.9}$$

Some potential reactions about M-S-H formation were recently proposed also by Li *et al.*,[26] that reported the formation M-S-H in the form of Chrysotile ($(MgO)_3 \cdot (SiO_2)_2 \cdot (H_2O)_2$) and Talc ($(MgO)_3 \cdot (SiO_2)_4 \cdot H_2O$):

$$\mathrm{MgO + 2\,H^+ \longrightarrow Mg^{2+} + H_2O} \tag{1.10}$$

$$\mathrm{SiO_2 + 2\,OH^- \longrightarrow H_2SiO_4^{2-}} \tag{1.11}$$

$$\mathrm{SiO_2 + OH^- + H_2O \longrightarrow H_3SiO_4^-} \tag{1.12}$$

$$\mathrm{Mg^{2+} + 2\,OH^- \longleftrightarrow Mg(OH)_2} \tag{1.13}$$

$$\mathrm{3\,Mg^{2+} + 6\,OH^- + 2\,SiO_2 \longleftrightarrow (MgO)_3 \cdot (SiO_2)_2 \cdot (H_2O)_2 + H_2O} \tag{1.14}$$

$$\mathrm{3\,Mg^{2+} + 6\,OH^- + 4\,SiO_2 \longleftrightarrow (MgO)_3 \cdot (SiO_2)_4 \cdot H_2O + 2\,H_2O} \tag{1.15}$$

The formation of a layer-lattice type M-S-H has been demonstrated also in sample prepared by mixing hydrated sylicilic acid and magnesium hydroxide[28] or, more recently, in systems produced by blending a $Mg(OH_2)$ slurry with silica fume.[29] In all cases, it has been reported that the composition of M-S-H is mainly dependent on Mg/Si ratio, the curing temperature and pH.[27, 30–32] In particular, pH plays a main role in the formation of M-S-H gel: the concentration of Mg^{2+} increases significantly with the decrease of pH value, while silanols benefit from high values of pH. At pH >10.5 the solubility of Mg^{2+} decreases;[26] while, at pH >9 silica is strongly ionized, becoming more soluble and favoring M-S-H formation.[33, 34]

A renewed interest in M-S-H cements, from both an academic and practical point of view, recently came from the discover of magnesium silicate hydrate phase in radioactive waste disposal applications. M-S-H was found at the clay cement interface, even when calcium based cements were used.

1.2.2 M-S-H in radioactive waste disposal

The occurrence of poorly crystalline magnesium silicate hydrate has been reported in many environments: carbonate successions, contaminated soils, glass alteration, phyllosilicate synthesis, concrete formulations and cement-clay interactions. In the framework of radioactive waste disposal in deep geological repository, low-pH cementitious materials allow to minimize chemical reactions at the interfaces between cement materials and the clay.[32] Recent investigations have shown that the decrease of pH near the cement-clay interface and the diffusion of magnesium ions from the clay towards the cement can lead to a magnesium enriched zone associated with leaching and carbonation, leading to the decalcification of the C-S-H.[35–37] Therefore, there is a growing interest for using M-S-H as potential low-pH cements for nuclear waste encapsulation,[34] *e.g.* M-S-H have been reported as a good matrix for the encapsulation of Magnox sludge, a Mg-Al alloy used to clad natural uranium fuel, which accumulates $Mg(OH)_2$.[32] Depending on their radioactive content and abundance of long-lived radionuclides, radioactive wastes are often described as low, intermediate or high-level.

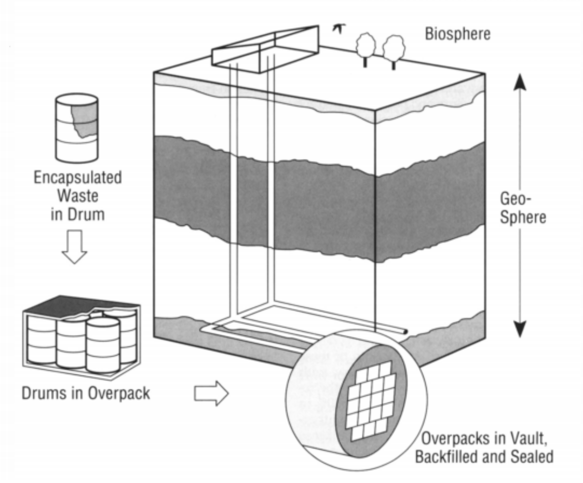

Figure 1.9: Conceptual design for a deep repository for low and intermediate-level radioactive waste. Reproduced with permission from reference [38].

Cements already play a major role in the engineered structures for low and intermediate-level radioactive wastes. They are used both as structural elements and for the encapsulation, to provide a physico-chemical barrier to radionuclides migration.[38, 39] The performances of the multiple barrier (waste, buffer, engineering disturbed zone and host rock) is fundamental [39–41] and the recent discoveries concerning the interactions between the different parts suggest that M-S-H should be preferred to C-S-H in some applications. In figure 1.9, a scheme of the design for a deep repository is shown.

1.2.3 C-S-H and M-S-H

Calcium and magnesium silicate hydrate are analogous gel phases with significantly different structures. Although both phases are poorly crystalline and have a variable chemical composition, their chemistry and differences at the microscale lead to disparities in mechanical properties and durability for the associated cements.[42–44]

C-S-H has been extensively studied and, as anticipated in section 1.1.1, it consists of nanometer-scale solid particles that are packed or agglomerated into randomly oriented structures with gel pores.[10, 12] C-S-H can be treated as a gelled colloid or a granular material, a concept that was first indicated by observations of very large local deformations on drying, in excess of 20%, far greater than is possible for continuous porous materials.[45] In 1999 Sherer[46] reported that since capillary pores (*i.e.* voids originally occupied by excess water) exist in cement paste, then C-S-H does not fills spaces, and he claimed that it is more appropriate to call it "precipitate, rather than gel." Anyway, the local structure of a precipitate is not very different from that of a gel: a continuous solid network is immersed in a continuous liquid phase, both having colloidal dimensions.[46] C-S-H can be appropriately described as an *aggregation of precipitated colloidal-sized particles that undergoes chemical aging*[47] and in the literature it is still commonly referred as a binder gel phase. The microstructure of a cement paste can be described as in figure 1.10: the gel consists of assemblies of hydrated globules immersed in aqueous solvent or air, depending on the equilibrium water content, and the globules are multilamellar objects with an average thickness of about 4.2 nm. The dimension of the globules is dependent on the total water content, while the morphology is very likely depending on the ways of preparing samples.[49] According to the Jennings-Tennis model,[50] two regions of C-S-H can be recognized, based on their density: High density C-S-H and Low Density C-S-H. The resulting porous structure present small gel pores (SGP, $1-3$ nm) and large gel pores (LGP, $3-12$ nm). The water inside the globules is located both in the interlamellar spaces and in very small intraglobular pores (IGP, ≤ 1 nm).[45, 49, 51]

M-S-H is an amorphous phase, showing low intensity and broad X-ray diffraction signals, with short range stacking order, but its structure is not yet fully understood. Roosz *et al.*[32] developed a model to explain its structure, reported

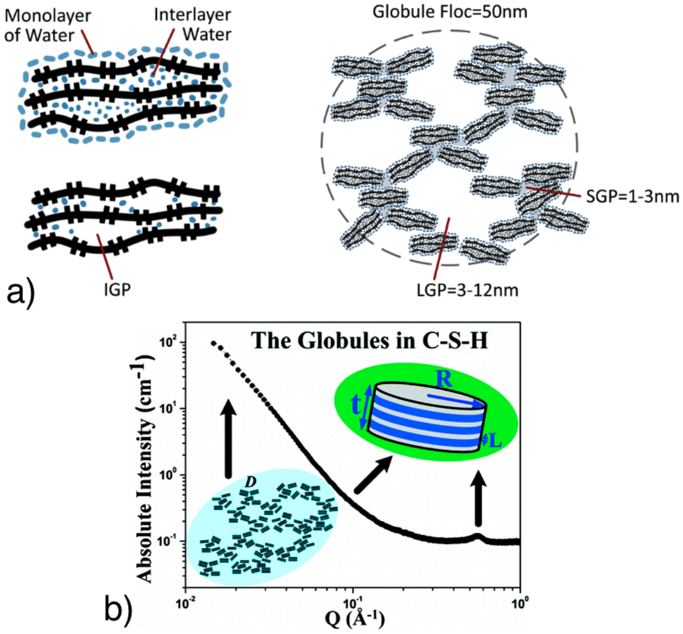

Figure 1.10: a)Jenning model for C-S-H showing packing of globules with large, small and intraglobular gel pores; b) basic building block of C-S-H gel, which were determined by small-angle neutron scattering technique. Adapted with permissions from references [48] and [49]. Copyright (2012) American Chemical Society.

as turbostratic Mg-Si phyllosilicate. Since the only Mg-Si phyllosilicate whose structure has been refined is talc, it was used as starting model for M-S-H (see figure 1.11). Contemporary, Nied *et al.*[34] suggested that M-S-H structure is related to talc at low Mg/Si ratio and to serpentine at high Mg/Si ratio, but further investigation are necessary.

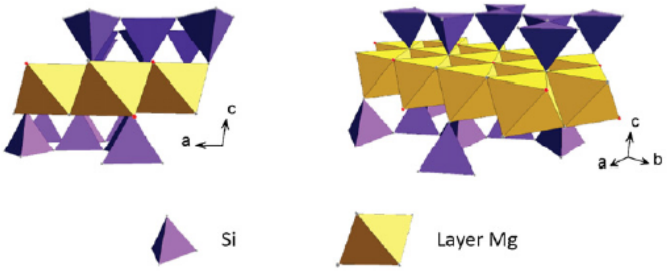

Figure 1.11: Mg-Si phyllosilicate layer structure. Reproduced with permission from reference [32].

The use of wide- and small-angle X-ray scattering is also reported in the literature to investigate the structures of both C-S-H and M-S-H binder phases at a nanoscale level. Recently Chiang *et al.*[43] investigated the multiscale structure of C-S-H and M-S-H binder gel phases, both separately and mixed, and they found significant differences in the primary unit at the nanoscale. While C-S-H primary unit is a multilayer-disk-like globule, M-S-H is composed by polydisperse spherical globules. Figure 1.12 show the results of the model used for pure C-S-H phase at different Ca/Si ratios (fig. 1.12 a), for pure M-S-H phase (MSH in fig. 1.12 b) and for non-pure M-S-H prepared by mixing MgO/SiO_2 (MSH* in fig. 1.12 b). The pure synthesized phases where prepared by precipitation according to the method described by Brew and Glasser.[30, 52] As a consequence of their intrinsic shape differences, C-S-H and M-S-H morphologies also differ, as shown in figure 1.13, and the two gel phases are reported to be essentially immiscible. In synthetic samples containing both calcium and magnesium in the presence of silica sources both C-S-H and M-S-H gel phases form, but, even in this case, they remain segregated in different regions and with very little uptake of calcium in M-S-H and magnesium in C-S-H. This can be also explained considering the different sizes of Mg^{2+} and Ca^{2+} ions (0.8 and 1.1 Å, respectively). Lothenbach *et al.*[44] reported that in C-S-H silica is organized in single chain, while in M-S-H silica sheets are present. Moreover, it is already known that the molar Ca/Si ratio in C-S-H varies approximately from 0.7 to 1.5 and the Mg/Si ratio in M-S-H varies approximately from 0.7 to 1.3.

Anyway, in practical applications, C-S-H and M-S-H phases were found to co-exist in some cases and the formation of separate phases observed in laboratory further confirmed the experimental results reported at the clay/cement interface, even if the reciprocal effect on calcium and magnesium silicate hydrate has not yet been unraveled. [37, 41, 44]

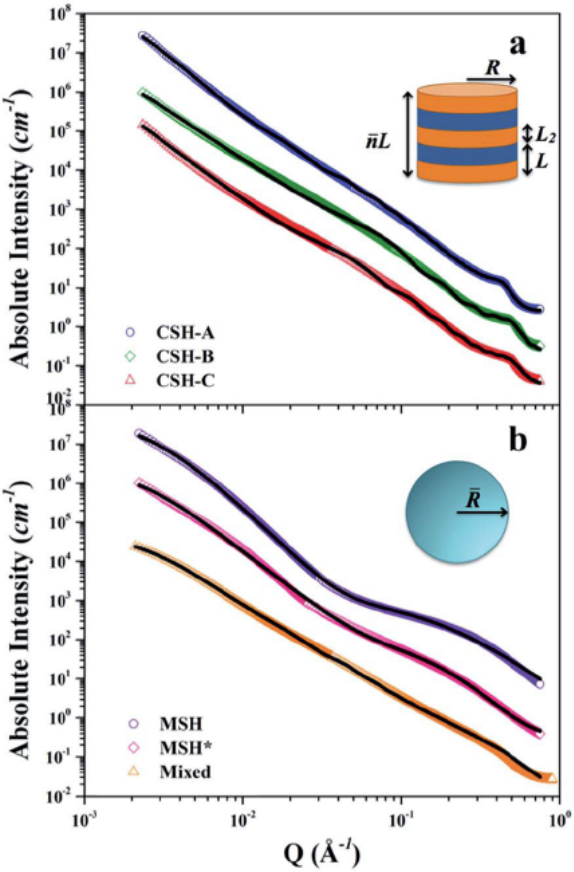

Figure 1.12: Model fitting results of SAXS data for a) C-S-H and b) M-S-H and mixed samples. Fitting curves are denoted by black lines. The experimental and fitting intensities are shifted on the y-axes for the sake of clarity. Reproduced with permission from reference [43].

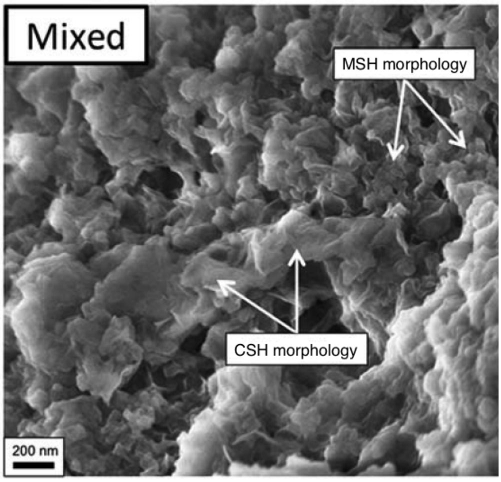

Figure 1.13: SEM image of a mixed M-S-H and C-S-H sample. Reproduced with permission from reference [43].

1.3 Additives

Admixtures for concrete are defined by Taylor *et al.* as "materials, other than hydraulic cements, water or aggregate, that are added immediately before or during mixing". Such materials added to cements during the manufacture are called additives.[9]

1.3.1 Use of additives in traditional cements

In the literature many materials have been reported as additives in Portland cement and in practical applications, they are commonly used to improve specific properties of concrete. The most important ones are added to accelerate or retard setting or hardening, to decrease the amount of water necessary to obtain a given degree of workability or to entrain air, that allow to increase the resistance to damage from freezing.[9, 53] As an example, polymeric superplasticizers have greatly contributed to the improvement of high performances concretes. Such compounds confer high workability, keeping low the water content and, therefore, ensuring a high mechanical strength, shrinkage and durability, since these properties that are strictly linked to the water amount used in the preparation of the cement pastes. It has been previously reported that the increase

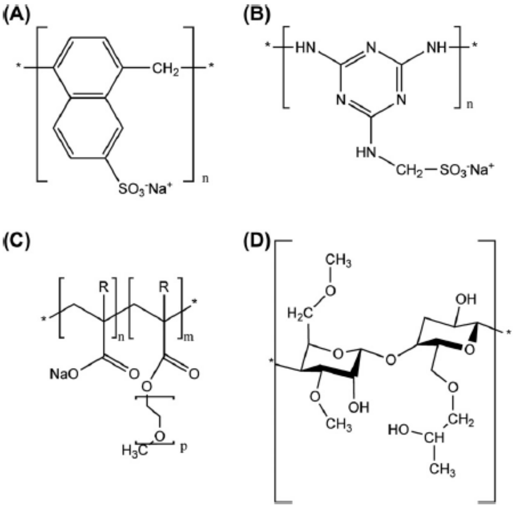

Figure 1.14: Some of the most common used chemical additives: A) polynaphthalen sulphonic salts, B) polymelamine sulphonic salts, C) comb polymer with acrylic (R = H) or methacrylic (R = CH_3) backbone and polyethoxylic side chains, D) methyl hydroxy-ethyl cellulose. Reproduced with permission from reference [2].

of fluidity by the addition of a water reducer is connected with the adsorption of the admixture molecules on the solid surface, that favors the dispersion by modifying the zeta potential.[54–56] The first-generation superplasticizers were sodium salts of sulfonated naphtalene-formaldehyde copolymers or sulfonated melamine-formaldehyde copolymers. Nowadays, polyacrylic or polycarboxylic polymers are commonly preferred, because they not only affect the hydration of PC, but also produce a retardation in the setting time. Figure 1.14 shows some of the most common superplasticizers used with Portland cements.[2, 54]

It has been recently reported that the substitution of anion functions on polycarboxylate (PCE) by PO_4^{2-} or by two vicinal COO^- (see Figure 1.15) supplies an improvement toward the sensitivity to sulfate concentrations and consequently solves the problem of incompatibility with sulfate compounds encountered with classical PCE superplasticizers. Phosphate groups present weak affinity for both ettringite ($Ca_6Al_2(SO_4)_3(OH)_{12} \cdot 26\,H_2O$) and calcite ($CaCO_3$). Nevertheless, they lower the affinity and increase the adsorption on ettringite with respect to calcite, suggesting a potential selectivity for aluminate phases that makes this polymers more sensible to cement composition.[57] The literature, including papers, patents and other descriptions of proprietary materials, is voluminous and some guidelines were even drawn, in order to help the cement industry to tailor the additives (both in terms of molecular weight, side chains lenght and side chains density) for specific applications.[58–60]

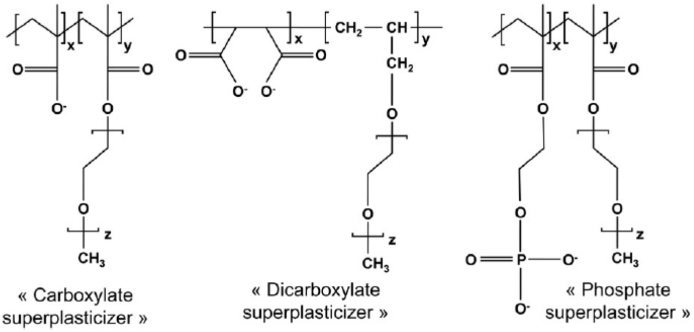

Figure 1.15: Chemical structure of some modified superplasticizers. Reproduced with permission from reference [57].

1.3.2 Sodium hexametaphosphate in MgO/SiO_2 cement

Despite the growing interest in the study of magnesium silicate hydrate, research on the possible additives to be used with this cements is still at its beginning.

In the literature, only one additive is reported as efficient with MgO/SiO_2 cements: sodium hexametaphosphate (HMP), shown in figure 1.16.

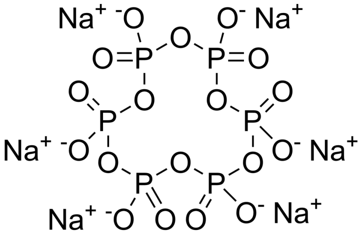

Figure 1.16: Sodium hexametaphosphate. Reproduced with permission from reference [61].

The use of HMP as a water reducer with MgO and silica was reported by Wei and cooworkers in 2011,[31] but they did not focused on its effect, neither they discuss why HMP was chosen among all the possible alternatives. A few years later, the use of HMP as a dispersant was further confirmed and it was evidenced that the use of about 1 wt% of HMP with MgO/SiO_2 allows the reduction of the water/solid ratio and the improvement of the compressive strength, with minimal impact on M-S-H formation.[29, 62] Very recently it was better investigated the role of HMP in MgO/SiO_2 cement pastes, even if it is still unclear why HMP is the only used additive with this kind of cements. Nowadays it is known that HMP inhibits the formation of brucite when MgO is hydrolyzed, probably due to the adsorption of phosphate species on MgO which prevents the nucleation of $Mg(OH)_2$. HMP does not appear to alter the structure of M-S-H, although it retards the kinetic of conversion of amorphous silica to M-S-H.[29] When proper amounts of HMP is used, a rise in Mg^{2+} species in solution occurs, the pH is elevated and SiO_2 dissolution is enhanced. In this conditions, M-S-H can form quickly without competition for Mg^{2+} ions by $Mg(OH)_2$ precipitation.[63] The use of HMP may enable the use of M-S-H as encapsulant for low and high-water content sludges without the occurrence of bleed water, which would need to be decanted and treated as a secondary waste stream if PC was used to treat the sludges.[29] In other applications, HMP is commonly used in the manufacture of soap, metal finishing, water treatment, detergents, metal planting and as deflocculant for clays. In this case, the deflocculant effect occurs by increasing the negative charge on clay micelles. It can also adsorb as an anion to give complexes with the flocculant cations and substitute cations in the double layer of the clay with Na^+ cations. Moreover, HMP is reported to improve the separation of serpentine from pyrite, as it changes the surface potential and disperse the mineral.[64]

In the literature, the adsorption of additives on MgO surface is reported to avoid or inhibit dissolution of magnesia and, in some cases, precipitation of brucite.[27] On the other hand, M-S-H is reported to have sorptive potential for K and Cs and the lowering of pure fluid alkali contents in slag-cement blends is in part attributed to their sorption into M-S-H.[30, 52]

1.3.3 Nanotubular reinforcing additives

Cement based materials are resistant to compression, but they exhibit brittle behavior under tension. Therefore, reinforcing additives are generally used to resist tensile stresses. PC concrete is traditionally reinforced, either by metallic bars uniformly distributed (to avoid macro-cracking) or by randomly oriented steel, glass or synthetic fibres (to avoid microcracks, generally occurring at early stage of hydration). These traditional approaches relate to scale too large to affect the chemical and mechanical damage that begins at the nanoscale. Carbon nanotubes (CNTs) have excellent mechanical properties and, if combined with Portland cement, potentially allow the obtainment of a nanocomposite materials with superlative mechanical properties. Nevertheless, the use of CNTs is hampered by their intrinsically hydrophobic nature and their chemical incompatibility with cement hydrated phases.[65] Moreover, the highly attractive van der Waals forces between CNTs create coherent agglomerate that prove difficult to disperse within the cement paste. The use of proper dispersant, such as polcarboxylates, may lead to a good dispersion without affecting paste workability,[66] but alternative solutions with higher compatibility could be more appropriate.

In the case of M-S-H cements, pH values around 10 are involved and the use of metallic reinforcing bars is hindered, because only at higher pH (~ 12) a passivating film forms on the surface of the steel, making it more resistant to corrosion.[67, 68] Thus, the use of alternative reinforcing fibres is necessary in this case to tailor cements and to allow an enhancement of the properties by bottom-up approach.

There is still little knowledge on the use of reinforcing nanocomposites in Portland cement and even less when alternative cements are used. In order to engineer concrete, it is fundamental to choose reinforcing fibres compatible with the evolving phases commonly present in a cement paste and potential nanomaterials to be used in concrete industry are some nanoclays.[69] Nanoclays are nanoparticles of layered mineral silicate and, depending on their chemical composition and morphology are organized into several classes: montmorillonite, bentonite, kaolinite, hectorite and halloysite. They can be organically-modified to obtain organoclays, hybrid organic-inorganic nanomaterials.[70] Nanotubular clays, such as halloysites and imogolites are perfectly compatible with the hydrated phases of cements and, due to their 1-D geometry may be perfect for reinforcing purpose. As a matter of fact, recent studies showed that incorporation of halloysites can cause a remarkable increase in mechanical performances of polymeric matrixes. Moreover, reinforcement of polymeric materials with imogolites is also reported in the literature.[71]

1.3.3.1 Halloysites

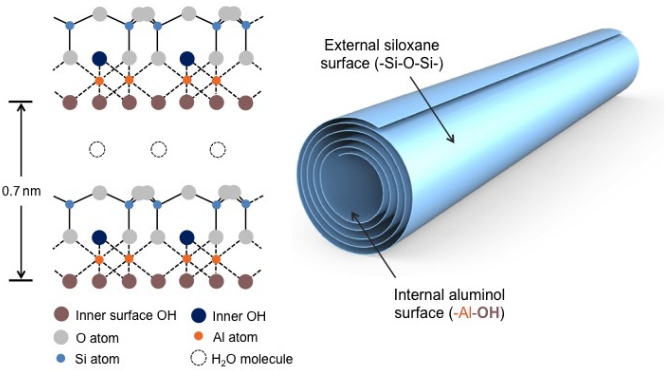

Figure 1.17: Halloysite clay nanotube. Reproduced with permission from reference [72].

Halloysites (HNTs) are aluminosilicate clay minerals, $Al_2Si_2O_5(OH)_4$, that typically form by hydrothermal alteration. HNTs are chemically similar to kaolin, but they typically show a hollow nanotubular structure formed by multiple rolled layers, as shown in figure 1.17. HNTs naturally occur in many morphologies (figure 1.18), but the tubular shape is predominant. Tubular layered halloysites can be found in two common polymorphs: a hydrated form, $Al_2Si_2O_5(OH)_4 \cdot 2\,H_2O$, with interlayer spacing of 10 Å and a anhydrous form, with interlayer spacing of 7 Å.[71, 73] HNTs have length from the submicron scale to several microns (up to 30 μm), inner diameter of 10 - 100 μ and outer diameter of 30 - 190 μm.[74] They exhibit a high length to diameter ratio and a large specific surface area, with SiO_2 on the outer surface and Al_2O_3 on the inner surface.[70]

HNTs are available in abundance in many location around the world, they are low cost and nontoxic.[77, 78] They present high mechanical strength and modulus and they are being used for many varieties of biological and non-biological applications.[79] Above all, HNTs have been used for antibacterial, catalytic, optical, electrical, magnetic and energy storage applications. Some of their key properties, such as the structural stability under heating or in acidic/alkaline dispersion and the site-specific availability for surface modification have been extensively studied in the literature and allow their use in new applications. For

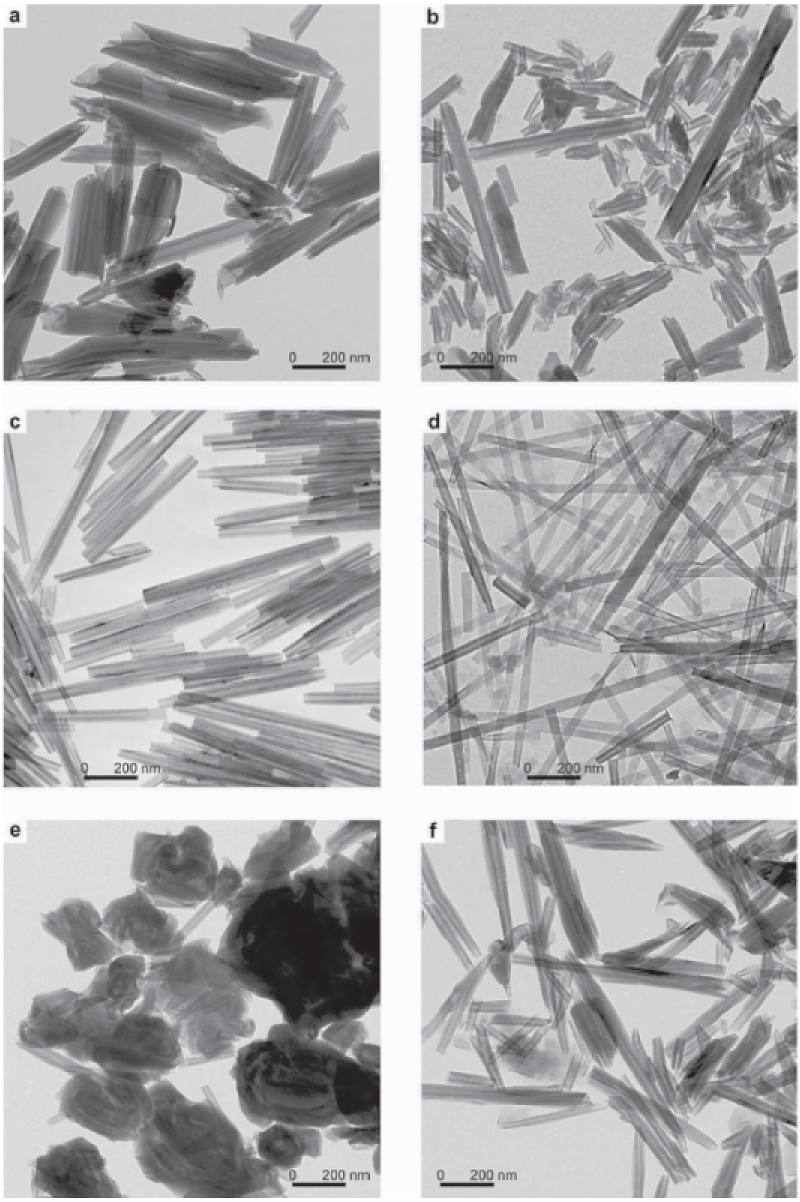

Figure 1.18: TEM images showing different morphologies of halloysites from different geological setting: a) Matauri Bay, New Zeland; b) Dragon Mine, Utah; c) Camel Lake, South Australia; d) Patch Nickel mine, Western Australia; e) Te Puke, New Zeland; f) Jarrahdale, Western Australia. Reproduced with permission from reference [71, p. 98].

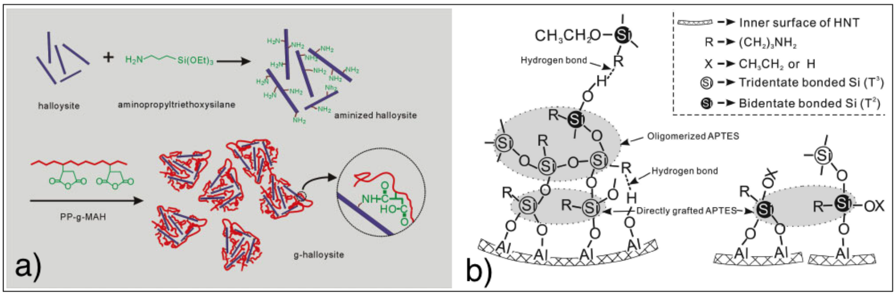

Figure 1.19: a) Schematic surface grafting of HNTs;[75] b) schematic representation of a mechanism of cross-linked network formation and grafting between bidentate bonded Si and AlOH groups. Reproduced with permission from reference [76]. Copyright (2008) American Chemical Society.

example, as shown in figure 1.19, the functionalization of clays with organosilane has been explored in the literature, in order to improve their dispersion in polymer matrices, for reinforcing purposes.[73, 75, 76]

1.3.3.2 Imogolites

Imogolites (IMOs) are aluminum silicate minerals, $Al_2SiO_3(OH)_4$, that naturally occur in soils formed from volcanic ash and in other weathered pyroclastic deposit. IMOs were first described in 1962 by Yoshinaga and Aomine and their name derives from the Japanese word *imogo*, for the brownish yellow soil of Japan where they were found.[80, 81] Imogolites show tube-like morphology, as shown in figure 1.20, consisting of a gibbsite cylinder ($Al(OH)_3$), exposing aluminol groups, with ortosilicate groups in the internal cavity.[82] They typically have inner diameter of 1 nm, outer diameter of 2 - 2.7 nm and length up to 1 μm. IMOs are biocompatible clays with excellent adsorption

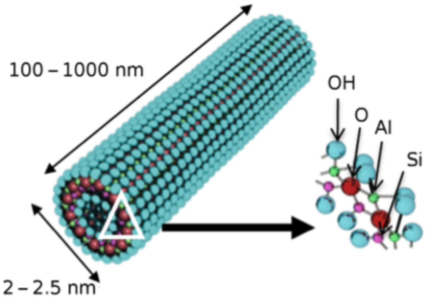

Figure 1.20: Schematic representation of the structure of an imogolite nanotube. Reproduced with permission from reference [83].

properties.[71] Nowadays, they are mainly used as arsenic retention agent, as a catalyst support and as a constituent of nanowires structures.[84] Similar to halloysite, modification of imogolite surface can be achieved taking advantages from the different surface chemistry of the inner and outer sheets. Modifications can be obtained either by direct synthesis methods, which is based on the replacement of the silicon precursors used in the reaction mixture if IMOs are synthetically prepared, or by post-synthetic functionalization.

1.4 Aim of the work

During my PhD I focused my work on the investigation of MgO/SiO_2 cements. The identification of M-S-H phase in key environments related to nuclear waste disposal recently highlighted the importance of developing a full structural characterization of that gel. Moreover, magnesium based cements could be a promising alternative to traditional cements, because of the reduced CO_2 emission associated to MgO/SiO_2 cement production, with respect to the enormous emission related to Portland cement preparation. Aiming to an improvement on the knowledge of M-S-H, which would pave the way for tailoring the macroscopic properties of such eco-sustainable cements by means of a bottom-up approach,[12, 43, 85, 86] my research was focused on the characterization of MgO/SiO_2 cements alone, mixed with traditional cements and in presence of various additives.

First, magnesium silicate hydrate has been structurally characterized with a multi-technique approach, including a detailed solid-state NMR investigation, performed at the CNR and the University of Pisa in the framework of the project FIR2013-RBFR132WSM. The hydration product at ambient conditions of a mixture of highly reactive MgO and SiO_2 has been fully characterized and the structure of M-S-H has been unraveled.

A second part of my PhD concerned the combination of traditional Portland cement with MgO-based cement. I studied the hydration kinetics and phases formed in cementitious formulations prepared by mixing MgO/SiO_2 and Portland cement in different proportions. Even if calcium and magnesium silicate hydrate phases are reported to form separate domains when mixed, the possibility of preparing a paste with both MgO/SiO_2 and PC can not be excluded *a priori*. The possibility of combining MgO/SiO_2 with PC could theoretically lead to the reduction on CO_2 emissions. Moreover, M-S-H phase were found to coexist with C-S-H in practical applications at the cement/clay interface, but the mutual effects of their simultaneous hydration were not known. In this framework, I investigated the reciprocal effects of MgO/SiO_2 and Portland cements when they simultaneously hydrate. The possibility of combining M-S-H and C-S-H gel phases has been exploited and the effects of the composition on the characteristics of the final material was evaluated.

Another fundamental part of my PhD concerned the evaluation of the effects of phosphate additives on the formation and structure of magnesium silicate hydrate. Nowadays, sodium hexametaphosphate is the only used additive with MgO/SiO_2 cement. It is already known that it confers higher fluidity with minimal impact on M-S-H formation, but its mechanism of action is still unknown and in the literature is not reported why exactly this salt was chosen. I decided to investigate also the effect of similar additives to MgO/SiO_2: sodium trimetaphosphate (TMP) and sodium orthophosphate (OP). MgO/SiO_2 pristine sample has been compared to pastes prepared respectively with HMP, TMP and OP, at a constant Mg:P ratio. The hydration reaction has been investigated, while the phases formed during the reaction of hydration have been characterized. I studied the adsorption isotherms of the chosen additives on the pure reactants and on MgO/SiO_2 mixtures, to evaluate their adsorption process and to hypothesize their mechanism of action. Moreover, the micro- and nano-mechanical properties of these samples have been investigated. The elastic modulus of the samples has been evaluated via statistical high-speed nanoindentation (performed in collaboration with Roma III University) and it has been compared to the hardness, evaluated via Vickers hardness test.

The next section of my PhD was dedicated to the investigation of the effects of aluminate phases on MgO/SiO_2 cements. In calcium-based cements tricalcium aluminate phase (C_3A) is responsible for the strength development of the pastes at short hydration time. I decided to evaluate its effect also on magnesium-based cement. Moreover, as anticipated, since in some applications calcium- and magnesium-based cement coexist, it is important to understand the effects of the aluminate phases, commonly present in PC formulations and in clays, on M-S-H binder gel phase. Together with C_3A I decide to study also the effect of imogolite, a nanoclay tubular additive exposing aluminol sites. The idea was to combine the reinforcing purpose of IMO geometry with the desirable effect of the aluminate phase.

Finally, the last part of my PhD was focused on the investigation of the effects of another tubular aluminosilicate nanoclay: halloysite. Similarly to IMOs, HNTs are perfectly compatible with silicate hydrate binder gel phases and therefore could be used as nanotubular reinforcing fibres. HNTs were used both pristine and functionalised with phosphate groups, to evaluate the combination of the reinforcing purpose of the nanoclays with the fluidificant effect of phosphate groups.

2 Materials and Methods

2.1 Materials

In all samples described in this thesis MgO and SiO_2 were mixed in a $1:1$ molar ratio and at predetermined times roughly 1 g of paste was withdrawn and freeze-dried to stop the hydration reaction. These samples were then used for the characterization analyses (section 2.2.1).

Chapter 3 and Chapter 4 are referred to periclase (MgO) and silica fume (SiO_2) supplied by Sigma-Aldrich. CEM I Portland cement, used in Chapter 4, was obtained from Italcementi (Bergamo, Italy). The main characteristics of these powders are summarized in Table 2.1.The reactivity of periclase was measured according to the test proposed by van der Merwe *et al.*[87] and resulted to be 80 s, which indicates that the powder is highly reactive. In a typical reaction, the paste was prepared by manually mixing 4 g of solids with 8 g of milliQ

Table 2.1: Characteristics of the reagents used for the cases of study reported in Chapter 3 and 4. ^{a} Measured by means of a Coulter SA 3100 analyzer.

	MgO	SiO_2	Portland cement
Chemical composition (%)			
$Si0_2$		≥ 99	19.81
Al_2O_3			5.41
Fe_2O_3			3.96
CaO			66.60
MgO	≥ 99		2.50
SO_3			1.25
Na_2O			0.11
K_2O			0.17
SrO			0.04
Mn_2O_3			0.02
P_2O5			0.09
TiO_2			0.2
BET surface area (m^2/g)^a	121 ± 5	395 ± 25	1.5 ± 0.1
Mean particle size (μm)	44	5	20

Table 2.2: Characteristics of the reagents used for the cases of study reported in Chapter 5, 6 and 7. BET surface area was measured by means of a Coulter SA 3100 analyzer. The reactivity of MgO was measured according to the test proposed by van der Merwe *et al.*.[87]

Reagent	Purity (%)	BET (m^2/g)	Reactivity (s)
MgO	$\geq$ 97.5	2.52	40
$Si0_2$	90	4.33	

water, *i.e.* at a water to solid weight ratio (w/s) of 2. The pastes were stored at 20 °C in a polyethylene bag to avoid air contact and prevent carbonation.

For Chapter 5, 6 and 7 highly reactive MgO was obtained by Lehmann&Voss&Co and silica was obtained by Elkem. The main characteristics of these raw materials are summarized in Table 2.2. Typically, the solid was previously dry mixed and then gradually added to milliQ water by manually mixing at a water to solid weight ratio (w/s) of 0.8. The pastes were stored at 20 °C in a polyethylene bag to avoid air contact and prevent carbonation.

For the comparison of different phosphate salts (Chapter 5), commercially available sodium hexametaphosphate ($(NaPO_3)_6$, CarloErba), sodium trimetaphosphate ($(NaPO_3)_3$, CarloErba) and sodium ortophosphate (Na_3PO_4, CarloErba) were used.

Concerning the evaluation of the effects of aluminate additives (Chapter 6), tricalcium aluminate was obtained from Italcementi (Bergamo, Italy) and the imogolites were synthesized by following a method already known in the literature.[88] Aluminum-tri-sec-butoxide, tetraethyl orthosilicate and perchloric acid were purchased from Aldrich.

Halloysite nanoclays (Chapter 7) were purchased from Aldrich. For their functionalization, commercially available 4-bromobutyryl chloride (95%, Aldrich), phosphoric acid (85%, Carlo Erba), triethylamine (>99.9%, Chromanorm), dimethylformamide (>99%, Carlo Erba), acetone (99%, Aldrich), 3-amminopropyltriethoxysilane ($\geq$ 98%, Sigma-Aldrich), NH_4OH (28-30%, Sigma-Aldrich), ε-caprolactone (97%, Sigma-Aldrich), NH_4Cl (99%, Lancaster), NaH (95%, Aldrich), phosphorous oxychloride (98%, Fluka), ethanol (99.2%, Carlo Erba), dichloromethane (99%, Carlo Erba), toluene (99.8%, Aldrich) were used.

2.2 Methods

2.2.1 Characterization of cements

During cement hydration many different reactions occur, as already presented in Chapter 1. In order to follow the reaction of hydration with time and to monitor the binder gel phase formation, a multi-technique approach is commonly applied, including pH measurement, differential scanning calorimetry (DSC), thermogravimetric analysis (TGA), Fourier Transform IR spectroscopy (FTIR), X-ray diffraction analysis (XRD), solid state NMR (SS-NMR), scanning electron microscopy (SEM) and atomic force microscopy (AFM). In particular, monitoring phases evolution with time allows following the variation of the composition, while controlling the kinetic of the hydration reaction and the mechanical properties are technologically important targets. Figure 2.1 shows concrete at different length scale, accessed by different methods.

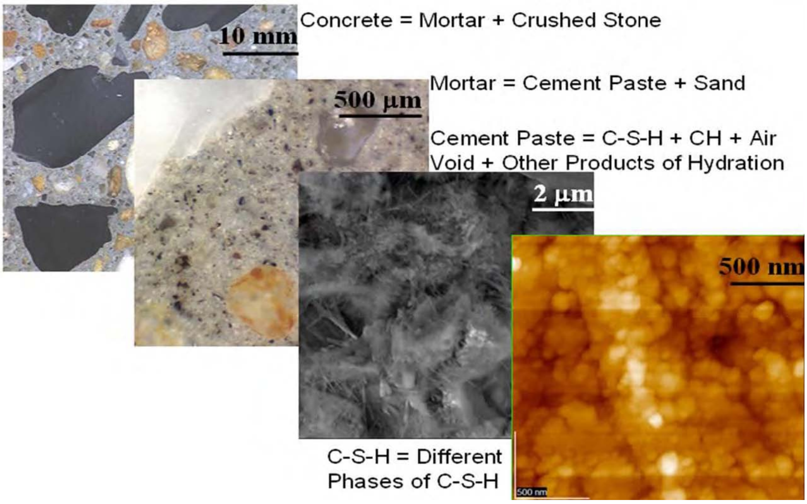

Figure 2.1: Concrete at different length scale. Reproduced with permission from reference [89].

As an example, in figure 2.2 the typical diffraction patterns of M-S-H and C-S-H pure phases are reported, together with the corresponding morphology.

In this thesis pH measurements were performed with a BASIC 20 Crison pH meter using the method previously described by Zhang *et al.*.[90] Briefly, 1 g of the paste was added to a polyethylene container with 10 g of distilled water. The tube was then sealed and constantly stirred in an orbital shaker.

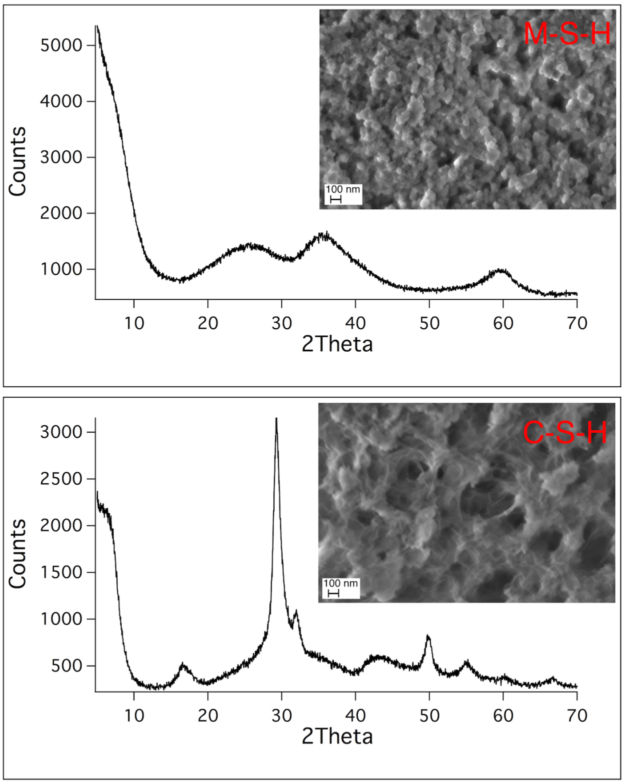

Figure 2.2: XRD diffractograms and SEM images of pure M-S-H and C-S-H phases.

At different time intervals, the solid particles were allowed to settle, and the pH of the supernatant was measured.

Thermogravimetry was conducted on a STD Q600 (TA Instruments, Philadelphia, USA) instrument, operating from room temperature to 1000 °C at 10 °C min^{-1}, in nitrogen flux.

Fourier transform infrared spectra were acquired between 4000 and 400 cm^{-1} by means of a BioRad FTS-40 spectrometer (Biorad, Cambridge, MA, USA) with a DTGS TEC detector (32 scans, resolution of 2 cm^{-1}). 1 mg of each sample was homogenized with 100 mg of KBr and pressed to obtain a pellet.

X-ray diffractograms were recorded with an XRD Bruker New D8 Da Vinci instrument operating at 40 kV and 40 mA, with a Cu source (emitting radiation at a wavelength of 1.54 Å). The scanning region was in the 2θ range 5° - 70°, with 0.05° per step.

Solid-state NMR experiments were carried out on a Varian InfinityPlus 400 spectrometer working at ^{1}H, ^{29}Si and ^{27}Al Larmor frequencies of 400.35, 79.48 and 104.32 MHz, respectively. These experiments were performed at the CNR and the University of Pisa, in the framework of the project FIR2013-

RBFR132WSM.

Relaxation decay data from Carr-Purcell-Meiboom-Gill (CPMG) experiments were inverted to give T_2 distributions by the algorithm UPEN implemented in UpenWin 1.05 software. ^{1}H NMR measurements were performed at 20.7 MHz using a Niumag permanent magnet interfaced with a Stelar PCNMR console. Experimental FIDs acquired on resonance using the solid echo pulse sequence were fitted to a linear combination of a Gaussian and one or two exponential functions using a non-linear least squares procedure implemented in the Mathematica environment. These experiments were performed at the CNR and the University of Pisa, in the framework of the project FIR2013-RBFR132WSM.

Scanning electron microscopy images were collected on uncoated fracture surfaces with a field-emission Σigma (Carl Zeiss) microscope, with an accelerating potential of 2 kV.

For atomic force microscopy analysis, nano- and micro-indentation tests, the samples were cast in polyethylene cylindrical moulds and stored at room temperature at a constant humidity (RH = 97%). After 28 and 60 days from the preparation, the samples were polished and the hydration was stopped by washing with isopropyl alcohol. AFM images were collected with a XE7 system (Park System Corp., Korea). The images were collected in contact mode, using a pyramidal-shaped tip with Al-coating (CONTSCR 10M). Many different areas of 10×10 μm^2, 5×5 μm^2 and 2×2 μm^2 were scanned for each sample.

Surface area measurements were performed by means of a Coulter SA 3100 analyser.

2.2.2 Mini-slump test

Among all the detailed information that can be gained from the application of many techniques, in cement field some easy methods are still common to fastly evaluate material performances, such as the so called mini-slump test. This is a low-cost rapid method that allows to evaluate the fluidity of a cement paste. As already mentioned (see paragraph 1.3.1), the obtainment of a workable paste with the lowest water to cement ratio allows the preparation of cements with high mechanical strength, shrinkage and durability. Mini-slump test is a workability test in which a mini-cone is used (see figure 2.3). This cone has dimensions proportional to those of the Abrams cone, commonly used by workers in the same way to classify different kind of cements.

In this thesis, this apparatus was used for the determination of the spreading out diameters of the investigated samples in presence of different additives. The cone was filled with freshly prepared paste and, after 1 minute, lifted with

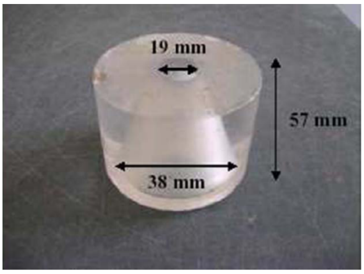

Figure 2.3: The mini-cone. Reproduced with permission from reference [91].

a rapid motion. I then determinate the average diameter of the fresh specimen, as it is connected to the workability of the paste.[92]

2.2.3 Kinetics of hydration

Understanding the kinetic mechanism of cement hydration is useful from both academic and practical points of view.[93] The kinetic of hydration is strictly related to the evolution of the cement microstructure, which in turns influences the mechanical properties and durability of concrete, affecting the strength, elastic modulus, toughness, diffusivity and permeability of the final material.[94] Because of the exothermic nature of the reactions taking place between the anhydrous phases and water during cement hydration, the process in usually monitored by calorimetry.[95]

The hydration of traditional PC powders is a complex multi-stage process with a well-known scheme. Figure 2.4, recorded during cement hydration with isothermal calorimetry, shows the typical heat evolution versus time. Initially (stage I in figure 2.4), water is adsorbed on the surface of the dry powder and a small fraction of silicate and aluminate phases dissolves to produce portlandite, while aluminate phases are converted quickly generating a strong heat evolution. The second period, induction period or dormant period (stage II), is characterized by a very low heat evolution. Stage III, or acceleration period, starts when new silicate and aluminate phases begin to precipitate from the solution, nucleating on the existing grains. In this period the nucleation and growth processes highly increase the rate of the hydration reaction and the formation of several colloidal complex phases. During stage IV, deceleratory period, the hydration rate decreases and, finally, a slow continuous reaction occurs during the diffusional period (stage V), when the chemical rate is determined by the diffusion of the reacting species from the solution through the hydrated phases, to reach the anhydrous grains.[2, 9, 96] Various methods can be used for the investigation of the hydration kinetics, such as heat of

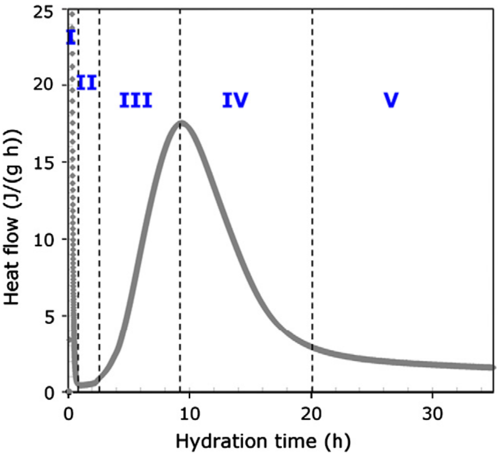

Figure 2.4: Typical evolution of the heat flow during the hydration process of a cement/water paste. Five characteristic stages are indicated. Reproduced with permission from reference [2].

solution calorimetry, semi-adiabatic calorimetry and isothermal calorimetry (IC). IC is probably the most known technique to access the hydration kinetics in cement field, but it allows to follow the process only in the first days of hydration, because at longer times the evolved heat becomes too low to be distinguished from the instrumental baseline.[97] To overcome this lack, in 2002 an alternative method based on differential scanning calorimetry was proposed by Damasceni *et al.*.[95] Since DSC method is based on discrete measurements, it is not limited by the evolved heat and allows the acquisition of data until the very end of the hydration process. Moreover, this method has been demonstrated to be in full agreement with IC technique. This indirect approach is based on the quantification of the free water as Free Water Index (FWI). Samples are frozen and then melted at constant rate, to observe the melting peak of the free, still unreacted, water. This signal, shown in fig. 2.5, decreases with time, as water is consumed by the hydration reaction. The peak is integrated to extract the melting enthalpy of water ΔH_{exp} and to calculate FWI:

$$FWI = \frac{\Delta H_{exp}}{\phi_w \Delta H_{theor}} \tag{2.1}$$

where ϕ_w is the original weight fraction of water in the paste and ΔH_{theor} is the theoretical value of the melting enthalpy of water (333.4 J/g).[2, 51, 54]
The kinetic analysis can be further used to obtain information about the activation energies and the rate constants of the developing hydrated phases. In the last decades, the nucleation and growth period taking place during the hydration of tricalcium silicate/water pastes was modeled by the Avrami-Erove'ev kinetic law to evaluate the rate constants of the process.[98, 99] In

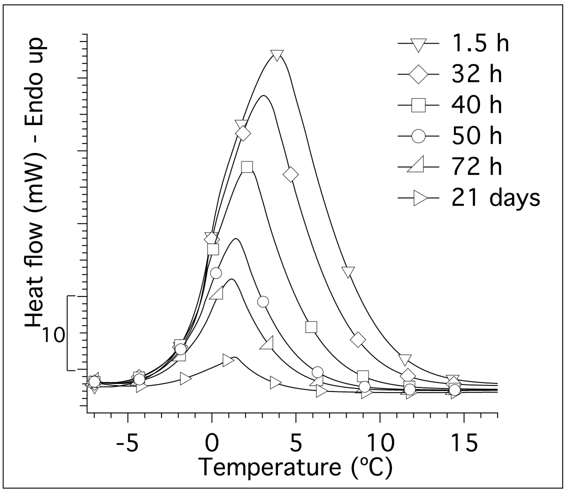

Figure 2.5: Evolution of the melting enthalpy of water during the hydration of a Portland cement sample. Reprinted with permission from Paper V. Copyright (2017) American Chemical Society.

this framework, DSC method was used, for example, to investigate the effect of some of the most used cement additives, by applying a combined model with the Avrami-Erove'ev law and a three-dimensional diffusion equation.[54] More recently, some authors pointed out that the Avrami-Erove'ev equation can not completely satisfy the cement hydration process. Above all, the assumption that the probability of nucleation of the hydrating phases is the same in the whole volume is not appropriate to describe the process of hydration of cements, as it is commonly accepted that it occurs preferentially at the grain boundaries. The Boundary Nucleation and Growth Model (BNGM) derived by Thomas overcame this inconsistency. This model, originally developed for solid phase transformations, can properly describe the process of cement hydration, even using less parameters than the Avrami-Erove'ev model. BNGM describes the hydration kinetics with two independent rate constants: k_B, which describes the rate at which the surfaces become covered with hydration products and k_G, that is the rate at which the pore space between the particles fills in with products.[97, 100] BNGM model has been used in the literature for calcium-based cements (Portland cement and tricalcium silicate), but Thomas *et al.*[101] recently reported that it can be successfully applied also to the hydration process of MgO. The original BNGM approach has been, then, modified to directly analyze the time evolution of the Free Water Index as accessed by the DSC protocol. Therefore, the application of a generalized BNGM fitting combined with three-dimensional diffusional model has been used to describe quantitatively the hydration process accessed by DSC. Figure 2.6

shows the FWI *vs.* time experimental data acquired for a MgO/SiO_2 cement, together with the best fitting curve obtained by BNGM + diffusional combined model. The model accurately describes all the three hydration periods accessed by DSC method: induction period, nucleation and growth period, diffusional period. The curve shows a short initial induction period, lasting until time t_i, where FWI remains ≈ 1. Then, the nucleation and growth period starts, with a consistent decrease of FWI as a function time. Finally, the diffusional period occurs, starting at time t_d, where the change in the curve slope suggests that the rate limiting process becomes a diffusion limited behavior, similarly to the Portland case.

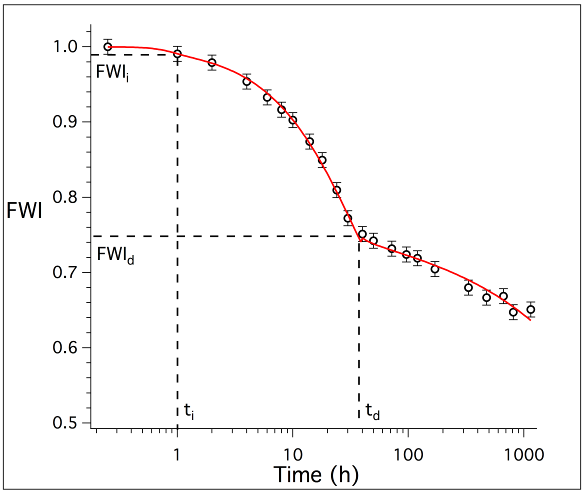

Figure 2.6: Hydration kinetics of MgO/SiO_2 paste reported as FWI *vs.* time. Black markers represent the experimental data; red line is the global fitting curves according to the BNGM + diffusional model. Reprinted with permission from Paper V. Copyright (2017) American Chemical Society.

In this thesis, DSC measurements were performed using a DSC Q2000 calorimeter from TA Instruments (New Castle, USA). About 50 mg of paste was transferred soon after mixing in a steel pan (diameter 7.4 mm, capacity 60 μL) and sealed with an appropriate cover, equipped with an O-ring, to avoid water leaking. The pan was maintained at 20 °C in a thermostatic bath. Samples were periodically analyzed with the following temperature program: equilibrate to -60 °C, isothermal for 4 minutes, ramp from -60 °C to +30 °C at 5 °C/min.

2.2.4 Low-temperature differential scanning calorimetry

Low-temperature differential scanning calorimetry (LT-DSC) can be used to investigate the microstructure of cement pastes, as it is able to provide important information on the porosity and on the fractality of the porous evolving matrices by means of rapid and nondestructive measurements. In particular, LT-DSC gives a semiquantitative estimation of the evolving porosity (capillary, small gel, and large gel pores), the depercolation threshold of the capillary pores, and the fractal dimension associated with the probed porosity.[51, 102–107] The method relies on the experimental evidence that when a pure substance is confined in nanometric cavities, the equilibrium conditions of its solid, liquid and gas phases depend on the curvature of the interface.[108, 109] For this reason, the solidification/melting temperature of a liquid confined in a porous material depends on the size of the pores and the energy involved in the phase transition is directly related to the pore volume, assuming that the liquid saturates the pores. Thermoporometry can also provide information on the shape of the pores, by comparing the cooling and heating thermograms obtained in the temperature range from ambient to -80 °C.[102, 108, 110]

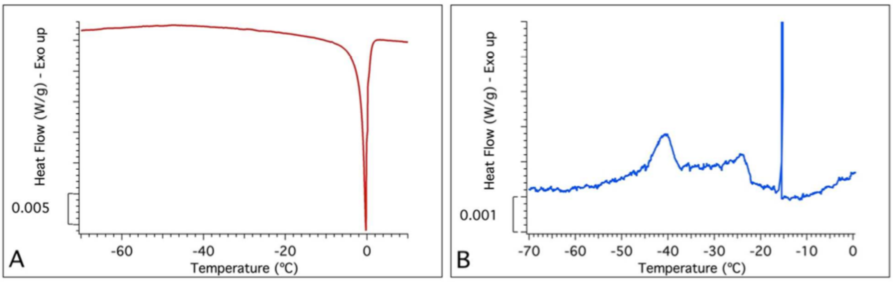

Figure 2.7: Heating scan (A) and cooling scan (B) of a typical LT-DSC thermogram recorded on a cementitious sample saturated with water. Reprinted with permission from Paper V. Copyright (2017) American Chemical Society.

The heating scans (from -80 °C to room temperature) of the DSC thermograms (an example is reported in Figure 2.7 A) show a single hump in the -50 °C - 0 °C temperature range due to the characteristics of the cement microstructure, and in particular to the continuous distribution of the pore sizes. The melting occurs progressively from the fractions confined in the smallest cavities to the fractions present in the largest ones. By contrast, the freezing process occurs in a discontinuous way and the cooling scans show some definite peaks (figure 2.7 B). This behavior arises from the combination of heterogeneous and homogeneous freezing mechanisms of water. At low degree of cooling, only the heterogeneous nucleation is possible,[111] while at lower temperature the size of the pores decreases and the homogeneous nucleation process can occur. In

this conditions, the process starts at the pore entrance, where the liquid water is in contact with the surrounding ice, which constitutes a preferential site for the nucleation (for more detailed information the reader can refer to the publication Paper V, reprinted with permission at the end of this thesis).[111, 112]
In the case of cement, the developing phases originate three classes of nanometric porosities: interlayer lamellar porosity (IGP < 1 nm), small gel pores (SGP $1-3$ nm, $\sim$-40°C) and large gel pores (LGP $3-12$ nm, -20/-35 °C). The water inside IGP cannot freeze and, thus, can not be detected by LT-DSC. The amount of water in SGP, LGP and capillary pores can be calculated by integrating each peak and considering the variation with temperature of the standard enthalpy of fusion of ice.[113]

LT-DSC measurements were performed by means of a Q2000 DSC, TA Instruments (New Castle, USA). Samples were prepared by manually mixing water with solid; after 24 hours of hydration they were crashed and put under water at 20 °C, in order to saturate the porosity. The temperature program for each measurement was: ramp from 5 °C to -80 °C at 0.5 °C/min; equilibrate to 25 °C.

2.2.5 Mechanical properties at the nanoscale

Although cementitious construction materials are mainly used in a large scale, fundamental mechanical properties (such as strength, ductility, creep, shrinkage and fracture) largely depend on structural elements and phenomena that are effective at the micro- and nano-scale.[89] Therefore, measuring mechanical properties at the nanoscale is a key to understand inhomogeneous materials.[114] Porosity, density and morphology are major factors controlling strength and modulus of cements, together with the initial composition.[115] However, the strong heterogeneity and multiscale structure of cements make the study of their mechanical properties very challenging. One of the main goal is that of controlling macroscopic properties from the nanoscale level, starting from the determination of the local properties, particularly the hardness and elastic modulus of cementitious materials. Nowadays, the improved availability of depth-sensing micro- and nanoindentation has made possible to study mechanical properties of various phases in cement-based materials.[86, 116] Also AFM can be potentially applied to measure mechanical properties at smaller scale, but the surface preparation is much more difficult and thus it is not widely used in this aspect.[114]

2.2.5.1 Microindentation

In the literature, microindentation apparatus were extensively used to carry out microstrength testing.[117] A fixed load is applied and then the dimension of the resultant indentation is measured by microscopic analysis. Among the varieties of indentor geometry, Vickers indentor is probably one of the most used and Vickers test is commonly used for both hardness and microhardness test. Vicker indenter has a diamond shape (square based pyramid) and the hardness value, H_v (MPa), is defined as the ratio between the applied load and the contact area, determined from the dimension of the residual indentation (see figure 2.8a):

$$H_v = \frac{P}{A} = 2P\frac{\frac{sin\alpha}{2}}{d^2} = 1.8544\frac{P}{d^2} \tag{2.2}$$

where P is the load (N), A is the surface area of indentation (mm^2) and α is the face of angle of indenter at 136°.[118] The corresponding Vickers hardness number, HV, is:

$$HV = \frac{F}{A} = 1.8544\frac{F}{d^2} \tag{2.3}$$

where F is the force (kgf) and A the surface area of indentation (mm^2). HV is expressed in kilograms-force per square millimeter (kgf/mm^2) and is usually given without units.[119][120] The contact region under the indenter is reported to consist of an expanding core, in an ideally plastic region, with an elastic matrix that lies beyond it (see figure 2.8b). After the indentation, the diagonals of the contact area should be measured and, since it has been reported in the literature that it is particularly important to be accurate in this step, the preparation of the surface results to be crucial.[118] Typically, the extent of an indentation depends on the material phase and it is important to choose properly the load and time of the analysis to obtain reliable results.[121]

2.2.5.2 Nanoindentation

Similarly to microindentation, nanoindentation tests consist of establishing contact between an indenter and a sample. A typical test is composed of a loading and unloading response. In this case, the load (P) and the penetration depth (h) are measured and Berkovich indenter are popular tips with three-sided pyramid geometry. Figure 2.9 shows a P-h curve for a test. The analysis of P-h curves allows the derivation of the indentation hardness (H) and elastic modulus (M):

$$H = \frac{P_{max}}{A_C} \tag{2.4}$$

$$M = \frac{\sqrt{\Pi}}{2}\frac{S}{\sqrt{A_C}} \tag{2.5}$$

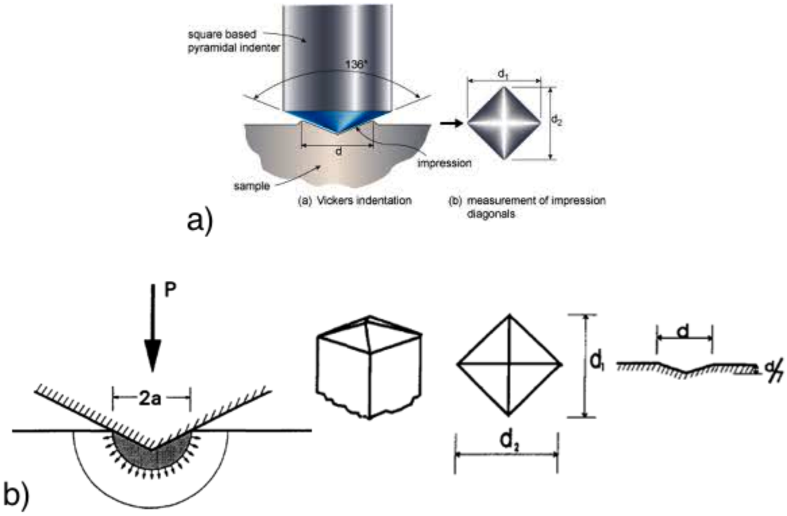

Figure 2.8: a) Scheme of the Vickers hardness test method.[122] b) Simplified description of the stress field under the indenter assuming elastic-plastic behavior, Vickers indenter and indentation. P = load, 2a = d = indentation diagonal. Adapted with permission from reference [121].

where the unloading indentation stiffness is $S = (dP/dh)_{h=h_{max}}$ and A_C is the projected area of the hardness impression. The contact area A_C can be extrapolated from the maximum depth with the Oliver and Pharr method ($P = A_C(h - h_f)^m$, where A_C, h_f and m are material constants that can be determined by at least squares fitting procedure).[123, 124] Figure 2.10 shows typical P-h curve for heterogeneous samples, such as cements. E_r, the effective modulus of the material, is obtained using the equation $\frac{1}{E_r} = \frac{1-\nu^2}{E} + \frac{1-\nu_i^2}{E_i}$, where where ν_i and E_i are the Poisson coefficient and the elastic properties of the diamond indenter and v is the Poisson coefficient of the measured phase.[125] In these case, a large array of nanoindentation tests needs to be carried out and analyzed to discriminate the different phases. Nanoindentation analysis may be performed over a regular grid, while imaging the location of each indent to determine the phase investigated. FESEM (field emission scanning electron microscope) is used to serve this purpose, together with EDS (quantitative energy dispersive spectrometer) analysis that allows the determination of phases composition point-by-point.[89] By nanoindentation mapping it is possible to correlate mechanical properties of specific phases with their morphology, as shown in figure 2.11. In table 2.3, elastic modulus and hardness of different constituents of PC are reported.

Furthermore, an improved high-speed statistical nanoindentation method has been recently proposed for highly heterogeneous matrices. The method, further

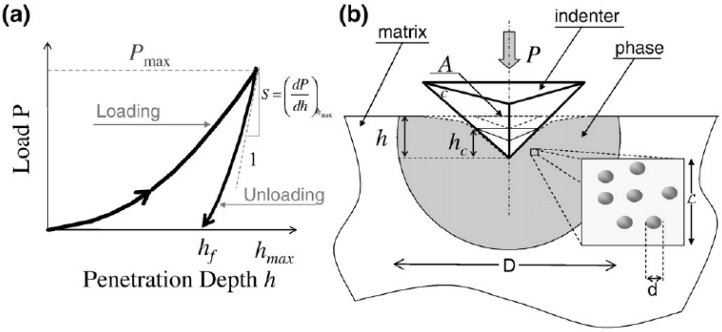

Figure 2.9: a) A typical load-indentation depth P-h curve; b) Schematic representation of an indentation test with a Berkovic indenter on a homogeneous phase. Reproduced with permission from reference [123].

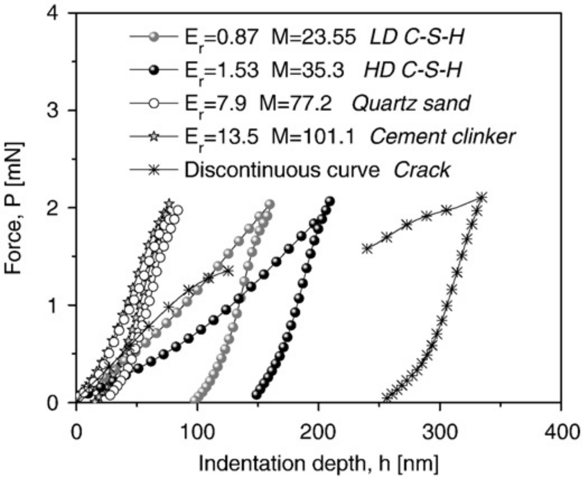

Figure 2.10: Indentation response force *vs.* indentation depth. M is the elastic modulus and E_r is the effective modulus of the material. Reproduced with permission from reference [123].

implemented and optimized by several groups, is based on the realization of grids of hundreds of nanoindentation tests coupled with a statistical analysis (deconvolution) for the identification of the different mechanical phases and their distribution over the sampled area. Assuming that the distribution of the elastic modulus is well approximated by a Gaussian curve, the average property of each phase can by obtained by fitting the experimental frequency distribution of the mechanical property either with the theoretical probability density function or with the cumulative distribution function.[126] The principle of high speed statistical nanoindentation is described in figure 2.12.

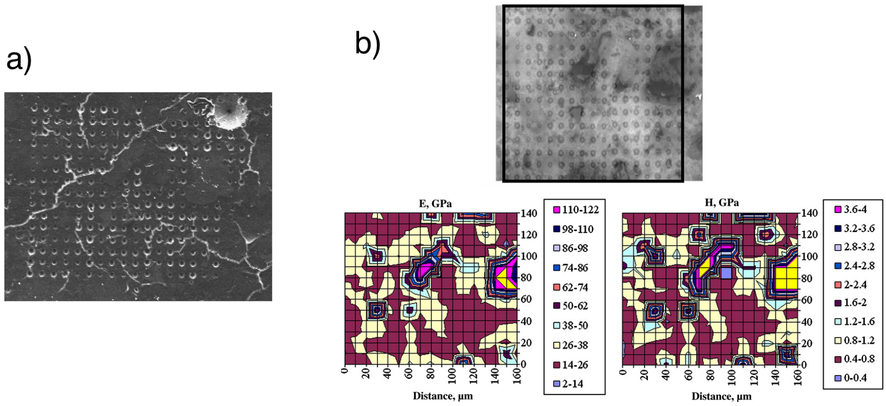

Figure 2.11: a) Secondary electron image of the area of indents on the cement sample. Note how the indented size, or even the presence of a visible indents, varies with the phase type, in response to mechanical properties. b) Maps of mechanical properties (elastic modulus E and hardness H) together with the corresponding optical microscopic image. Adapted with permission from reference [116].

In this thesis, Vickers micro-hardness tests were performed by a micro indenter (Remet HX-1000 TM) with a Vickers tip for a load of 25 g for 10 s of indentation time at room temperature. To obtain reliable values, 10 points were tested for each sample. The size of indentation impression was measured by an optical microscope, with the software AUTOVICKERS (Remet).

Nano-indentation tests were performed using a Keysight G200 Nano Indenter, equipped with a Nano-positioning stage, DCM II head with a Berkovich tip, equipped with high-speed (express test) options. Nanoindenter frame stiffness and tip area function were calibrated by testing on a fused quartz reference

Table 2.3: Comparison of the elastic moduli and hardness of different phases present in cement. S.D. = standard deviation. *a*: data otained by nanoindentation analysis;[125] *b*: data obtained by nanoindentation mapping test.[116].

	Elastic Modulus		Hardness	
phase	E (GPa)	S.D.	H (GPa)	S.D.
C_3S^a	135	7	8.7	0.5
C_2S^a	130	20	8.0	1.0
C_3A^a	145	10	10.8	0.7
C_4AF^a	125	5	9.5	1.4
C_3S^a	135	7	8.7	0.5
LD-CSH^b	23.4	3.4	0.73	0.15
HD-CSH^b	31.4	2.1	1.27	0.18

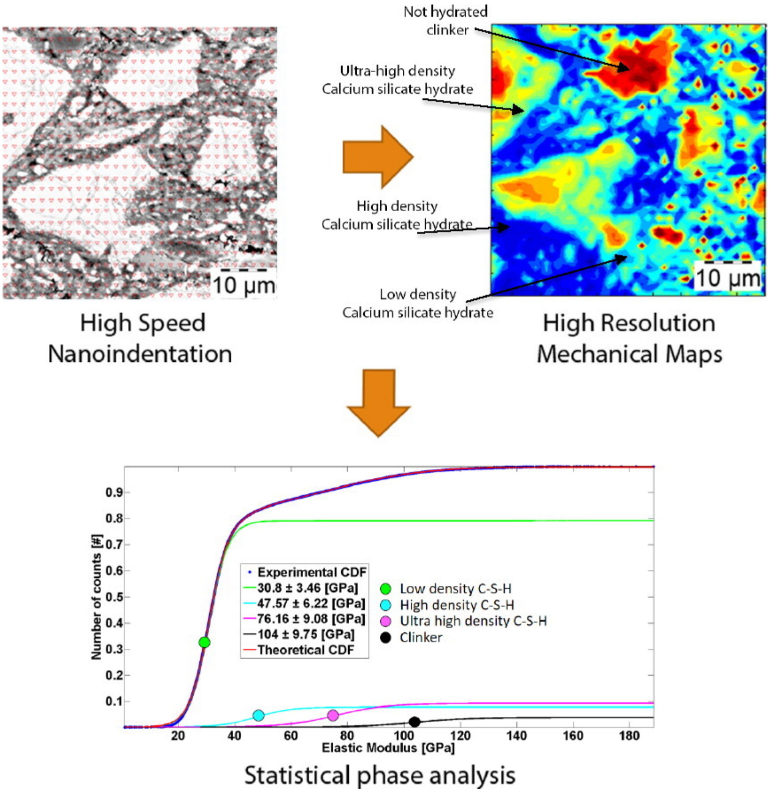

Figure 2.12: Statistical nanoindentation method to map the mechanical properties of multi-phase materials: a grid of tests is performed on calcium-based cement and the mechanical map is extracted by the statistical analysis. The cumulative distribution function plot of obtained properties (elastic modulus and/or hardness) are analyzed through deconvolution processes, in order to identify mechanical phases. Reproduced with permission from reference [126].

sample, according to the ISO 14577 standard. High-speed tests were obtained by setting up multiple arrays of 15 x 15 indents, over an area of 100 x 100 μm^2, with a maximum depth of 300 nm. Statistical deconvolution on the Cumulative Distribution Functions (CDF) was performed to obtain the number, distribution and elastic moduli of the mechanical phases in the material. These experiments were performed in the framework of a collaboration with with Riccardo Moscatelli and Marco Sebastiani from the University of Rome III.

2.2.6 Adsorption isotherms

Adsorption process concerns the adhesion of atoms, ions, or molecules from a gas, liquid or dissolved solid to a surface. The adsorption isotherms are curves relating the amount of adsorbed species as a function of pressure (if gas) or concentration (if liquid). The quantity adsorbed is commonly normalized by the mass of the adsorbent to allow comparison between different materials.[127–130] The isotherm shape depends on the mechanism of adsorption and on the affinity between the adsorbent and the surface and many models were developed to describe them.[127] Moreover, investigating the adsorption isotherms at different temperatures can allow the evaluation of the enthalpic and entropic contributions to the interface interaction.[131] In solution, the study of the mechanism of adsorption is important for the comprehension of various phenomena and is one of the most commonly used method to characterize the interaction between additives and porous surfaces.

In cement field, understanding the mechanism of adsorption of the additives is important from many points of view and several articles report the study of superplasticizers adsorption on PC.[132–135]

2.2.6.1 Classification of the adsorption isotherms

One of the most detailed classification for the Solid State Adsorption (SSA) isotherms was proposed by Giles *et al.*.[127, 136] The authors provided a theoretical treatment for the classification of solute adsorption able to describe any curve shape, valid whether the adsorbing surface is energetically uniform or nonuniform. Figure 2.13 shows the classification they made in four main classes. The *S-curve* relates to a cooperative adsorption and occurs when solute-solute forces are stronger than the solute-substrate ones. Therefore, in this type of isotherms, molecules generally adsorb as cluster (see also fig. 2.14 a). The *L-curve*, *i.e. Langmuir*, is the most common type and is well described by the Langmuir model. In this case the adsorption is favored and solute-substrate forces are stronger than solute-solute ones (see fig. 2.14 b). The *H-curve*, *i.e. high-affinity*, shows up when the adsorbate-substrate affinity is particularly high. Finally, *C-curve* is the *constant partition* case. This class can be explained considering an increase of surface available for the adsorption: when the substrate is saturated new adsorption sites are generated and, therefore, the adsorbent surface increases.

All the groups are further divided in five subgroups. Subgroup *1* shows up when solute concentration is insufficient to complete a monolayer on the solid surface. In subgroup *2* a monolayer has been completed, at the plateau. When a second layer of asdorbent rapidly form on the surface the plateau can be

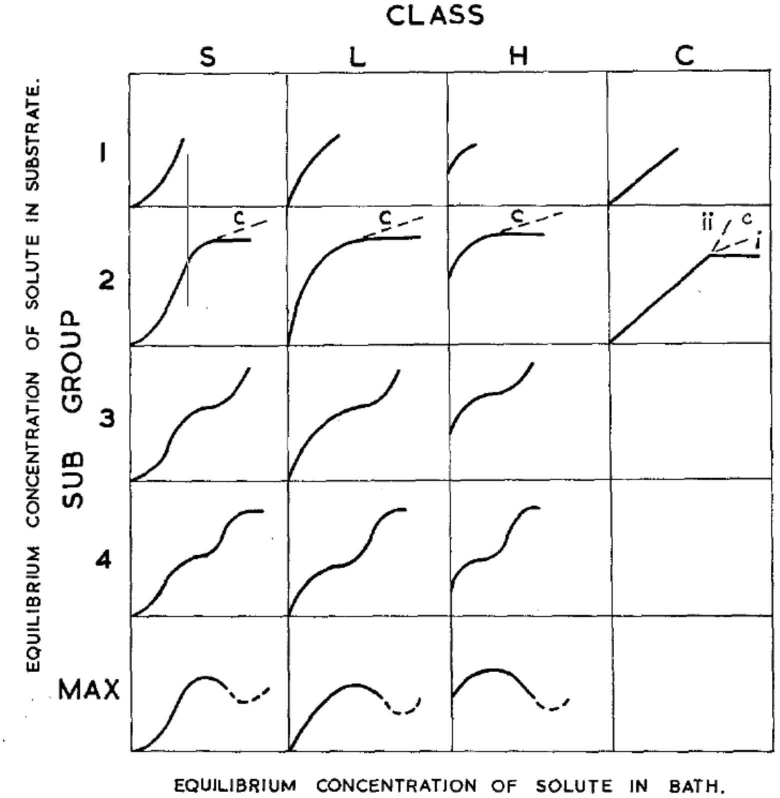

Figure 2.13: System of isotherm classification. Reproduced with permission from reference [127].

absent and the curve has an inflection point and keeps on rising. This behavior is described by subgroup *3*. In subgroup *4* generally a second layer is adsorbed, but sometimes it can be due to a molecular reorganization on the substrate. Finally, subgroup *MAX* related to desorption phenomena, occurring at high concentration and strong solute-solute interaction.[127, 136]

2.2.6.2 Equilibrium models

Over the years, a wide variety of equilibrium isotherm models have been formulated: Langmuir, Freundlich, Branauer-Emmett-Teller, Sips...[129] The concave isotherm, *L-* or *H-curve*, is the most widely met. This type of isotherm can be well described if proper models are used,[137, 138] including Langmuir and Freundlich models that are probably the most common:

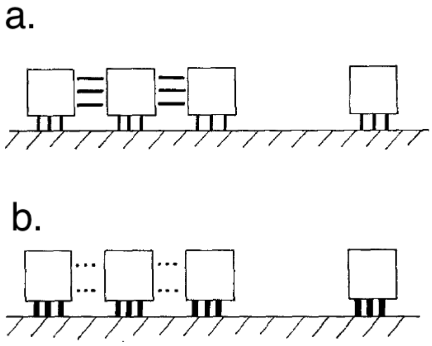

Figure 2.14: Sketch illustrating bonding effects at the substrate surface. a. The solute-solute forces are strong relative to those between solute and substrate. b. There are relatively strong attractive forces between solute molecules and substrate, but very weak forces between solute molecules themselves. Adapted with permission from reference [127].

- **Langmuir Model** Langmuir model was originally derived for gas adsorption but it can be applied also to liquid adsorption on solid surface, by replacing the gas pressure with solute concentration. This model assumes monolayer adsorption on a finite number of equivalent sites. Langmuir equation can be expressed as:

  $$\frac{y}{y_{max}} = \frac{K * c}{(1 + K * c)} \tag{2.6}$$

  where y is the amount of adsorbate in the adsorbent at equilibrium, y_{max} is the amount of substance in a completed monolayer (*i.e.* the maximum monolayer coverage capacity), c is the adsorbate equilibrium concentration in solution and K is the Langmuir adsorption equilibrium constant.[129, 139]

- **Freundlich Model** Freundlich model can be applied to multilayer adsorption and is widely applied to heterogeneous systems.[129] This model is based on the following relation:

  $$Q = FC^n \tag{2.7}$$

  where Q is the adsorbed quantity, C is the remained solute concentration, F is the Freundlich isotherm constant and n is a constant related to the adsorption intensity ($n < 1$).[129, 137]

In this thesis, suspensions obtained by adding 10 mL of the phosphate additive solutions at different concentrations to 0.8 mg of solid (MgO, SiO_2 and

MgO/SiO_2) were kept under agitation at controlled temperature for predetermined times. The suspensions were then removed from the thermostatic bath and rapidly transferred to a multispeed centrifuge (4 minutes at 9000 rpm). The liquids were filtered by Whatman cellulose nitrate membranes (0.45 μm) and submitted to ICP analysis. The amount of additive adsorbed on the substrate was calculated by subtraction from the P concentration in solution.

3 Structural characterization of magnesium silicate hydrate

This chapter is focused on the investigation of the formation of M-S-H by hydration of highly reactive MgO and silica fume. In spite of the potential importance of this new class of cements, that can be produced with minimal CO_2 emissions[3, 5, 14] and has been demonstrated to be particularly important in the containment of radioactive wastes,[29, 42, 90, 140, 141] the knowledge of the structural features of M-S-H and their dependence on reaction conditions are limited, mostly as a consequence of M-S-H amorphous nature.
In this framework, we used a multidisciplinary approach that allowed a detailed characterization of the structural features of M-S-H over different spatial scales, making possible the identification and quantification of coexisting talc-like and chrysotile-like nanometric domains. Two recent works proposed talc[32] and lizardite[29] as structural models for M-S-H, but the structural features of the domains in the M-S-H we investigated resemble much more to a mixture of talc and chrysotile. Therefore, this work represents a significant step towards the detailed characterization of M-S-H, which is fundamental to develop this cement and to tailor the macroscopic properties from the modification at the nanoscale. The product of hydration of MgO/SiO_2 mixture at a water to solid ratio $w/s = 2$ have been characterized for one month with a multi-technique approach (pH measurements, thermogravimetry and differential thermal analysis, X-ray powder diffraction, Solid State NMR, infrared spectroscopy and scanning electron microscopy). We applied for the first time quantitative ^{29}Si measurements combined with ^{1}H and two-dimensional ^{1}H - ^{29}Si experiments to gain insight into the structural features of the M-S-H binding phase on a molecular and nanometric scale. In particular, the use of SS-NMR in this study has been fundamental for the deep comprehension of the structural features of M-S-H, since it is an extremely powerful technique for the investigation of the structural and dynamic characteristics of complex solid materials and it can be applied also to such amorphous phases.[142]

This chapter reports a resume of the results obtained during my PhD concerning the structural characterization of magnesium silicate hydrate. For more detailed information the reader can refer to the corresponding publication, Paper I, reprinted with permission at the end of this thesis.

3.1 Results and discussion

The possibility of following easily the advancement of pH in cement formulations was previously reported by Zhang *et al.*.[90] In this study pH measurements were useful to prove the advancement of the reaction of hydration of MgO and SiO_2 to form M-S-H: pH value decreases from $\sim$ 10.5 in the first hours to $\sim$ 9 after three days, confirming the consumption of brucite ($pK_a \approx 10.5$) to give M-S-H. It has been recently reported that Mg^{2+} concentration increases lowering pH, while silanols solubilization is optimal for pH $>$ 9 and further increase with pH.[26, 33, 143] Moreover, it is already known that pH plays a major role in cement formulations and it was reported that M-S-H gel forms readily at pH value $\sim$ 9.5, which provides enough silica content to convert all the brucite into M- S-H gel.[90] We found that our sample maintains a pH value at the equilibrium of about 9 (see Paper I in Appendix), optimal to promote the precipitation of M-S-H gel.

Weight losses from room temperature up to 1000 °C were registered by means of thermogravimetric analysis of the pastes freeze-dried after 1, 7 and 28 days of hydration. This analysis was useful to investigate the decomposition of the different phases present in the sample and to monitor their evolution with time. In the first derivative of the thermogravimetric curves (DTG curves) we observed three principal weight losses that confirmed M-S-H precipitation (see Paper I in Appendix): the loss of physisorbed water at about 200 °C; the dehydroxylation of brucite at 310 - 400 °C; the dehydroxylation of M-S-H, ending around 800 °C. The peaks at lower and higher temperatures increase with time, confirming M-S-H formation, while the peak ascribable to $Mg(OH)_2$ decreases with time, as brucite is consumed by the reaction with silica.[29, 144] DTG curves were then deconvolved with Gaussian functions for a more detailed investigation of the phases evolution with time. We evidenced that the reaction proceeds through the very fast hydration of MgO to $Mg(OH)_2$, which is then consumed, until a small amount remains after 28 days. We also found that two contributes are present in the peak at lower temperature, one due to water adsorbed to M-S-H surface and the other arising from water inside pores.[29, 62] The temperature of the maximum of these peaks shifts to higher temperature with hydration time, probably because M–S–H pores decrease in size with the advancement of the reaction, strengthening the water/M–S–H interactions and, hence, increasing the evaporation temperature.

Looking at the DTA curves, shown in figure 3.1, it was possible to observe an additional, exothermic, peak at about 900 °C, not ascribable to weight losses. According to the literature, this effect is due to a solid phase transition of M-S-H to crystalline species.[29, 62, 145] Similar events were previously reported for the thermal treatment of talc ($Mg_3Si_4O_{10}(OH)_2$), which is converted to enstatite

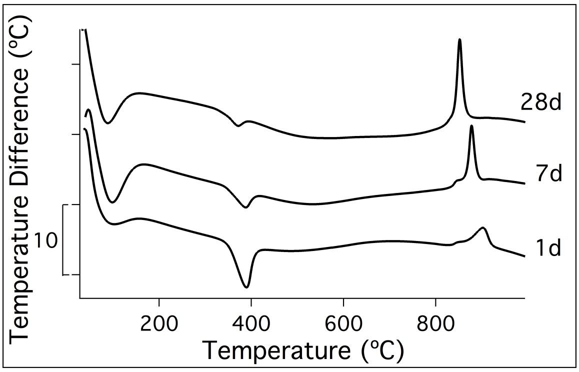

Figure 3.1: DTA profiles of MgO/SiO$_2$ sample after 1, 7 and 28 days of hydration. Curves have been offset for the sake of clarity. Reproduced from Paper I by permission of The Royal Society of Chemistry.

(MgSiO$_3$),[146] and for the thermal treatment of chrysotile (Mg$_3$Si$_2$O$_5$(OH)$_4$), which is converted to a mixture of enstatite and forsterite (Mg$_2$SiO$_4$).[147] These features sharpen and shift to lower temperature during the hydration. To further investigate this crucial aspect we decided to study the structure of the sample via XRD and SS-NMR also on heated samples.

XRD diffractograms recorded on samples at 1, 7 and 28 days of hydration before and after heating to 900 °C are shown in figure 3.2. XRD patterns show broad peaks, typical of M-S-H amorphous phase, increasing with time, while the intensity of Mg(OH)$_2$ crystalline signals decrease.[52, 148] The patterns of the heated samples revealed the presence of enstatite and forsterite phases, confirming the hypothesis suggested by the thermal analysis. Periclase was also observed, as it derives from brucite dehydroxylation. We found that the relative amount of the phases changes in time, indicating that M-S-H evolves and its structure changes with time.

SS-NMR investigation was crucial to quantitatively follow the evolution of the phases constituting M-S-H. This study was performed at the CNR and the University of Pisa, in the framework of the project FIR2013-RBFR132WSM. ^{29}Si DE-MAS spectra were recorded on samples at 1, 7 and 28 days of hydration and analyzed with a global fitting, as shown in figure 3.3. The analysis of the spectrum of MgO/SiO$_2$ after 28 days allowed five M–S–H signals to be identified for an accurate reproduction. In particular, two peaks can be ascribed to different Q^1 (OMg)(OSi)(OH)$_2$ species (-79.6 and -82.1 ppm), indicated as Q^{1A} and Q^{1B}. One signal was due to Q^2 (OMg)(OSi)$_2$OH sites (-86.3 ppm) and two more peaks were ascribed to two different Q^3 (OMg)(OSi)$_3$ silicon sites (-92.9 and -95.2 ppm), Q^{3A} and Q^{3B}. The ^{29}Si DE-MAS spectra of the samples cured 1 day and 7 days were well reproduced using the same peaks, with the

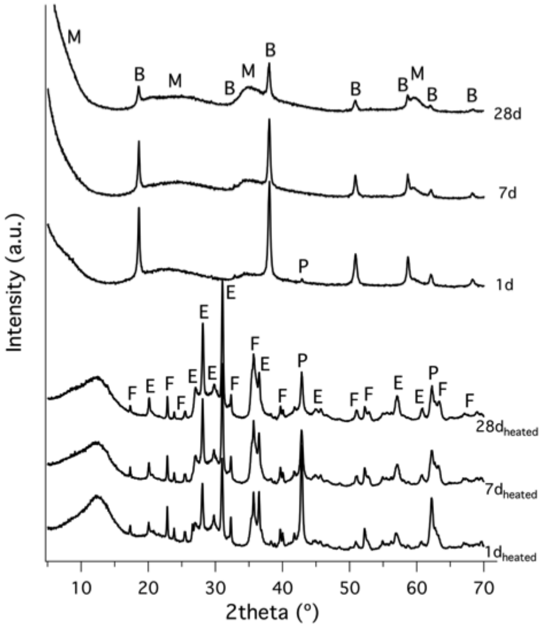

Figure 3.2: XRD diffractograms of samples sample after 1, 7 and 28 days of hydration before and after heating to 900 °C. Curves have been offset for the sake of clarity. M: M-S-H; B: brucite; P: periclase; E: enstatite, F: forsterite. Reproduced from Paper I by permission of The Royal Society of Chemistry.

addition of two peaks for the Q^3 $Si(OSi)_3OH$ (-102.0 ppm) and Q^4 $Si(OSi)_4$ (-111.5 ppm) sites of silica. In order to obtain quantitative information, the areas were scaled on the basis of the corresponding ^{29}Si T^1 values. In the literature, ^{29}Si T^1 of M-S-H were not previously reported and quantitative analysis were only mentioned.[145] Therefore, to the best of our knowledge, this work reported for the first time quantitative data for M-S-H phase.

FTIR data were also recorded and a deconvolution of the 1300 - 850 cm^{-1} range was performed. This spectral range is particularly interesting because it contains multiple absorptions, due to the stretching and bending vibration of Si-O bond. The combination of quantitative SS-NMR and FTIR allowed to follow the evolution of the silicatic chain polymerization in the growing process of M-S-H. We found that silica is hydrated and almost completely consumed in 28 days of hydration, while M-S-H forms. Different silicon species were identified and quantified: M-S-H structure was found to be consistent with the presence of talc- and chrysotile-like nanodomains.[52, 149–151] Figure 3.4 shows talc- and chrysotile-like domains. Chrysotile is a phyllosilicate consituted by T-O layers, where T indicates SiO_4^{2-} tetrahedra and O stands for a sheet of Mg^{2+} cations octahedrally coordinated to hydroxyl groups and to the apical oxygen atoms of the T sheets. Talc is a T-O-T phyllosilicate. The almost

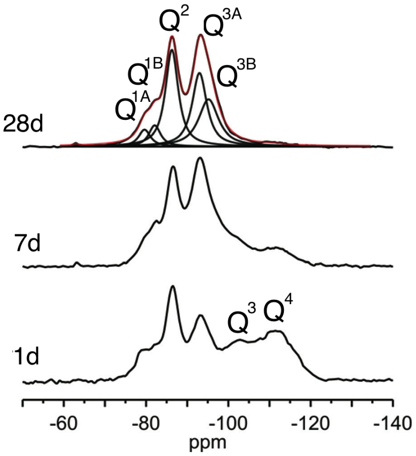

Figure 3.3: ^{29}Si DE-MAS spectra of MgO/SiO_2 spectra after 1, 7 and 28 days of hydration. For the spectrum at 28 days, also the fitted spectrum and the single peaks are reported. Reproduced from Paper I by permission of The Royal Society of Chemistry.

complete absence of SiO_2 and $Mg(OH)_2$ after 28 days (inferred from ^{29}Si SSNMR and XRD experiments) allows to conclude that in M-S-H Mg and Si are in an approximately 1:1 ratio, that reflects into a 1:1 molar mixture of talc- and chrysotile-like domains.

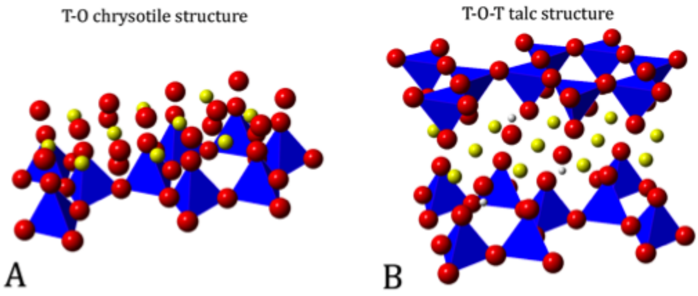

Figure 3.4: Scheme of (A) chrysotile and (B) talc. Blue tetrahedra represent Si species. Red, yellow and white spheres represent O, Mg and H atoms, respectively. Reproduced from Paper I by permission of The Royal Society of Chemistry.

4 Simultaneous hydration of MgO/SiO_2 and Portland cement mixtures

This chapter is focused on the study of several mixtures of MgO/SiO_2 and Portland cement. Such formulations are promising in view of two compelling environmental issues: reducing the large CO_2 emissions associated to Portland production and the encapsulation of nuclear waste. The inferior mechanical properties of MgO-based cements with respect to CaO-based cements have been correlated to the different structures of the respective binder phases,[43] as well as to the different distribution of water inside them.[152] In the perspective of preparing low-pH cementitious formulations for nuclear waste immobilization, it is important to investigate the hydration process and the structural properties of the hydrated phases of MgO-based formulations also containing Portland cement. Some work has been done in this field, addressing the possible intercalation of Mg^{2+} in C-S-H[153–155] and the interaction between M-S-H and C-S-H.[43, 56, 156]

In this framework, we prepared formulations containing MgO/SiO_2 and PC in different proportions, to evaluate their mutual effects. The combination of ^{29}Si and ^{27}Al MAS NMR, thermogravimetry, XRD, FTIR and SEM analysis elucidated the effects of composition and hydration time on the formation of M-S-H and/or C-S-H and their structural features. The hydration kinetics were studied by analyzing the trend of FWI, measured on the pastes by means of DSC (see 2.2.3). These curves have been fitted with a combined BNGM/diffusional model that accurately describes all the profiles and the best fitting parameters were extracted to compare the different formulations. ^1H transverse relaxation times (T_2) were measured to further get information on the kinetics of the hydration process and on the evolution of the porous structure, since ^1H NMR relaxometry gives unique information on the evolution of the state of the water and the pore network during cement hydration.[157–160] The dependence of T_2 values of water protons inside pores on the surface-to-volume ratio and on a specific surface relaxivity has been exploited to distinguish and quantify different water populations.[161–165] Moreover, an estimate of C-S-H and M-S-H pore dimensions has been obtained by low-temperature DSC.

Overall, the results show that suitable mixture of MgO/SiO_2 and PC could be used to modify the properties of the hydrated phases by tailoring the composition, with potential application in the storage of nuclear waste in clayey disposal.

This chapter reports a resume of the results obtained during my PhD concerning the study of the simultaneous hydration of MgO/SiO_2 and Portland cement mixtures. For more detailed information the reader can refer to the corresponding publications (Paper II, Paper III and Paper IV), reprinted with permissions at the end of this thesis.

4.1 Investigated samples

The composition of the prepared pastes is reported in table 4.1, together with the abbreviated notation employed to indicate the samples throughout the chapter. MgO and SiO_2 were mixed in a 1:1 molar ratio and the w/s was equal to 2 in all the formulations. Since a specific knowledge of the hydration of each component is needed to understand their individual contributions to the overall process, together with samples containing different amounts of MgO/SiO_2 and Portland cement, we also investigated one sample containing only MgO/SiO_2 (this sample is the same prepared in Chapter 3), one containing only PC and another made with PC and SiO_2. The sample containing Portland cement and silica (which is named CS), without periclase, allowed to discriminate and to better evaluate the effect of the so-called pozzolanic reaction between SiO_2 and portlandite on the properties of the hydrated phases.[166–168]

Table 4.1: Composition of the samples as wt% of MgO (M), SiO_2 (S) and Portland cement (C).

Sample	M (wt%)	S (wt%)	C (wt%)
MS100	40	60	0
MS80C20	32	48	20
MS50C50	20	30	50
MS20C80	8	12	80
C100	0	0	100
CS	0	37.5	62.5

4.2 Phases characterization

The parallel analysis of the DTG curves (figure 4.1) and of the pH *vs.* time profiles (figure 4.2) provides information on the nature of the hydrated phases formed in the samples. Looking first at the two samples composed by only either MgO/SiO_2 or PC, the different shape between room temperature and 200 °C can be considered as diagnostic of the phases composition: in MS100 the sharp peak at about 65 °C arises from the elimination of water from M-S-H,[29, 144] while in C100 the curve below 200 °C is broad and composed by multiple contributions, due to the decomposition of C-S-H and aluminate phases.[9] At higher temperature well-defined peaks due to the decomposition of brucite (370 °C)[34] and portlandite (440 °C)[169] occur. The decrease of

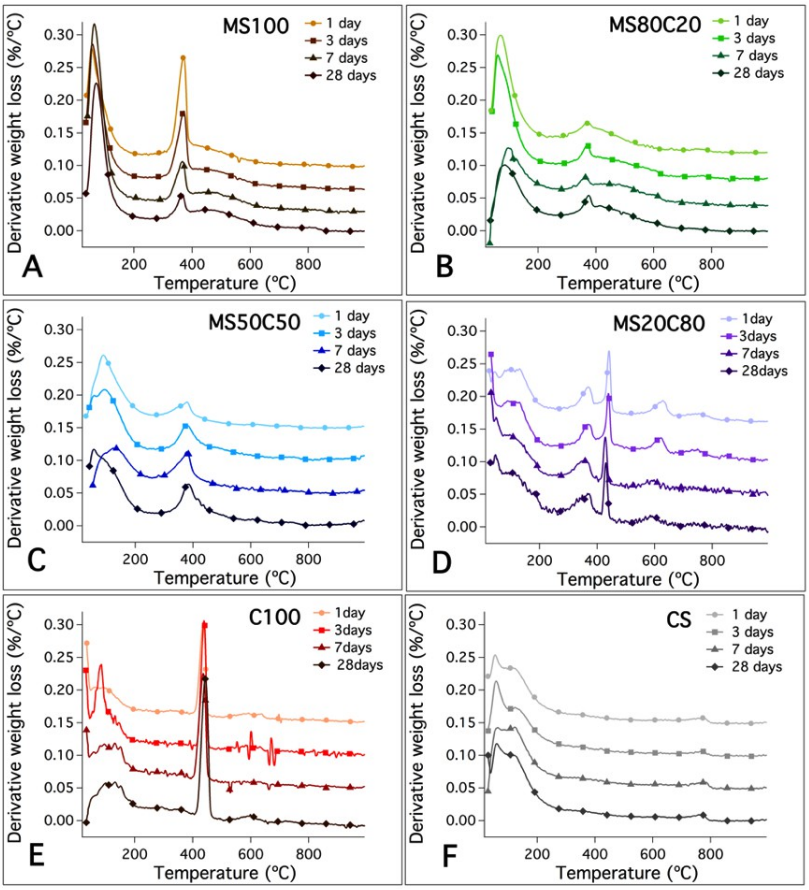

Figure 4.1: DTG curves for all the investigated samples at different hydration times. The curves have been offset for the sake of clarity.

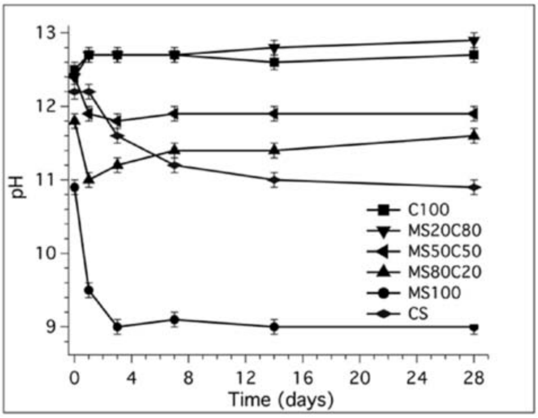

Figure 4.2: Trends with time of pH (±0.1) of the investigated samples. Reprinted with permission from Paper III.

brucite with time indicates the occurrence of the reaction with silica and is also evident from the pH value, which decreases from 11 to ~ 9.[148, 170] On the contrary, in C100, portlandite peak increases with time and pH raises from 12.4 to 12.7, as a consequence of the hydration reaction. MS100 also shows a broad feature at 300-600 °C, due to the loss of hydroxyl groups of M-S-H.[171] When PC is mixed with SiO$_2$ (CS sample) the reaction produces C-S-H and no Ca(OH)$_2$ is observed, as confirmed by the decrease of pH value during the first month of hydration. MS80C20 shows features strongly resembling those of MS100 both in terms of position and shape, suggesting that M-S-H is the main hydrated phase, together with Mg(OH)$_2$. However there is low amount of brucite already after 1 day of hydration, in spite of the relatively high pH value (11.5 - 11.8), suggesting that the reaction of production of M-S-H occurs very fast. This evidence seems to be in contrast with the literature, reporting 9 - 11 as the favored pH range for the formation of M-S-H. We hypothesize that in this sample the abundant formation of M-S-H occurs very fast in the first three days and then brucite starts to accumulate, as evidenced also by XRD (discussed throughout this paragraph). By increasing PC percentage, the shape of the DTG curves drastically changes, showing the appearance of different contributions, similar to those of C100. In the hydroxide region, MS50C50 sample shows a peak at 380 °C, a temperature higher than in MS100, which could be due to the presence of a mixed Ca/Mg hydroxide.[42] On the other hand, in this region MS20C80 shows two defined peaks arising from brucite and portlandite. This is the only mixed sample whose pH is sufficiently high to allow the precipitation of both these two phases.

DTA thermograms were also investigated, to observe the exothermic recrystallization events occurring at high temperatures. DTA curves between 700 and

1000 °C are shown in figure 4.3. MS100 and MS80C20 show similar features, ascribed to solid phase transitions of talc- and chrysotile-like sub-nanometric domains in M-S-H. In MS50C50 a single peak is present after 1 day and then two signals can be distinguished, ascribable to both a different nanometric structure of M-S-H or to recrystallization processes of C-S-H. Indeed, tobermorite, constituting C-S-H, converts to wollastonite at 850 - 860 °C[172] and the same peaks are present also in CS sample. C100 and MS20C80 samples do not show significant signals.

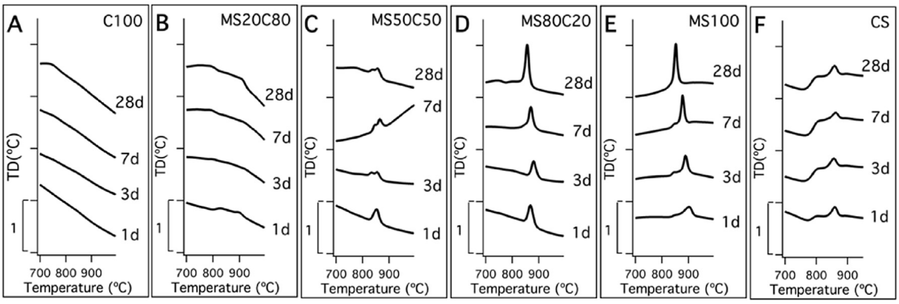

Figure 4.3: DTA curves in the 700 - 1000 °C range. Curves have been offset for the sake of clarity. Reprinted with permission from Paper III.

FTIR spectra of the C100, MS20C80, MS50C50, MS80C20 and MS100 samples after 28 days of hydration are reported in figure 4.4. The 1300 - 800 cm^{-1} spectral range shown in figure is particularly interesting because it includes the frequencies of the Si-O vibrations. MS100 and MS80C20 spectra resemble each other. The band at $\approx$ 1070 cm^{-1} is ascribable to M-S-H and increases with time, while the signal at 800 cm^{-1}, due to silica, decreases. On the other hand, the spectrum of MS20C80 is similar to that of C100. The signal at 1110 cm^{-1} is ascribable to the stretching of SiO_4^{4-} in alite and belite and it decreases with increasing the hydration time. The peak at 980 cm^{-1} is due to Q^2 SiO_4^{4-} in C-S-H and it increases with time. MS50C50, instead, shows peculiar spectral features and the broad band at $\approx$ 1000 cm^{-1} can not be unequivocally ascribed to a specific hydrated phase.[44]

Figure 4.5 reports the XRD diffractograms of the investigated samples after 28 days of hydration. In MS100 and MS80C20, M-S-H is the main hydrated phase (broad signals at $\sim$ 23, 35 and 59 °). The crystalline peaks of $Mg(OH)_2$ are very weak in MS80C20, confirming that in this sample M-S-H formation is favored by the presence of PC. On the other hand, portlandite is the main crystalline phase in C100 and it is also possible to recognize many different phases commonly present in hydrated PC. In the 29 - 33 ° range, peaks attributed to residual anhydrous phases are present, together with a broad signal ascribed to C-S-H.[44] The diffractogram of MS20C80 displays most of the peaks observed for

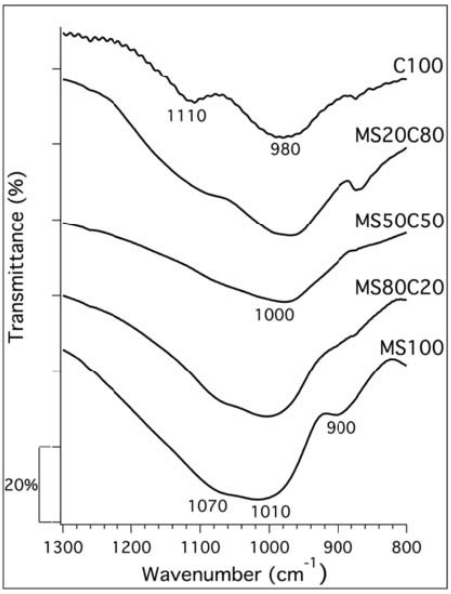

Figure 4.4: FTIR spectra of C100, MS20C80, MS50C50, MS80C20 and MS100 samples at 28 days of hydration in the 1300 - 800 cm^{-1} range. Reprinted with permission from Paper III.

C100, while MS50C50 closely resembles CS, suggesting a poor reactivity of the magnesium-binder phases. In both MS20C80 and MS50C50 the broad peaks expected for M-S-H could not be easily distinguish, indicating that this phase did not form in large amount. Moreover, in MS50C50 no portlandite is present, as it is consumed by the reaction with silica to form C-S-H.

Figure 4.6 shows ^{29}Si DE-MAS spectra of the samples hydrated for 28 days. The spectra were reproduced with the minimum number of peaks necessary and the values of the area of the signals were obtained from the fitting. Moreover, since it was already suggested that in the samples containing both Mg and Ca M-S-H and C-S-H gels form in separate phases, the ^{29}Si DE-MAS spectra of mixed samples were analyzed as sums of the signals of M-S-H and C-S-H. As described in Chapter 3, the spectrum of MS100 hydrated 28 days is constituted by five signals: two peaks at -78.5 and -81.0 ppm arising from two different Q^1 Si(OMg)(OSi)$(OH)_2$ species (Q^{1A} and Q^{1B}), a signal at -85.1 ppm due to Q^2 Si(OMg)$(OSi)_2$OH sites, and two peaks centered at -91.8 and -94.0 ppm ascribed to two different Q^3 Si(OMg)$(OSi)_3$ silicon species (Q^{3A} and Q^{3B}). By comparing the spectra of MS100 and MS80C20 it can be concluded that the main silicate hydrate phase formed is M-S-H. On the contrary, after 28 days of hydration C100 gives rise to the typical spectrum of hydrated Portland cement: at -71.3 ppm the signal (Q^0) of unreacted belite is evident, while residual alite

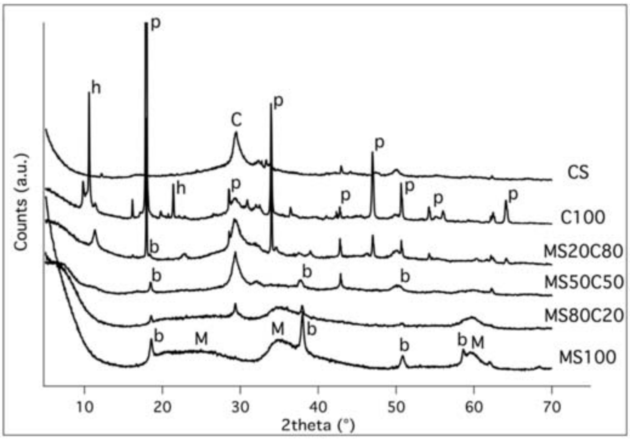

Figure 4.5: XRD patterns of all the investigated samples at 28 days of hydration. The assignment of the peaks is reported in the figure using the following abbreviations: p (portlandite), C (C-S-H), h (hemicarboaluminate), b (brucite), M (M-S-H). Curves have been offset for the sake of clarity. Reprinted with permission from Paper III.

gives rise to weak and broad signals between -70 and -74 ppm. The peaks at lower chemical shift arise from C-S-H, and in particular from Q^1 (-78.8 ppm) and Q^2 sites ($Q^{2(I)}$ at -81.7 ppm and $Q^{2(II)}$ at -84.5 ppm). According to the dreierketten model, generally used to describe C-S-H as constituted by linear chains in which silicate tetraedra are coordinated to calcium cations, in the silicate chains there are paired tetrahedra (Q^{2p}) linked by bridging (Q^{2b}) tetrahedra, while Q^1 species are the silicon nuclei in the terminal tetrahedra. Moreover, in C-S-H Al^{3+} can substitute Si^{4+}, especially in the bridging sites (Q^{2b}). The comparison between the spectra of C100 and MS20C80 strongly suggests that C-S-H is the main silicate hydrate phase formed, although with a different condensation degree. In agreement with other findings, MS50C50 shows features attributable both to M-S-H and C-S-H phases. Signals typical of C-S-H are present also in CS, but with different relative intensities, due to a higher condensation degree of tobermorite chains in C-S-H, as a consequence of the pozzolanic reaction between silica and portlandite.[167, 168, 173] When C-S-H is the main phase, taking into account the dreirketten model, it is also possible to calculate the minimum and maximum values for the mean chain length. When M-S-H is the only binder phase instead, it is possible to calculate a condensation degree. The comparison of the ^{29}Si DE-MAS spectra of each sample at different hydration times and the corresponding intensities of the signals further provided interesting information on the kinetics of formation of M-S-H and C-S-H and on the evolution of their structure with time. We evidenced significant differences in the reaction degree of M-S-H sheets and in the length of C-S-H chains. M-S-H formed in mixtures is characterized by a prevalence of serpentine-like domains over talc-like ones, compatible with high Mg/Si ratio. The structure of C-S-H is also significantly different from that obtained in sole PC, as silica favors the formation of longer chains. Moreover, ^{27}Al DE-MAS spectra can be evaluated to gain information on the aluminum-containing species. We found that the addition of MgO/SiO_2 to PC influences the nature and the relative populations of the aluminate phases.

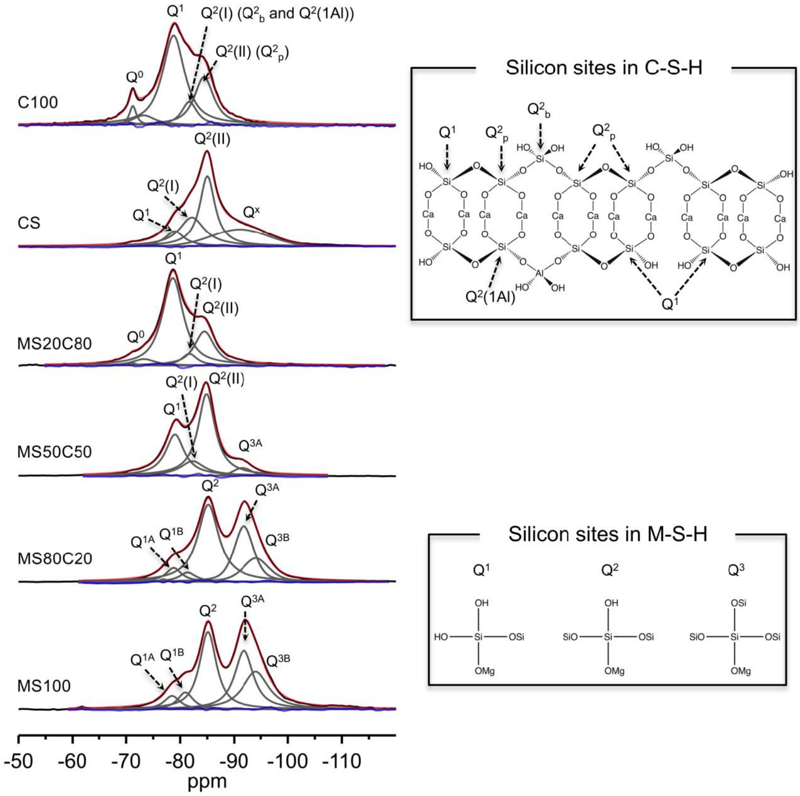

Figure 4.6: ^{29}Si DE-MAS spectra of all the samples after 28 days of hydration with spectral fittings and signal assignment. Reprinted with permission from Paper II.

4.3 Kinetics of hydration

The hydration kinetics of each cement formulations was followed by determining the fraction of unreacted water as a function of hydration time. Figure 4.7 shows the obtained FWI *vs.* hydration time profiles. All the investigated curves were accurately described by a BNGM/diffusional model and the best-fit parameter were calculated. The addition of small amount of PC to the

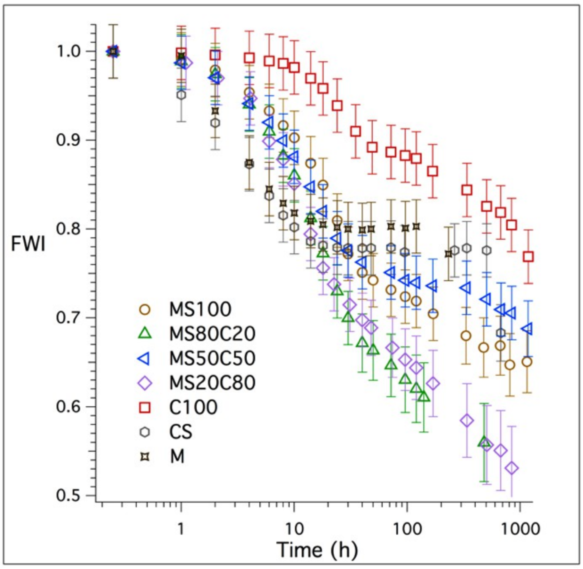

Figure 4.7: FWI as a function of hydration time for all the investigated samples.

MgO/SiO_2 mixture results in a faster hydration and formation of M-S-H, while in mixtures containing larger amounts of PC, M-S-H formation is hindered and C-S-H forms faster than in neat Portland cement. These differences in the hydration kinetics can be understood considering also the pH value established in the pastes and the presence of fumed silica. C100 sample shows the well known shape associated to PC: induction period (1 - 8 h), acceleration period (10 - 30 h), diffusional period (> 30 h). When silica fume is present (CS sample) the water consumption is very rapid and no induction is observed. Therefore, in agreement with the literature, silica accelerates C-S-H formation.[174] The hydration of MgO to form brucite shows a short induction period and then rapidly occurs. When silica is present (MS100 sample) the shape completely changes and the water consumption is initially slower. Then a nucleation-and-growth period occurs and the final part of the curve suggests a diffusion-controlled mechanism, similarly to the Portland case. The kinetics of MS/C samples follow almost the same trend of MS100 in the first 10 h, indicating that MgO hydration is the most rapid process, independently to the relative amounts of reagents used. At longer hydration times, some differences appear and MS50C50 shows the lowest water consumption. On the contrary, MS80C20 and MS20C80 show lower FWI values, suggesting a synergistic effect in the formation of the hydrated phases.

The three stages of hydration evidenced by FWI trends can be distinguished also by following the evolution of the T_2 distributions as a function of the hydration time, t_H. This study was performed at the CNR and the University of Pisa, in the framework of the project FIR2013-RBFR132WSM, and further confirms the evidences here reported. ^{1}H transverse relaxation times (T_2) of the different fractions of water inside the pastes were investigated by means of a Carr-Purcell-Meiboom-Gill (CPMG) pulse sequence.[175] Relaxation decay data from CPMG sequence experiments were inverted to give T_2 distributions, to get information not only on the kinetics, but also on the evolution of the porous structure (see next paragraph).

4.4 Porous structure evolution

^{1}H NMR relaxometry gave information on the formation of the porous structure of the investigated phases during the hydration. T_2 values of proton of water inside pores depends on the surface-to-volume ratio of pores and on a specific surface relaxivity. Therefore, it allows to distinguish and quantify different water populations.[161–163, 176] Analyses of ^{1}H Free Induction Decay (FID) allowed protons to be singled out and quantified.[159, 160, 177] ^{1}H T_2 relaxation time distributions were investigated for all the mixtures hereby considered at different hydration times, up to one month of hydration. For PC and mixtures forming C-S-H as the main binder phase, a substantial change in pore size distribution occurs during the paste hardening, while in MgO/SiO_2 mixtures, where M-S-H forms as main binder phase, a more gradual and less pronounced evolution of the porous structure is observed. For C100 the trend of the more mobile water is in agreement with those previously reported for white and ordinary cement.[163, 164, 176–178] T_2 evolution of MS100 starts faster than in C100, then the microstructure of the paste changes while M-S-H forms during the first 40 h. In the case of MS80C20, the evolution of T_2 distributions is analogous to that observed for MS100, but with a longer induction period and a longer decrease of pore sizes (100 h instead of 40 h) than MS100. On the other hand, MS20C80 resembles C100, suggesting an analogous development of the gel structure but with an accelerated kinetics, probably due to silica presence. For MS50C50, again, the evolution of T_2 can not be straightforward associated to that of either C100 or MS100. Initially it resembles MS100, then, after 30 h, it becomes more similar to C100.
To estimate the pore dimensions it could be possible to use the relationship:

$$\frac{1}{T_2} \approx \frac{\varepsilon S}{V} \frac{1}{T_2^{surf}} \tag{4.1}$$

where T_2 is the measured spin-spin relaxation time, T_2^{surf} is the T_2 value for water molecules adsorbed on the surface, ε is the thickness of the adsorbed water layer and S and V are the pore surface area and volume, respectively. Planar pores could be assumed for C-S-H,[45] while pores with spherical shapes should be more appropriate for M-S-H.[43] Anyway, this equation is strictly valid within the fast diffusion regime and only in the case of fully saturated pores.[179, 180] Moreover, ε/T_2^{surf} can largely vary, depending on the presence of paramagnetic impurities. Therefore, we decided to use low-temperature DSC to highlight the differences between M-S-H and C-S-H porous structures. Figure 4.8 shows representative selection of ^{1}H T_2 relaxation time distributions after one month of hydration, together with SEM images.

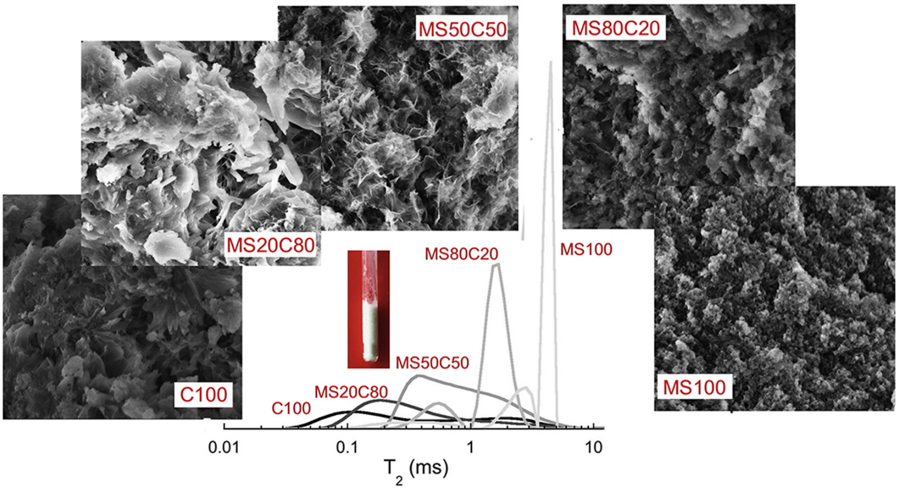

Figure 4.8: ^{1}H T_2 relaxation time distributions of the investigated samples together with SEM images (50 KX) after 28 days of hydration. Reprinted with permission from Paper IV.

The cooling scans of the LT-DSC thermograms obtained for MS100 and C100 samples at 28 days of hydration are reported in figure 4.9. The results showed that, upon slow cooling, the freezing of water present in the samples occurs at sub-zero temperatures, showing well-defined peaks. A sharp peak between -10 and -20 °C is present, due to crystallization of bulk water, while water confined in nanometric pores freezes at lower temperatures.[51, 102, 109, 110, 181] In particular, a characteristic peak centered at about $-40°$C can be observed in both samples. MS100 also shows another broad feature in the temperature range between -25 and -35 °C. According to the literature, these peaks are indicative of water confined in pores whose size ranges between 1-3 nm ($\sim -40°$C) and 3-12 nm (between -25 and -35 °C).[51, 181] The differences between M-S-H and C-S-H phases and the absence of interlayer spaces in M-S-H are in agreement with the globular structure proposed by Chiang *et al.*[43] and might explain the inferior mechanical properties usually observed

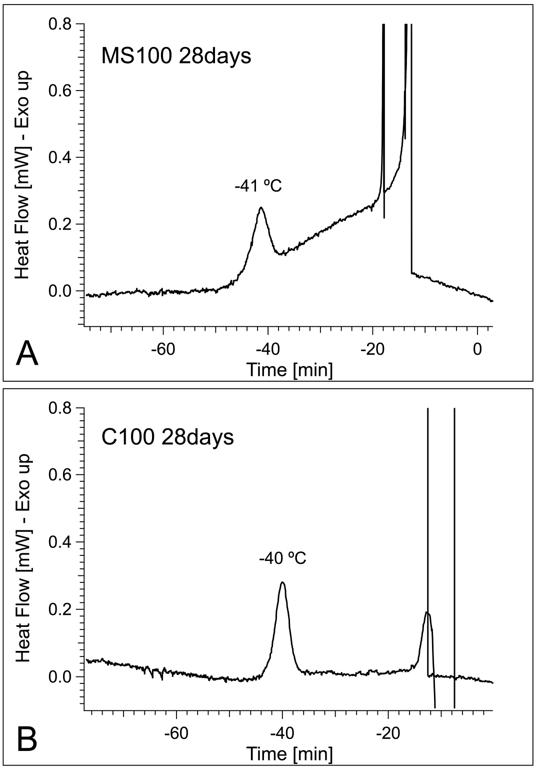

Figure 4.9: Cooling scans of the thermograms of the MS100 (A) and C100 (B) cement pastes at 28 days of hydration. Reprinted with permission from Paper IV.

for MgO-based cements.

5 Effect of phosphate based additives on the formation and structure of magnesium silicate hydrate

The third topic I have addressed in my PhD is the evaluation of the effects of three phosphate based additives on the hydration and structure of M-S-H. Nowadays, sodium hexametaphosphate ($(NaPO_3)_6$, HMP) is the only additive used with MgO-SiO_2 cement, while in CaO-based cement many additives are commonly used to modulate performances to specific applications. Recently, some authors reported the investigation of M-S-H precipitation in presence of HMP, to reduce the water content of the pastes maintaining a good workability, which is an essential task for practical applications. It has been evidenced that the addition of about 1 wt% of HMP confers the higher fluidity with minimal impact on M-S-H formation,[29, 62, 63, 140, 182, 183] but its effect on the structure and mechanical properties at the micro- and nano-scale level are still poorly known. In this framework, we investigated the effect of three different phosphate additives on MgO/SiO_2 mixtures: sodium hexametaphosphate, sodium trimetaphosphate ($(NaPO_3)_3$, TMP) and sodium ortophosphate (Na_3PO_4, NaP). Our goal was to compare the effect of different additives using the same Mg:P ratio, to understand why exactly sodium hexametaphosphate was used in the literature and to evaluate the possibility of using other phosphate-based additives. Mini-cone slump test was used for a qualitative evaluation of the additives effect on the workability of the pastes and DSC allowed to study their kinetics of hydration. The phases formed at different hydration times have been characterized using TGA, FTIR and XRD, to follow the hydration reaction. Furthermore, pH measurements provided useful information and the morphologies of the samples have been investigated using SEM. For the first time, the mechanical properties of these materials have been compared. We investigated the micro-hardness of the prepared samples using Vickers hardness test, while the nano-mechanical properties were evaluated using statistical high-speed nanoindentation. We found that the hydration reaction and the mechanical properties of the cement pastes are affected by the composition of the samples and OP emerged as the most promising additive. Moving a step forward, to understand the mechanism of adsorption of these additives on the pastes we investigated also the adsorption isotherms of HMP, TMP and OP on MgO, SiO_2 and MgO/SiO_2 substrates. The idea was to better understand why OP works better than the other additives, even better than the actually used HMP. However, the systems resulted to be more complicated than expected and it was not possible to get information on the thermodynamic aspects of the adsorption processes.

5.1 Preparation of the samples

Pastes were prepared by mixing $MgO:SiO_2$ in a 1:1 molar ratio (± 0.1). Phosphate additives were premixed with the solid and then they were added to water at w/s = 0.8. When present, 1wt% of HMP was used (weight percentage is referred to the total amount of MgO/SiO_2), corresponding to Mg:P = 1:0.01. Then, for the other additives, the same Mg:P ratio was used. $(NaPO_3)_6$, $(NaPO_3)_3$ and Na_3PO_4 were used to compare different phosphate based additives. For the mini-slump test a higher water to solid ratio (w/s = 2) and an automatic mixer were used.
The notation that will be used throughout the chapter is reported in table 5.1.

Table 5.1: Composition of the investigate samples and corresponding notation. Weight percentage are referred to the total amount of MgO/SiO_2.

	MSH	MSH+HMP	MSH+TMP	MSH+OP
MgO (wt%)	40	40	40	40
SiO_2 (wt%)	60	60	60	60
HMP (wt%)		1		
TMP (wt%)			1	
OP (wt%)				3.2

5.2 Phases characterization

Mini-slump test was used to measure the spreading out diameter of a volume of cement paste.[91] This test, initially developed for PC,[184, 185] has been recently reported also for MgO/SiO_2 cements, to evaluate the effect of the composition on the workability of the paste.[29] Figure 5.1 shows the results obtained by mini-slump tests. The presence of phosphates (Fig. 5.1 B, C and

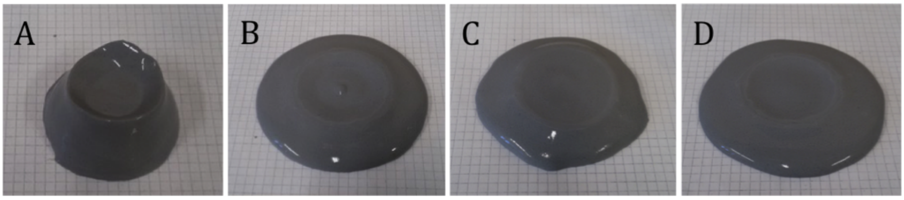

Figure 5.1: Mini slump test: A) MSH; B) MSH+HMP; C) MSH+TMP; D) MSH+OP.

D) increases the fluidity of the pastes, leading to a higher spread of the cement cone with respect to the sample without additive (Fig. 5.1 A). OP seems to show an even better fluidificant effect with respect to HMP, which, nowadays, is the only used additive with MgO/SiO_2 pastes. On the contrary, TMP (Fig. 5.1 C) has inferior fludificant effect than the other investigated phosphates salts.

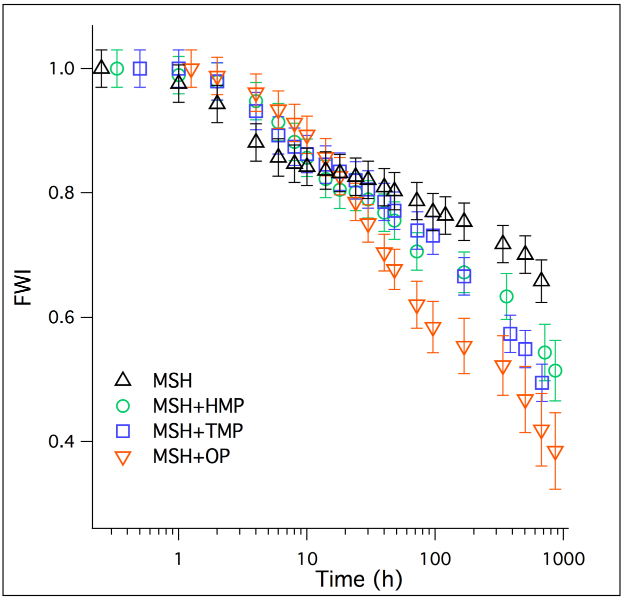

Figure 5.2: FWI as a function of hydration time for all the investigated samples.

Figure 5.2 shows the FWI *vs.* time profile of the investigated samples. The curves do not significantly differ in the first 14 hours. The hydration of the samples shows a short induction period (~1 h) in which almost no water reacts (FWI≈ 1), followed by the acceleration period, when FWI decreases because of the nucleation and growth of the hydrated phases. Then, the change in the curve slope is due to the modification of the rate-limiting mechanism, from nucleation-and-growth to a diffusion-limited behavior.[98] At long hydration times, some differences occur. The presence of the additives leads to lower FWI, due to a higher consumption of water. The process of hydration is more efficient and, thus, M-S-H precipitation is enhanced. In particular, OP presence enhances the hydration reaction even more than HMP and TMP.

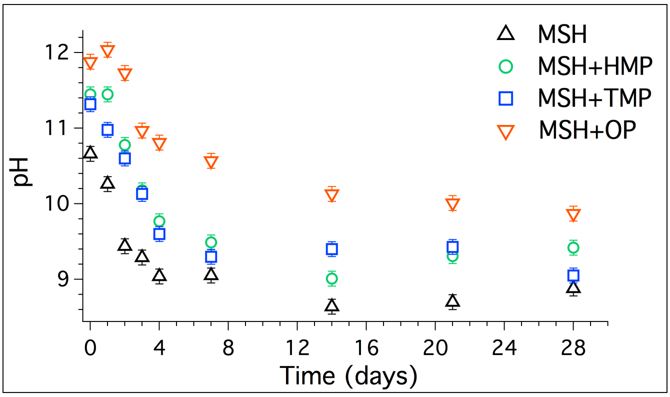

Figure 5.3: pH trends with time of the investigated samples.

Figure 5.3 shows the pH variation of the mixtures. pH values decrease in the first two weeks for all the samples and then remains almost constant, reaching a plateau. In MSH sample, pH is initially affected by the presence of $Mg(OH)_2$ (pKa $\approx$ 10.5), then it decreases to $\sim$ 9 because of the consumption of brucite in the reaction with hydrated silica and, finally, it remains stabilized at this value. The observed pH trend is well in agreement with the literature and the sample maintains the optimal pH value to promote the precipitation of M–S–H gel.[14, 33, 143] In the samples with additives the trend is similar to the MSH case, but the values of pH are higher for the entire investigated period and this effect is particularly pronounced for OP. Moreover, in the presence of HMP and especially OP, the very initial trend of pH can be considered as constant. It was already reported in the literature that HMP presence increases the pH of MgO/SiO_2 paste[63] and we experienced the same behavior for all the three phosphate salts investigated. According to Jia *et al.*, the higher pH may allow increasing the dissolution of SiO^{4-} ions into solution that react with Mg^{2+} ions and water to form M-S-H gel, while $Mg(OH)_2$ formation is inhibited.[63]

Figure 5.4 shows the weight losses of the samples at different hydration times. The corresponding TG/DTG curves (here not shown) showed various signals, in agreement with the previous reported results for M-S-H: between room temperature and 200 °C the elimination of physisorbed water from M-S-H occurs, at about 370 °C there is the decomposition of brucite and at higher

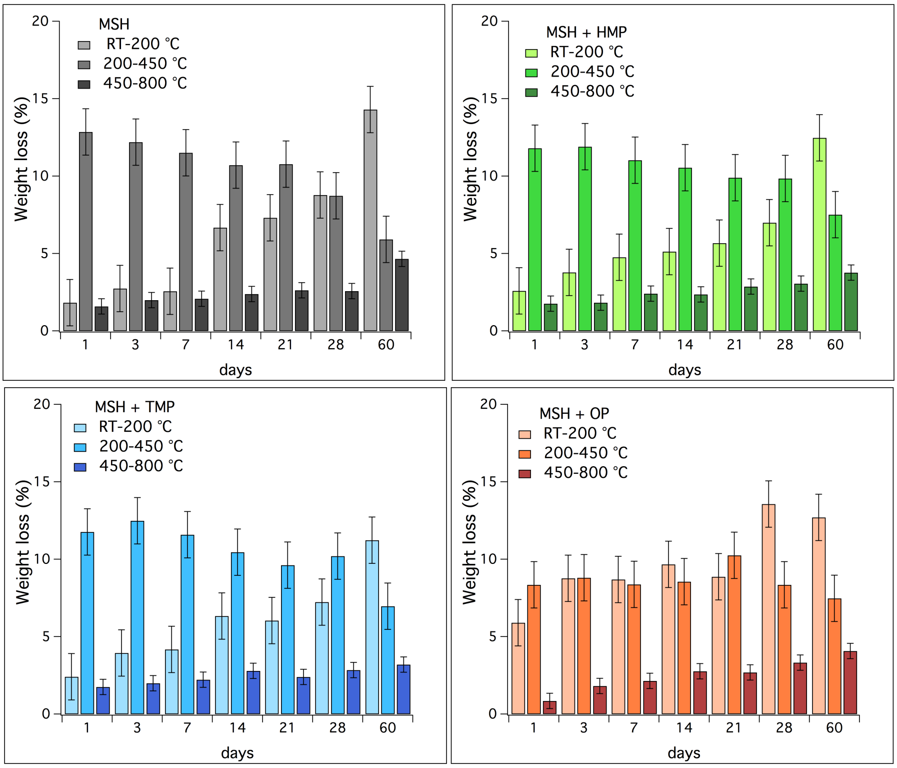

Figure 5.4: Weight losses (%) the investigated samples in the RT - 200 °C, 200 - 450 °C and 450 - 800 °C temperature ranges.

temperature (450 - 800 °C) the dehydroxilation of M-S-H occurs.[29, 62] Therefore, in figure 5.4 is reported the evolution of the signals in these three temperature ranges: RT - 200 °C, 200 - 450 °C and 450 - 800 °C. As it can be observed, with increasing the hydration time the amount of brucite decreases (200 - 400 °C interval) for MSH pristine and in presence of HMP and TMP additives, while the amount of M-S-H increases (RT - 200 °C and 450 - 800 °C temperature ranges) for all the samples. In the presence of OP, slightly lower amount of $Mg(OH)_2$ can be observed at short hydration time with respect to MSH sample, and this signal remains almost constant in the entire investigated period. The high amount of brucite observed after 28 and 60 days of hydration for MSH+OP sample, apparently discordant with XRD and FTIR results, can be explained taking into account the error bars of these signals. Concerning the signal between RT and 200 °C, MSH after 60 days shows the higher weight loss. MSH+HMP and MSH+TMP present the same behavior of MSH, but they show lower amounts of physisorbed water on M-S-H after two months of hydration. On the other hand, MSH+OP seems to reach a plateau after

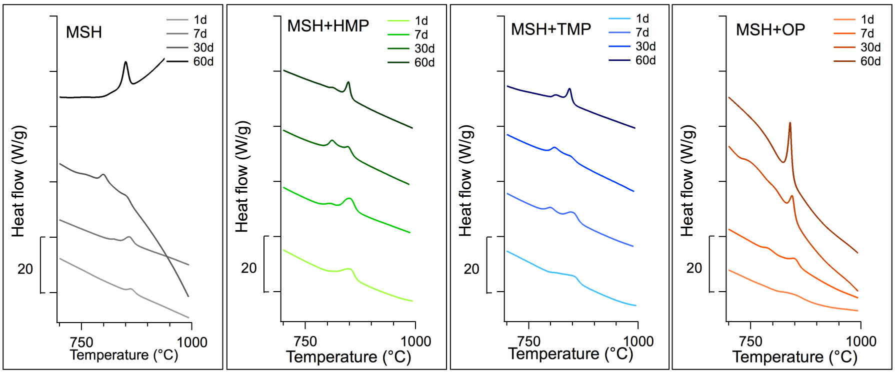

Figure 5.5: Weight corrected heat flow *vs.* temperature of the investigated samples in the 700 - 1000 °C temperature range.

30 days. Finally, the signal attributed to M-S-H dehydroxilation resembles for all the investigated samples, even if, also in this case, the higher weight losses were observed for MSH sample. The apparent discrepancy between the low FWI and the high signal in the RT - 200 °C range for MSH sample at 60 days of hydration could be explained assuming that the M-S-H binder phase formed in this sample has more hydroxyl groups than in the other samples. The evaluation of the silicatic chain condensation of M-S-H phase in these samples using ^{29}Si NMR would confirm this hypothesis.
Figure 5.5 shows DTA curves in the 700 - 100 °C temperature range at different hydration times. Looking at these curves, it is interesting to focus the attention on the exothermic events occurring at these temperatures, attributed to solid phase transition of M–S–H to crystalline species.[29, 62] It was already evidenced (Chapter 3) the presence in M-S-H of talc and chrysotile-like subnanometric domains, that convert to enstatite and forsterite at about 800 °C. These peaks observed at $\sim$ 810 and 850 °C progressively sharpens during the hydration, shifting at lower temperatures, for all the investigated samples. For MSH and MSH+OP, after 60 days only the peak at higher temperature is still present, suggesting that at longer hydration times talc-like domains are favored in these samples. In presence of OP, the signal attributed to M-S-H recrystallization events is particularly intense, while MSH+HMP and MSH+TMP resemble each other and show signals less intense in this range of temperature.

Figure 5.6 reports the XRD diffractograms of the investigated samples. Brucite is the main crystalline phase, whereas, as already reported in the literature, the broad peaks at roughly 23°, 35° and 59° are consistent with the XRD pattern of the amorphous M-S-H phase.[30, 33] For MSH, MSH+HMP and MSH+TMP samples, it is possible to notice a decrease of brucite peaks with hydration time,

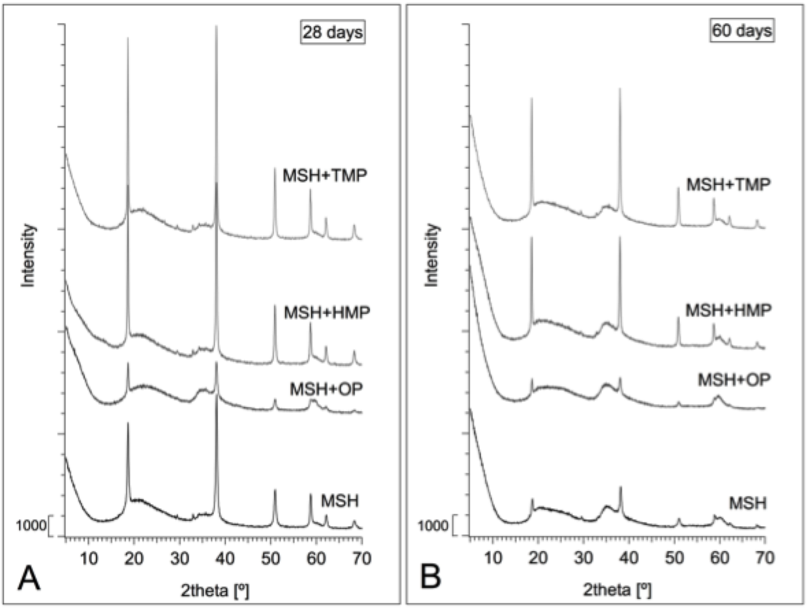

Figure 5.6: XRD diffractograms of the investigated samples after 28 and 60 days of hydration.

as its consumption occurs to produce M-S-H. In the presence of HMP and TMP the amount of brucite is higher than in pristine MSH, contrarily to what reported in the literature by Jia *et al.* that observed an inhibition of brucite precipitation in presence of HMP for samples with much higher water content (w/s = 10).[63] On the other hand, in MSH+OP sample brucite signals after 30 and 60 days of hydration slightly differ and XRD suggests that OP presence lower the amounts of brucite at longer hydration times.

Figures 5.7 and 5.8 report the FTIR spectra of the investigated samples. The 3900 - 2500 cm^{-1} spectral range (5.7) is particularly indicative because it includes the frequencies of the OH vibrations. As already reported, M-S-H sample shows Mg-OH stretching vibrations at 3680 cm^{-1} and other OH vibrations at 3300 cm^{-1}.[34, 44] The signal at $\sim$ 3700 cm^{-1} decreases with increasing the hydration time, due to the consumption of $Mg(OH)_2$ in the reaction with silica, to form M-S-H binder gel phase. In presence of HMP and TMP higher amounts of $Mg(OH)_2$ are present in all the spectra, while OP presence seems to enhance $Mg(OH)_2$ consumption, in accordance with XRD analysis. These results suggest that OP presence enhances M-S-H gel formation affecting $Mg(OH)_2$ consumption. The signal at lower wavenumber is assigned to M-S-H and it increases with time in all the samples, confirming the formation of the binder gel phase. The broad signal at $\sim$ 3300 cm^{-1} is more

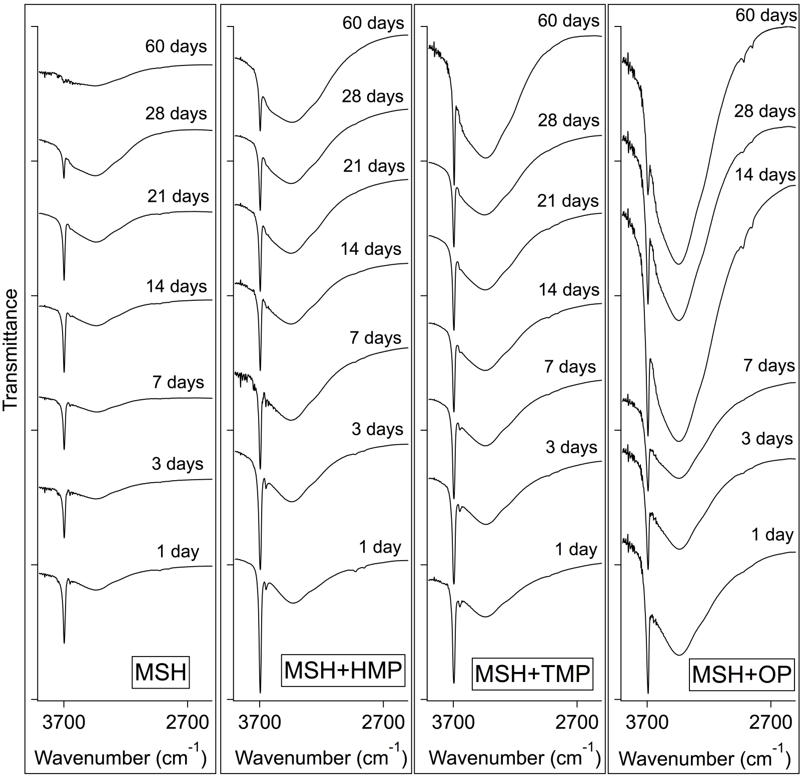

Figure 5.7: FTIR spectra at different days of hydration in the 3900 - 2500 cm^{-1} range.

intense in MSH+HMP, MSH+TMP and MSH+OP, thus M-S-H precipitation is enhanced. In particular, MSH+OP sample shows a very intense peak at ∼ 3300 $^{-1}$, increasing more and more with the hydration time. These results confirm that OP has a very strong effect on M-S-H, improving its formation even more than HMP.

The 1400-600 cm^{-1} spectral range (figure 5.8) is particularly indicative because it includes the frequencies of the Si-O Q^n vibrations (Q^n denotes a Si tetrahedron with n bridging oxygen atoms). Si-O Q^3 and Q^4 stretching occur above 1200 cm^{-1}, Si-O Q^2 stretching occurs at 1070 and 1020 cm^{-1}, while Si-O Q^2 bending occurs at 850 - 900 cm^{-1}.[29, 44] The broad bands between 1300 and 950 cm^{-1} progressively shift toward low wavenumbers with time, as SiO_2 is consumed and M-S-H precipitates and grows, confirming the formation of the binder gel phase. Moreover, the peak at about 800 cm^{-1}, due to the presence of SiO_2, decreases with time as it is consumed by the reaction with $Mg(OH)_2$. In the presence of HMP and TMP the shift toward low wavenumber is enhanced. By comparing the spectra at 60 days of hydration it can be seen

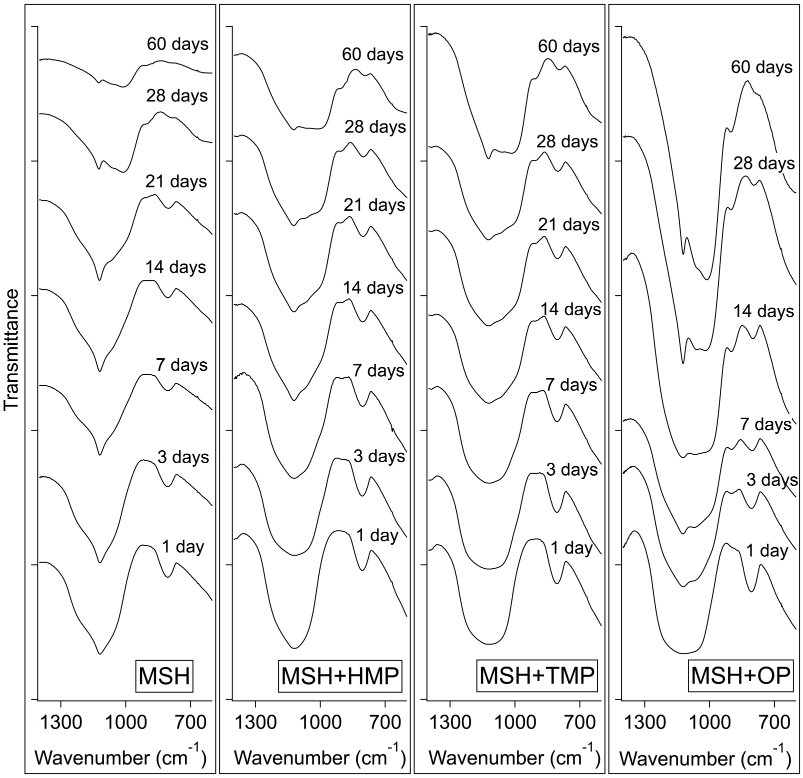

Figure 5.8: FTIR spectra at different days of hydration in the 1400 - 600 cm^{-1} range.

that the signals arising from Si-O vibrations are more intense in the presence of additive than in the pristine sample. Anyway, at long hydration time, the amount of unreacted silica is higher in presence of HMP and TMP, as evidenced by the presence of the signal at 800 cm^{-1}, absent on the MSH sample after 28 and 60 days of hydration. OP has even more effect on these signals. OP presence enhances and accelerates the shift at lower wavenumber of these peaks and the signals arising from silanol groups are more intense already after 7 days of hydration. After two months in MSH+OP sample the signals at 1070 and 1020 cm^{-1} are very intense and silica is almost completely consumed, as suggested by the absence of the peak at 800 cm^{-1}, in agreeement with XRD results.

Figure 5.9 and 5.10 show the morphologies of the investigated samples after 28 and 60 day of hydration. In the images, it is possible to recognize globular spheres, typical of unreacted silica, and the morphology of the amorphous binder phase, M-S-H gel. After two months of hydration the amount of SiO_2 decreases in all the samples, as evidenced by the other techniques, and a more

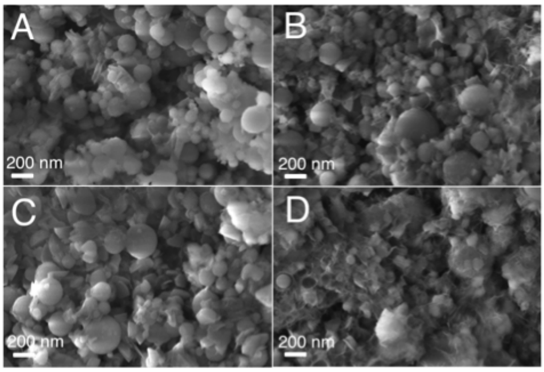

Figure 5.9: SEM images after 28 days of hydration: A) M-S-H; B) M-S-H + HMP; C) M-S-H + TMP; D) M-S-H +OP.

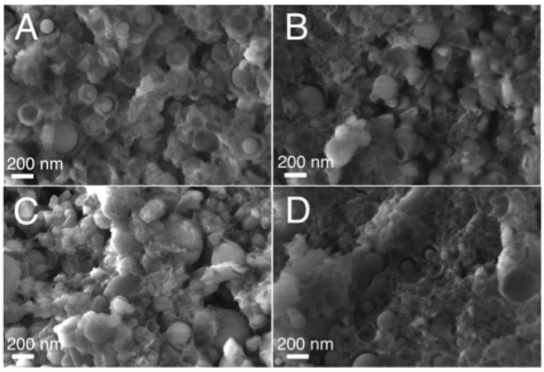

Figure 5.10: SEM images after 60 days of hydration: A) M-S-H; B) M-S-H + HMP; C) M-S-H + TMP; D) M-S-H +OP.

abundant amorphous structure is present in the images. By comparing the different samples at the two investigated times of hydration, it is evident that OP presence enhances the consumption of silica and the precipitation of M-S-H gel more than the other investigated additives. In presence of HMP, M-S-H phase is more abundant with respect to pristine MSH sample, both after about one and two months of hydration, but the effect is less evident than in the case of OP. In MSH+OP after 60 days of hydration, silica is almost completely consumed and it is even possible to recognize many holes left by consumed silica (see figure 5.10 D). On the contrary, in presence of TMP the morphology of the sample is very similar to that of the pristine MgO/SiO_2 sample and it is possible to recognize abundant unreacted silica, even after two months of hydration.

The results here presented suggest that HMP, TMP and OP can be properly used to increase the workability of MgO/SiO_2 pastes, as evidenced by the

slump test. HMP and TMP do not significantly affect M-S-H precipitation, while OP seems to even promote the formation of M-S-H binder gel phase. OP presence enhances the consumption of water (see FWI *vs.* time curves) and the obtainment of M-S-H binder phase, as evidenced by heat flow *vs.* time curves, XRD diffractograms and FTIR spectra. These results will be further validated by SS-NMR analysis that is still in progress.
Some discussion can be done concerning the comparison between the investigated salts. It is already known that at neutral pH the hydrolysis processes of HMP are slow[131, 186, 187] and if the measurements are performed at short time range, the presence of hydrolysis products of HMP can be neglected. On the contrary, in our condition HMP is not the only phosphate species to be expected, as the alkaline pH of our systems allows the hydrolysis of the species in solution. As a matter of fact, the rate of hydration of meta- and pyro-phosphates in strongly acid and alkaline (> 9) solution is reported to be very rapid.[188] We can conclude that ortophosphate should be the most abundant species in our systems, when HMP were used. Some work has been done also concerning the study of TMP under different conditions and it has been reported that the hydrolysis of TMP can occur in strongly alkaline medium. It is already known that TMP is hardly hydrolyzed at slightly acid pH, while at pH ≈ 13 it immediately dissolves and tripolyphosphate form. TMP hydrolysis is immediate and strongly correlated to the base concentration with a degradation inhibition starting from pH 11. The reaction produces phosphate diester and phosphate monoester in 2:1 ratio.[189] Therefore, in our system containing TMP, we had mainly phosphate diester. These considerations suggest that in the presence of phosphates, instead of the differences between HMP, TMP and OP, the driving force that makes phosphate-based additives so efficient with MgO/SiO_2 cement is probably the availability of ortophosphate in the pastes. This explanation can clarify why OP works even better than HMP and why TMP is less efficient. The future perspective of this study will be the quantification of the amount of ortophosphate that these salts generates in the cement paste. In the literature various papers were published concerning the evaluation of different phosphate species in solution[188, 190–192] and the identification of the phosphate species generated by HMP and TMP in our conditions will eventually confirm that the presence of ortophosphate species is the key point for the use of this kind of additives.

5.3 Investigation of the mechanical properties

We studied the mechanical properties of MSH, MSH+HMP and MSH+OP using micro- and nano-indentation tests. MSH+TMP was not studied with these techniques because the workability obtained with trimetaphosphate was

Table 5.2: Roughness parameter R_a for MSH, MSH+HMP and MSH+OP after 28 days of hydration.

	R_{MSH} (nm)	$R_{MSH+HMP}$ (nm)	R_{MSH+OP} (nm)
28 days	20 ±1	22 ±9	14 ±8

inferior than in the other samples and the presence of TMP did not influence M-S-H formation as positively as OP. Therefore, we decided to compare MSH, MSH+HMP and MSH+OP mechanical properties at the nanoscale to evaluate, for the first time, the effect of the actually used additive, HMP, and the effect of OP, that emerged, from the analysis we performed, as an even more efficient additive for MgO/SiO_2 cement.

In order to evaluate their mechanical properties, samples were first properly polished. The procedures commonly used with Portland cement were not suitable for MgO/SiO_2 cements, as it was not possible to obtain a sufficiently low roughness. Therefore, we set up a new polishing procedure and the samples were polished down to a surface roughness $R_a < 100$ nm (calculated using a optical profilometer). In order to get a quick, repeatable and high level of polishing without losing the right hydration level, a multi-step polishing process was established. The samples were polished using a manual polisher without water (to avoid additional hydration) using successive abrasive papers, alternated with 1 minute of sonication in isopropyl alcohol: A/O (aluminium oxide) film of 30μm at 225 rpm (20 seconds), A/O film of 12 μm at 225 rpm (15 seconds), A/O film of 5 μm at 225 rpm (30 seconds) and diamond film of 1μm at 150 rpm (45 seconds). To control surface morphology and roughness, the surface of the samples was evaluated using optical microscopy and confocal profilometer analyses. Figure 5.11 shows the AFM images of the investigated samples after 28 days of curing and table 5.2 reports the roughness parameters (R_a) of the samples. It can be seen that the presence of the additives does not influence the morphology of the binder at the microscopic level and R_a parameters of the three investigated samples do not significantly differ.

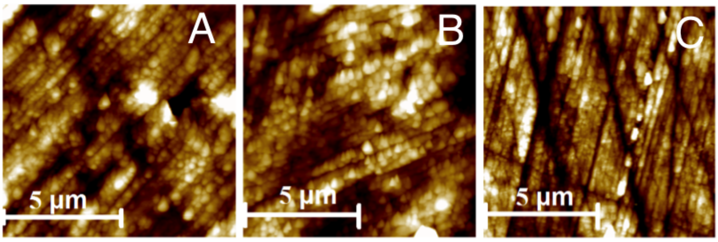

Figure 5.11: AFM images after 28 days of hydration: A) MSH; B) MSH+HMP; C) MSH+OP.

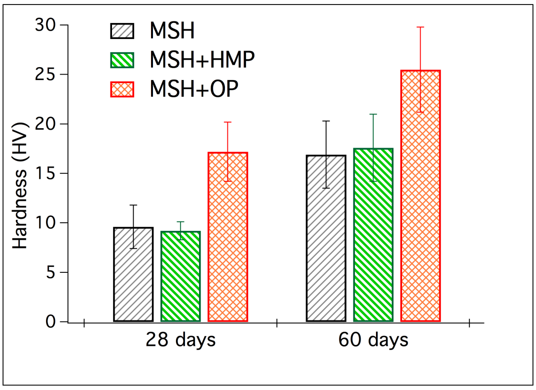

Figure 5.12: Micro-indentation results on MSH, MSH+HMP and MSH+OP samples after 28 and 60 days of hydration. The micro-hardness results here shown are an average of 10 tests, with the corresponding error bars.

Figure 5.12 shows the Vickers hardness test results versus the hydration time of the investigated samples. For all the samples, the micro-hardness increases with time, because it is influenced by the formation of M-S-H phase, that is reported to keep on occurring for long hydration time.[27] The hardness of MSH+HMP sample does not significantly differ from that of the pure MSH sample, while MSH+OP shows higher hardness values at both 28 and 60 days of curing. OP presence increases the micro-hardness of MgO/SiO_2 paste probably because it enhances M-S-H precipitation, as evidenced in the previous section.

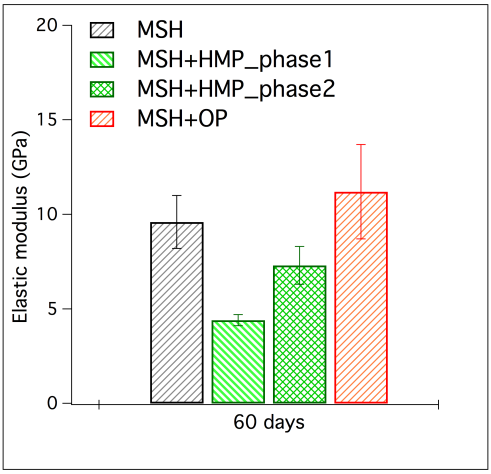

Figure 5.13: Nano-indentation results on MSH, MSH+HMP and MSH+OP samples after 60 days of hydration.

Figure 5.13 shows the elastic modulus after 60 days of hydration. The use

of high-speed nanoindentation approach, performed in collaboration with the University of Rome III, allowed achieving real micron-scale spatial resolution for mechanical property. We found that the presence of HMP lowers the elastic modulus at the nanoscale level, while OP seems to slightly increase it. For MSH+HMP sample, two phases were discriminated during the analysis, but they are both attributable to M-S-H binder phase, also considering that after 60 days of hydration magnesium silicate hydrate is the main phase of this sample.
The lower elastic modulus observed for MSH+HMP with respect to MSH could seem in contrast with the results achieved from microindentation test. Anyway, from microindentation test we gained information on a major scale and the hardness values here reported are related to aggregated phases. On the other hand, nanoindentation relates to smaller scale, to single phases present in the sample. With this technique the elastic modulus is a more representative parameter for this kind of materials, because hardness would be affected by porosity and heterogeneity of the material. As a matter of fact, we can not directly correlate hardness and elastic modulus, arising from different techniques and, thus, from different scales. The future perspective of this study will concern the investigation of the correlation between these parameters.

5.4 Isotherms of adsorption

We studied the isotherms of adsorption of HMP, TMP and OP on MgO, SiO_2 and MgO/SiO_2. We are interested in investigating what happens at the beginning of the process, in the early hours when the reagents are in contact. The evaluation of the interactions of the salts with the reactants in the early stage of the hydration allows to study the effects that they would have in practical systems, where the anhydrous phases are premixed with the additives and then hydrated. Therefore, we investigated the adsorption processes on MgO/SiO_2, and not on already formed M-S-H gel phase.

First, we studied different adsorption isotherms at various times of adsorption, to evaluate the stabilization time and the dependence of the adsorbent concentration on contact time. For this purpose, the curves of HMP adsorption on MgO/SiO_2 at 1, 2, 3 and 4 h at 20° were studied. The curves, reported in figure 5.14, were almost identical, suggesting that already after 1 h the system is at the equilibrium. Thus, we investigated the isotherms of adsorption after 1 h, considering the adsorption an equilibrium phenomenon.

Figure 5.15 shows the adsorption isotherms on MgO substrate. The adsorption of all the three phosphate salts is favored on MgO. These curves can be classified as L-curve.[193, 194] In this case, we can conclude that there are relative strong

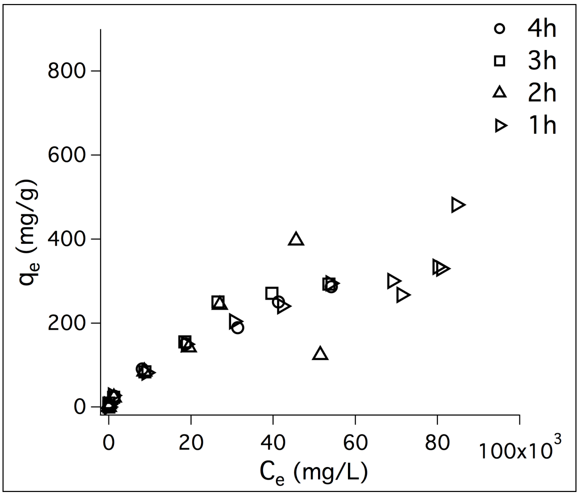

Figure 5.14: Isotherms of adsorption of HMP on MgO/SiO$_2$ at 1, 2, 3 and 4 h at 20 °C.

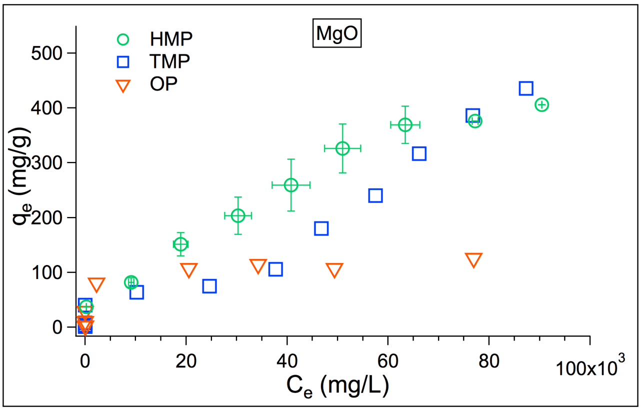

Figure 5.15: Isotherms of adsorption of the investigated phosphate salts on MgO at 20 °C.

attractive forces between solute molecules and substrate, but weak solute-solute forces.

Figure 5.16 shows the adsorption isotherms on SiO$_2$. When the phosphate salts adsorb on silica there is a cooperative-adsorption and the isotherm can be classified as S-type, by following the Giles classification.[193, 194] In this case, the adsorption on the substrate is not favored and the solute-solute forces are stronger than the solute-substrate ones.

Figure 5.17 shows the adsorption isotherms on MgO/SiO$_2$. Concerning the

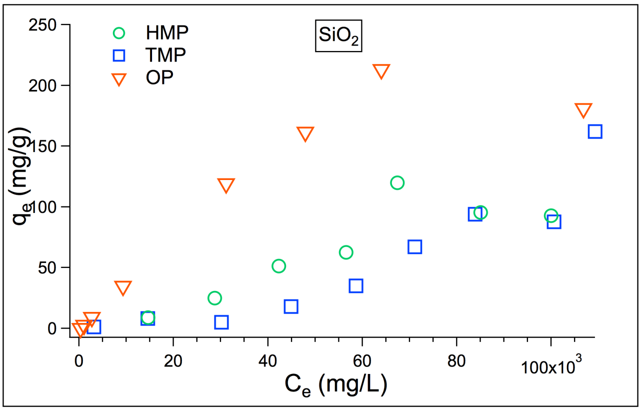

Figure 5.16: Isotherms of adsorption of the investigated phosphate salts on SiO_2 at 20 °C.

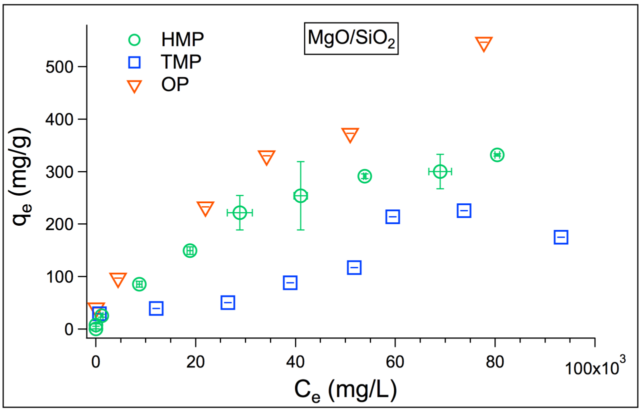

Figure 5.17: Isotherms of adsorption of the investigated phosphate salts on MgO/SiO_2 at 20 °C.

adsorption on MgO/SiO_2 substrate, the process is not favored for TMP (S-type curve), while it is favored for HMP and OP (L-type curves).[193, 194] For HMP and OP, the adsorption on MgO/SiO_2 is similar to that on MgO, suggesting that the affinity of the adsorbate with MgO (or $Mg(OH)_2$ forming during MgO hydration) is the driving force even in the case of MgO/SiO_2 substrate. Looking at the figure 5.18, in the curves of HMP and OP it can be noticed a plateau of adsorption, concerning the formation of the first monolayer of adsorbate on the adsorbent. Since the adsorption of HMP and OP on MgO/SiO_2 seems to follow the Langmuir model, we decided to fit the curves to extract information about the area occupied by each molecule on the surface. The idea was to compare the experimental area with the area theoretically occupied by each molecule, calculated by applying a formula already known in literature for the volume[195] and approximating the projection of the adsorbate on the surface. In the literature, a similar approach was previously applied to study the geometry of the adsorption of HMP on kaolinite.[131] Similarly, we aimed at comparing the experimental and theoretical area occupied by HMP and OP on the surface, to investigate the coverage of the surface and to hypothesize the disposition of the molecules. The formula to calculate the experimental area occupied by each molecule on the surface is the following:

$$Area_{experimental} = \frac{Area_{MgO/SiO_2}}{mol_{adsorbed} * N_{Avogadro}} \tag{5.1}$$

This calculation needs to known the value of the surface area of the samples, Area$_{MgO/SiO_2}$, and the moles of adsorbate adsorbed, $mol_{adsorbed}$, that can be extracted from the Langmuir model application. By measuring the surface area of the samples, we found that the area of pristine MgO/SiO$_2$ is higher than the area of MgO/SiO$_2$+HMP and MgO/SiO$_2$+OP. These variations of areas in presence of the adsorbates suggested that the systems were more complicated than expected and the necessary conditions for the application of the Langmuir model were not respected.

The XRD diffractograms of MgO/SiO$_2$ substrate resulting from the adsorption of HMP at different concentrations, TMP and OP at 200 mM (that is the maxim concentration used in the adsorption isotherms), are shown in figure 5.19, together with the curve of pristine MgO/SiO$_2$ hydrated 1 h in the same conditions used for the isotherms of adsorption. Solids have been freeze-dried before the analysis. We evidenced that not only the area, but also the composition of the substrate changes when the adsorbates are added (in terms of quantity of MgO, Mg(OH)$_2$ and M-S-H phase). We concluded that the Langmuir model could not be applied to gain information on the thermodynamic aspects of the adsorption process, neither it was possible to understand the disposition of the molecules on the substrate as expected. On the other hand, we observed that the presence of phosphate additives influences the phases forming in the early stage of hydration.

The future perspectives of this work will concern the study of the effects of phosphate additives on the reagents in the early hydration, to understand their influence on the surface area of the substrate. The presence of different phosphate species in solution might be responsible for the differences encountered using XRD analysis. The future developments will include also the evaluation of a new model, to properly describe the complex processes of adsorption of HMP and OP, taking into account the variation of surface area and the substrate dependence on adsorbate presence.

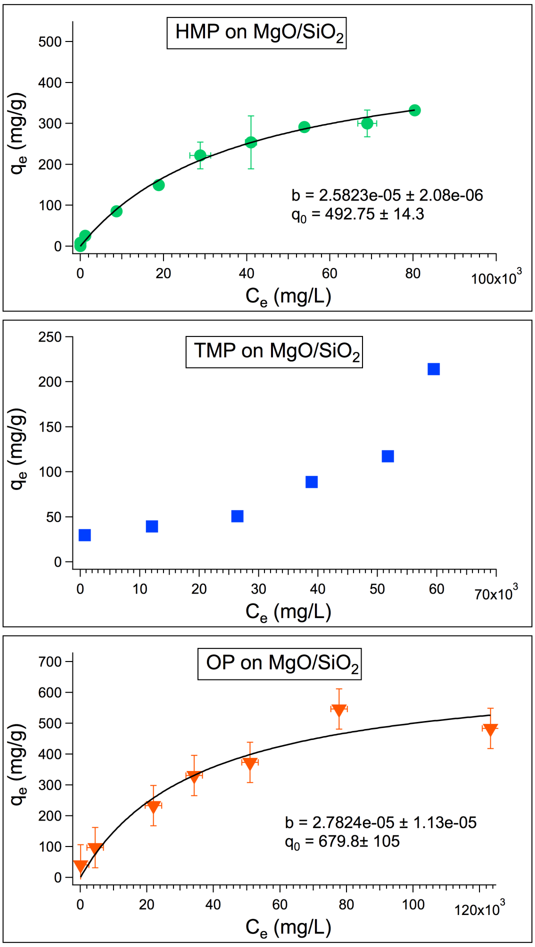

Figure 5.18: Isotherms of adsorption of the investigated phosphate salts on MgO/SiO_2 at 20 °. Black lines are the Langmuir fitting curves, used for HMP and OP additives.

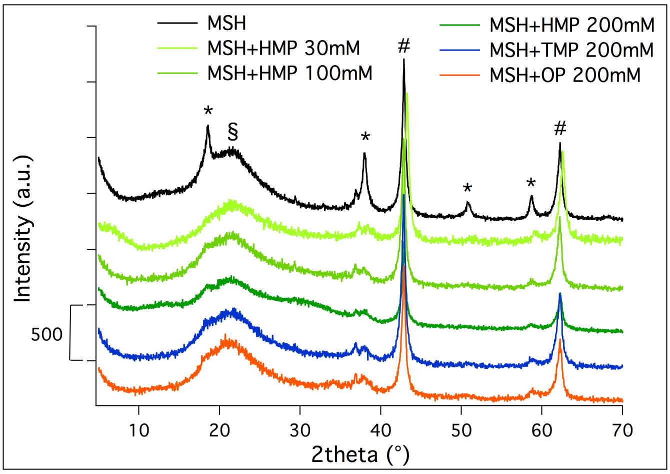

Figure 5.19: XRD diffractograms of pristine MgO/SiO$_2$ (hydrated 1 h in the same conditions used for the isotherms of adsorption) and of MgO/SiO$_2$ substrate resulting from the adsorption of HMP, TMP and OP at 20 °C. Curves have been offset for the sake of clarity. $\star$: Mg(OH)$_2$; #: MgO; §: M-S-H and SiO$_2$.

6 Effects of aluminate additives on MgO/SiO_2 cements

This chapter reports the study of the effects of two aluminate additives on the formation and properties of M-S-H. Tricalcium aluminate phase (C_3A) is commonly present in Portland formulations and it is already known that C_3A is responsible for the strength development of the pastes at short hydration time. Since in some applications calcium- and magnesium-based cement coexist, it is important to understand the effects of the aluminate phases, commonly present in PC formulations and clays, on M-S-H binder gel. We decided to evaluate the effect of two aluminate-based additives on MgO/SiO_2 cement: C_3A and imogolite (IMO). IMOs are nanoclay tubular additives exposing aluminol sites and they have been studied in this project to evaluate if it was possible to combine the reinforcement of nanotubular fibres with the effects reported for aluminate phases in PC.

The hydration kinetics of the pastes were studied using DSC and the pH of the pastes was monitored, as it provides important information on phases evolution and it is a key parameter for practical applications. The phases formed at different hydration times have been characterized using XRD, TGA and FTIR. The morphologies of the samples have been investigated using SEM. We found that C_3A negatively affects MgO/SiO_2 hydration reaction and limits the formation of M-S-H. On the other hand, IMOs do not affect M-S-H formation. We compared the mechanical properties of MgO/SiO_2 pristine and in presence of imogolites, to evaluate if the presence of the fibres had increased the strength of the samples at the micro-scale. The micro-hardness of the prepared samples were investigated using Vickers hardness test, while the nano-mechanical properties were evaluated using statistical high-speed nanoindentation. The results evidenced that the presence of imogolites only slightly increases the mechanical properties of MgO/SiO_2 cement.

6.1 Imogolite synthesis

Imogolite clays were synthesized following a procedure adapted from Koenderink *et al.*.[88] Aluminum-tri-sec-butoxide and tetraethyl orthosilicate were added to a percloric acid solution preheated at 70 °C, at a Si:Al:HClO$_4$ = 1:2:1 ratio. A white precipitate formed immediately upon mixing. The reaction mixture was stirred under reflux for 5 h and gradually cleared. Then, the solution was refluxed at 100 °C for a week. The resulting solution was dialyzed against deionized water using a dyalisis tubing cellulose membrane to remove unreacted reagents and small molecules. A precipitate formed and it was concentrated by centrifugation and freeze-dried to be used as additive. The obtained fluffy material was characterized by means of TEM images (see figure 6.1) and XRD diffractograms (see figure 6.2) that confirmed the obtainement of imogolites. In figure 6.1 it is possible to distinguish imogolite fibres and aggregates. The formation of aggregates is attributed to the formation of H-bonds between the fibres, enhanced by the freeze-drying process.

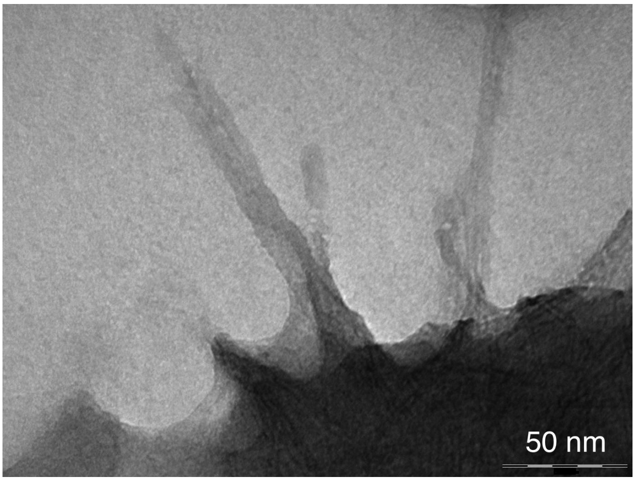

Figure 6.1: TEM image of the synthesized imogolites.

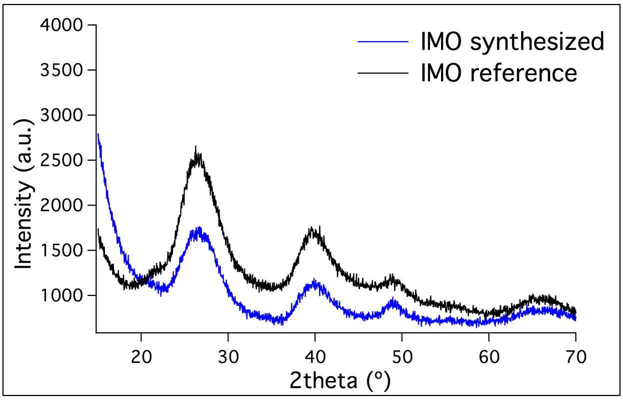

Figure 6.2: Comparison between the synthesized imogolites and a reference sample.

6.2 Preparation of the samples

The samples were prepared by mixing MgO:SiO_2 at a water to solid ratio of 0.8. When present, aluminate additives were premixed with the solid at 10 wt% ratio. Pristine MgO/SiO_2 sample is the same investigated in Chapter 5 (MSH).

Table 6.1 reports the notation that will be used throughout the chapter.

Table 6.1: Composition of the investigate samples and corresponding notation. Weight percentage are referred to the total amount of MgO/SiO_2.

	MSH	MSH+C_3A	MSH+IMO
MgO (wt%)	40	40	40
SiO_2 (wt%)	60	60	60
C_3A (wt%)		10	
IMO (wt%)			10

6.3 Phases characterization

Figure 6.3 shows the FWI *vs.* time curves. The curves do not differ in the entire investigated period and, thus, we can conclude that neither C_3A nor imogolites influence the kinetic of the hydration reaction. As already reported in Chapter 5 for sample MSH, there is a short induction period (up to 1 h), between 1 and 10 h the acceleration period occurs, when FWI decreases because of the nucleation and growth of the hydrated phases, and finally it is possible

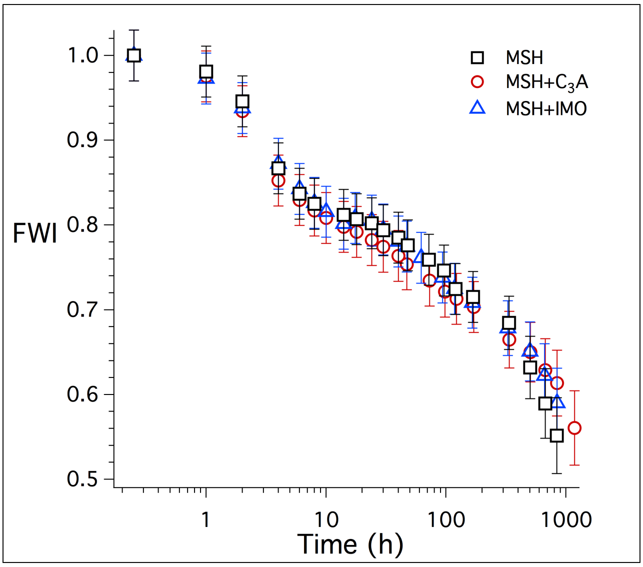

Figure 6.3: FWI as a function of hydration time.

to recognize a change in the slope of the curves, due to the modification of the rate-limiting mechanism, from nucleation-and-growth to a diffusion-limited behavior.[98]

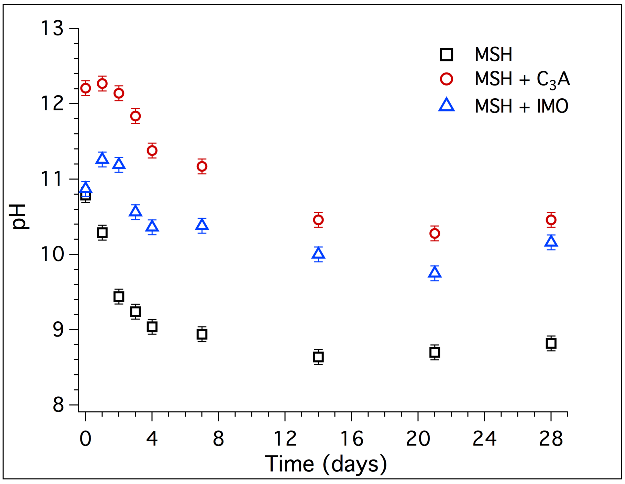

Figure 6.4: Trends of pH with time (±0.1) of the investigated samples.

Figure 6.4 shows the variation of pH values over a period of 28 days. The pH *vs.* time trend of MSH starts to decrease immediately after mixing and, then, reaches a plateau after about two weeks. In MSH sample, the pH is initially affected by the presence of brucite, then it decreases to ∼ 9 because of the consumption of brucite in the reaction with hydrated silica.[14, 26, 33, 143] In the presence of additives the values of pH are higher in the entire investigated period and this effect is particularly pronounced for C_3A. The pH of MSH+C_3A initially remains constant, while in MSH+IMO sample it increases in the first day and then decreases. In both cases, a plateau is reached after about two weeks: MSH+C_3A stabilized at ∼ 10.5, while MSH+IMO stabilized at ∼ 10.2. This effect is probably due to the presence of high amounts of $Mg(OH)_2$ (pKa ≈ 10.5), that kept the pH of these formulations at higher values than in pristine MSH.

Figure 6.5 shows the XRD diffractograms of the investigated samples after 7, 28 and 60 days of hydration. The broad peaks at about 23°, 35° and 59° are attributed to the amorphous M-S-H phase, while brucite crystalline phase is responsible for the signals at ∼ 20°, 33°, 38°, 51°, 59°, 62° and 69°.[30, 33] At about 20° occurs also a peak attributed to SiO_2, well evident in the diffractograms after 7 days of hydration, when unreacted silica and $Mg(OH)_2$ are still abundant. The intensity of the peaks attributed to $Mg(OH)_2$ decreases with time in all the three samples, but when C_3A and IMO are added more brucite remains, even at long hydration times. This result is in agreement with the high pH values registered for MSH+C_3A and MSH+IMO samples. On the other hand, the signals attributed to M-S-H phase increase with time, especially in MSH and MSH+IMO samples, confirming the formation of the binder gel phase.

DTA curves registered on the samples after 60 days of hydration are shown in figure 6.6. Four signals are present in the reported curves: the first signal (< 200 °C) arises from the elimination of physisorbed water from M-S-H; the second peak (∼ 370 °C) is due to the decomposition of brucite; and the last two signals (∼ 810 and ∼ 850 °C) are attributed to solid phase transitions of M–S–H to crystalline species.[29, 62] By comparing the peak at about 370 °C we can see in MSH+C_3A and MSH+IMO samples that high amount of brucite is still present after 60 days of hydration, as suggested by pH measurements and further confirmed by XRD analysis. On the contrary, in MSH sample $Mg(OH)_2$ is almost completely consumed after 60 days of hydration. Looking at the signals at lower and higher temperature, we can notice some other differences. When C_3A is added, the signals assigned to M-S-H are very low. In this case it seems that very scarce amount of M-S-H forms, even after 60 days of hydration. On the contrary, in presence of IMO the peak at ∼ 100 °C is even more intense than in MSH case. At higher temperatures, two signals are present in MSH+IMO sample, while MSH presents only one peak and MSH+C_3A shows only a very low wide signal. As already known, at temperature > 800°C, talc and chrysotile-like subnanometric domains of M-S-H, convert to enstatite

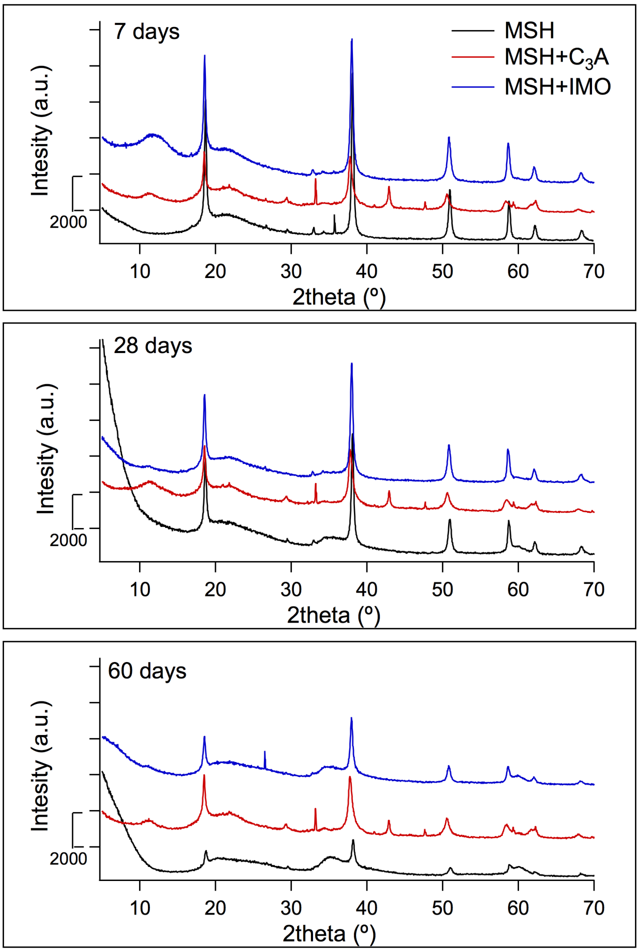

Figure 6.5: XRD diffractograms of the investigated samples after 7, 28 and 60 days of hydration.

and forsterite.[29, 62, 145, 147] The difference in MSH and MSH+IMO curves suggests that M-S-H phase in these samples differs and probably the talc and chrysotile-like domains form in different ratios.

Figure 6.7 reports the FTIR spectra of the samples after 60 days of hydration. A sharp peak at $\sim$ 3700 cm^{-1}, attributed to brucite, is present in MSH+C$_3$A and MSH+IMO spectra. The broad absorption at about 3400 cm^{-1} and the band at 1640 cm^{-1} can be ascribed to OH stretching and bending, respectively.[34, 44] These signals are present in all the three investigated samples, but in MSH+C$_3$A sample the signal at 1640 cm^{-1}, typical of M-S-H, has a very low intensity. On the other hand, the bands at 560 and 460 cm^{-1} assigned to MgO vibrations are particularly intense in MSH+C$_3$A sample. In the 1300

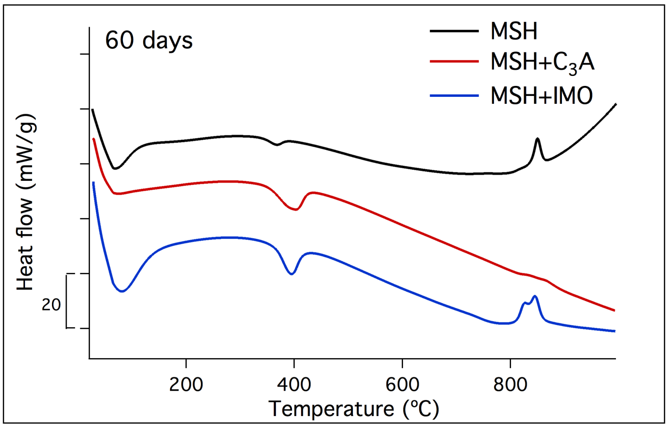

Figure 6.6: DTA curves of the investigated samples after 60 days of hydration.

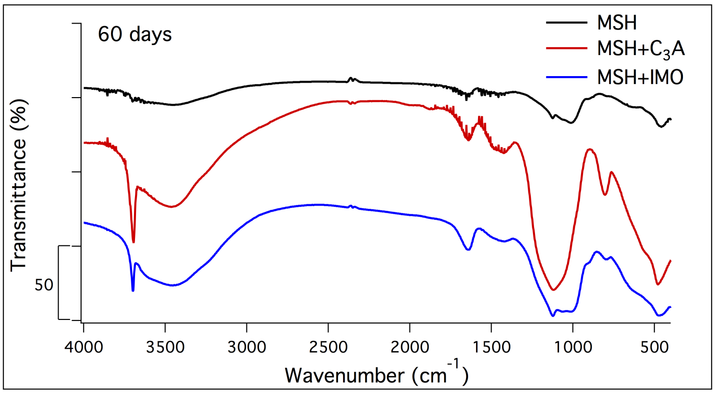

Figure 6.7: FTIR spectra of the investigated samples after 60 days of hydration.

– 750 cm^{-1} spectral range, multiple absorptions occur, due to the stretching and bending vibrations of Si–O. In particular, the peak at about 800 cm^{-1} is attributed to Si–O vibrations from unreacted silica and this peak is particularly intense in MSH+C_3A sample. The presence of high amounts of unreacted MgO and SiO_2 further confirms that in MSH+C_3A the formation of M-S-H is inhibited. Moreover, the broad bands between 1300 and 950 cm^{-1} in MSH and MSH+IMO samples are at lower wavenumbers than in MSH+C_3A sample, since in these cases SiO_2 was consumed and M-S-H precipitated.[29, 44]

Figure 6.8 shows the morphologies of the investigated samples after 60 days of hydration. In MSH (figure 6.8 A) and MSH+IMO (figure 6.8 C), it is possible to recognize a diffuse filamentous morphology attributed to the amorphous binder phase, M-S-H gel. The morphology of MSH+IMO sample is very similar to that of pristine MgO/SiO_2 sample and it is possible to recognize many holes

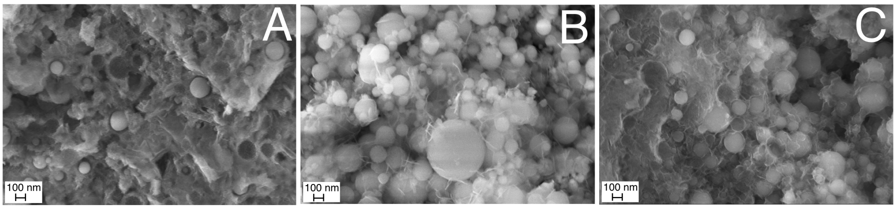

Figure 6.8: SEM images of the investigated samples after 60 days of hydration: A) MSH; B) MSH+C_3A; C) MSH+IMO.

left by consumed silica. In MSH+C_3A sample (figure 6.8 B) many globular spheres are present, typical of unreacted silica. These findings further confirm the results obtained with the other technique: C_3A inhibits the formation of M-S-H and, even after long hydration time many unreacted species are still present in this sample. On the other hand, IMOs slightly affect the formation of M-S-H: higher amounts of brucite were found in MSH+IMO than in pristine MSH and M-S-H gel seems to contain talc and chrysotile-like sub-nanometric domains in different ratio when IMOs are present.

6.4 Mechanical properties

We evaluated the mechanical properties at the micro-scale of MSH and MSH+-IMO. MSH+C_3A sample was not studied with micro- and nano-indentation techniques, since it was not possible to obtain a proper polishing of the surface. Moreover, we already evidenced that C_3A inhibits the precipitation of M-S-H binder gel phase, so the use of C_3A additive was not promising for the goals of this study.
MSH and MSH+IMO samples were polished down to a surface roughness $R_a < 100$ nm, following the procedure described in Chapter 5.

Figure 6.9 shows the micro-indentation results for MSH and MSH+IMO samples after 28 days of hydration. We found that IMO presence increases the micro-hardness of MgO/SiO_2 paste. Figure 6.10 shows the elastic modulus of MSH and MSH+IMO samples after 28 days of hydration, performed in collaboration with the University of Roma TRE. Even in this case we found that IMO presence increases the elastic modulus of MgO/SiO_2 paste, but the effect was less evident than in the Vickers hardness test.

The investigation of the mechanical properties using micro- and nano-indentation evidenced that imogolites slightly increase the hardness and elastic modulus of MgO/SiO_2 paste after about one month of hydration. The use of IMOs allows the obtainment of tiny improvement and the presence of aluminol groups on

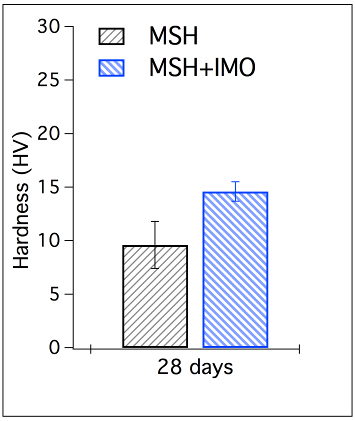

Figure 6.9: Micro-indentation results on MSH and MSH+IMO samples after 28 days of hydration. The micro-hardness results here shown are an average of 10 tests, with the corresponding error bars.

IMO does not influence MgO/SiO_2 hydration, while C_3A has even negative effects. The use of similar additives in MgO/SiO_2 formulations seems to be precluded and the effect of tricalcium aluminate, possibly present, should be taken into account. In particular, since we evidenced the negative effect of C_3A on MgO/SiO_2 hydration, the presence of this aluminate phase in PC should be considered when MgO/SiO_2 and calcium-based cement are in contact, like in nuclear waste encapsulation applications.

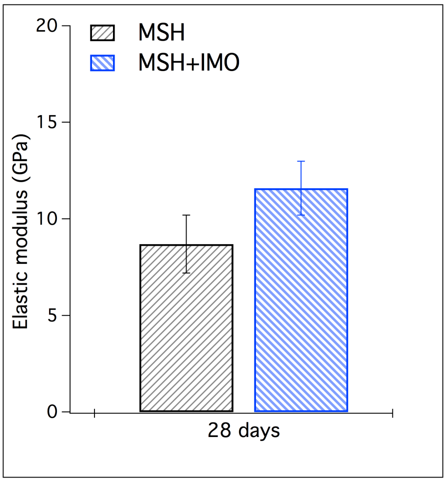

Figure 6.10: Nano-indentation results on MSH and MSH+IMO samples after 28 days of hydration.

7 Halloysite incorporation in MgO/SiO_2 cements

The last topic I have addressed in my PhD concerns the evaluation of the effect of halloysites (HNTs) on MgO/SiO_2 cements, both pristine and functionalized with phosphate groups. In the previous chapter we investigated the effect of imogolites for reinforcing purposes, but we found that aluminate presence may inhibits M-S-H formation. In this chapter we focused on the evaluation of another alumosilicate clay, halloysites, that expose silanol groups instead of aluminol sites. It was already reported in the literature that sodium hexametaphosphate has positive effect on MgO/SiO_2 hydration reaction and we found that the presence of ortophosphate improves the precipitation of M-S-H binder phase and increases the mechanical properties of MgO/SiO_2 cements (Chapter 5). In this framework, we functionalized halloysites with phosphate groups and we evaluated the possibility of combining the reinforcing characteristic of HNTs with the reported effects of phosphate groups.
We studied the hydration kinetics of the samples using DSC and we characterized the phases formed at different hydration times using TGA and XRD, while the pH of the pastes has been monitored with time. The micro-hardness of the prepared samples was evaluated using Vickers hardness test and the elastic modulus was studied using statistical high-speed nanoindentation. We found that HNT and HNT-PO_4 have very slight effects on MgO/SiO_2 hydration. The presence of both these additives do not significantly affect M-S-H formation and also the mechanical properties were similar to that of pristine MgO/SiO_2.

7.1 HNT functionalization with phosphate groups

We tried two synthetic pathways to prepare halloysites functionalized with phosphate groups :

1. **Pathway 1:** in the first synthetic pathway we used 4-bromobutyryl chloride and phosphoric acid, as shown in figure 7.1. 4-Bromobutyryl chloride was added to HNT in dimethylformamide and stirred for 5 days in presence of NaH. The hydroxyl groups of HNTs reacted with

the acyl carbon of 4-bromobutyryl chloride and the obtained product (HNT-Br) was washed with acetone and centrifuged. We controlled the obtainment of the reaction product using FTIR (see figure 7.3). The signal at ∼ 1640 cm^{-1}, attributed to OH^- of HNTs, shifted to higher wavenumber, confirming the estereous bond in HNT-Br. The next step was a nucleofilic substitution. HNT-Br were stirred 5 h at 80 °C with phosphoric acid and triethylamine in dimethylformamide, to obtain HNT-PO_4. Phosphoric acid was used in excess to ensure the substitution of phosphate groups at the end of the chain. HNT-PO_4 was washed with water, centrifuged and freeze-dried. ICP-AES allowed to quantify the amount of phosphorous on HNTs surface and to ensure the presence of phosphate groups on HNTs surface. We found that only a partial coverage of HNTs with phosphate groups occurred.

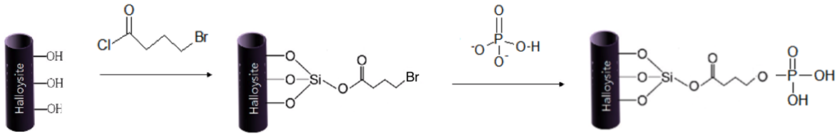

Figure 7.1: Pathway 1: synthesis of halloyistes functionalized with phosphate groups.

2. **Pathway 2:** the second pathway we used to modify the surface of halloysites was inspired to a method previoulsy reported in the literature.[196–198] We used 3-amminopropyltriethoxysilane (APTES), ε-caprolactone and phosphorous oxychloride, as shown in figure 7.2. In the first step, APTES was added to HNT in ethanol in presence of NH_4OH, used to ensure a pH of about 9. The product (HNT-NH_2) was washed with ethanol, centrifuged and dried. To ensure a total coverage of HNTs, we used APTES in excess and we evaluated the reaction product using FTIR (figure 7.4). We confirmed the functionalization of HNT with APTES from the peak at 2930 cm^{-1}, attribute to C-H stretching from CH_2 groups, from the band at 3200 - 3500 cm^{-1}, attributed to N-H stretching of NH_2 group, and from the signal at 1250 cm^{-1}, due to N-H scissoring (see figure 7.4). Then, HNT-NH_2 were mixed with ε-caprolactone in dichloromethane and CH_3ONa at 50 °C for 2 days. The product (HNT-OH) was quenched with NH_4Cl, washed with ethanol, centrifuged and dried. After this reaction, the signal attributed to NH_2 were no more detectable, confirming the reaction with caprolactone and the obtainment of HNT-OH. Moreover, the large band in the 2900 - 3150 cm^{-1} spectral range (figure 7.4) confirmed the presence of many CH_2 groups. HNT-OH were finally mixed with triethylamine in toluene

and then a solution of phosphorous oxichloride in toluene was added. The mixture was stirred for 3 days and we progressively evaluated the presence of phosphate groups on HNTs. The solid was washed with water, centrifuged and freeze-dried. We monitored the presence of phosphorous using ICP-AES, to ensure the functionalization of HNTs with phosphate groups. We found that after 3 days of stirring, the surface was almost completely covered by phosphate groups.

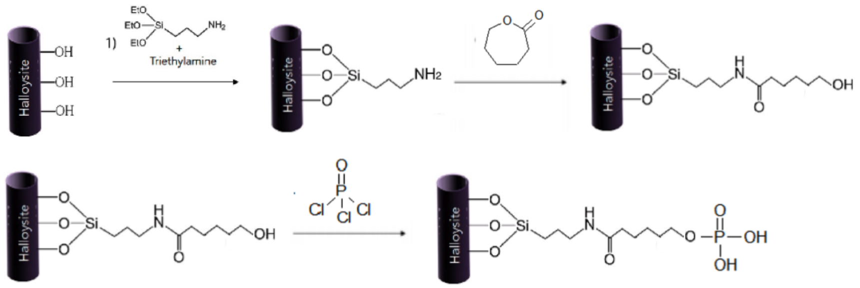

Figure 7.2: Pathway 2: synthesis of halloyistes functionalized with phosphate groups.

As anticipated, ICP-AES technique was used to compare the coverage of halloysite surface with phosphate groups. It is already known that organosilanes with long alkyl chains typically have an area per molecule ≤ 0.5 nm^2.[199] Starting from the BET surface area of the used halloysites (20 m^2/mg) and considering that the area occupied by each silanol group of APTES is 0.5 nm^2, we can calculate how many APTES are necessary to totally cover HNT surface. Then, hypothesizing that each silanol properly reacted and finally expose phosphate group, we can calculate how many phosphorus atoms would be present at the maximum coverage. We found that using the first procedure (pathway 1) we obtained only a partial coverage, while using the second procedure (pathway 2) we obtained HNTs totally exposing phosphate groups. Therefore, we used the second procedure for the functionalization of the halloysites used in this study.

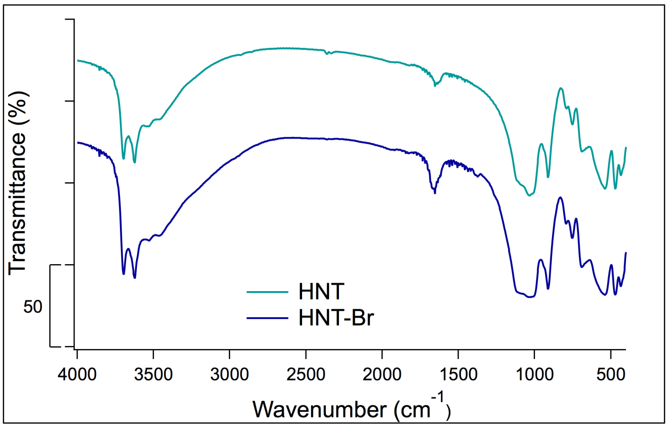

Figure 7.3: FTIR spectra of HNT and HNT-Br (pathway 1).

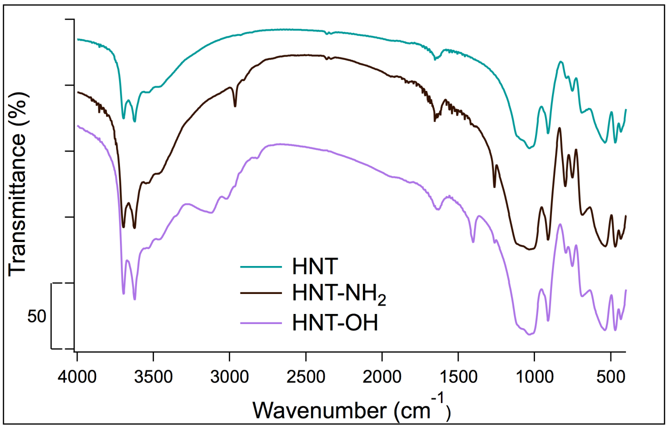

Figure 7.4: FTIR spectra of HNT, HNT-NH_2 and HNT-OH (pathway 2).

7.2 Preparation of the samples

Pastes were prepared by mixing $MgO:SiO_2$ at a water to solid ratio of 0.8. When present, halloysites were premixed with the solid at 10 wt% ratio (with respect to MgO/SiO_2). Pristine MgO/SiO_2 sample was the same investigated in Chapter 5. Table 7.1 reports the notation that will be used throughout the chapter.

Table 7.1: Composition of the investigate samples and corresponding notation. Weight percentage are referred to the total amount of MgO/SiO_2.

	MSH	MSH+HNT	MSH+HNT-PO_4
MgO (wt%)	40	40	40
SiO_2 (wt%)	60	60	60
HNT (wt%)		10	
HNT-PO_4 (wt%)			10

7.3 Phase characterization

Figure 7.5 shows the FWI *vs.* time curves. In the first hours of hydration, the curves do not differ and the presence of halloysites do not influence the kinetic of hydration of MgO/SiO_2 paste. Then, after about 100 h, some differences occur. In the diffusional period, HNT and HNT-PO_4 leads to lower FWI and, thus, the hydration reaction seems to be slightly favored at long hydration times when halloysites are present.

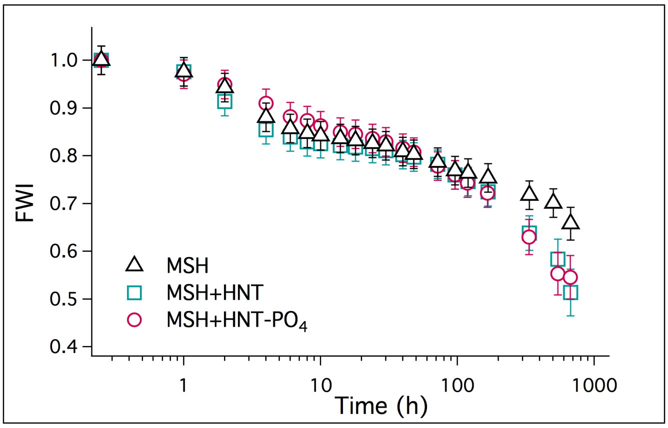

Figure 7.5: FWI as a function of hydration time for all the investigated samples.

Figure 7.6 shows the variation of pH values over a period of 28 days. The pH is initially affected by the presence of brucite ($pK_a \approx 10.5$), then it decreases to ~ 9 because of the consumption of brucite in the reaction with hydrated silica.[14, 26, 33, 143] The pH *vs.* time trend of the investigated samples starts to decrease immediately after mixing and reaches a plateau after about two weeks of hydration. In the presence of the additives some differences occur at the beginning of the plateau (after about 10 days) and MSH+HNT and

MSH+HNT-PO$_4$ formulations reach values slightly higher. Anyway, this is a very weak effect and after 28 days the differences are minimal.

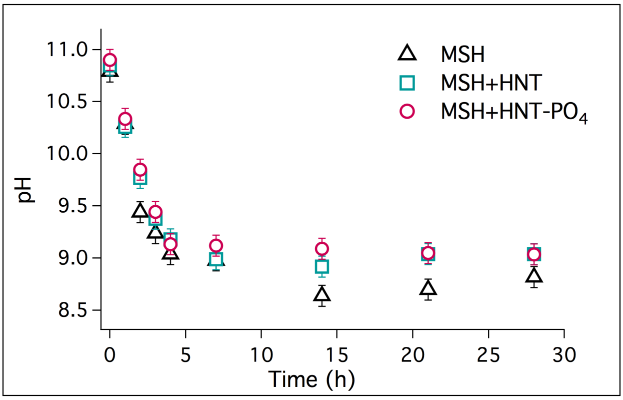

Figure 7.6: Trends with time of pH (±0.1) of the investigated samples.

Figure 7.7 shows the derivative curves of the weight losses of the samples at different hydration times (on the left) with the corresponding heat flow curves in the 700 - 1000 °C (on the right). DTG curves show various signals, as expected for MgO/SiO$_2$ cement: between room temperature and 200 °C there is a broad signal attribute to the elimination of physisorbed water from M-S-H, at ∼ 370 °C there is a sharp signal due to the decomposition of brucite and in the 450 - 800 °C range there is a large signal, due to the dehydroxilation of M-S-H.[29, 62] It can be observed that for all the investigated samples the amount of brucite decreases with time, while the amount of M-S-H increases with increasing the hydration time.

Concerning the DTA signals, in this temperature range we can observe the exothermic signals attributed to the recrystallization of talc and chrysotile-like sub-nanometric domains of M-S-H binder phase.[29, 62, 145, 147] These peaks observed at ∼ 810 and 850 °C progressively sharpens during the hydration. In MSH and MSH+HNT after 58 days only the peak at higher temperature is still present, suggesting that at longer hydration times talc-like domains are favored. On the contrary, DTA curve of MSH+HNT-PO$_4$ sample after 58 days of hydration shows two signals, suggesting that M-S-H phase in this sample differs from that in MSH and MSH+HNT, and the talc and chrysotile-like domains formed in different ratio.

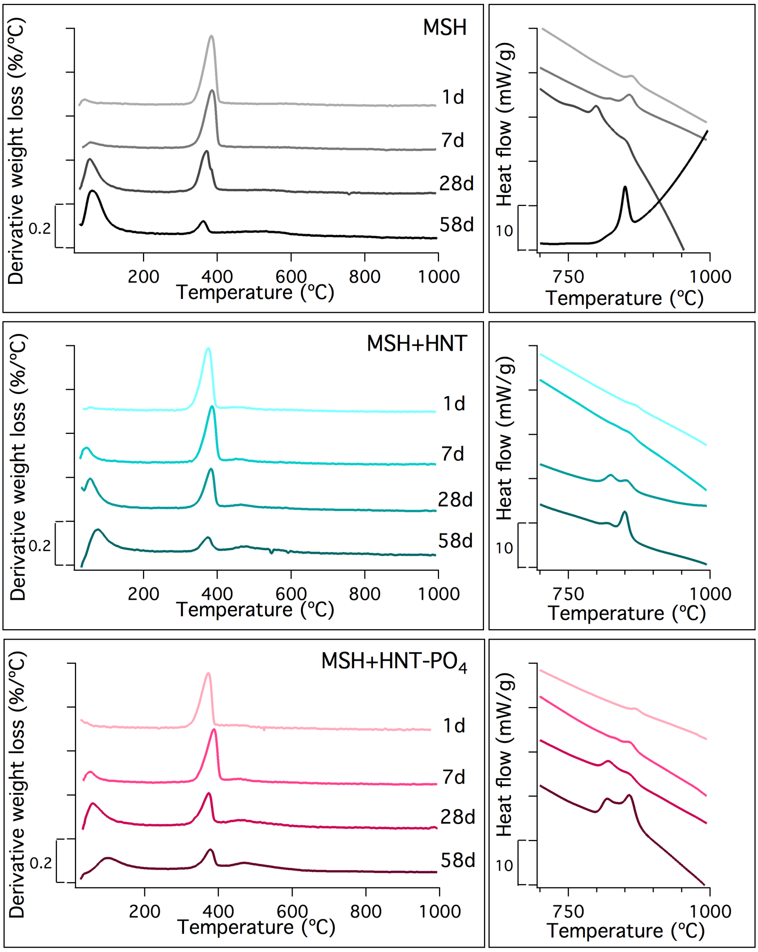

Figure 7.7: DTG curves (on the left) and DTA curves (on the right) of the investigated samples at different hydration times. The curves have been offset for the sake of clarity.

Figure 7.8 shows the XRD diffractograms of the investigated samples at 7, 28 and 58 days of hydration. Brucite is the main crystalline phase (signals at about 20°, 33°, 38°, 51°, 59°, 62° and 69°), whereas the broad peaks at roughly 23°, 35° and 59° are consistent with the XRD pattern of the amorphous M-S-H phase.[30, 33] For all the samples, it is possible to notice a decrease of brucite peaks with hydration time in accordance with TG results, as its consumption occurred to produce M-S-H. The amount of brucite in MSH+HNT-PO_4 is slightly higher than in MSH and MSH+HNT.

The results here presented suggest that both HNT and HNT-PO_4 does not significantly influence MgO/SiO_2 hydration. The phosphate groups that are

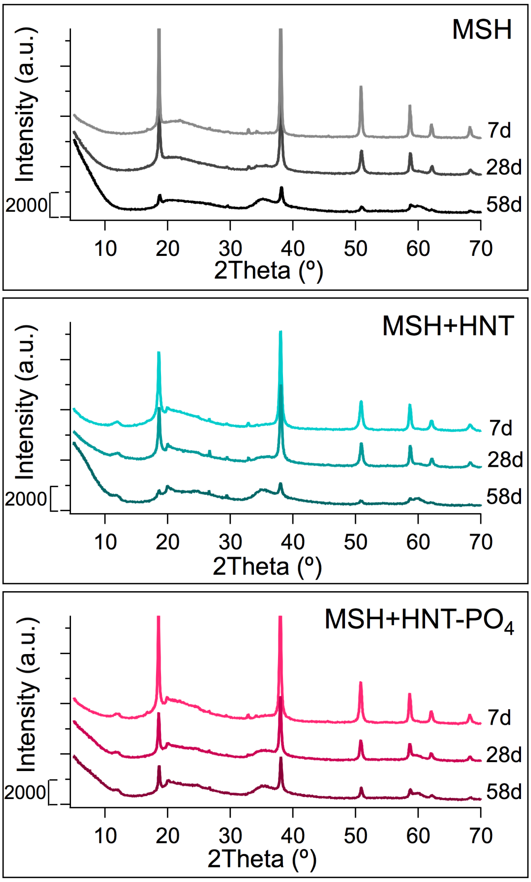

Figure 7.8: XRD patterns of the investigated samples at 7, 28 and 58 days of hydration. Curves have been offset for the sake of clarity.

present on HNT-PO$_4$ surface did not allow to observe the same effects found for ortophosphate additives in Chapter 5. It might be hypothesize that phosphates are hindered by HNT in the interaction with M-S-H. Even so, we decided to evaluate if the presence of HNT fibres increased the mechanical properties at the micro-scale.

7.4 Mechanical properties

The samples were polished down to a surface roughness $R_a < 100$ nm, following the procedure described in Chapter 5, and then analyzed using Vickers hardness test and nanoindentation express test.

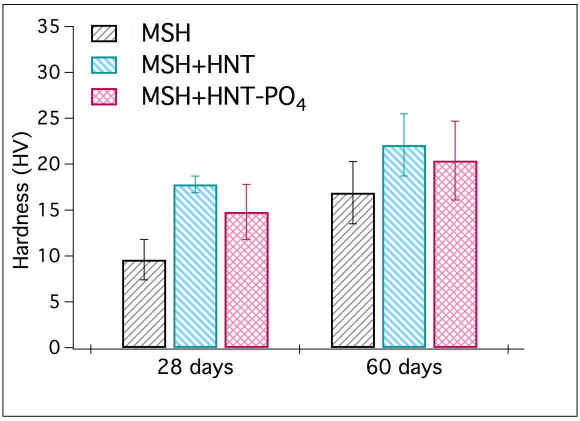

Figure 7.9: Micro-indentation results on M-S-H, M-S-H + HNT and M-S-H + HNT-PO_4 samples after 28 and 60 days of hydration. The micro-hardness results here shown are an average of 10 tests, with the corresponding error bars.

Figure 7.9 shows the micro-indentation results on MSH, MSH+HNT and MSH+HNT-PO_4 samples after 28 days of hydration. HNT presence increases the micro-hardness value of MgO/SiO_2 paste after 28 days of hydration, but after 60 days this difference decreases. MSH+HNT-PO_4 sample shows micro-hardness values intermediate between MSH and MSH+HNT samples. We found that the presence of halloysites increases the hardness at the micro-scale in the first month of hydration, but at longer hydration time the effect is negligible. Surprisingly, HNT-PO_4 do not have reinforcing effect on MgO/SiO_2 cement.

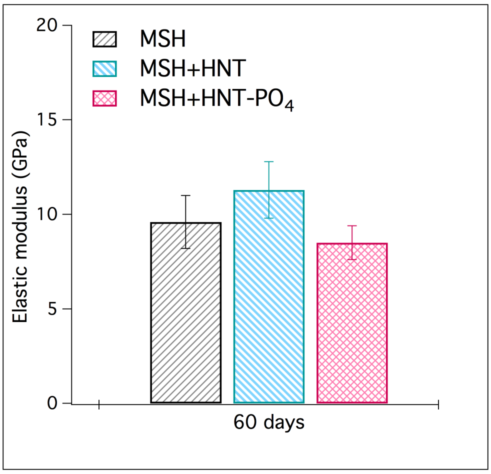

Figure 7.10: Nano-indentation results on M-S-H, M-S-H + HNT and M-S-H +HNT-PO_4 samples after 60 days of hydration.

Figure 7.10 shows the elastic modulus of MSH, MSH+HNT and MSH+HNT-PO$_4$ samples after 28 days of hydration, performed in collaboration with the University of Roma TRE. We found that HNT presence very slightly increases the elastic modulus of the pristine MSH paste, while MSH+HNT-PO$_4$ sample shows the lowest value. The investigation of the mechanical properties using micro- and nano-indentation analysis evidenced that at long hydration time, MSH, MSH+HNT and MSH+HNT-PO$_4$ samples strongly resemble each other.

The results here reported show that the functionalization of halloysites with phosphate groups did not allow to combine the reinforcing effect expected from halloysites with the improvement associated to phosphate. On the contrary, the presence of phosphate groups on HNT surface even lowers the slight improvement obtained with halloysites. Similarly to what observed for imogolites in Chapter 6, the use of halloysites did not allow an improvement in the mechanical properties. Therefore, the use of nanotubular clay fibres did not show reinforcing effects on MgO/SiO$_2$ cement.

Conclusions

This work of thesis describes the preparation and the physico-chemical characterization of different formulations of MgO/SiO_2 cement. During my PhD, I have explored the possibility of tailoring the final performances of MgO/SiO_2 cement by changing the initial composition, in a bottom-up approach.
Magnesium silicate hydrate cements are suited for specialist applications, where their potential for CO_2 emissions reduction can be exploited, but the low strength and the pH, non sufficiently high to passivate steel reinforcing bars, limit their use and the possibility of replacing Portland cement. The identification of M-S-H in key environments related to nuclear waste disposal recently highlighted the importance of developing a full structural characterization of that gel. Moreover, even if research interest in MgO/SiO_2 cement is growing, only one additive has been used with this new kind of cement, while in traditional Portland cement many different additives are commonly used to modulate performances to specific applications. In this framework, my PhD research was focused on the characterization of MgO/SiO_2 cements alone, mixed with traditional cements and in presence of various additives. My PhD can be divided in five main parts of research activity.

In the first part of this thesis, magnesium silicate hydrate binder gel phase has been structurally characterized with a multi-technique approach, including a detailed solid-state NMR investigation, performed at the CNR and the University of Pisa in the framework of the project FIR2013-RBFR132WSM. The reaction of MgO and SiO_2 at room temperature leads to the formation of an amorphous phase constituted by an intimate mixture of subnanometre-sized domains with local structures resembling those of chrysotile and talc. A quantitative analysis enabled us to conclude that talc-like and chrysotile-like domains are in approximately 1:1 ratio and M-S-H has a high degree of condensation. In this study, for the first time, we gained insight into the structural features of M-S-H binding phase on a molecular and sub-nanometeric scale.

The second part of my PhD concerned the combination of traditional Portland cement with MgO-based cement. A set of samples made of different proportions of MgO/SiO_2 and Portland cements have been subjected to hydration and analyzed by means of complementary characterization techniques. We obtained valuable information on the effects of the composition on the amount and structure of the silicate binder phases formed during hydration, M-S-H and C-S-H, which resulted to be substantially phase-separated. These results represent an important step toward the control of the formation of hydrated phases and the regulation of pH of the final material in all those applications where Portland cement and MgO/SiO$_2$ cements coexist.

The next parts of my research activity consisted in the modification of the composition of the pastes by the introduction of different additives, whose exploitation in MgO/SiO$_2$ cement was not reported yet.
A fundamental part of my PhD concerned the evaluation of the effects of phosphate additives on the formation and structure of magnesium silicate hydrate. Nowadays, sodium hexametaphosphate is the only used additive with MgO/SiO$_2$ cement and it is reported to have fludificant effect on the cement pastes, but its mechanism of action is still unknown. We compared the effect of three phosphate-based additives to MgO/SiO$_2$ cement: sodium hexametaphosphate, sodium trimetaphosphate and sodium ortophosphate. We obtained information on the effect of these additives on the hydration reaction, on their influence on the precipitation of M-S-H binder gel phase and on their interaction with the solid phase of cement. Moreover, we investigated the mechanical properties of the samples using Vickers hardness test and statistical high-speed nanoindentation, performed in collaboration with the University of Roma TRE. Phosphate-based additives have been extensively investigated throughout this work and proposed as additives to be used in MgO/SiO$_2$ cement formulation. We found that sodium ortophosphate shows fluidificant effects even higher than sodium hexametaphosphate and it enhances M-S-H precipitation even more than the additive used nowadays. On the contrary, sodium trimetaphosphate resulted to be less efficient than the other salts. We suggest that the availability of ortophosphate is the cause of the effects that were previously associated to sodium hexametaphosphate in MgO/SiO$_2$ formulation. Therefore, we propose sodium ortophosphate as an additive to be used in magnesium silicate hydrate cement.

The next section of my PhD was dedicated to the investigation of the effects of aluminate phases on MgO/SiO$_2$ cements. In calcium-based cements tricalcium aluminate phase is responsible for the strength development at short hydration time and, since in some applications calcium- and magnesium-based cement coexist, we investigated the aluminate effect also on M-S-H. Together with C$_3$A we evaluated also the effect of imogolite, a nanotubular additive exposing aluminol sites, to combine the reinforcing purpose of 1-D fibres with the effect of the aluminate phase. We found that C$_3$A limits M-S-H formation and negatively affect MgO/SiO$_2$ hydration reaction, while IMOs do not influence the hydration reaction neither the binder precipitation. We also evaluated if

IMOs improve the hardness and elastic modulus of the pastes, but the results evidenced that the presence of imogolites only slightly increases the mechanical properties of MgO/SiO_2 cement.

Finally, the last part of this thesis was focused on the investigation of the effects of another tubular aluminosilicate nanoclay: halloysite. HNTs expose silanol groups and, therefore, are perfectly compatible with M-S-H cement. We also modified HNTs surfaces by functionalizing them with phosphate groups, to evaluate the possibility of combining the reinforcing characteristic of HNTs fibres with the effects associated to phosphates. We found that the presence of HNTs, both pristine and functionalised with phosphate groups, does not significantly affect M-S-H formation, neither its mechanical properties.

In conclusion, the work done during my PhD course evidenced that it is possible to tailor the macroscopic properties of eco-sustainable MgO/SiO_2 cements and the use of proper formulations allows the obtainment of properties that well fit practical applications. This thesis provides novel insights on the use of magnesium silicate hydrate cement and the effects of various additives on this material have been evaluated. The study described in this thesis has no claim to be exhaustive. Some work has been done for the prediction of the final properties of materials with different composition, but a lot of research still needs to be done, since all the potentiality of this cement has not been exploited yet. However, the understanding that we obtained paves the way for the improvement of magnesium silicate hydrate cements and for the development of their applications.

Bibliography

[1] Marcus Vitruvius Pollio, *De architectura*, Vol. Building materials (15 BC).

[2] F. Ridi, et al., Journal of Colloid and Interface Science **357**, 255 (2011).

[3] E. M. Gartner, et al., Cement and Concrete Research **41**, 736 (2011).

[4] M. Fry, Geoforum **49**, 127 (2013).

[5] R. J. Flatt, et al., Journal of the European Ceramic Society **32**, 2787 (2012).

[6] R. Courland, *Concrete Planet: The Strange and Fascinating Story of the World's Most Common Man-Made Material* (Prometheus Books, 2011).

[7] P. Hewlett, *Lea's Chemistry of Cement and Concrete* (Butterworth-Heinemann, 2003).

[8] `https://www.britannica.com/technology/cement-building-material`.

[9] H. F. W. Taylor, *Cement chemistry*, 2nd ed (T. Telford, London, 1997).

[10] J. J. Thomas, et al., The Journal of Physical Chemistry C **114**, 7594 (2010).

[11] H. M. Jennings, Cement and Concrete Research **30**, 101 (2000).

[12] H. M. Jennings, et al., Cement and Concrete Research **41**, 727 (2011).

[13] A. J. Allen, et al., Nature Materials **6**, 311 (2007).

[14] M. Schneider, et al., Cement and Concrete Research **41**, 642 (2011).

[15] `https://www.globalefficiencyintel.com`.

[16] F. Xi, et al., Nature Geoscience **9**, 880 (2016).

[17] C. Shi, et al., Cement and Concrete Research **41**, 750 (2011).

[18] M. Achternbosch, et al., in Proceedings of the 14th International Congress on the Chemistry of Cement, (2015).

[19] I. Garcia-Lodeiro, et al., Journal of Sustainable Cement-Based Materials **4**, 140 (2015).

[20] M. Juenger, et al., Cement and Concrete Research **41**, 1232 (2011).

[21] S. A. Walling, et al., Chemical Reviews **116**, 4170 (2016).

[22] M. Achternbosch, et al., *Are new magnesia-based cements the future Part 2 Novacem-an assessment of new developments*, 2012.

[23] N. Vlasopoulos, *Process for producing cement binder compositions containing magnesium*, 2012.

[24] L. S. M. Evans, Imperial College, *Novacem: Carbon Negative Cement and the Green Cement Bond*, Warsaw, 2010.

[25] D. Haoliang, et al., in 14th international congress on the chemistry of cement, beijing, Vol. 1 (2015), p. 1.

[26] Z. Li, et al., Construction and Building Materials **61**, 252 (2014).

[27] J. Szczerba, et al., Thermochimica Acta **567**, 57 (2013).

[28] J. Temuujin, et al., Journal of the American Ceramic Society **81**, 754 (1998).

[29] S. A. Walling, et al., Dalton Trans. **44**, 8126 (2015).

[30] D. Brew, et al., Cement and Concrete Research **35**, 77 (2005).

[31] J. Wei, et al., Journal of Wuhan University of Technology-Mater. Sci. Ed. **26**, 745 (2011).

[32] C. Roosz, et al., Cement and Concrete Research **73**, 228 (2015).

[33] F. Jin, et al., Cement and Concrete Composites **52**, 27 (2014).

[34] D. Nied, et al., Cement and Concrete Research **79**, 323 (2016).

[35] A. Jenni, et al., Physics and Chemistry of the Earth, Parts A/B/C **70-71**, 71 (2014).

[36] A. Dauzères, et al., Cement and Concrete Research **58**, 76 (2014).

[37] A. Dauzeres, et al., Cement and Concrete Research **79**, 137 (2016).

[38] F. P. Glasser, et al., MRS Bulletin **19**, 33 (1994).

[39] S. Norris, Geological Society, London, Special Publications **400**, 1 (2014).

[40] E. C. Gaucher, et al., Waste Management **26**, 776 (2006).

[41] G. Kosakowski, et al., Physics and Chemistry of the Earth, Parts A/B/C **64**, 65 (2013).

[42] L. J. Vandeperre, et al., Journal of materials in civil engineering **20**, 375 (2008).

[43] W.-S. Chiang, et al., J. Mater. Chem. A **2**, 12991 (2014).

[44] B. Lothenbach, et al., Cement and Concrete Research **77**, 60 (2015).

[45] H. M. Jennings, Cement and Concrete Research **38**, 275 (2008).

[46] G. W. Scherer, Cement and Concrete Research **29**, 1149 (1999).

[47] J. J. Thomas, et al., Cement and Concrete Research **36**, 30 (2006).

[48] `http://www.cementlab.com/C-S-H_Colloid_Model.htm`.

[49] W.-S. Chiang, et al., J. Phys. Chem. C **116**, 5055 (2012).

[50] Jennings, H. M., et al., Journal of the American Ceramic Society **77**, 3161 (1994).

[51] F. Ridi, et al., The Journal of Physical Chemistry B **113**, 3080 (2009).

[52] D. Brew, et al., Cement and Concrete Research **35**, 85 (2005).

[53] J. Plank, et al., Cement and Concrete Research **78**, 81 (2015).

[54] F. Ridi, et al., The Journal of Physical Chemistry B **107**, 1056 (2003).

[55] A. Papo, et al., Cement and Concrete Research **34**, 2097 (2004).

[56] W.-S. Chiang, et al., Journal of Colloid and Interface Science **398**, 67 (2013).

[57] F. Dalas, et al., Cement and Concrete Research **67**, 21 (2015).

[58] C. Giraudeau, et al., Journal of the American Ceramic Society **92**, 2471 (2009).

[59] A. Zingg, et al., Cement and Concrete Composites **31**, 153 (2009).

[60] F. Winnefeld, et al., Cement and Concrete Composites **29**, 251 (2007).

[61] `https://en.wikipedia.org/wiki/Sodium_hexametaphosphate`.

[62] T. Zhang, et al., Cement and Concrete Research **65**, 8 (2014).

[63] Y. Jia, et al., Cement and Concrete Research **89**, 63 (2016).

[64] Y.-p. Lu, et al., Transactions of Nonferrous Metals Society of China **21**, 208 (2011).

[65] H. Manzano, et al., Advanced Materials **24**, 3239 (2012).

[66] F. Collins, et al., Cement and Concrete Composites **34**, 201 (2012).

[67] A. Bentur, et al., *Steel Corrosion in Concrete: Fundamentals and civil engineering practice* (CRC Press, Oct. 1997).

[68] M. Moreno, et al., Corrosion Science **46**, 2681 (2004).

[69] N. Farzadnia, et al., Cement and Concrete Research **48**, 97 (2013).

[70] E. Joussein, et al., *Halloysite clay minerals - A review*, Vol. 40 (2005).

[71] P. Pasbakhsh, et al., *Natural mineral nanotubes: properties and applications* (CRC Press, Apple Academic Press, 2015).

[72] `http://halloysiteexpert.com/properties-applications/`.

[73] Y. Zhang, et al., Applied Clay Science **119**, 8 (2016).

[74] P. Yuan, et al., Applied Clay Science **112-113**, 75 (2015).

[75] M. Du, et al., Polymer International **59**, 574 (2010).

[76] P. Yuan, et al., The Journal of Physical Chemistry C **112**, 15742 (2008).

[77] K. Prashantha, et al., Journal of Applied Polymer Science **130**, 313 (2013).

[78] R. Kamble, et al., Journal of advanced scientific research **3** (2012).

[79] D. Rawtani, et al., Rev. Adv. Mater. Sci **30**, 282 (2012).

[80] `https://www.mindat.org/min-2021.html`.

[81] `http://webmineral.com/data/Imogolite.shtml.Wd4o_yN97yk`.

[82] Cradwick, P. D. et al., nature physical science **240**, 187 (1972).

[83] W. Ma, et al., J. Mater. Chem. **22**, 11887 (2012).

[84] R. I. González, et al., The Journal of Physical Chemistry C **118**, 28227 (2014).

[85] A. Bouguerra, et al., Cement and concrete research **28**, 1179 (1998).

[86] G. Constantinides, et al., Materials and structures **36**, 191 (2003).

[87] E. M. Van der Merwe, et al., Journal of thermal analysis and calorimetry **77**, 49 (2004).

[88] G. H. Koenderink, et al., Journal of Colloid and Interface Science **216**, 429 (1999).

[89] P. Mondal, “Nanomechanical Properties of Cementitious Materials”, PhD thesis (Northwestern University, 2008).

[90] T. Zhang, et al., Cement and Concrete Research **41**, 439 (2011).

[91] M. K. Guellil, et al., Journal of Materials Science and Engineering. A **3** (2013).

[92] A. Mebrouki, et al., Journal of Applied Sciences **9**, 4127 (2009).

[93] J. W. Bullard, et al., Cement and Concrete Research **41**, 1208 (2011).

[94] I. Pane, et al., Cement and Concrete Research **35**, 1155 (2005).

[95] A. Damasceni, et al., The Journal of Physical Chemistry B **106**, 11572 (2002).

[96] C. Jolicoeur, et al., Cement and Concrete Composites **20**, 87 (1998).

[97] J. J. Thomas, et al., The Journal of Physical Chemistry C **113**, 19836 (2009).

[98] S. A. FitzGerald, et al., Chemistry of materials **10**, 397 (1998).

[99] E. Fratini, et al., The Journal of Physical Chemistry B **106**, 158 (2002).

[100] J. J. Thomas, Journal of the American Ceramic Society **90**, 3282 (2007).

[101] J. J. Thomas, et al., Journal of the American Ceramic Society **97**, 275 (2014).

[102] K. Ishikiriyama, et al., Journal of Colloid and Interface Science **171**, 103 (1995).

[103] D. H. Bager, et al., Cement and Concrete Research **16**, 709 (1986).

[104] D. H. Bager, et al., Cement and Concrete Research **16**, 835 (1986).

[105] D. H. Bager, et al., Cement and Concrete Research **17**, 1 (1987).

[106] D. P. Bentz, Journal of the American Ceramic Society **89**, 2606 (2006).

[107] F. Ridi, et al., The Journal of Physical Chemistry C **117**, 25478 (2013).

[108] R Defay, et al., Journal of Colloid and Interface Science **58**, 498 (1977).

[109] M. Brun, et al., Thermochimica Acta **21**, 59 (1977).

[110] M. R. Landry, Thermochimica Acta **433**, 27 (2005).

[111] E. W. Hansen, et al., J. Phys. Chem. B **101**, 7027 (1997).

[112] E. Sanz, et al., J. Am. Chem. Soc. **135**, 15008 (2013).

[113] J. Rault, et al., Eur. Phys. J. B **36**, 627 (2003).

[114] C. Hu, et al., Construction and Building Materials **90**, 80 (2015).

[115] R. F. Feldman, et al., Cement and Concrete Research **6**, 389 (1976).

[116] W. Zhu, et al., Materials Characterization **58**, 1189 (2007).

[117] W. Zhu, et al., Cement and Concrete Research **27**, 1701 (1997).

[118] S. Igarashi, et al., Advanced Cement Based Materials **4**, 48 (1996).

[119] J. Gong, et al., Journal of the European Ceramic Society **19**, 2625 (1999).

[120] D. L. Joslin, et al., Journal of Materials Research **5**, 123 (1990).

[121] T. Hemalatha, et al., Materials and Structures **48**, 3719 (2015).

[122] `http://www.twi-global.com`.

[123] L. Sorelli, et al., Cement and Concrete Research **38**, 1447 (2008).

[124] W. C. Oliver, et al., Journal of Materials Research **7**, 1564 (1992).

[125] K. Velez, et al., Cement and Concrete Research **31**, 555 (2001).

[126] M. Sebastiani, et al., Materials & Design **97**, 372 (2016).

[127] C. H. Giles, et al., Journal of colloid and interface science **47**, 755 (1974).

[128] D. H. Everett, et al., eds., *Adsorption from Solution* (Academic Press, London ; New York, 1983).

[129] K. Foo, et al., Chemical Engineering Journal **156**, 2 (2010).

[130] L. Ferrari, et al., Journal of Colloid and Interface Science **347**, 15 (2010).

[131] E. Castellini, et al., Journal of Colloid and Interface Science **292**, 322 (2005).

[132] D. Bonen, et al., Cement and Concrete Research **28**, 1423 (1995).

[133] K.-C. Hsu, et al., Cement and concrete composites **21**, 425 (1999).

[134] B.-G. Kim, et al., Cement and Concrete research **30**, 887 (2000).

[135] K. Yamada, et al., Cement and Concrete Research **31**, 375 (2001).

[136] C. H. Giles, et al., Journal of Colloid and Interface Science **47**, 766 (1973).

[137] G. Limousin, et al., Applied Geochemistry **22**, 249 (2007).

[138] C. Hinz, Geoderma **99**, 225 (2001).

[139] I. Langmuir, Journal of the American Chemical Society, 1848 (1917).

[140] T. Zhang, et al., Journal of Sustainable Cement-Based Materials **1**, 34 (2012).

[141] K.-Y. Hwang, et al., CLEAN - Soil, Air, Water **42**, 355 (2014).

[142] M. Geppi, et al., Applied Spectroscopy Reviews **44**, 1 (2008).

[143] F. Jin, et al., Thermochimica Acta **566**, 162 (2013).

[144] T. Zhang, et al., Cement and Concrete Research **65**, 8 (2014).

[145] J. S. Hartman, et al., Physics and chemistry of minerals **17**, 1 (1990).

[146] K. J. D. MacKenzie, et al., Thermochimica Acta **244**, 195 (1994).

[147] K.J.D. MacKenzie, et al., American Mineralogis **79**, 43 (1994).

[148] F. Jin, et al., Cement and Concrete Composites **52**, 27 (2014).

[149] J. Temuujin, et al., Journal of Solid State Chemistry **138**, 169 (1998).

[150] G. L. Kalousek, et al., Journal of the American Ceramic Society **37**, 38 (1954).

[151] J. C.-S. Yang, Journal of the American Ceramic Society **43**, 542 (1960).

[152] P. Le, et al., Journal of Colloid and Interface Science **469**, 157 (2016).

[153] L. Fernandez, et al., Journal of Materials Science **43**, 5772 (2008).

[154] Z. Pytel, et al., ResearchGate **65**, 81 (2000).

[155] O. P. Shrivastava, et al., Cement and Concrete Research **21**, 83 (1991).

[156] B. Lothenbach, et al., Cement and Concrete Research **77**, 60 (2015).

[157] J.-P. Korb, Current Opinion in Colloid & Interface Science **14**, 192 (2009).

[158] P. F. Faure, et al., Magnetic Resonance Imaging **26**, 1183 (2008).

[159] V. Bortolotti, et al., Cement and Concrete Research **42**, 577 (2012).

[160] A. Valori, et al., Cement and Concrete Research **49**, 65 (2013).

[161] P. McDonald, et al., Cement and Concrete Research **40**, 1656 (2010).

[162] A. Muller, et al., Microporous and Mesoporous Materials **178**, 99 (2013).

[163] A. Pop, et al., Applied Magnetic Resonance **44**, 1223 (2013).

[164] A. C. A. Muller, et al., J. Phys. Chem. C **117**, 403 (2013).

[165] M. Gombia, et al., J. Phys. Chem. B **114**, 1767 (2010).

[166] I. G. Richardson, Cement and Concrete Research **34**, 1733 (2004).

[167] A. R. Brough, et al., Journal of materials science **30**, 1671 (1995).

[168] J. Haas, et al., Cement and Concrete Research **68**, 124 (2015).

[169] T. Zhang, et al., in Nuwcem, avignon (2011), pp. 582–591.

[170] Z. Li, et al., Construction and Building Materials **61**, 252 (2014).

[171] Z. D. Rong, et al., Construction and Building Materials **Complete**, 446 (2014).

[172] D. S. Klimesch, et al., Thermochimica Acta **334**, 115 (1999).

[173] G. Sun, et al., Journal of the American Ceramic Society **82**, 3225 (1999).

[174] E.-H. Kadri, et al., Construction and Building Materials **11**, 3388 (2009).

[175] S. Meiboom, et al., Review of Scientific Instruments **29**, 688 (1958).

[176] M. Bligh, et al., Cement and Concrete Research **83**, 131 (2016).

[177] J. Greener, et al., Journal of the American Ceramic Society **83**, 623 (2000).

[178] A. C. A. Muller, et al., Cement and Concrete Research **74**, 116 (2015).

[179] K. R. Brownstein, et al., Phys. Rev. A **19**, 2446 (1979).

[180] W. P. Halperin, et al., Magnetic Resonance Imaging, Proceedings of the Second International Meeting on Recent Advances in MR Applications to Porous Media **12**, 169 (1994).

[181] F. Ridi, et al., The Journal of Physical Chemistry C **117**, 25478 (2013).

[182] T. Zhang, et al., in Nuwcem, avignon (2011), pp. 582–591.

[183] W. Jiangxiong, et al., Journal of Wuhan University of Technology-Mater. Sci. Ed. **21**, 88 (2006).

[184] D. L. Kantro, Cement, Concrete and Aggregates **2**, 95 (1980).

[185] N. Roussel, et al., Cement and Concrete Research, 817 (2005).

[186] E. Thilo, Angewandte Chemie **4**, 1061 (1965).

[187] G. Kura, Journal of Chromatography A **447**, 91 (1988).

[188] R. A. Morgen, et al., Industrial & Engineering Chemistry **35**, 821 (1943).

[189] S. Lack, et al., Carbohydrate Research **342**, 943 (2007).

[190] S. P. Damle, et al., Archives of biochemistry and biophysics **49**, 58 (1954).

[191] A. B. Gerber, et al., Analytical Edition **10**, 519 (1938).

[192] R. N. Bell, Analytical Chemistry, 97 (1947).

[193] C. H. Giles, et al., Journal of Colloid and Interface Science **47**, 755 (1974).

[194] C. H. Giles, et al., Journal of Colloid and Interface Science **47**, 766 (1974).

[195] Y. H. Zhao, et al., The Journal of Organic Chemistry **68**, 7368 (2003).

[196] P. Yuan, et al., The Journal of Physical Chemistry C **112**, 15742 (2008).

[197] Y. Joo, et al., The Journal of Physical Chemistry C **116**, 18230 (2012).

[198] P. Yuan, et al., Applied Clay Science **112-113**, 75 (2015).

[199] K. Fujiwara, et al., Analytical Sciences **25**, 241 (2009).

Appendix

List of Publications

- **Paper I**: Tonelli, M.; Martini, F.; Calucci, L.; Fratini, E.; Geppi, M.; Ridi, F.; Borsacchi, S.; Baglioni, P. *Structural investigation of magnesium silicate hydrate.* **Dalton Transaction**, 2016, **45**, 3294-3304. DOI: 10.1039/c5dt03545g.
- **Paper II**: Martini, F.; Tonelli, M.; Calucci, L.; Geppi, M.; Ridi, F.; Borsacchi, S. *Hydration of* MgO/SiO_2 *and Portland cement mixtures: a structural investigation of the hydrated phases by means of X-ray diffraction and Solid State NMR spectroscopy.* **Cement** & **Concrete Research**, 2017, **102**, 60-67. DOI: 10.1016/j.cemconres.2017.08.029.
- **Paper III**: Tonelli, M.; Martini, F.; Calucci, L.; Geppi, M.; Borsacchi, S.; Ridi, F. *Traditional Portland cement and innovative MgO-based cement : a promising combination?.* **Physics and Chemistry of the Earth**, 2017, **99**, 158-167. DOI: 10.1016/j.pce.2017.01.011.
- **Paper IV**: Martini, F.; Calucci, L.; Geppi, M.; Tonelli, M.; Ridi, F.; Borsacchi, S. *Monitoring the hydration of MgO-based cement and its mixtures with Portland cement by* ^1H *NMR relaxometry.* **Microporous and Mesoporous Materials**, 2017. DOI: 10.1016/j.micromeso.2017.05.031.
- **Paper V**: Ridi, F.; Tonelli, M.; Fratini, E.; Chen, S.H; Baglioni, P. *Water as a probe of the colloidal properties of cement.* **Langmuir**, 2017. DOI: 10.1021/acs.langmuir.7b02304.

In the following pages a reprint of all the manuscripts published during the period of my PhD, related to the work here presented, is reported. All the papers are reprinted with permission from the publisher.

Paper I

Dalton Transactions

PAPER

View Article Online
View Journal | View Issue

Cite this: *Dalton Trans.*, 2016, **45**, 3294

Structural characterization of magnesium silicate hydrate: towards the design of eco-sustainable cements†

M. Tonelli,‡[a] F. Martini,‡[b] L. Calucci,[b] E. Fratini,[a] M. Geppi,[c] F. Ridi,*[a] S. Borsacchi*[b] and P. Baglioni[a]

Received 10th September 2015,
Accepted 4th January 2016

DOI: 10.1039/c5dt03545g

www.rsc.org/dalton

Magnesium-based cement is one of the most interesting eco-sustainable alternatives to standard cementitious binders. The reasons for the interest towards this material are twofold: (i) its production process, using magnesium silicates, brine or seawater, dramatically reduces CO_2 emissions with respect to Portland cement production, and (ii) it is very well suited to applications in radioactive waste encapsulation. In spite of its potential, assessment of the structural properties of its binder phase (magnesium silicate hydrate or M–S–H) is far from complete, especially because of its amorphous character. In this work, a comprehensive structural characterization of M–S–H was obtained using a multi-technique approach, including a detailed solid-state NMR investigation and, in particular, for the first time, quantitative ^{29}Si solid-state NMR data. M–S–H was prepared through room-temperature hydration of highly reactive MgO and silica fume and was monitored for 28 days. The results clearly evidenced the presence in M–S–H of "chrysotile-like" and "talc-like" sub-nanometric domains, which are approximately in a 1 : 1 molar ratio after long-time hydration. Both these kinds of domains have a high degree of condensation, corresponding to the presence of a small amount of silanols in the tetrahedral sheets. The decisive improvement obtained in the knowledge of M–S–H structure paves the way for tailoring the macroscopic properties of eco-sustainable cements by means of a bottom-up approach.

1. Introduction

In the last decade, research efforts on the investigation of magnesium-based cements have significantly grown for two main reasons, both concerning sustainable chemistry: they can be employed for radioactive waste encapsulation,[1–3] and, most important, they have been recognized as a promising alternative to the common CaO-based (Portland) cements in applications requiring pH lower than 11.[4–6] The great amount of emitted CO_2 associated with the manufacture of Portland cement, in fact, requires urgent measures to move towards eco-sustainable strategies in the field of building materials production.[7–11]

Magnesium-based cements are generally obtained by hydration of reactive periclase (MgO) in the presence of silica sources to produce magnesium silicate hydrate (M–S–H) gel.[12–17] Because of the low abundance of natural MgO, some sustainable processes to obtain reactive MgO from abundant starting sources have been recently proposed. One viable solution is to obtain reactive periclase from magnesium silicates (among the main constituents of the Earth's crust) according to the method developed by a start-up company of the Imperial College of London.[18] Another possibility, which is gaining renewed interest in the scientific community, is the production of reactive MgO from the treatment of brine or seawater.[19] Obtaining MgO from these alternative sources largely reduces CO_2 emissions with respect to those associated with the production of Portland cement.

The use of magnesium-based cements in real applications is currently restricted, mainly because of the limited comprehension of both the structure of the M–S–H gel and the hydration process that causes its precipitation. Furthermore, the mechanical properties of MgO-based cements are inferior to those of traditional cements,[5] limiting their use to specific applications. The literature on Portland cement and, in particular, on the structural properties of C–S–H clearly demonstrates that a deep understanding of the microstructure is

---

[a] Department of Chemistry "Ugo Schiff" & CSGI, University of Florence, Sesto Fiorentino 50019, Florence, Italy. E-mail: francesca.ridi@unifi.it; Tel: +39-055-4573015

[b] Istituto di Chimica dei Composti OrganoMetallici, Consiglio Nazionale delle Ricerche – CNR U.O.S. di Pisa, Pisa 56124, Italy. E-mail: silvia.borsacchi@pi.iccom.cnr.it; Tel: +39-050-3153052

[c] Department of Chemistry and Industrial Chemistry, University of Pisa, Pisa 56124, Italy

† Electronic supplementary information (ESI) available: pH measurements, mass losses from TG measurements, ^{1}H–^{29}Si CP-MAS spectra, FTIR spectra deconvolution. See DOI: 10.1039/c5dt03545g

‡ These authors contributed equally.

essential in order to predict the macroscale mechanical properties.[20] For this reason, planning a serious scale-up of the production of any new building material requires an in-depth, multi-scale investigation of its structural properties. So far, the reported studies on MgO-based cements have evidenced that the properties of M–S–H depend on temperature,[17] the relative amounts of reagents,[21] and the reactivity of precursors.[12,22,23] Recent papers have reported on the characterization of the reaction products[3,14]§ and on the investigation of the M–S–H microstructure by using small-angle scattering techniques,[24] but a full characterization of this binder is still lacking.

In this study, the hydration product at ambient conditions of a mixture of highly reactive MgO and silica fume has been characterized during the first 28 days. No plasticizing polymers have been added in the investigation of the pristine M–S–H gel structure, and reactants were chosen to favour the formation of the hydrated phase. We adopted a multi-technique approach (solid-state NMR, infrared spectroscopy, X-ray powder diffraction, scanning electron microscopy, differential thermal analysis, thermogravimetry) aiming at the complete characterization of the material. Solid-state NMR (SSNMR) is an extremely powerful technique for the investigation of the structural properties of complex solid materials, either crystalline or amorphous.[25] In particular, ^{29}Si SSNMR has been extensively applied to the study of traditional CaO-based cements, largely contributing to the definition of the structural model of the amorphous C–S–H binding phase.[26] On the contrary, the application of SSNMR to M–S–H has been relatively limited so far; in particular, only ^{29}Si and, in some cases, ^{25}Mg monodimensional spectra, giving qualitative information on M–S–H gels obtained by means of different strategies, have been reported.[3,21,27–31] In this work, we applied for the first time quantitative ^{29}Si measurements, combined with ^{1}H and two-dimensional ^{1}H–^{29}Si experiments, to the hydration products of the MgO/SiO$_2$ mixture, with the aim of gaining insights into the structural features of the M–S–H binding phase on a molecular and sub-nanometric scale.

2. Experimental section

2.1. Materials

Periclase (MgO) and silica fume were supplied by Sigma-Aldrich. The main characteristics of these powders are summarized in Table 1. The reactivity of periclase was measured according to the test proposed by van der Merwe *et al.*[32] and resulted to be 80 s, which indicates that the powder is highly reactive.

MgO and SiO$_2$ were mixed in a 1 : 1 molar ratio. In a typical reaction, the MgO/SiO$_2$ (MS) paste was prepared by manually mixing 4 g of solids with 8 g of milliQ water, *i.e.* at a water-to-solid weight ratio (w/s) of 2. The paste was stored at 20 °C in a polyethylene bag to avoid air contact and prevent carbonation.

Table 1 Characteristics of the reagents

Reagent	Particle average size (by gas sorption analysis)	Purity	Specific surface [m^2 g^{-1}]
MgO	44 μm	>99%	121 ± 5
SiO$_2$	5 μm[a]	>99%	395 ± 25

[a] This size results from the agglomeration of 7 nm particles (as declared by Sigma).

At 1, 7 and 28 days after preparation, roughly 1 g of paste was withdrawn and freeze-dried to stop the hydration reaction. An abbreviated notation is used throughout this paper to refer to MS paste freeze-dried at different days of hydration: MS_1d (1 day), MS_7d (7 days) and MS_28d (28 days).

2.2. Methods

pH measurements were performed with a BASIC 20 Crison pH meter using the method previously described by Zhang *et al.*[5] Briefly, 1 g of the paste was added to a polyethylene container with 10 g of distilled water. The tube was then sealed and constantly stirred in an orbital shaker. At different time intervals, the solid particles were allowed to settle, and the pH of the supernatant was measured.

Fourier transform infrared (FTIR) spectra were acquired between 4000 and 400 cm^{-1} by means of a BioRad FTS-40 spectrometer (Biorad, Cambridge, MA, USA) with a DTGS TEC detector (32 scans, resolution of 2 cm^{-1}). 1 mg of each sample was homogenized with 100 mg of KBr and pressed to obtain a pellet.

Thermogravimetry (TG) was conducted on a STD Q600 (TA Instruments, Philadelphia, USA) instrument, operating from room temperature to 1000 °C at 10 °C min^{-1}, in nitrogen flux.

X-ray (XRD) diffractograms were recorded with an XRD Bruker New D8 Da Vinci instrument operating at 40 kV and 40 mA, with a Cu source (emitting radiation at a wavelength of 1.54 Å). The scanning region was in the 2θ range 5°–70°, with 0.05° per step. XRD spectra were recorded on MS_1d, MS_7d, MS_28d samples before and after heating at 900 °C.

Scanning electron microscopy (SEM) images were collected on uncoated fracture surfaces with a field-emission ΣIGMA (Carl Zeiss) microscope, with an accelerating potential of 2 kV. Surface area measurements were performed by means of a Coulter SA 3100 analyser.

Solid-state NMR (SSNMR) experiments were carried out on a Varian InfinityPlus 400 spectrometer working at ^{1}H and ^{29}Si Larmor frequencies of 400.35 and 79.48 MHz, respectively, equipped with 3.2 and 7.5 mm probeheads. 1D ^{29}Si experiments were carried out using the 7.5 mm probehead, spinning the samples at a MAS frequency of 5.5 kHz and under ^{1}H high-power decoupling. The ^{29}Si direct excitation–magic angle spinning (DE-MAS) spectra were recorded using a 90° excitation pulse with a duration of 6 μs and a recycle delay of 20 s, accumulating 4000 transients. ^{1}H–^{29}Si cross-polarization (CP)-MAS spectra at variable contact time were recorded using a linear ramp for CP and a ^{1}H TPPM high-power decoupling, with a recycle delay of 2 s. ^{29}Si T$_1$'s were determined using a

---

§ During the review process of the present article, the following paper concerning M-S-H characterization has been published: D. Nied, K. Enemark-Rasmussen, E. L'Hopital, J. Skibsted and B. Lothenbach, *Cem. Concr. Res.*, 2016, **79**, 323.

saturation-recovery pulse sequence with a train of 100 90° saturating pulses and recovery delays between 0.01 and 600 s, accumulating, for each delay value, 180 transients. ^{1}H MAS and ^{1}H–^{29}Si FSLG-HETCOR experiments were carried out on the 3.2 mm probehead at a MAS frequency of 20 kHz. ^{1}H MAS spectra were recorded accumulating 32 transients with a recycle delay of 2 s, while the ^{1}H–^{29}Si FSLG-HETCOR spectrum was recorded with a contact time of 0.6 ms (which was chosen for having enough magnetization transfer from protons to silicon nuclei, at the same time minimizing the effects of proton spin-diffusion), accumulating 1968 transients per 64 rows. All the experiments were performed at room temperature, using air as spinning gas. Tetramethyl silane was used as a primary chemical shift reference for all nuclei, while 3-(trimethylsilyl)-1-propane-sulfonic acid sodium salt and isopropanol were employed as secondary references for ^{29}Si and ^{1}H, respectively.

3. Results

3.1. pH measurements

pH measurements (Fig. S1, ESI†) were performed on hydrated MS, proving the advancement of the reaction over a period of 28 days. In the first hours, the pH value is affected by the presence of brucite ($Mg(OH)_2$), which is reported to have $pK_a \approx 10.5$. After 3 days, the pH of the sample decreases to ~9 because of the consumption of brucite in the reaction with hydrated silica and, then, it remains stabilized at this value up to 28 days. The observed pH trend is well in agreement with the description recently provided by Li *et al.*,[14] indicating that, from 3 to at least 28 days of hydration, the sample maintains the optimal pH value to promote the precipitation of M–S–H gel.[12,14]

3.2. TG/DTA analysis

Fig. 1A illustrates the weight losses from room temperature up to 1000 °C registered by means of thermogravimetric analysis on MS paste samples freeze-dried after 1, 7 and 28 days of hydration (MS_1d, MS_7d and MS_28d). Three principal mass losses can be observed (Table S1 of ESI†): one from room temperature to about 200 °C, the second approximately in the 310–400 °C range, and the last ending at around 800 °C. The first can be attributed to the loss of physisorbed water still present after the freeze-drying process. The second loss is ascribed to the dehydroxylation of residual brucite formed by hydration of MgO and not reacted with silica.[13] The mass loss at higher temperature arises from the decomposition of M–S–H due to the loss of its hydroxyl groups.[13]

Fig. 1B shows the DTA data for the MS_1d, MS_7d and MS_28d samples. The endothermic events around 100 °C and 400 °C correspond to the mass loss from M–S–H and $Mg(OH)_2$, respectively. An exothermic event, which is not associated to a mass loss, is registered for all the investigated samples between 800 and 900 °C. According to the literature, this effect is due to a solid phase transition of M–S–H to crystalline species.[3,13] This thermal feature progressively sharpens during the hydration, also shifting at lower temperatures. Similar crystallization events have been reported for the thermal treatment of amorphous talc, which is converted to enstatite ($MgSiO_3$),[33] and for the thermal treatment of chrysotile, which produces a mixture of enstatite and forsterite (Mg_2SiO_4).[34] In the thermograms of MS_1d and MS_7d, two exothermic peaks are observed at ~850 °C, indicating the formation of two crystalline species. To further understand the transformations associated with these exothermic effects, structural XRD analyses and ^{29}Si SSNMR experiments were performed on samples heated to 900 °C, which are reported in sections 3.3 and 3.4, respectively.

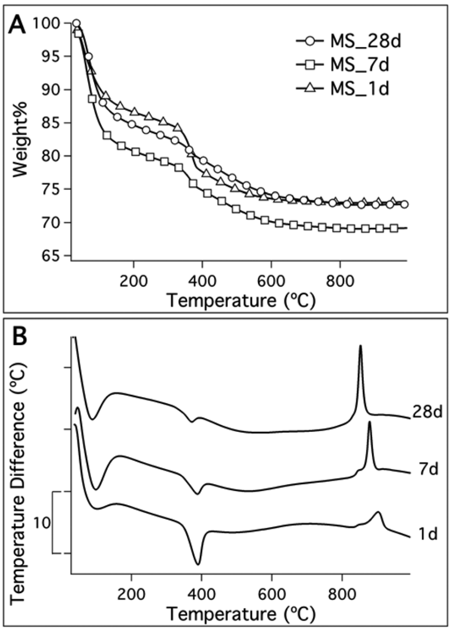

Fig. 1 (A) TG scans of MS_1d, MS_7d and MS_28d. B) DTA profiles of MS_1d, MS_7d and MS_28d. The DTA curves have been offset for the sake of clarity.

For a detailed investigation of the decomposition of the different phases present in the samples, we calculated the first derivative of the thermogravimetric curves, and we performed a deconvolution of the obtained DTG curves with Gaussian functions.[35–37] Fig. 2 illustrates the results of the analysis, and Table 2 reports the parameters (temperature of the maximum, T_{max}, and area) of each Gaussian peak.

Two peaks (#1 and #2) are present from room temperature to 200 °C. The area of #1 increases in the first week of hydration and then slightly decreases. Peak #2 appears at lower temperature for the MS_1d sample compared to MS_7d and MS_28d samples, and it has a markedly larger area: this is probably due to a significant contribution from water adsorbed on reagents (especially SiO_2) not yet reacted after 1 day. According to the literature,[3] #1 can be assigned to water

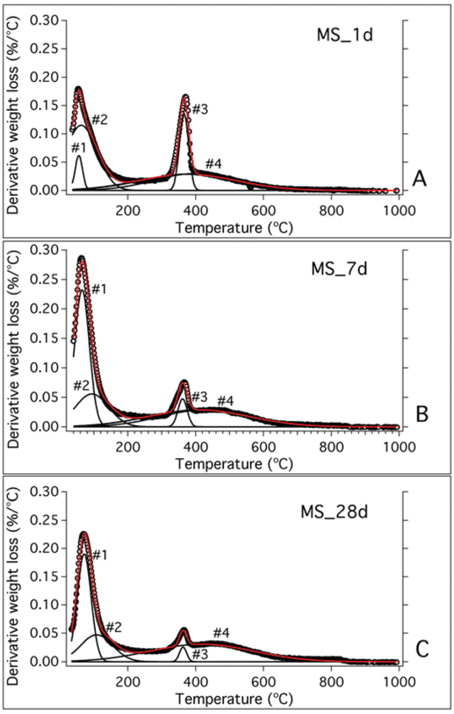

Fig. 2 Deconvolution of the DTG curves of (A) MS_1d, (B) MS_7d and (C) MS_28d samples. Black markers represent the experimental data; red lines are the global fitting curves; the Gaussian peaks obtained by the fitting procedure are shown as black lines.

Table 2 Position and percentage area of the Gaussian peaks resulting from the deconvolution of DTG curves. Uncertainties are reported in parentheses

		MS_1d	MS_7d	MS_28d
Peak 1	T_{max}/°C (±5)	55	65	71
	Area/% (±8%)	6	40	35
Peak 2	T_{max}/°C (±5)	62	94	109
	Area/% (±10%)	45	21	21
Peak 3	T_{max}/°C (±3)	365	361	363
	Area/% (±1%)	15	3	3
Peak 4	T_{max}/°C (±5)	376	409	418
	Area/% (±15%)	34	34	41

adsorbed on M–S–H surface, which increases until the binder phase formation is almost completed, while #2, once the reagents have reacted completely, is due to water confined in the pores of M–S–H.[13] T_{max} of these peaks shifts to higher temperature with hydration time, probably because M–S–H pores decrease in size with the advancement of the reaction, strengthening the water/M–S–H interactions and, therefore, increasing the evaporation temperature. A shift to higher temperature is also observed for the large peak in the 200–800 °C range (#4), which is assigned to the dehydroxylation of M–S–H.[13] The sharp peak at about 360 °C (#3) is due to $Mg(OH)_2$ dehydroxylation: its area decreases as a function of the hydration time as brucite is converted to M–S–H.

3.3. XRD analysis

Fig. 3 (top) shows the XRD diffractograms of MS_1d, MS_7d and MS_28d. In all cases, brucite appears as the main crystalline phase. In the MS_1d diffractogram, only a small peak due to periclase is present, indicating that after 24 hours almost all the MgO is hydrated. This peak completely disappears after 7 days. According to previous studies,[12,21] the broad peaks typical of an amorphous phase, observed in the 5–10°, 17–28°, 32–39° and 58–62° ranges, are consistent with the XRD pattern of the M–S–H phase. By following the evolution of the XRD diffractograms during hydration, it is observed that the intensity of the brucite peaks decreases as time passes, while that of the M–S–H signals increases.

In order to better characterize the phases formed at high temperature, as indicated by DTA, XRD diffractograms were also recorded on MS_1d, MS_7d and MS_28d samples after heating to 900 °C. A similar analysis was recently reported by Walling *et al.*[3] XRD patterns of heated samples (bottom part of Fig. 3) revealed the presence of periclase [AMCSD: 0000501], forsterite [AMCSD: 0000276], and clinoenstatite [AMCSD: 0010589] crystalline phases. Periclase derives from the dehydroxylation of brucite upon heating, while forsterite and clinoenstatite are anhydrous magnesium silicates arising from M–S–H. Clinoenstatite is a polymorph of enstatite, already

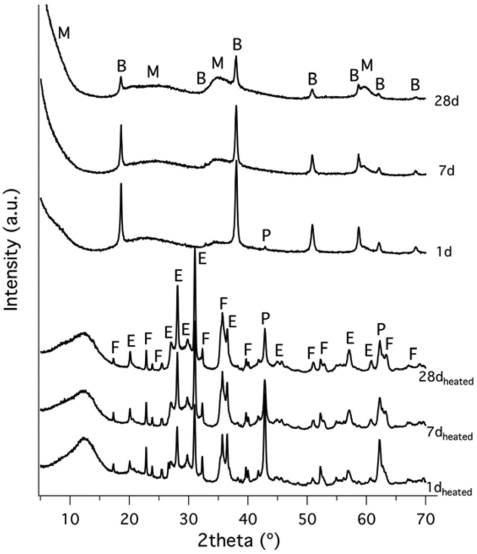

Fig. 3 XRD patterns of MS_1d, MS_7d and MS_28d samples before and after heating to 900 °C. Curves have been offset for the sake of clarity. M: M–S–H; B: brucite; P: periclase; E: enstatite; F: forsterite.

observed as a crystallization product of heated M–S–H gels, here recognized from the characteristic ^{29}Si SSNMR signals (*vide infra*).

3.4 Solid-state NMR investigation

3.4.1. ^{29}Si spectra. ^{29}Si DE-MAS spectra of MS pastes freeze-dried after 1, 7 and 28 days of hydration are reported in Fig. 4. All the spectra show quite broad and partially overlapped signals, as expected considering the amorphous character of both silica and M–S–H.

Typical signals of M–S–H[3,21,27–31] and silica can be recognized in the spectral regions approximately between −100 and −75 ppm, and between −125 and −95 ppm, respectively. In order to identify the different signals, the spectra were fitted using the minimum number of peaks necessary for an accurate reproduction. The analysis of the spectrum of MS_28d allowed five M–S–H signals to be identified. In particular, two peaks were found at −79.6 and −82.1 ppm, which can be ascribed to different Q^1 $\underline{\mathrm{Si}}(\mathrm{OMg})(\mathrm{OSi})(\mathrm{OH})_2$ species, indicated as Q^{1A} and Q^{1B}, respectively. One signal was identified at −86.3 ppm due to Q^2 $\underline{\mathrm{Si}}(\mathrm{OMg})(\mathrm{OSi})_2\mathrm{OH}$ sites. Two peaks, centred at −92.9 and −95.2 ppm and ascribed to two different Q^3 $\underline{\mathrm{Si}}(\mathrm{OMg})(\mathrm{OSi})_3$ silicon sites (Q^{3A} and Q^{3B}), were necessary for obtaining an accurate reproduction of the intense signal at the lowest chemical shift. The presence of two peaks underlying the Q^3 signal is also evident from the asymmetry of its lineshape in the ^{1}H–^{29}Si CP-MAS spectra recorded at different contact times (Fig. S2 of the ESI†), one of which is shown in Fig. 4. Moreover, the trends of the peak areas *vs.* contact time obtained for the Q^1, Q^2 and Q^3 peaks provided interesting information. In the fast CP regime ($T_{\mathrm{SiH}} < T_{1\rho}{}^{\mathrm{H}}$), which has been found to be valid for all the silicon nuclei of M–S–H (see ESI†), the increasing trend of the signal intensity at short contact times is governed by the so-called cross-polarization time constant, T_{SiH}. Considering that T_{SiH} usually increases with decreasing number of ^{1}H nuclei spatially close to ^{29}Si nuclei, the trend T_{SiH} (Q^{1A}) ≈ T_{SiH} (Q^{1B}) ≈ T_{SiH} (Q^2) < T_{SiH} (Q^{3A}) < T_{SiH} (Q^{3B}) obtained for the MS_28d sample corroborates the signal assignment and suggests that Q^{3A} silicons have a larger number of close protons (most probably Mg–OH) than Q^{3B} silicons.

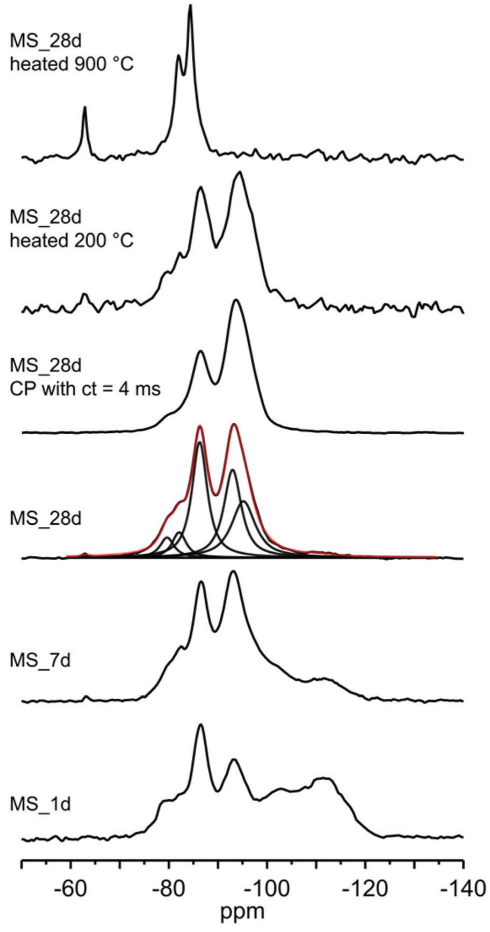

Fig. 4 ^{29}Si DE-MAS spectra of MS_1d, MS_7d and MS_28d samples and of MS_28d heated to 200 °C and to 900 °C. For MS_28d, the fitted DE-MAS spectrum, with the single peaks (in black), is reported (in red) over the experimental spectrum. The ^{1}H–^{29}Si CP-MAS spectrum of MS_28d, recorded with a contact time of 4 ms, is also shown.

The ^{29}Si DE-MAS spectra of MS_7d and MS_1d samples were well reproduced using the same peaks that fitted the spectrum of MS_28d (keeping fixed the chemical shifts, linewidths and Lorentzian/Gaussian ratios to the values reported in Table 3, and varying the intensities), with the addition of two peaks for the Q^4 ($\underline{\mathrm{Si}}(\mathrm{OSi})_4$) and Q^3 ($\underline{\mathrm{Si}}(\mathrm{OSi})_3\mathrm{OH}$) sites of silica at −111.5 and −102.0 ppm, respectively (Table 3). It must be said that in the case of MS_1d, due to the presence of an intense Q^3 silica signal, a comparably good spectral reproduction was also obtained, with a sole M–S–H Q^3 peak centred at −93.5 ppm. Moreover, an additional peak was found at −78.5 ppm for MS_1d and MS_7d, but, also considering the corresponding T_1 value (as discussed in detail in section 3.4.4), we believe that it arises from some anhydrous magnesium silicate species, for example $\mathrm{MgSiO_3}$.[27] In the spectra of MS_7d and MS_28d, a very weak but reproducible signal can be observed at −63 ppm, which could be tentatively assigned to another anhydrous form of magnesium silicate: for example, a chemical shift of −62 ppm has been reported for forsterite.[27,34]

In order to obtain quantitative information from the ^{29}Si spectra, the areas obtained from the fittings were suitably scaled on the basis of the corresponding ^{29}Si T_1 values, as described in section 3.4.4. The quantitative areas so obtained, which are directly proportional to the amount of the corresponding silicon nuclei, are reported in Table 3. The results clearly show that about 40% of silica is consumed in the first 24 hours; after 7 days, its amount is further halved; and after 28 days, an almost negligible amount remains. The faster decrease of the Q^4 signal with respect to Q^3 is in agreement

Table 3 Results obtained from the analysis of ^{29}Si SSNMR data. In the first two lines, the chemical shift (δ) and linewidth (Δ) of the peaks obtained by fitting the ^{29}Si DE-MAS spectra of MS_1d, MS_7d, and MS_28d are reported. Lorentzian to Gaussian ratios (L/G) of 0.9 and 0.2 were used for M–S–H and silica peaks, respectively. In the second block of lines, quantitative values of the areas underlying the peaks are reported as *A*%. As described in the text, *A*% values were obtained by multiplying the areas obtained from the fitting of the ^{29}Si DE-MAS spectra by the respective scaling factors, also reported in the table. The scaling factors were determined from ^{29}Si T_1 values measured for MS_28d. Values of T_1 and of the exponent β of the stretched exponential function used for fitting ^{29}Si magnetization recovery curves are also reported

	Q^{1A}	Q^{1B}	Q^2	Q^{3A}	Q^{3B}	Q^3 SiO_2	Q^4 SiO_2
δ/ppm	−79.6	−82.1	−86.3	−92.9	−95.2	−102.0	−111.5
Δ/Hz	276	273	297	337	458	570	815
A% MS_1d	2 ± 1	2 ± 1	15 ± 1	10 ± 2	8 ± 1	20 ± 5	44 ± 12
A% MS_7d	2 ± 1	4 ± 1	19 ± 1	22 ± 5	22 ± 2	15 ± 4	17 ± 5
A% MS_28d	4 ± 1	5 ± 1	29 ± 2	29 ± 6	33 ± 2	—	1 ± 1
T_1/s	40 ± 11	59 ± 16	65 ± 7	128 ± 62	99 ± 8	134 ± 38	134 ± 38
β	0.69 ± 0.11	0.62 ± 0.07	0.60 ± 0.03	0.47 ± 0.05	0.75 ± 0.03	1	1
Scaling factor	2.2 ± 0.3	2.5 ± 0.4	2.6 ± 0.1	2.9 ± 0.6	3.8 ± 0.2	7 ± 2	7 ± 2

with the fact that the reaction of silica with MgO is preceded by hydration, which transforms Q^4 into Q^3 sites. In parallel with silica consumption, M–S–H signals increase. Interestingly, within the experimental errors, the ratio $Q^2 : Q^{3A} : Q^{3B}$ remains approximately 1 : 1 : 1 after 7 days of hydration.

^{29}Si DE-MAS spectra were also recorded for two samples of MS_28d heated to 200 and 900 °C (Fig. 4). While the former substantially shows the same signals observed for unheated MS_28d confirming that at this temperature only adsorbed water is removed, the latter has a completely different spectrum, characterized by the coexistence of a signal at −62 ppm, ascribable to forsterite, and two signals at −81 and −84 ppm, previously observed for clinoenstatite,[27,34] in agreement with XRD and DTA results.

3.4.2. ^{1}H spectra. Fig. 5 shows the ^{1}H-MAS spectra of MS_1d, MS_7d and MS_28d. It is worth recalling that in complex solid materials, it is very difficult to completely remove ^{1}H–^{1}H homonuclear dipolar couplings, which are responsible for the scarce spectral resolution observed and for the non-quantitative signal intensities. Nonetheless, in the spectra of MS samples, three main signals can be resolved centred at about 0.8, 4.7, and 6.5 ppm. The first signal seems to be structured in three components: the one at 0.4 ppm can be ascribed to MgOH protons of M–S–H with a likely contribution from protons of brucite at similar or lower chemical shift,[38] while the peaks appearing at about 0.8 and 1.3 ppm, observable also in the spectrum of silica (Fig. 5), can be due to silanols not involved in hydrogen bonds. The relatively narrow and intense peak resonating at 4.7 ppm can be assigned to physisorbed water present in the sample even after freeze-drying. At last, the broad peak centred at about 6.5 ppm can be ascribed to protons of silanol groups involved in hydrogen bonds, either among themselves or with water, which can itself contribute to this signal. It can be noticed that this signal and that of physisorbed water are also present, even if at a slightly different chemical shift, in the spectrum of silica.[39,40]

3.4.3. ^{1}H–^{29}Si HETCOR. To investigate the spatial proximities (of the order of a few Å) between silicon and hydrogen nuclei in M–S–H and confirm the ^{29}Si and ^{1}H signal assignment, we recorded a 2D ^{1}H–^{29}Si HETCOR spectrum of MS_28d.

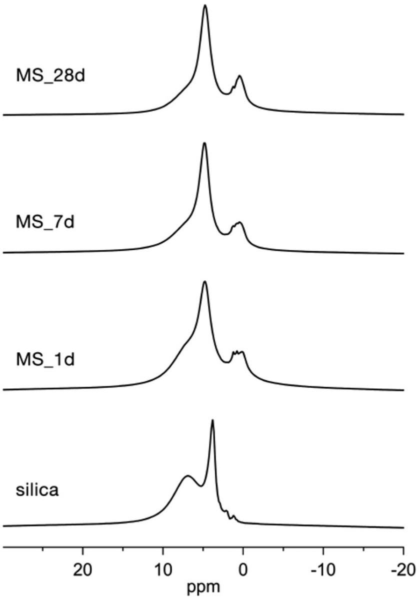

Fig. 5 ^{1}H MAS spectra of MS_1d, MS_7d and MS_28d and silica fume samples.

In the 2D map reported in Fig. 6, a very intense cross-peak is observed between Q^3 $\underline{\mathrm{Si}}(\mathrm{OMg})(\mathrm{OSi})_3$ silicon and Mg–O$\underline{\mathrm{H}}$ hydrogen nuclei. Correlations are also detected between Q^2 $\underline{\mathrm{Si}}(\mathrm{OMg})(\mathrm{OSi})_2\mathrm{OH}$ and MgO$\underline{\mathrm{H}}$ (even if a contribution from isolated SiO$\underline{\mathrm{H}}$ cannot be ruled out), as well as hydrogen-bonded SiO$\underline{\mathrm{H}}$ protons. Q^1 signals are probably too weak to be detected. The observed correlations confirm the proposed assignment of ^{29}Si and ^{1}H signals to M–S–H. Moreover, the absence of correlation with protons of hydrogen-bonded silanols indicates that the possible contribution from Q^2 or Q^1 sites of silica to the peaks ascribed to Q^3 silicon nuclei of M–S–H is negligible.

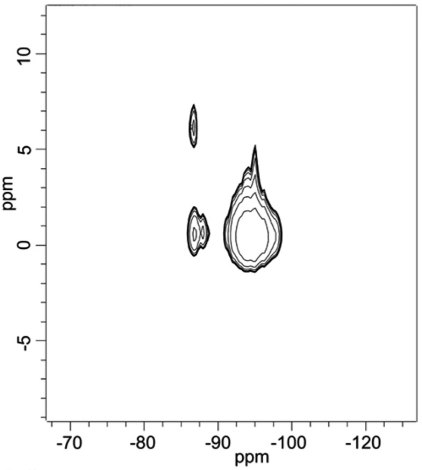

Fig. 6 ^1H–^{29}Si HETCOR spectrum of MS_28d.

3.4.4. $T_1(^{29}Si)$ and quantitative analysis of ^{29}Si spectra.

As anticipated in section 3.4.1, the ^{29}Si DE-MAS spectra shown in Fig. 4, recorded with a recycle delay between two consecutive transients of 20 s, cannot be *a priori* considered as quantitative, due to the usually very long (tens to hundreds of seconds) ^{29}Si spin-lattice relaxation time (T_1) values. Indeed, it is known that in obtaining quantitative NMR spectra of an X nucleus using a 90° direct excitation pulse, a recycle delay at least five times the T_1 of X must be used, which allows the X longitudinal magnetization to fully recover between two consecutive scans. However, the use of a sufficiently long recycle delay would enormously increase the time necessary to obtain a spectrum with good signal-to-noise ratio. Nevertheless, it is possible to also obtain quantitative information from spectra acquired with a short recycle delay by using suitable scaling factors that can be determined from T_1 values. To the best of our knowledge, so far, the ^{29}Si T_1 values of M–S–H have not been reported in the literature, and the quantitative analysis of the spectra is only rarely checked or discussed.[27] For this reason, we decided to measure the ^{29}Si T_1 values of M–S–H for MS_28d sample with a saturation-recovery experiment and use them to obtain quantitative information from our ^{29}Si DE-MAS spectra.[41] For most silicon species, the experimental magnetization recovery curves could not be satisfactorily reproduced with a mono-exponential function. On the other hand, the curves are well fitted by a stretched exponential function

$$M(t) = M_0(1 - \exp(-(t/T_1)^{\beta}))$$

with M_0, the equilibrium magnetization, and β ($0 < \beta \leq 1$), an exponent that takes into account the distribution of different situations, intrinsic in the disorder of the system, as pointed out in the literature for diamagnetic amorphous siliceous materials.[42,43] The T_1 and β values obtained are reported in Table 3. An estimate of ^{29}Si T_1 of silica was also obtained by fitting the sum of the areas of its Q^4 and Q^3 signals. Looking at M–S–H signals, it can be observed that T_1 values approximately increase from Q^{1A} and Q^{1B}, to Q^2, and to Q^3, in agreement with the decreasing number of bonded OH groups. Indeed, the dipolar interaction with spatially close ^1H nuclei should decrease the T_1 of ^{29}Si. The silicon species resonating at −78.5 ppm show a particularly long T_1 (150 ± 43 s, with $\beta = 1$), suggesting that they could either bear particularly mobile OH groups, or have no OH groups directly bonded.

T_1 values have been used to calculate the scaling factors (sf) for the different signals using the following equation:

$$\mathrm{sf} = N/(1 + N(1 - \exp(-(\mathrm{rd}/T_1)^{\beta})))$$

where N is the number of accumulated transients and rd is the recycle delay used for recording DE-MAS spectra.[41] The calculated sf values for the different ^{29}Si signals are reported in Table 3, from which it appears evident that DE-MAS spectra recorded with a recycle delay of 20 s cannot be considered quantitative. Since a large variation of the relaxation times can be reasonably excluded, we used T_1 values measured for MS_28d to also scale the spectra of MS_1d and MS_7d.

3.5. FTIR spectroscopy

Fig. 7 reports the FTIR spectra of the MS samples at different hydration times and of the unhydrated silica and MgO powders, for comparison. Table 4 summarizes the FTIR features present in the spectra. A sharp peak at 3695 cm^{-1}, attributed to brucite,[44] is present in all the spectra of MS samples. The intensity of this peak decreases with hydration time due to the reaction of brucite with silica. The broad absorption at about 3400 cm^{-1} and the band at 1640 cm^{-1} can be ascribed to OH stretching and bending, respectively. The feature at

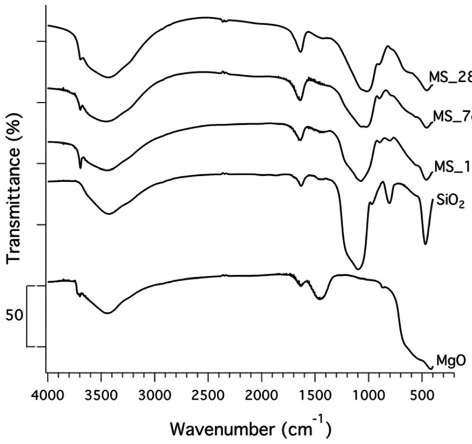

Fig. 7 FTIR spectra of MS_1d, MS_7d and MS_28d samples. The spectra of silica and MgO reactants are also reported for comparison. Curves have been offset for the sake of clarity.

Table 4 FTIR data of MS_1d, MS_7d, MS_28d, silica and MgO samples. Key: s-strong; m-medium; w-weak

	OH vibrations (cm^{-1})	Si–O vibrations (cm^{-1})	Mg–O vibrations (cm^{-1})
MS_1d	3695 m	1213 m	≈1450 m
	3200–3600 m	1078 s	560 w
	1643	987 w	463 s
		884 w	
		805 w	
MS_7d	3695 w	1194 m	≈1450 m
	3200–3600 m	1064 s	565 w
	1642	985 m	461 s
		889 w	
		769 w	
MS_28d	3695 w	1193 m	≈1450 m
	3200–3600 m	1050 s	465 m
	1640	977 w	
	650 w	885 w	
		734 w	
silica	3200–3600 m	1696 w	
	1632 w	1211 s	
		1087 s	
		1030 w	
		951 w	
		808 w	
MgO	3718 w		≈1450 m
	3200–3600 m		560 s
	1637 w		460 s

1696 cm^{-1} in the silica spectrum may be assigned to Si–OH vibrations,[3] indicating partial hydration of the powder. In the spectra of silica and MS samples, a band composed by multiple absorptions is present in the 1300–850 cm^{-1} range due to the stretching and bending vibrations of Si–O. The peak at about 770 cm^{-1} is attributed to Q^1 Si–O vibrations. The peak at 650 cm^{-1} in the spectrum of MS_28d can be attributed to a vibration similar to the libration of the Mg_3OH unit in magnesium phyllosilicates.[3] Bands at 560 and 460 cm^{-1} are assigned to MgO vibrations, as can be deduced from comparing the spectra of the MS samples with that of MgO.

The deconvolution of the spectra of silica and MS samples in the 1350–850 cm^{-1} spectral range, evidencing the evolution of silicatic chain polymerization in the growing M–S–H gel, is reported in the ESI as Fig. S4 and Table S3.†

3.6 SEM analysis

The microscopic analysis performed on MS_28d shows that the M–S–H morphology is rather homogeneous at the microscale level, and the globular nature of M–S–H particles becomes evident at high magnification (Fig. 8). The analysis highlighted that these interconnected and densely packed globules have an average size of ~30 nm, in accordance with the literature.[24]

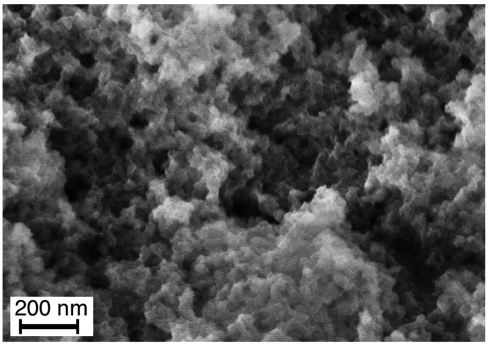

Fig. 8 SEM image of MS_28d.

4. Discussion

The combined analysis of the results obtained by XRD, TG/DTA, SSNMR, and FTIR on MgO/SiO_2/water samples freeze-dried after 1, 7 and 28 days of hydration proves that the M–S–H binder phase is already present after the first 24 hours of hydration and keeps on forming during the monitored 28 days. In particular, the pH measurements, X-ray diffraction and thermal data evidence that the reaction proceeds through the very fast hydration of MgO to form brucite, which is then consumed until a small residual amount remains at 28 days. Concurrently, as highlighted by ^{29}Si SSNMR, silica is hydrated and consumed in 28 days of hydration. The increasing intensity of the characteristic broad peaks in XRD patterns indicates the progressive formation of M–S–H, which is definitively proved by ^{29}Si, ^1H and 2D ^1H–^{29}Si SSNMR experiments. The detailed analysis of ^{29}Si SSNMR spectra and, in particular, the acquisition of quantitative data allowed the different silicon species present in M–S–H to be identified and quantified.

The structural features of M–S–H deserve particular discussion: indeed, several hypotheses have been previously proposed in the literature, but an unambiguous description has not yet been achieved due to the strongly amorphous character of the phase and the variety of techniques used for its characterization. Moreover, although SSNMR is particularly powerful for the structural investigation of amorphous materials, its application to M-S-H has been quite limited so far; in particular, no quantitative data have been reported yet. In this work, the analysis of ^{29}Si SSNMR spectra of M–S–H revealed different silicon local environments: in particular, a good spectral reproduction required at least two different signals for each Q^3 and Q^1 species and only one for the Q^2 species. The most intense Q^3 signals, which arise from the fully condensed $\underline{Si}(OMg)(OSi)_3$ species constituting the bulk of the material, can be exploited to recognize, inside the complex M–S–H phase, local silicon environments similar to those present in crystalline magnesium silicates, in the following indicated "crystal-like" domains. It must be pointed out that, with the chemical shift being a local property, these similarities can be established independently of the presence of a long-range order. Here, the strongly amorphous character of M–S–H, as established from X-ray diffraction, implies a distribution of chemical structures and, consequently, of ^{29}Si chemical shifts.

Therefore, the chemical shifts found for Q^{3A} and Q^{3B} species must be intended as those of the most representative "crystal-like" domains.

In the attempt to describe the structure of M–S–H, it is common in the literature to take as models 2 : 1 or 1 : 1 magnesium phyllosilicates, constituted by T–O–T and T–O layers, respectively, where T indicates a sheet of interconnected $(SiO_4)^{2-}$ tetrahedra and O stands for a sheet of Mg^{2+} cations octahedrally coordinated to hydroxyl groups and to the apical oxygen atoms of the T sheet(s). The ^{29}Si chemical shift of Q^{3A} (−92.9 ppm) coincides with that reported for the T–O phyllosilicate chrysotile,[34] a mineral of serpentine group, with formula $Mg_3Si_2O_5(OH)_4$ (see Fig. 9A). On the other hand, the signal of Q^{3B} (−95.2 ppm) appears quite close to that reported for talc, a T–O–T phyllosilicate with formula $Mg_3Si_4O_{10}(OH)_2$ (see Fig. 9B), whose Q^3 silicon nuclei resonate at about −97.7 ppm in the natural crystalline form, while a chemical shift of −95 ppm is reported for synthetic talc in the first stages of preparation.[33,45] The results obtained from the analysis of ^1H–^{29}Si CP-MAS spectra at variable contact time are, interestingly, in agreement with the proposed identification of Q^{3A} and Q^{3B} with silicon sites resembling those of chrysotile and talc. Indeed, the shorter T_{SiH} observed for Q^{3A} with respect to Q^{3B} is in agreement with the larger number of ^1H nuclei (Mg–OH) contained in the formula of chrysotile. Further and stronger evidence of the coexistence of "talc-like" and "chrysotile-like" domains in M–S–H arises from XRD and SSNMR experiments carried out on heated samples. In fact, the literature reports that upon heating up to 900 °C, chrysotile converts mainly to forsterite (Mg_2SiO_4) and in part to enstatite ($MgSiO_3$),[34] while talc, especially if amorphous, transforms into enstatite.[33] XRD and SSNMR experiments on heated samples clearly show signals of both forsterite and clinoenstatite, a polymorph of enstatite already reported as a crystallization product of heated M–S–H gels.[27] These data show a prevalence of clinoenstatite, which can be explained also considering that further clinoenstatite could form at the expense of forsterite.[33,34]

The almost complete absence of residual silica and brucite after 28 days of hydration (inferred from ^{29}Si SSNMR and XRD experiments, respectively) indicates that in the formed M–S–H phase, Mg and Si are in an approximately 1 : 1 molar ratio, corresponding to the initial molar ratio between MgO and silica. The talc and chrysotile minimal formulas (respectively, $Mg_3Si_4O_{10}(OH)_2$ and $Mg_3Si_2O_5(OH)_4$) suggest that in M–S–H, the proportion between "talc-like" and "chrysotile-like" domains is approximately 1 : 1 by mole. This should be reflected in a 2 : 1 ratio between "talc-like" and "chrysotile-like" silicon species. From the 1 : 1 ratio between the quantitative areas of ^{29}Si signals of Q^{3A} and Q^{3B}, it can be derived that most Q^2 silicon species in the MS_28d sample must be ascribed to "talc-like" domains.

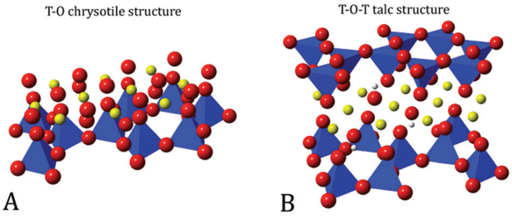

Fig. 9 Scheme of (A) chrysotile (database code AMCSD: 0019917) and (B) talc (AMCSD: 0010839) structures. Blue tetrahedra represent Si species. Red, yellow and white spheres represent O, Mg and H atoms, respectively.

Finally, it is worth noting that the structure of M–S–H appears to be very much condensed since its early formation, with a very small presence of silanols. For the MS_28d sample, an average condensation degree of about 84% can be calculated as:

$$CD = 100(3Q^3 + 2Q^2 + Q^1)/3(Q^3 + Q^2 + Q^1)$$

where the Q^i symbols indicate the corresponding quantitative signal areas determined from ^{29}Si DE-MAS spectra. The composition of M–S–H as constituted by both "talc-like" and "chrysotile-like" domains is consistent with previous results.[21,30,46,47] In particular, our data seem to well fit the description of "synthetic deweylite" given by Speakman and Majumdar as "a mixture of intimately interlayered badly crystallized talc and badly crystallized chrysotile".[48]

Two recent works proposed either talc[31] or lizardite[3] as the best structural model of M–S–H, although the reported data are not incompatible with the coexistence of chrysotile and amorphous talc. Lizardite and chrysotile are polymorphs, differing in the arrangement of T–O layers: while lizardite shows flat sheets, chrysotile has cylindrical layers; this results in a plate-like morphology for lizardite, and thin and flexible fibrils for chrysotile.[49] At the micrometric scale, our M–S–H samples do not show typical chrysotile (or talc) morphology (Fig. 8) as is expected considering the assessed disordered structure constituted by mixed subnanometre-sized "chrysotile-like" and "talc-like" domains. However, it is known that lizardite and chrysotile present some small structural differences at the sub-nanometric scale (weaker inter-layer hydrogen-bonds and slightly different thickness of the sheets in chrysotile)[50] that can be reflected by ^{29}Si chemical shift, reported to be −92.9 and −93.7 ppm for chrysotile and lizardite, respectively. Therefore, the chemical shift of Q^{3A} sites suggests that the structural features of T–O domains in the M–S–H here investigated resemble chrysotile more than lizardite.

5. Conclusions

Upon mixing highly reactive MgO and SiO_2 with water at room temperature, an M–S–H phase is formed within the first 24 hours of hydration, and its amount increases over the entire monitored period of 28 days. The reaction proceeds through the hydration of MgO to give $Mg(OH)_2$, which then reacts with silica. We used a multi-technique approach, including TG/DTA, XRD, FT-IR and SSNMR, to qualitatively and quantitatively follow the evolution of the hydration, as well as to obtain detailed structural information on M–S–H. Analysis of the data reveals that this reaction results in the formation of an amorphous phase that is constituted by an intimate mixture of subnanometre-sized domains with local structures resembling those of chrysotile and talc. The quantitative analysis of SSNMR data enabled us to conclude that the "talc-like" and "chrysotile-like" domains are approximately in a 1 : 1 molar ratio and that, on average, M–S–H has a high degree of condensation, corresponding to the presence of a small amount of silanols. Considering the strong amorphous character of M–S–H and the large variety of local structural motifs that can be formed, this work represents a significant step towards the detailed characterization of the M–S–H structure, which is of fundamental importance in view of the development of MgO-based eco-sustainable cements. This assessment of the M–S–H structure paves the way towards understanding and tailoring the macroscopic properties of the cement binder phase from modifications at the nanoscale.

Acknowledgements

This work was performed with the financial support of Ministero dell'Istruzione, Università e Ricerca scientifica MIUR (FIR2013 Project RBFR132WSM) and of Consorzio Interuniversitario per lo Sviluppo dei Sistemi a Grande Interfase, CSGI. Roberto Spiniello (ICCOM-CNR Pisa) is kindly acknowledged for its technical support.

References

1 T. Zhang, L. J. Vandeperre and C. R. Cheeseman, *J. Sustainable Cem.-Based Mater.*, 2012, **1**, 34.
2 K.-Y. Hwang, J.-Y. Seo, H. Q. H. Phan, J.-Y. Ahn and I. Hwang, *Clean: Soil, Air, Water*, 2014, **42**, 355.
3 S. A. Walling, H. Kinoshita, S. A. Bernal, N. C. Collier and J. L. Provis, *Dalton Trans.*, 2015, **44**, 8126.
4 L. J. Vandeperre, M. Liska, A. Al-Tabbaa and P. Claisse, in *Sustainable construction materials and technologies*, ed. T. R. Naik, E. Ganjian and Y.-M. Chun, Taylor & Francis/Balkema, Coventry, UK, 2007.
5 T. Zhang, C. R. Cheeseman and L. J. Vandeperre, *Cem. Concr. Res.*, 2011, **41**, 439.
6 F. Ridi, E. Fratini and P. Baglioni, *J. Colloid Interface Sci.*, 2011, **357**, 255.
7 A. J. Hunt, E. H. K. Sin, R. Marriott and J. H. Clark, *ChemSusChem*, 2010, **3**, 306.
8 E. A. Quadrelli, G. Centi, J.-L. Duplan and S. Perathoner, *ChemSusChem*, 2011, **4**, 1194.
9 M. Schneider, M. Romer, M. Tschudin and H. Bolio, *Cem. Concr. Res.*, 2011, **41**, 642.
10 E. M. Gartner and D. E. Macphee, *Cem. Concr. Res.*, 2011, **41**, 736.
11 R. J. Flatt, N. Roussel and C. R. Cheeseman, *J. Eur. Ceram. Soc.*, 2012, **32**, 2787.
12 F. Jin and A. Al-Tabbaa, *Cem. Concr. Compos.*, 2014, **52**, 27.
13 T. Zhang, L. J. Vandeperre and C. R. Cheeseman, *Cem. Concr. Res.*, 2014, **65**, 8.
14 Z. Li, T. Zhang, J. Hu, Y. Tang, Y. Niu, J. Wei and Q. Yu, *Constr. Build. Mater.*, 2014, **61**, 252.
15 J. Szczerba, R. Prorok, E. Śnieżek, D. Madej and K. Maślona, *Thermochim. Acta*, 2013, **567**, 57.
16 F. Jin and A. Al-Tabbaa, *Thermochim. Acta*, 2013, **566**, 162.
17 J. Wei, Q. Yu, W. Zhang and H. Zhang, *J. Wuhan Univ. Technol., Mater. Sci. Ed.*, 2011, **26**, 745.
18 N. Vlasopoulos, *Process for producing cement binder compositions containing magnesium*, WO/2012/028471, 2012.
19 H. Dong, U. Cise, A. Al-Tabbaa and E. Yang, *Feasibility Study of Synthesizing MgO from Local Waste Brine Using Aqueous Ammonia*, in 14th International Congress on the Chemistry of Cement, Beijing, 2015, vol. 1, p. 1.
20 H. M. Jennings and J. W. Bullard, *Cem. Concr. Res.*, 2011, **41**, 727.
21 D. R. M. Brew and F. P. Glasser, *Cem. Concr. Res.*, 2005, **35**, 85.
22 L. J. Vandeperre, M. Liska and A. Al-Tabbaa, *Cem. Concr. Compos.*, 2008, **30**, 706.
23 L. J. Vandeperre, M. Liska and A. Al-Tabbaa, *J. Mater. Civ. Eng.*, 2008, **20**, 375.
24 W.-S. Chiang, G. Ferraro, E. Fratini, F. Ridi, Y.-Q. Yeh, U.-S. Jeng, S.-H. Chen and P. Baglioni, *J. Mater. Chem. A*, 2014, **2**, 12991.
25 M. Geppi, S. Borsacchi, G. Mollica and C. A. Veracini, *Appl. Spectrosc. Rev.*, 2008, **44**, 1.
26 A. Rawal, B. J. Smith, G. L. Athens, C. L. Edwards, L. Roberts, V. Gupta and B. F. Chmelka, *J. Am. Chem. Soc.*, 2010, **132**, 7321.
27 J. S. Hartman and R. L. Millard, *Phys. Chem. Miner.*, 1990, **17**, 1.
28 J.-B. d' Espinose de la Caillerie, M. Kermarec and O. Clause, *J. Phys. Chem.*, 1995, **99**, 17273.
29 J. Temuujin, K. Okada and K. J. D. MacKenzie, *J. Am. Ceram. Soc.*, 1998, **81**, 754.
30 J. Temuujin, K. Okada and K. J. D. MacKenzie, *J. Solid State Chem.*, 1998, **138**, 169.
31 C. Roosz, S. Grangeon, P. Blanc, V. Montouillout, B. Lothenbach, P. Henocq, E. Giffaut, P. Vieillard and S. Gaboreau, *Cem. Concr. Res.*, 2015, **73**, 228.
32 E. M. Van der Merwe, C. Strydom and A. Botha, *J. Therm. Anal. Calorim.*, 2004, **77**, 49.
33 K. J. D. MacKenzie and R. H. Meinhold, *Thermochim. Acta*, 1994, **244**, 195.
34 K. J. D. MacKenzie and R. H. Meinhold, *Am. Mineral.*, 1994, **79**, 43.
35 O. Mendoza, G. Sierra and J. I. Tobón, *Constr. Build. Mater.*, 2014, **54**, 550.
36 J. Dweck, P. F. Ferreira da Silva, P. M. Büchler and F. K. Cartledge, *J. Therm. Anal. Calorim.*, 2002, **69**, 179.

37 F. Guirado, S. Galí and J. S. Chinchón, *Cem. Concr. Res.*, 1998, **28**, 381.

38 X. Xue and M. Kanzaki, *J. Phys. Chem. B*, 2007, **111**, 13156.

39 C. C. Liu and G. E. Maciel, *J. Am. Chem. Soc.*, 1996, **118**, 5103.

40 C. E. Bronnimann, R. C. Zeigler and G. E. Maciel, *J. Am. Chem. Soc.*, 1988, **110**, 2023.

41 R. Freeman and H. D. W. Hill, *J. Chem. Phys.*, 1971, **54**, 3367.

42 B. Pfleiderer, K. Albert, E. Bayer, L. Van de Ven, J. De Haan and C. Cramers, *J. Phys. Chem.*, 1990, **94**, 4189.

43 V. I. Bakhmutov, *Chem. Rev.*, 2011, **111**, 530.

44 http://rruff.info/Brucite/R050455.

45 A. Dumas, F. Martin, C. Le Roux, P. Micoud, S. Petit, E. Ferrage, J. Brendlé, O. Grauby and M. Greenhill-Hooper, *Phys. Chem. Miner.*, 2013, **40**, 361.

46 G. L. Kalousek and D. Mui, *J. Am. Ceram. Soc.*, 1954, **37**, 38.

47 J. C.-S. Yang, *J. Am. Ceram. Soc.*, 1960, **43**, 542.

48 K. Speakman and A. J. Majumdar, *Mineral. Mag.*, 1971, **38**, 225.

49 C. Rinaudo, D. Gastaldi and E. Belluso, *Can. Mineral.*, 2003, **41**, 883.

50 F. J. Wicks and E. J. W. Whittaker, *Can. Mineral.*, 1975, **13**, 227.

Electronic Supplementary Material (ESI) for Dalton Transactions.

Structural characterization of magnesium silicate hydrate: towards the design of eco-sustainable cements

Monica Tonelli[a], Francesca Martini[b], Lucia Calucci[b], Emiliano Fratini[a], Marco Geppi[c], Francesca Ridi[a]*, Silvia Borsacchi[b]* and Piero Baglioni[a]

[a] Department of Chemistry "Ugo Schiff" & CSGI, University of Florence, Sesto Fiorentino (FI) 50019, Italy

[b] Istituto di Chimica dei Composti OrganoMetallici, Consiglio Nazionale delle Ricerche – CNR U.O.S di Pisa, Pisa 56124, Italy

[c] Department of Chemistry and Industrial Chemistry, University of Pisa, Pisa 56124, Italy

1. pH measurements

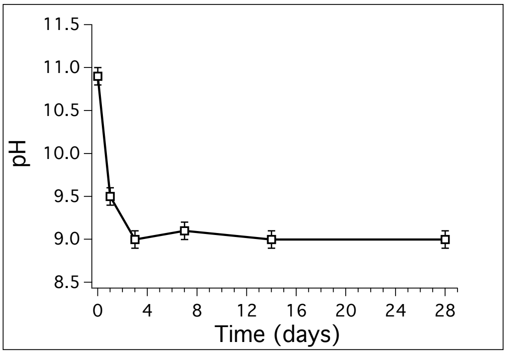

Figure S1. pH values of MS paste during the first 28 days of hydration.

2. Mass losses from TG measurements

Table S1. Mass losses from TG measurements during hydration.

	Mass loss from TG% curves (±0.5%)		
	RT-200 °C	310-400 °C	400-800 °C
MS_1d	13.4	6.8	4.6
MS_ 7d	19.4	4.0	5.4
MS_28d	15.3	3.2	6.5

3. ^{1}H-^{29}Si CP-MAS spectra at variable contact time

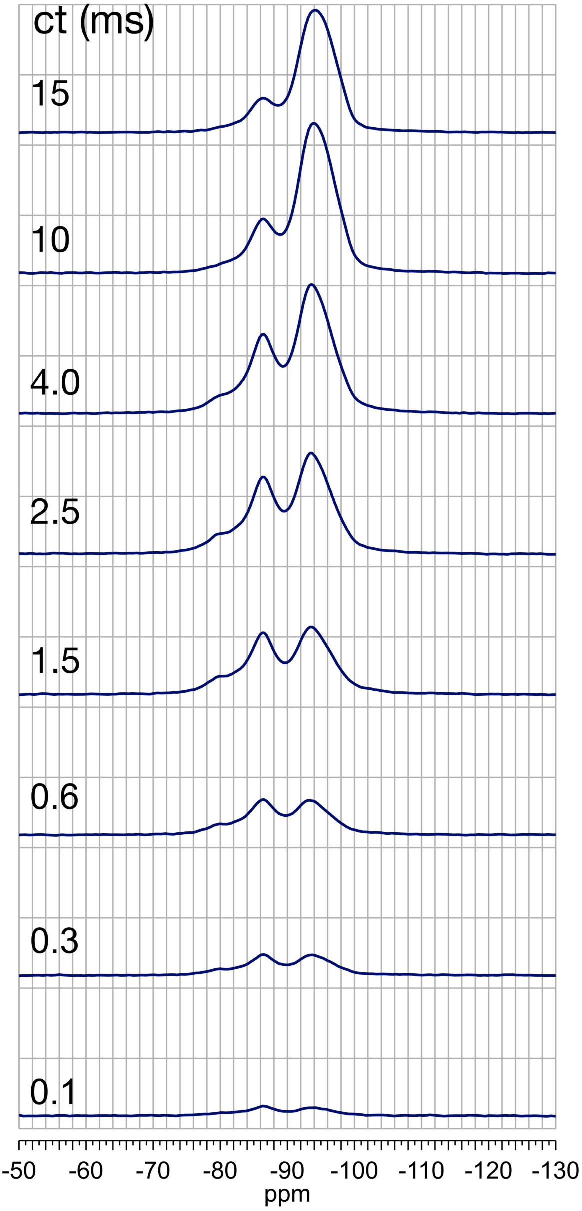

Figure S2. ^{1}H-^{29}Si CP-MAS spectra of MS_28d sample, recorded with the contact time (ct) values reported in the figure.

The ^{1}H-^{29}Si CP-MAS spectra recorded at different contact times (ct) have been successfully deconvoluted using the same peaks found from the fitting of ^{29}Si DE-MAS spectra.

The trends of the CP peak intensity vs. ct are typically fitted using the following equation [1]:

$$I(ct) = I_0 \frac{1}{(1 - T_{SiH} / T_{1\rho}^{H})} \left[\exp\left(-\frac{ct}{T_{1\rho}^{H}} \right) - \exp\left(-\frac{ct}{T_{SiH}} \right) \right]$$

where T_{SiH} is the so called cross-polarization time constant, $T_{1\rho}{}^{H}$ is the proton spin-lattice relaxation time in the rotating frame, and I_0 is the maximum intensity which could be theoretically obtained in a CP experiment, proportional to the intensity obtainable from a quantitative DE-MAS spectrum.

It is usually assumed that $T_{SiH} < T_{1\rho}{}^{H}$ (fast CP regime). In such case T_{SiH} is the time constant that determines the growth of the curve at short ct values, while $T_{1\rho}{}^{H}$ regulates the decrease at long ct values. However, one potential misinterpretation of the data might arise from the fast CP regime not being satisfied. Indeed, rarely, when Si and H nuclei are weakly dipolar coupled, their internuclear distance being quite large, the opposite situation $T_{SiH} > T_{1\rho}{}^{H}$ (slow CP regime) may occur. In this case the above equation still reproduces the experimental data, but the role of T_{SiH} and $T_{1\rho}{}^{H}$ is reversed with respect to the fast CP regime. A correct interpretation of the data therefore requires the knowledge of the CP regime. Although the same curve shape is obtained by exchanging T_{SiH} and $T_{1\rho}{}^{H}$ values, a striking difference between the two regimes is that the maximum value of I(ct) in the fast regime is quite close to I_0, while in the slow CP regime it is much lower, depending on T_{SiH} and $T_{1\rho}{}^{H}$ relative values [2]. In other words, fitting the same data with the assumption of fast CP regime gives a best-fitting I_0 value much lower than that obtained assuming a slow CP regime.

The CP intensity vs. ct curves were fitted for all silicon nuclei assuming a fast CP regime, and the best-fitting parameters (I_0, T_{SiH} and $T_{1\rho}{}^{H}$) so obtained are reported in Table S2. From the quantitative intensity values obtained from ^{29}Si DE-MAS spectrum (A%), reported in Table 3 of the manuscript, we found the ratios I_0/A%, which must be the same for all types of ^{29}Si nuclei, if I_0 is obtained assuming the correct CP regime. Considering the presence of close silanol protons, the fast CP regime can be safely assumed valid at least for Q^{1A}, Q^{1B} and Q^{2} silicons, for which I_0/A% values of 1.8, 2.2, and 2.0 were found. It can be seen that for Q^{3} silicons, for which the a priori assumption of one of the two CP regimes is more uncertain, I_0/A% values of the same order of magnitude (2.3 and 2.8) were obtained assuming the fast CP regime, while unacceptably larger values (16 and 9) were obtained assuming the slow CP regime. This is a clear indication that the fast CP regime is satisfied by all the silicons considered in this analysis.

Although the values of T_{SiH} reported in Table S2 are affected by quite large errors, the order T_{SiH} (Q^{1A})≈ T_{SiH} (Q^{1B})≈ T_{SiH} (Q^{2}) < T_{SiH} (Q^{3A}) < T_{SiH} (Q^{3B}) can be considered reliable, as also clearly observable from the slopes at short ct of the curves reported in Figure S3. This is in agreement with the fact that silanol protons contribute to the shorter T_{SiH} of Q^{1} and Q^{2} and suggests that Q^{3A} silicons have a larger number of close protons (Mg-OH) than Q^{3B} silicons.

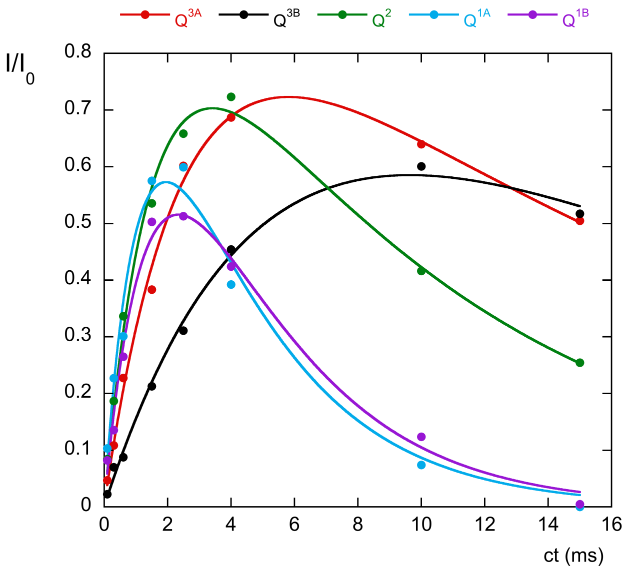

Figure S3. Experimental (points) and calculated (lines) values of I/I_0 vs contact time (ct) for the different peaks present in ^{1}H-^{29}Si CP-MAS spectra of MS_28d sample.

Table S2. Parameters obtained from the fitting of trends of the intensity vs the contact time for the different peaks present in the ^{1}H-^{29}Si CP-MAS spectra of the MS_28d sample, using the equation reported in the text.

	Q^{1A}	Q^{1B}	Q^2	Q^{3A}	Q^{3B}
I_0 (a.u.)	7 ± 1	11 ± 2	57 ± 4	67 ± 8	94 ± 8
T_{SiH} (ms)	1.2 ± 0.5	1.6 ± 0.4	1.6 ± 0.2	2.5 ± 0.4	6 ± 1
$T_{1\rho}^H$(ms)	4 ± 1	3.5 ± 0.9	10 ± 1	18 ± 4	18 ± 8

[1] W. Kolodziejski, J. Klinowski, Chem. Rev., 2002, 102, 613.

[2] C.A. Fyfe, D.H. Brouwer, P. Tekely, J. Phys. Chem. A, 2005, 109, 6187.

4. FTIR spectra deconvolution

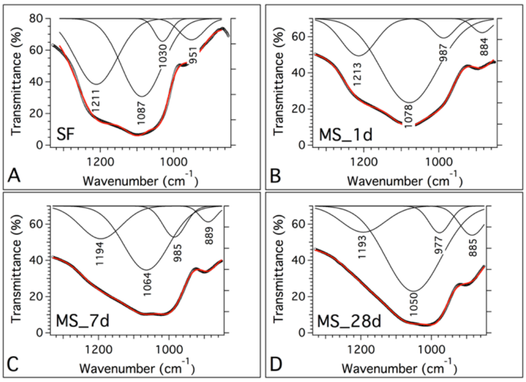

Figure S4. Deconvolution of FTIR spectra of Silica, MS_1d, MS_7d and MS_28d in the 1350-850 cm^{-1} range. Black markers and red lines represent experimental and calculated spectra, respectively. The Gaussian peaks obtained by means of the fitting procedure are shown as black lines.

Table S3. FTIR spectra deconvolution parameters for silica and MS_1d, MS_7d, MS_28d. Wavenumber of the maximum, Wn_{max} (cm^{-1}), and area (%) of the peaks are reported.

	silica	MS_1d	MS_7d	MS_28d
Wn_{max}	1211	1213	1194	1193
area	40.1	19.1	25.6	15.8
Wn_{max}	1087	1078	1064	1050
area	46.9	70.6	55.4	66.0
Wn_{max}	1030	987	985	977
area	5.3	6.3	13.9	7.8
Wn_{max}	951	884	889	885
area	7.7	3.9	5.1	10.3

Four Gaussian peaks were necessary to describe the vibrations of the Q^n silicon sites. According to the literature, the contribution at higher wavenumber is associated to the vibration of more condensed Si-O bonds. In particular the strong absorption at 1211 cm^{-1} in the silica spectrum is attributed to the vibration of Q^3 and Q^4 silicon sites [3]. Roughly at the same wavenumber the stretching of Q^3 silicon sites in M-S-H gel is also reported to occur [4]. The peak at higher wavenumber is observed to increase in the first week of hydration while it decreases afterwards. This fact can be explained considering that the disappearance of silica and the growth of M-S-H occur simultaneously. The same behaviour was already observed in the literature for M-S-H samples synthesized from solution [4]. It is worth noting that after 28 days silica is completely consumed (see SSNMR data), so the 1193 cm^{-1} peak can be entirely ascribed to the presence of Q^3 silicon sites in the M-S-H binder phase. The three other peaks in deconvoluted spectra are related to stretching and bending vibrations of Q^2 silicon sites [4]. Also in this case the trend of the areas vs hydration time is not monotonic.

[3] P. Yu, R. J. Kirkpatrick, B. Poe, P. F. McMillan, X. Cong, J. Am. Ceram. Soc., 1999, 82, 742.
[4] D.R.M. Brew, F.P. Glasser, Cem. Concr. Res., 2005, 35, 85.

Paper II

Cement and Concrete Research 102 (2017) 60–67

Contents lists available at ScienceDirect

Cement and Concrete Research

journal homepage: www.elsevier.com/locate/cemconres

Hydration of MgO/SiO_2 and Portland cement mixtures: A structural investigation of the hydrated phases by means of X-ray diffraction and solid state NMR spectroscopy

Francesca Martini[a,b,1], Monica Tonelli[c,1], Marco Geppi[a,b], Francesca Ridi[c,*], Silvia Borsacchi[a,*], Lucia Calucci[a]

[a] Institute for the Chemistry of OrganoMetallic Compounds, Italian National Research Council − CNR, 56124 Pisa, Italy
[b] Department of Chemistry and Industrial Chemistry, University of Pisa, 56124 Pisa, Italy
[c] Department of Chemistry "Ugo Schiff" & CSGI, University of Florence, 50019 Sesto Fiorentino (FI), Italy

ARTICLE INFO

Keywords:
Magnesium silicate hydrate (M-S-H)
Calcium silicate hydrate (C-S-H) (B)
MgO (D)
Portland cement (D)
Solid state NMR
X-ray diffraction (B)

ABSTRACT

The phases formed during the hydration of several MgO/SiO_2 and Portland cement mixtures were investigated by performing X-ray diffraction and ^{29}Si and ^{27}Al solid state NMR experiments on samples hydrated for 1, 7 and 28 days. The structural properties and relative amount of magnesium silicate hydrate (M-S-H) and calcium silicate hydrate (C-S-H) gels, which form as separate phases, were found to significantly depend on the initial composition of the mixtures. Faster hydration kinetics was observed for all mixtures with respect to the "pure" MgO/SiO_2 and Portland cement samples, pH and excess of silica playing a major role. Moreover, the addition of the MgO/SiO_2 mixture to Portland cement affects the formation of aluminum-containing hydrated phases.

1. Introduction

In the last years, the research on formulations alternative to Portland cement has progressively grown, with the aim of both reducing the environmental impact of CO_2 emissions associated to Portland production [1,2] and finding materials suitable for nuclear waste encapsulation. In fact, cement based containment is usually employed for storing low and intermediate level radioactive wastes to be disposed in clayey rock formations [3,4]. However, the high pH values (≥ 13.5) often encountered for Portland cement pore solution have been proved to cause a degradation of clay barriers [5]. On the other hand, when low-pH cement formulations based on Portland or blast furnace slag cements are used, decalcification, leaching and carbonation processes may occur in the calcium silicate hydrate (C-S-H) binder phase at the clay-cement interface, leading to the formation of silica gel. Formation of magnesium silicate hydrate (M-S-H) was observed as a consequence of the reaction between silica gel and magnesium present in high concentration either at the decalcified cement/clay interface or in the interstitial solution of the clay [3,6,7]. Recently, hydration of highly reactive magnesium oxide in the presence of silica was exploited to produce a low-pH cement [8,9], particularly suited for the encapsulation of Magnox (Mg-Al alloy) nuclear waste [10]. During the hydration of MgO/SiO_2 mixtures, periclase reacts with water to form brucite ($Mg(OH)_2$), which promptly reacts with silica to produce M-S-H as binder phase; the structural characteristics of this phase were assessed [10,11,12,13].

In view of the potential applications of low-pH cements, the study of mixed formulations of MgO/SiO_2 and Portland cement is important to understand the structure of C-S-H and M-S-H phases formed upon hydration. It was recently reported that M-S-H and C-S-H gels remain segregated in different domains when they coexist in geological repositories for radioactive waste encapsulation [6]. The formation of separate M-S-H and C-S-H gels was also observed by Lothenbach et al. [14] and by Chiang et al. [15] in the hydration of CaO, MgO, and SiO_2 mixtures.

Data pointing to the same description were acquired by us on mixtures of MgO/SiO_2 and Portland cement [16]. Moreover, for these samples a strong influence of the mixture composition on the pH of the aqueous phase in contact with the cementitious materials and on the relative amount of the formed C-S-H and M-S-H phases was observed. In

---

Abbreviations: M-S-H, magnesium silicate hydrate; C-S-H, calcium silicate hydrate; w/s, water to solid ratio; M, MgO; S, SiO_2; C, Portland cement; SSNMR, solid state Nuclear Magnetic Resonance; DTA, differential thermal analysis; DE, direct excitation; MAS, magic angle spinning; FTIR, Fourier transform infrared; XRD, X-ray diffraction; RD, reaction degree; CD, condensation degree; MCL_{min}, minimum mean chain length; MCL_{max}, maximum mean chain length; MCL, mean chain length

[*] Corresponding authors.

E-mail addresses: francesca.ridi@unifi.it (F. Ridi), silvia.borsacchi@pi.iccom.cnr.it (S. Borsacchi).

[1] These authors contributed equally to this work.

http://dx.doi.org/10.1016/j.cemconres.2017.08.029
Received 17 March 2017; Received in revised form 28 August 2017; Accepted 29 August 2017

Table 1
Chemical composition and physical properties of MgO, SiO_2 and Portland cement.

	MgO	SiO_2	Portland cement
Chemical composition (%)			
SiO_2		≥ 99	19.81
Al_2O_3			5.41
Fe_2O_3			3.96
CaO			66.60
MgO	≥ 99		2.50
SO_3			1.25
Na_2O			0.11
K_2O			0.17
SrO			0.04
Mn_2O_3			0.02
P_2O_5			0.09
TiO_2			0.2
BET surface area (m^2/g)[a]	121 ± 5	395 ± 25	1.5 ± 0.1
Mean particle size (μm)	44	5	20

[a] Measured by means of a Coulter SA 3100 analyzer.

particular, X-ray diffraction (XRD) and ^{29}Si Solid State Nuclear Magnetic Resonance (SSNMR) experiments carried out on samples hydrated for 28 days showed that, when low amounts of MgO/SiO_2 (up to 50 wt%) are present, C-S-H is the main binder phase formed, whereas M-S-H is the prevailing binder phase for samples with MgO/SiO_2 content of at least 80 wt%. The evolution of free water content and of water dynamics during the hydration of the same mixtures was monitored by means of Differential Scanning Calorimetry [16] and ^{1}H spin-spin relaxation time NMR measurements [17], giving insights into the hydration kinetics.

In the present work, we applied XRD and ^{29}Si- and ^{27}Al SSNMR to the same mixtures to characterize in detail the phases formed at different hydration times (from 1 to 28 days). The analysis of quantitative ^{29}Si SSNMR spectra allowed the relative amount of C-S-H and M-S-H and their features to be determined as a function of mixture composition and hydration time. Samples obtained by separate hydration of Portland cement, of a MgO/SiO_2 mixture, and of a mixture of Portland cement and SiO_2 (useful to discriminate the role of the pozzolanic reaction) were also investigated for comparison.

2. Materials and methods

2.1. Materials

Commercial highly reactive periclase (MgO, Sigma-Aldrich) and fumed silica (SiO_2, Aldrich) were used. CEM I Portland cement was obtained from Italcementi (Bergamo, Italy). The chemical composition and physical properties of raw materials are listed in Table 1.

2.2. Sample preparation

The composition of the dry mixtures used to prepare the pastes is reported in Table 2 together with the abbreviated notation employed to indicate the samples throughout the paper. A water to solid ratio (w/s) of 2 was used in all the formulations, this being the minimal ratio needed to obtain a workable paste for the MS100 sample. Typically, 4 g of solid powders were premixed, and then mixed with 8 g of milliQ water. When present, MgO and SiO_2 were mixed in a 1:1 mol:mol ratio.

Immediately after mixing, the pastes were enclosed in polyethylene bags and stored in a thermostatic bath at 20 °C. After 1, 3, 7 and 28 days from the preparation, ~1 g of paste was withdrawn, cooled in liquid nitrogen and freeze-dried (50 mTorr, 24 h) to stop the hydration reaction.

Table 2
Amount (wt%) of MgO (M), SiO_2 (S), and Portland cement (C) in the dry mixtures used to prepare the samples.

Sample	M	S	C
MS100	40	60	0
MS80C20	32	48	20
MS50C50	20	30	50
MS20C80	8	12	80
C100	0	0	100
CS	0	37.5	62.5

2.3. Methods

X-ray diffractograms were recorded with a XRD Bruker New D8 Da Vinci instrument operating at 40 kV and 40 mA, with a Cu source (emitting radiation $\lambda = 1.54$ Å). Data were collected in the 2θ range between 5° and 70°, with an increment of 0.05°.

SSNMR spectra were recorded on a Varian InfinityPlus 400 spectrometer working at ^{1}H, ^{29}Si, and ^{27}Al Larmor frequencies of 400.35, 79.48 and 104.32 MHz, respectively. ^{29}Si Direct Excitation Magic Angle Spinning (DE-MAS) spectra were recorded using a 7.5 mm probehead, exploiting a DE experiment with a ^{29}Si 90° pulse with a duration of 6 μs, spinning the samples at a MAS frequency of 5.5 kHz and under ^{1}H high-power decoupling. For all the samples (except for MS100) a recycle delay of 10 s between two consecutive transients was used. This value resulted to be long enough to ensure the spectra to be quantitative, because ^{29}Si T_1's are shortened by the interaction with paramagnetic species present in Portland cement. For all the ^{29}Si DE-MAS spectra approximately 8,000 transients were accumulated. The ^{29}Si chemical shift scale was referred to 3-(trimethylsilyl)-1-propane-sulfonic acid sodium salt as secondary reference at 1.46 ppm, and TMS as primary one. ^{27}Al DE-MAS spectra were recorded using a 3.2 mm probehead, exploiting the DE pulse sequence with a ^{27}Al excitation pulse selective for the central transition with a duration of 0.85 μs, corresponding to a nominal 30° pulse. All the ^{27}Al spectra were recorded under ^{1}H high-power decoupling, spinning at a MAS frequency of 20 kHz, and accumulating approximately 25,000 transients, with a recycle delay of 2 s. ^{27}Al chemical shifts were referred to the signal (at 0 ppm) of aluminum in a standard 1.1 mol/kg solution of $Al(NO_3)_3$ in D_2O. All the spectra were recorded at room temperature, using air as spinning gas.

3. Results

3.1. X-ray diffraction

Fig. 1 reports the X-ray diffractograms of the investigated samples at different times of hydration.

In MS100 (Fig. 1A), brucite is the main crystalline phase at all hydration times, whereas the broad peaks at about 23°, 35° and 59° are consistent with the pattern of the amorphous M-S-H phase [8,13,18]. Small peaks ascribed to unreacted periclase are also observed. The intensity of the peaks of brucite and periclase decreases with increasing the hydration time, while that of M-S-H peaks correspondingly increases.

In the diffractograms of C100 (Fig. 1E), the most intense peaks are due to portlandite ($Ca(OH)_2$), their intensity increasing with hydration time. In the 29–33° range, different contributions can be observed, ascribable both to the anhydrous phases (alite and belite) of Portland cement and to poorly ordered tobermorite (broad peak at 29.3°), the latter being indicative of the presence of C-S-H [14]. As the hydration reaction proceeds with formation of C-S-H, the intensity of the anhydrous phase peaks decreases, while that of the tobermorite peak increases. Peaks of other phases commonly present in hydrated Portland cement, such as AFm species (monosulphoaluminate, hemicarboaluminate, and monocarboaluminate), can also be identified in

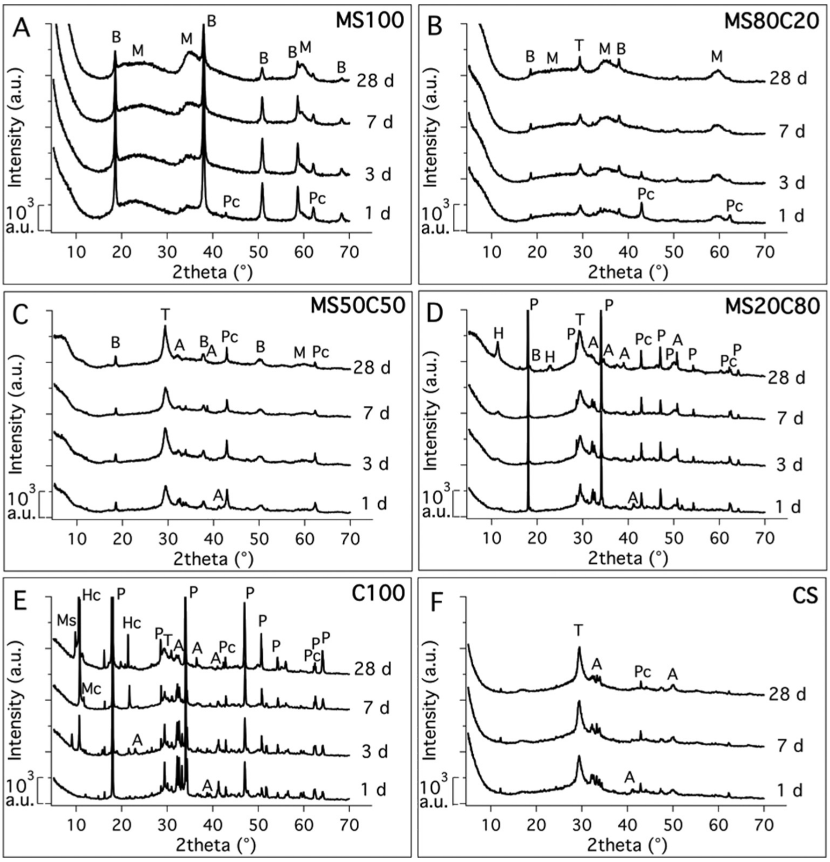

Fig. 1. X-ray diffractograms of all the investigated samples at the indicated hydration times (days, d). The assignment of the peaks is also reported, using the following abbreviations: B (brucite), M (M-S-H), T (tobermorite), A (alite and belite), P (portlandite), Pc (periclase), Mc (monocarboaluminate), Ms. (monosulphoaluminate), Hc (hemicarboaluminate), H (hydrotalcite). Diffractograms have been offset for the sake of clarity. The diffractograms of MS100 at different hydration times and those of the other samples hydrated for 28 days are the same shown in refs. [13] and [16], respectively.

the diffractograms, most of them increasing with the hydration time. The presence of carbonate phases can be ascribed to a small degree of carbonation of the samples, most likely arising from exposure to air.

The X-ray diffractograms of MS80C20 (Fig. 1B) show the same peaks observed for MS100, with the additional peak at 29.3° due to tobermorite. Differently from MS100, the intensity of the M-S-H peaks only slightly increases with the hydration time, while that of brucite and tobermorite peaks remains practically constant.

The diffractograms of MS20C80 (Fig. 1D) display most of the peaks observed for C100, in particular those of unreacted alite and belite, tobermorite and portlandite. In addition, the pattern of hydrotalcite is detected, which can overlap to the peak of monocarboaluminate (at ~10°). The evolution of the intensity of the peaks of the different phases with increasing the hydration time indicates that tobermorite increases together with hydrotalcite, whereas alite and belite decrease and portlandite remains almost constant. On the other hand, no peaks characteristic of the M-S-H phase are detected. Moreover, the typical brucite pattern is absent in the diffractograms of all samples, but that hydrated for 28 days (weak signal at 18.4°). Typical signals of unreacted periclase are also observed at all hydration times.

In the diffractograms of MS50C50 (Fig. 1C) and CS (Fig. 1F) the peak of tobermorite is clearly seen at 29.3°, its intensity increasing with hydration time. Peaks of alite and belite are also observed, with small and practically constant intensity over the whole hydration period, while peaks characteristic of portlandite are not observed at any time. For MS50C50, peaks of brucite are also observed, their intensity remaining almost equal at all the hydration times. The broad peaks of M-S-H can be hardly distinguished, indicating that this phase does not form in a large amount.

3.2. ^{29}Si SSNMR

^{29}Si DE-MAS spectra of the samples hydrated for 28 days are shown and assigned in Fig. 2; the chemical shift values and the areas of the different signals determined by spectral fitting are reported in Tables 3 and 4, respectively.

As extensively described in a recent paper [13], the spectrum of MS100 hydrated for 28 days is constituted by five signals arising from M-S-H silicon species. In particular, the two peaks observed at −78.5 and −81.0 ppm arise from two different Q^1 $\underline{Si}(OMg)(OSi)(OH)_2$ species (Q^{1A} and Q^{1B}), the signal at −85.1 ppm is due to Q^2 $\underline{Si}(OMg)(OSi)_2OH$ sites, and the two peaks centered at −91.8 and −94.0 ppm can be ascribed to two different Q^3 $\underline{Si}(OMg)(OSi)_3$ silicon species (Q^{3A} and Q^{3B}) (Fig. 2 and Table 3). The Q^3 signals have chemical shift values typical of Mg-phyllosilicates, and have been ascribed to serpentine-like (Q^{3A}) and talc-like (Q^{3B}) subnanometre-sized domains in M-S-H [13].

On the other hand, after 28 days of hydration C100 gives rise to the typical spectrum of hydrated Portland cement (Fig. 2 and Table 3). At −71.3 ppm the signal (Q^0) of unreacted belite is evident, while residual alite gives rise to weak and broad signals between −70 and −74 ppm [19]. The peaks at lower chemical shift arise from C-S-H, and in particular from Q^1 (−78.8 ppm) and Q^2 sites (Q^2(I) at −81.7 ppm and Q^2(II) at −84.5 ppm). It is generally accepted that C-S-H is constituted by linear silicate dreierketten chains in which silicate tetrahedra are

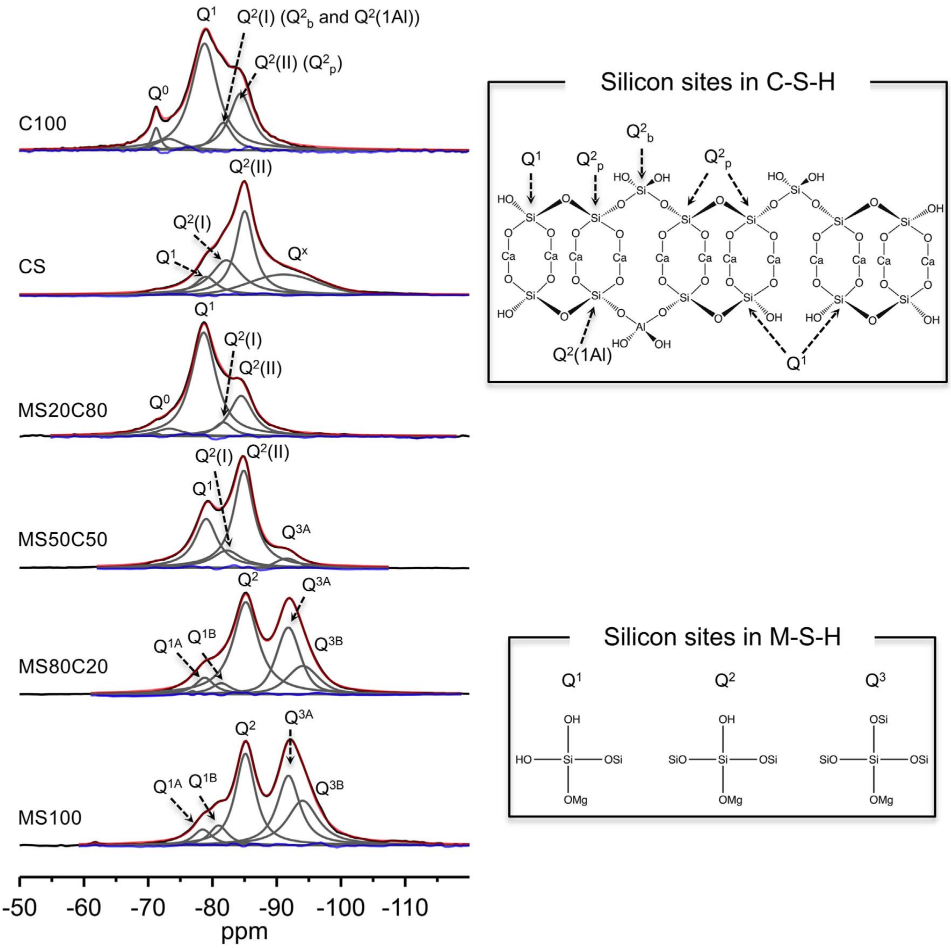

Fig. 2. ^{29}Si DE-MAS spectra of all the samples after 28 days of hydration with spectral fitting and signal assignment. The experimental spectra are the same shown in ref. [16]. Inset showing C-S-H structure has been adapted with permission from ref. [28].

coordinated to Ca^{2+} ions [20,21]. Within this model, the chains are constituted by paired tetrahedra (Q_p^2) linked by bridging (Q_b^2) tetrahedra, with a repeating basic unit of two Q_p^2 and one Q_b^2, while Q^1 species are the silicon nuclei in the terminal tetrahedra (Fig. 2). Moreover, in C-S-H Al^{3+} can substitute Si^{4+}, especially in the bridging sites (Q_b^2), changing the neighboring Q^2 Si species into Q^2(1Al). While it is commonly accepted that Q_p^2 silicon nuclei resonate at about −85 ppm, signals or shoulders appearing between this signal and that of Q^1 have been assigned to Q^2(1Al) and, usually at slightly lower chemical shift, to Q_b^2, and also to not better identified, distorted Q^2 sites [19,22,23,24,25,26,27,28,29,30,31]. Here, the intrinsically scarce spectral resolution and the complexity of the samples, especially of the mixed ones, preclude a detailed analysis of the ^{29}Si spectra in the Q^2 region. Therefore, the spectra were reproduced with the minimum

Table 3
Values of the ^{29}Si chemical shifts (δ in ppm) of silicon sites (Q^i) of the investigated samples after 28 days of hydration, as obtained from spectral fitting. The uncertainty on δ values is ± 0.1 ppm.

Phase	C-S-H					M-S-H				
Silicon site	Q^0	Q^1	Q^2(I)	Q^2(II)	Q^x	Q^{1A}	Q^{1B}	Q^2	Q^{3A}	Q^{3B}
C100	− 70.2 ÷ − 73.3	− 78.8	− 81.7	− 84.5	–	–	–	–	–	–
CS	–	− 79.0	− 82.2	− 85.1	− 91.1	–	–	–	–	–
MS20C80	− 70.2 ÷ − 73.3	− 78.6	− 81.7	− 84.5	–	–	–	–	–	–
MS50C50	–	− 79.1	− 82.3	− 84.9	–	–	–	–	− 91.6	–
MS80C20	–	–	–	–	–	− 78.8	− 81.4	− 85.2	− 91.8	− 94.2
MS100[a]	–	–	–	–	–	− 78.5	− 81.0	− 85.1	− 91.8	− 94.0

[a] The chemical shift values of MS100 differ by 1.1–1.2 ppm with respect to those reported in ref. [13] due to a misset of the chemical shift scale in the previously published paper.

Table 4
Values of the areas (%) underlying the signals (Q^i) observed in ^{29}Si DE-MAS spectra of the investigated samples, after 1, 7 and 28 days of hydration, as obtained from spectral fitting following the criterion described in the text. Maximum errors are 10% on MCL_{min} and MCL_{max} and 2% on RD and CD.

Sample	Hydration time (days)	C-S-H							SiO_2		M-S-H						RD[b](%)
		Q^0	Q^1	Q^2(I)	Q^2(II)	Q^x	MCL_{min}[a]	MCL_{max}[a]	Q^3	Q^4	Q^{1A}	Q^{1B}	Q^2	Q^{3A}	Q^{3B}	CD[a] (%)	
C100	1	53	32	5	10	–	2.9	3.1	–	–	–	–	–	–	–	–	47
	7	39	41	7	13	–	3.0	3.1	–	–	–	–	–	–	–	–	61
	28	11	54	10	25	–	3.3	3.5	–	–	–	–	–	–	–	–	89
CS	1	5	7	21	37	26	19	22	–	4	–	–	–	–	–	–	93
	7	4	8	26	38	22	18	20	–	2	–	–	–	–	–	–	95
	28	0	9	27	40	24	17	20	–	–	–	–	–	–	–	–	100
MS20C80	1	22	57	3	15	–	2.6	2.7	–	3	–	–	–	–	–	–	77
	7	15	65	5	15	–	2.6	2.7	–	–	–	–	–	–	–	–	85
	28	6	64	6	24	–	2.9	3.0	–	–	–	–	–	–	–	–	94
MS50C50	1	1	21	9	53	9	7.9	8.3	–	6	–	–	–	1	–	–	99
	7	–	27	17	49	4	6.8	7.4	–	–	–	–	–	3	–	–	100
	28	–	30	13	53	–	6.5	7.0	–	–	–	–	–	4	–	–	100
MS80C20	1	–	–	–	–	–	–	–	2	3	6	6	52	24	7	73	95
	7	–	–	–	–	–	–	–	–	–	8	6	49	26	11	74	100
	28	–	–	–	–	–	–	–	–	–	6	4	48	27	15	77	100
MS100	1	–	–	–	–	–	–	–	20	43	2	2	15	10	8	79	37
	7	–	–	–	–	–	–	–	15	16	2	4	19	22	22	85	69
	28	–	–	–	–	–	–	–	–	–	4	5	29	29	33	84	100

[a] Calculated using the formulas defined in the text.

[b] Calculated using the formulas defined in the text considering the M-S-H phase for MS100 and MS80C20, and the C-S-H phase for C100, MS20C80, MS50C50, and CS.

number of peaks necessary: Q^2(I) could include both Q^2_b and Q^2(1Al), while Q^2(II) is ascribed to Q^2_p (Table 3). The areas of the signals obtained from the spectral fitting are reported in Table 4. Taking into account the dreierketten chain model for C-S-H, two limit values for the mean chain length (MCL) could be calculated, considering that either the Q^2(I) signal arises only from Q^2(1Al) silicon nuclei ($MCL_{max} = 2(1 + (Q^2(II) + 1.5Q^2(I))/Q^1)$), or no Q^2(1Al) sites are present ($MCL_{min} = 2(1 + (Q^2(II) + Q^2(I))/Q^1)$), where Q^i here and in the other equations indicates the area of the corresponding Q^i signal. These two limit values are very similar (3.5 and 3.3, Table 4) and slightly larger than those reported for Portland cements hydrated for 12 months [20].

As far as the mixed samples are concerned, previous works [14,15,32] indicated that, in samples containing both Mg and Ca, M-S-H and C-S-H gels essentially form as separate phases. Since our previous investigations [16,17] on hydrated MgO/SiO_2/Portland cement mixtures pointed in the same direction, we analyzed the ^{29}Si DE-MAS spectra of mixed samples as sums of the signals of C-S-H and M-S-H.

The spectrum of MS80C20 after 28 days of hydration (Fig. 2 and Table 3) could be well reproduced with the same signals observed for MS100 (except for minor differences in the chemical shifts of Q^{1A} and Q^{1B}), clearly indicating the formation of M-S-H as the predominant phase. However, the intensity of the Q^{3B} signal is reduced with respect to MS100, while that of Q^2 is increased (Table 4). No diagnostic signals of C-S-H are observed, although it is possible that some minor C-S-H signals (for instance those of Q^2 sites) are overwhelmed by M-S-H ones. Assuming the presence of M-S-H only, we could calculate a condensation degree as $CD = 100 \times (3Q^3 + 2Q^2 + Q^1)/3(Q^3 + Q^2 + Q^1)$, finding a value of 77%, lower than that of MS100 (84%) (Table 4).

On the other hand, the spectrum of MS20C80 (Fig. 2) clearly resembles that of C100 and it could be finely reproduced using the same peaks, although with some differences in the relative intensities. In particular, a higher relative intensity of the Q^1 signal is found with respect to C100 and the calculated MCL consequently results slightly smaller (Table 4). Q^3 signals diagnostic for M-S-H are not detected.

The spectrum of MS50C50 (Fig. 2) shows signals ascribable to both C-S-H and M-S-H (Table 3). A weak signal is clearly observed at −91.6 ppm, which can be recognized as that of Q^{3A} sites of M-S-H. However, the most intense signals in the spectrum can be well reproduced with the Q^1 and Q^2 peaks of C-S-H, suggesting the prevalence of this phase. Actually, with respect to C100, the chemical shift values of these two signals are slightly more negative and their relative intensity is substantially reversed, suggesting the formation of a much more condensed C-S-H phase; in fact, MCL limit values of 6.5 and 7 are calculated (Table 4). The ^{29}Si DE-MAS spectrum of CS is similar to that of MS50C50 (Fig. 2), although with a higher Q^2/Q^1 ratio and MCL limit values of 17 and 20 (Table 4). It must be noticed that in the spectrum of CS an additional very broad signal is observed, centered at about −91.1 ppm (indicated as Q^x in Fig. 2, Tables 3 and 4). This signal has been already reported in the literature for similar samples and ascribed to either some species formed by silica hydration and possibly bonded to C-S-H or to disordered C-S-H sites cross-linking different chains [24,29,33].

The comparison of the ^{29}Si DE-MAS spectra of each sample registered after 1, 7 and 28 days of hydration (Fig. 3) and of the corresponding signal intensities (Table 4) provides interesting indications on the kinetics of formation of the C-S-H and M-S-H phases and on the evolution of their structure with time.

Looking at the spectra, it can be observed that SiO_2 (broad signals between −120 and −95 ppm) is almost completely consumed already after 1 day of hydration for MS80C20, while it is still abundant for MS100. The corresponding reaction degree, calculated as $RD = 100 \times (Q^1 + Q^2 + Q^3)/(Q^1 + Q^2 + Q^3 + Q^3_{silica} + Q^4_{silica})$, is 95% and 37% for MS80C20 and MS100, respectively (Table 4). Moreover, RD reaches 100% already after 7 days for MS80C20 and only after 28 days for MS100. For both samples, the M-S-H phase becomes more condensed with the progress of hydration, as indicated by the increasing relative intensity of Q^3 peaks, even if the final condensation degree is slightly lower for MS80C20 (77% vs. 84%, Table 4).

The spectra of C100 (and the data reported in Table 4) clearly show that after 1 day of hydration a considerable amount of reactants (belite and alite), giving rise to Q^0 peaks, is still present. The corresponding reaction degree, which was calculated as $RD = 100 \times (Q^1 + Q^2)/(Q^0 + Q^1 + Q^2)$, is 47% and it increases up to 89% after 28 days of hydration (Table 4). Moreover, with the progress of the hydration reaction MCL of C-S-H slightly increases, in agreement with the literature [20].

MS20C80 shows an evolution with the hydration time similar to that observed for C100, but with a faster consumption of the anhydrous calcium silicate reactants. This effect is even more pronounced for MS50C50 and CS, as shown by the RD values reported in Table 4.

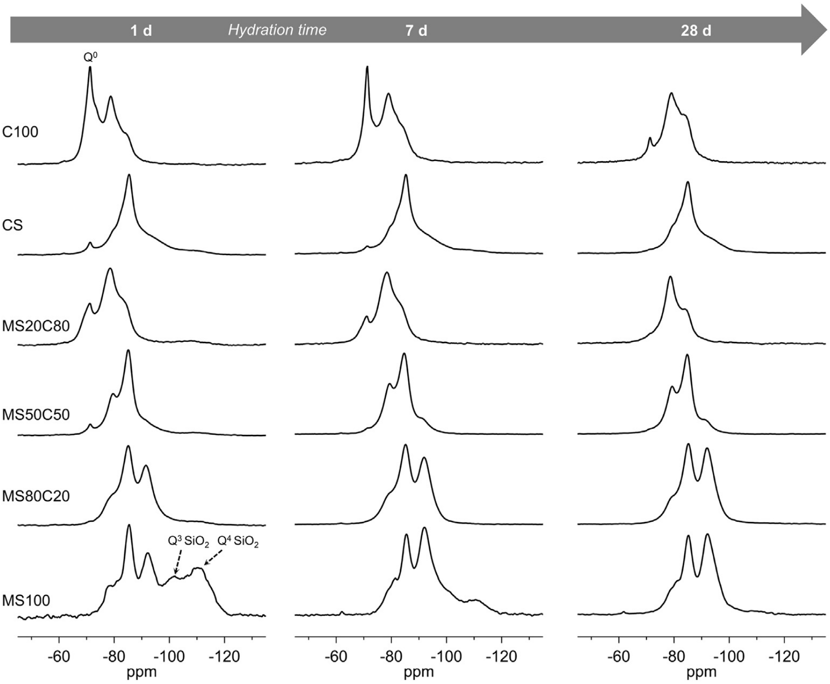

Fig. 3. ^{29}Si DE-MAS spectra of all the samples after 1, 7 and 28 days of hydration. Spectra of MS100 are the same reported in ref. [13].

3.3. ^{27}Al SSNMR

^{27}Al DE-MAS spectra, which provide useful information on the aluminum containing species present [19,25,27,28,29,31,34,35], are reported in Fig. 4 for samples containing Portland cement after 28 days of hydration.

The spectra of C100, MS20C80, MS50C50, and MS80C20 (Fig. 4) show the typical signals already reported for hydrated Portland cement. Two peaks are present at about 13 and 10 ppm: the former can be ascribed to Al(VI) in ettringite ($Ca_6Al_2(SO_4)_3(OH)_{12}\cdot 26H_2O$), the latter to Al(VI) in the AFm species, for instance monosulphoaluminate ($Ca_4Al_2SO_4(OH)_{12}\cdot 6H_2O$), hemicarboaluminate ($Ca_4Al_2(CO_3)_{0.5}(OH)_{13}\cdot 5.5H_2O$), and monocarboaluminate ($Ca_4Al_2(CO_3)(OH)_{12}\cdot 5H_2O$). In the MgO containing samples, hydrotalcite can also contribute to the signal at 10 ppm. With increasing the MgO/SiO_2 content, the intensity of the ettringite peak increases. In the spectrum of C100 an additional broad signal due to Al(VI) species is observed, centered at about −5 ppm, previously ascribed to hydrated products with structures related to $Ca_3Al_2(SiO_4)_3$ and $Ca_3Al_2(OH)_{12}$ ("hydrogrossular") or to aluminate hydrates associated with the presence of iron [19,29]. In the spectra of all samples, the broad signal at about 30 ppm arises from Al(V) species, and it has been previously attributed to five-coordinated Al^{3+} substituting for Ca^{2+} in the inter-layer space of C-S-H [34,36]. Another broad signal is clearly observed between 50 and 80 ppm, arising from Al(IV) sites that can be present in residual reactants (tricalcium aluminate, aluminoferrite, alite and belite) [19], but also as substitutes of tetrahedral silicon in C-S-H and in M-S-H. Indeed, with increasing the MgO/SiO_2 content, an increasing intensity is observed at lower chemical shift, in agreement with data reported in the literature for C-S-H with decreasing Ca/Si ratio [31,37,38] and for magnesium phyllosilicates [39].

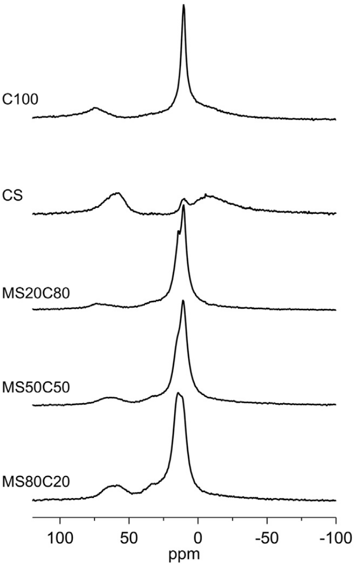

Fig. 4. ^{27}Al DE-MAS spectra of all Portland-containing samples after 28 days of hydration.

The spectrum of CS after 28 days of hydration appears very different from those of the other samples (Fig. 4), showing a weak signal ascribable to AFm, no peak of ettringite, an intense Al(IV) signal and the broad peak centered at about −5 ppm already observed for C100.

For MS80C20 and C100 ^{27}Al DE-MAS spectra were recorded also after 1 and 7 days of hydration (Fig. 5). It can be noticed that, after 1 day of hydration, both samples show signals of AFm (and of hydrotalcite for MS80C20) and that at −5 ppm, while the ettringite peak is visible only for C100. Minor contributions from Al(IV) and Al(V) are also observed, which increase with increasing the hydration time. At 7 days the signal at −5 ppm is not observed anymore for MS80C20, while that of ettringite becomes evident and that of AFm is increased. On the other hand, for C100 the biggest change is the increase of AFm

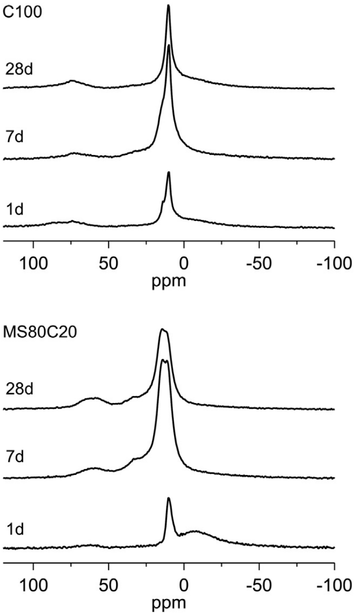

Fig. 5. ^{27}Al DE-MAS spectra of C100 (top) and MS80C20 (bottom) samples after the indicated hydration times (in days).

and ettringite signals. From 7 to 28 days of hydration Al(VI) species decrease for both samples, with the disappearance of the ettringite peak only for C100.

4. Discussion

As already reported [13], hydration of a 1:1 mol:mol mixture of MgO and SiO_2 (MS100) leads to the formation of M-S-H and brucite, the amount of M-S-H phase progressively increasing at the expenses of brucite and SiO_2 with increasing the hydration time. In particular, a detailed analysis of ^{29}Si DE-MAS NMR spectra showed that, after 28 days, silica is completely consumed (RD = 100%) and in the "amorphous" M-S-H phase serpentine-like and talc-like sub-nanometric domains coexist. As expected, hydration of Portland cement (C100) brings to the formation of C-S-H and portlandite. XRD and ^{29}Si SSNMR data, here obtained at different hydration times, clearly indicate that the amount of both phases increases with the progress of hydration, confirming DTA and FTIR results reported in ref. [16].

As far as the mixtures are concerned, the deconvolution of ^{29}Si SSNMR spectra shows that different amounts of C-S-H and M-S-H phases form depending on the composition, as proposed in ref. [16], and allows their relative proportion to be quantified as a function of the hydration time. Moreover, the influence of the mixtures composition on structural features such as MCL for C-S-H and CD for M-S-H could be assessed.

In the case of MS80C20, M-S-H is the main silicate hydrate phase at all hydration times, a minor amount of C-S-H being detected only in X-ray diffractograms. The M-S-H phase forms much more rapidly in MS80C20 than in MS100, as indicated by the almost complete consumption of silica observed in the ^{29}Si DE-MAS spectrum and the small amount of brucite detected by XRD already after 1 day of hydration. These findings are in agreement with the faster kinetics of hydration of MS80C20 highlighted by Free Water Index (FWI) [16] and ^{1}H NMR relaxometry [17] measurements and can be related to the higher pH measured in the supernatant aqueous phase [16]. In fact, although at pH > 10.5 the solubility of Mg^{2+} ions decreases ($pK_a \cong 10.5$ for brucite), high pH values (> 9) favor the formation of silicate anions [40,41], possibly increasing the reactivity of silica with Mg^{2+} ions to give M-S-H. Differences are also observed in the nanostructure of the M-S-H gels formed in MS80C20 and MS100: for MS80C20 the analysis of ^{29}Si DE-MAS spectra highlights a prevalence of serpentine-like domains over talc-like ones, which suggests a higher Mg/Si ratio in the gel, and a lower CD at all the hydration times.

On the other hand, in the case of MS20C80, XRD and ^{29}Si SSNMR data clearly indicate that C-S-H is the main silicate hydrate phase, accompanied by the precipitation of portlandite. The main Mg-containing phase is brucite, in agreement with the very high pH (12.7) measured for this sample [16]. With respect to C100, the formation of C-S-H is faster, as revealed by the higher RD determined from ^{29}Si DE-MAS spectra especially at early hydration times, and in accordance with FWI and ^{1}H NMR relaxometry results [16,17]. Moreover, MCL of the silicate chains is slightly lower than in C100.

As far as MS50C50 is concerned, C-S-H is the main silicate hydrate phase, as shown by XRD and ^{29}Si SSNMR data. No evidence of portlandite ($pK_a \cong 12.5$) precipitation is found, due to the relatively low pH measured for this sample [16] and/or to the occurrence of the pozzolanic reaction between $Ca(OH)_2$ and silica [20]. Furthermore, the presence of a large amount of silica, favoring the pozzolanic reaction [20,31,33,42], can also be related to the faster hydration kinetics and the formation of longer C-S-H chains (RD = 99% and MCL ~ 8 after 1 day of hydration), as revealed by the analysis of the ^{29}Si DE-MAS spectra. Silica particles can also act as nucleating centers for the formation of C-S-H [43]. In the case of CS, which contains Portland cement and silica in the same molar ratio as MS50C50, values of about 18 for MCL of C-S-H chains were determined from ^{29}Si DE-MAS spectra. The smaller MCL value found for MS50C50 can be ascribed to the slightly higher Ca/Si ratio resulting from the partial consumption of silica for the formation of M-S-H [14,32,38].

Besides the Ca and Mg silicate hydrate phases and hydroxides, for all mixtures containing Portland cement, XRD and, especially, ^{27}Al SSNMR spectroscopy allowed Al(VI) containing phases (i.e. ettringite, hydrotalcite and AFm phases) to be detected. Moreover, Al(V) and Al(IV) species incorporated into the C-S-H gel were revealed. For MS50C50 and, especially, MS80C20, both containing M-S-H, the chemical shift of Al(IV) species is compatible with aluminum substitution for tetrahedral silicon in magnesium phyllosilicates [39], but also with substitution of Al^{3+} for silicon atoms in a C-S-H phase with low Ca/Si ratio and large MCL values [38]. For CS, the higher intensity of the Al(IV) signal compared with that observed for the other samples can be ascribed to a larger inclusion of aluminum in the silicate chains of C-S-H. ^{27}Al NMR spectra recorded on C100 and MS80C20 as a function of the hydration time suggest that the presence of MgO/SiO_2 favors the formation of hydrogrossular or an aluminate hydrate associated with iron components at short hydration times and maintains ettringite for longer times.

5. Conclusions

The combination of XRD, ^{29}Si- and ^{27}Al SSNMR spectroscopy measurements provided valuable information on the effects of composition on the amount and structure of the M-S-H and C-S-H binder phases formed during the hydration of MgO/SiO_2 and Portland cement mixtures. In particular, significant differences in the reaction degree of both phases, in the condensation degree of the M-S-H sheets and in the length of the C-S-H chains were found.

The addition of a small amount of Portland cement to the MgO/SiO_2 mixture results in a faster formation of M-S-H, while in mixtures containing larger amounts of Portland cement M-S-H formation is hindered and C-S-H forms faster than in neat Portland cement. These differences in the hydration kinetics can be understood considering the pH value established in the pastes and the presence of fumed silica, previously highlighted.

M-S-H formed in mixtures is characterized by a prevalence of serpentine-like domains compatible with a higher Mg/Si ratio. The structure of the C-S-H gel formed in mixtures is also significantly different from that obtained by hydration of the sole Portland cement. In fact, silica favors the formation of longer silicate chains, due to the occurrence of the pozzolanic reaction. Moreover, the addition of MgO/SiO_2 to Portland cement influences the nature and the relative populations of the aluminum-containing phases.

Funding

This work was supported by Ministero dell'Istruzione, Università e Ricerca scientifica MIUR (FIR2013, grant number: RBFR132WSM) and by Consorzio Interuniversitario per lo Sviluppo dei Sistemi a Grande Interfase, CSGI.

References

[1] R.J. Flatt, N. Roussel, C.R. Cheeseman, Concrete: an eco material that needs to be improved, J. Eur. Ceram. Soc. 32 (2012) 2787–2798.

[2] S.A. Walling, J.L. Provis, Magnesia-based cements: a journey of 150 years, and cements for the future? Chem. Rev. 116 (2016) 4170–4204.

[3] A. Dauzeres, P. Le Bescop, P. Sardini, C. Cau Dit Coumes, Physico-chemical investigation of clayey/cement-based materials interaction in the context of geological waste disposal: experimental approach and results, Cem. Concr. Res. 40 (2010) 1327–1340.

[4] F.P. Glasser, M. Atkins, Cements in radioactive waste disposal, MRS Bull. 19 (1994) 33–38.

[5] G. Kosakowski, U. Berner, The evolution of clay rock/cement interfaces in a cementitious repository for low- and intermediate level radioactive waste, Phys. Chem. Earth 64 (2013) 65–86.

[6] A. Dauzeres, G. Achiedo, D. Nied, E. Bernard, S. Alahrache, B. Lothenbach, Magnesium perturbation in low-pH concretes placed in clayey environment—solid characterizations and modeling, Cem. Concr. Res. 79 (2016) 137–150.

[7] J.L. Garcia Calvo, A. Hidalgo, C. Alonso, L. Fernández Luco, Development of low-pH cementitious materials for HLRW repositories: resistance against ground waters aggression, Cem. Concr. Res. 40 (2010) 1290–1297.

[8] T. Zhang, C.R. Cheeseman, L.J. Vandeperre, Development of low pH cement systems forming magnesium silicate hydrate (M-S-H), Cem. Concr. Res. 41 (2011) 439–442.

[9] T. Zhang, L.J. Vandeperre, C.R. Cheeseman, Development of Magnesium Silicate Hydrate Cement System for Nuclear Waste Encapsulation, NUWCEM, Avignon, 2011, pp. 582–591.

[10] S.A. Walling, H. Kinoshita, S.A. Bernal, N.C. Collier, J.L. Provis, Structure and properties of binder gels formed in the system $Mg(OH)_2$–SiO_2–H_2O for immobilization of Magnox sludge, Dalton Trans. 44 (2015) 8126–8137.

[11] C. Roosz, S. Grangeon, P. Blanc, V. Montouillout, B. Lothenbach, P. Henocq, E. Giffaut, P. Vieillard, S. Gaboreau, Crystal structure of magnesium silicate hydrates (M-S-H): the relation with 2:1 Mg–Si phyllosilicates, Cem. Concr. Res. 73 (2015) 228–237.

[12] D. Nied, K. Enemark-Rasmussen, E. L'Hopital, J. Skibsted, B. Lothenbach, Properties of magnesium silicate hydrates (M-S-H), Cem. Concr. Res. 79 (2016) 323–332.

[13] M. Tonelli, F. Martini, L. Calucci, E. Fratini, M. Geppi, F. Ridi, S. Borsacchi, P. Baglioni, Structural characterization of magnesium silicate hydrate: towards the design of eco-sustainable cements, Dalton Trans. 45 (2016) 3294–3304.

[14] B. Lothenbach, D. Nied, E. L'Hôpital, G. Achiedo, A. Dauzères, Magnesium and calcium silicate hydrates, Cem. Concr. Res. 77 (2015) 60–68.

[15] W.-S. Chiang, G. Ferraro, E. Fratini, F. Ridi, Y.-Q. Yeh, U.S. Jeng, S.-H. Chen, P. Baglioni, Multiscale structure of calcium-and magnesium-silicate-hydrate gels, J. Mater. Chem. A 2 (2014) 12991–12998.

[16] M. Tonelli, F. Martini, L. Calucci, M. Geppi, S. Borsacchi, F. Ridi, Traditional Portland cement and MgO-based cement: a promising combination? Phys. Chem. Earth 99 (2017) 158–167.

[17] F. Martini, L. Calucci, M. Geppi, M. Tonelli, F. Ridi, S. Borsacchi, Monitoring the hydration of MgO-based cement and its mixtures with Portland cement by ^{1}H NMR relaxometry, Micropor. Mesopor. Mater. (2017), http://dx.doi.org/10.1016/j.micromeso.2017.05.031.

[18] D.R.M. Brew, F.P. Glasser, Synthesis and characterization of magnesium silicate hydrate gels, Cem. Concr. Res. 35 (2005) 85–98.

[19] A. Rawal, B.J. Smith, G.L. Athens, C.L. Edwards, L. Roberts, V. Gupta, B.F. Chmelka, Molecular silicate and aluminate species in anhydrous and hydrated cements, J. Am. Chem. Soc. 132 (2010) 7321–7337.

[20] I.G. Richardson, Tobermorite/jennite- and tobermorite/calcium hydroxide-based models for the structure of C-S-H: applicability to hardened pastes of tricalcium silicate, β-dicalcium silicate, Portland cement, and blends of Portland cement with blast-furnace slag, metakaolin, or silica fume, Cem. Concr. Res. 34 (2004) 1733–1777.

[21] I.G. Richardson, The calcium silicate hydrates, Cem. Concr. Res. 38 (2008) 137–158.

[22] A.R. Brough, C.M. Dobson, I.G. Richardson, G.W. Groves, Application of selective ^{29}Si isotopic enrichment to studies of the structure of calcium silicate hydrate (C-S-H) gels, J. Am. Ceram. Soc. 77 (1994) 593–596.

[23] H. Zanni, R. Rassem-Bertolo, S. Masse, L. Fernandez, P. Nieto, B. Bresson, A spectroscopic NMR investigation of the calcium silicate hydrates present in cement and concrete, Magn. Reson. Imaging 14 (1996) 827–831.

[24] X. Cong, R.J. Kirkpatrick, ^{29}Si MAS NMR study of the structure of calcium silicate hydrate, Adv. Cem. Based Mater. 3 (1996) 144–156.

[25] P. Faucon, T. Charpentier, D. Bertrandie, A. Nonat, J. Virlet, J.C. Petit, Characterization of calcium aluminate hydrates and related hydrates of cement pastes by ^{27}Al MQ-MAS NMR, Inorg. Chem. 37 (1998) 3726–3733.

[26] G. Sun, A.R. Brough, J.F. Young, Si NMR study of the hydration of Ca_3SiO_5 and β-Ca_2SiO_4 in the presence of silica fume, J. Am. Ceram. Soc. 82 (1999) 3225–3230.

[27] M.D. Andersen, H.J. Jakobsen, J. Skibsted, Incorporation of aluminum in the calcium silicate hydrate (C-S-H) of hydrated Portland cements: a high-field ^{27}Al and ^{29}Si MAS NMR investigation, Inorg. Chem. 42 (2003) 2280–2287.

[28] M.D. Andersen, H.J. Jakobsen, J. Skibsted, Characterization of white Portland cement hydration and the C-S-H structure in the presence of sodium aluminate by ^{27}Al and ^{29}Si MAS NMR spectroscopy, Cem. Concr. Res. 34 (2004) 857–868.

[29] G. Le Saoût, E. Lécolier, A. Rivereau, H. Zanni, Chemical structure of cement aged at normal and elevated temperatures and pressures, part I: class G oilwell cement, Cem. Concr. Res. 36 (2006) 71–78.

[30] G. Le Saoût, E. Lécolier, A. Rivereau, H. Zanni, Chemical structure of cement aged at normal and elevated temperatures and pressures, part II: low permeability class G oilwell cement, Cem. Concr. Res. 36 (2006) 428–433.

[31] E. L'Hôpital, B. Lothenbach, G. Le Saout, D. Kulik, K. Scrivener, Incorporation of aluminum in calcium-silicate-hydrates, Cem. Concr. Res. 75 (2015) 91–103.

[32] E. Bernard, B. Lothenbach, F. Le Goff, I. Pochard, A. Dauzères, Effect of magnesium on calcium silicate hydrate (C-S-H), Cem. Concr. Res. 97 (2017) 61–72.

[33] A.R. Brough, C.M. Dobson, I.G. Richardson, G.W. Groves, A study of the pozzolanic reaction by solid-state ^{29}Si nuclear magnetic resonance using selective isotopic enrichment, J. Mater. Sci. 30 (1995) 1671–1678.

[34] M.D. Andersen, H.J. Jakobsen, J. Skibsted, A new aluminum-hydrate species in hydrated Portland cements characterized by ^{27}Al and ^{29}Si MAS NMR spectroscopy, Cem. Concr. Res. 36 (2006) 3–17.

[35] X. Pardal, F. Brunet, T. Charpentier, I. Pochard, A. Nonat, ^{27}Al and ^{29} Si solid-state NMR characterization of calcium-aluminosilicate-hydrate, Inorg. Chem. 51 (2012) 1827–1836.

[36] P. Faucon, A. Delagrave, C. Richet, J.M. Marchand, H. Zanni, Aluminum incorporation in calcium silicate hydrates (C-S-H) depending on their Ca/Si ratio, J. Phys. Chem. B 103 (1999) 7796–7802.

[37] G.K. Sun, J.F. Young, R.J. Kirkpatrick, The role of Al in C–S–H: NMR, XRD, and compositional results for precipitated samples, Cem. Concr. Res. 36 (2006) 18–29.

[38] E. L'Hôpital, B. Lothenbach, D.A. Kulik, K. Scrivener, Influence of calcium to silica ratio on aluminum uptake in calcium silicate hydrate, Cem. Concr. Res. 85 (2016) 111–121.

[39] R.A. Kinsey, R.J. Kirkpatrick, J. Hower, K.A. Smith, E. Oldfield, High resolution aluminum-27 and silicon-29 nuclear magnetic resonance spectroscopic study of layer silicates, including clay minerals, Am. Mineral. 70 (1985) 537–548.

[40] Z. Li, T. Zhang, J. Hu, Y. Tang, Y. Niu, J. Wei, Q. Yu, Characterization of reaction products and reaction process of MgO–SiO_2–H_2O system at room temperature, Constr. Build. Mater. 61 (2014) 252–259.

[41] F. Jin, A. Al-Tabbaa, Strength and hydration products of reactive MgO–silica pastes, Cem. Concr. Compos. 52 (2014) 27–33.

[42] J. Haas, A. Nonat, From C–S–H to C–A–S–H: experimental study and thermodynamic modeling, Cem. Concr. Res. 68 (2015) 124–138.

[43] L.P. Singh, A. Goel, S.H. Bhattacharyya, G. Mishra, Quantification of hydration products in cementitious materials incoporating silica nanoparticles, Front. Struct. Civ. Eng. 10 (2016) 162–167.

Paper III

Physics and Chemistry of the Earth 99 (2017) 158–167

Contents lists available at ScienceDirect

Physics and Chemistry of the Earth

journal homepage: www.elsevier.com/locate/pce

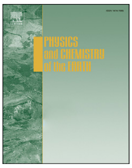

Traditional Portland cement and MgO-based cement: a promising combination?

Monica Tonelli [a], Francesca Martini [b], Lucia Calucci [c], Marco Geppi [b, c], Silvia Borsacchi [c], Francesca Ridi [a, *]

[a] *Department of Chemistry "Ugo Schiff" & CSGI, University of Florence, Sesto Fiorentino (FI), 50019, Italy*
[b] *Department of Chemistry and Industrial Chemistry, University of Pisa, Pisa 56124, Italy*
[c] *Istituto di Chimica dei Composti OrganoMetallici, Consiglio Nazionale delle Ricerche – CNR S.S. di Pisa, Pisa 56124, Italy*

ARTICLE INFO

Article history:
Received 29 July 2016
Received in revised form
24 January 2017
Accepted 30 January 2017
Available online 2 February 2017

Keywords:
Radioactive waste encapsulation
Magnesium silicate hydrate
Calcium silicate hydrate
Eco-sustainable cement
Portland cement

ABSTRACT

MgO/SiO_2 cements are materials potentially very useful for radioactive waste disposal, but knowledge about their physico-chemical properties is still lacking. In this paper we investigated the hydration kinetics of cementitious formulations prepared by mixing MgO/SiO_2 and Portland cement in different proportions and the structural properties of the hydrated phases formed in the first month of hydration. In particular, the hydration kinetics was investigated by measuring the free water index on pastes by means of differential scanning calorimetry, while the structural characterization was carried out by combining thermal (DTA), diffractometric (XRD), and spectroscopic (FTIR, ^{29}Si solid state NMR) techniques. It was found that calcium silicate hydrate (C-S-H) and magnesium silicate hydrate (M-S-H) gels mainly form as separate phases, their relative amount and structural characteristics depending on the composition of the hydrated mixture. Moreover, the composition of the mixtures strongly affects the kinetics of hydration and the pH of the aqueous phase in contact with the cementitious materials. The results here reported show that suitable mixtures of Portland cement and MgO/SiO_2 could be used to modify the properties of hydrated phases with potential application in the storage of nuclear waste in clayey disposal.

1. Introduction

Over the last decades the use of cement became crucial in radioactive waste disposal, thanks to its capability of immobilizing inorganic species arising from liquid, solid or heterogeneous matrices. Porous cementitious grouts are ideal backfills for the disposal of low- and intermediate-level waste in vaults, as they can buffer the pH of pore water over an extended period of time (Norris et al., 2014). However, chemical gradients possibly form at the interface between cement and the natural environment, which may cause significant changes in mineralogy and in the chemical conditions at the interface. In particular, neutral pH and high salt concentration in the interstitial water of clayey rocks may alter the cementitious matrix, producing carbonation, ettringite precipitation or leaching phenomena. In turn, when traditional Portland cement is used, the alkaline pH of the pore solution is responsible for the degradation of the clay and the modification of its porosity (Bartier et al., 2013; Dauzères et al., 2010; Gaboreau et al., 2011; Gaucher and Blanc, 2006; Jenni et al., 2014).

An enhancement of the compatibility between cement and clayey rocks has been observed for newly introduced low-pH cementitious binders, developed by mixing Portland cement with silica fume, fly ashes, or other pozzolanic materials that react with portlandite. However, leaching and carbonation phenomena still occur in the calcium silicate hydrate (C-S-H) binder phase formed with these formulations, resulting in a decrease in strength development. At the same time, magnesium enrichment is reported in the decalcified areas, with formation of the magnesium silicate hydrate (M-S-H) phase, a colloidal gel analogous to C-S-H (Dauzères et al., 2014, 2016; García Calvo et al., 2010; Jenni et al., 2014). Recently, a cementitious formulation based on magnesium, in the place of calcium, has been developed by taking advantage of the hydration reaction of light-burned periclase (MgO) in the presence of silica: the hydration of MgO produces brucite ($Mg(OH)_2$), which promptly reacts with SiO_2 to form M-S-H (Zhang

---

* Corresponding author.
E-mail address: francesca.ridi@unifi.it (F. Ridi).

http://dx.doi.org/10.1016/j.pce.2017.01.011

et al., 2012). M-S-H also forms by hydrating $Mg(OH)_2$ in the presence of a silica source (Walling et al., 2015). The presence of brucite buffers pH to a value of about 10, which decreases to 9 when $Mg(OH)_2$ is consumed with formation of M-S-H. This pH value, much lower than that obtained by hydration of Portland cement, is more suitable for the stabilization of nuclear wastes. Therefore, Portland-based pastes containing MgO are potentially useful to enhance the compatibility of clayey rocks with the cementitious matrix in waste immobilization. In particular, for wastes coming from Magnox reactors a low pH also favours the passivation of both Mg and Al alloys (Walling et al., 2015).

In the last years, the properties of M-S-H have been investigated (Nied et al., 2016; Roosz et al., 2015; Tonelli et al., 2016), but further work is needed to fully clarify its features. In particular, in the perspective of preparing low-pH cementitious formulations for nuclear waste immobilization, it is important to investigate the hydration process and the structural properties of the hydrated phases of MgO-based formulations also containing Portland cement. Some work has been done in this field, especially addressing the possible intercalation of Mg^{2+} in C-S-H (Fernandez et al., 2008; Pytel and Malolepszy, 2000; Shrivastava et al., 1991) and the interaction between M-S-H and C-S-H (Chiang et al., 2014, 2013; Lothenbach et al., 2015).

In this paper we report a study of the hydration kinetics and the structural properties of the hydrated phases of cementitious formulations containing different amounts of MgO/SiO_2 and Portland cement. In particular, the hydration kinetics was studied by analysing the trend of free water index (FWI), measured on pastes by means of differential scanning calorimetry (DSC), as a function of the hydration time (up to 1 month). The structural characterization of the hydrated phases at different hydration times was performed on freeze-dried samples by a combination of calorimetric (DTA), diffractometric (XRD), and spectroscopic (FTIR, ^{29}Si Solid State NMR (SSNMR)) techniques. A sample containing Portland cement and SiO_2, but not MgO, was also investigated in order to better evaluate the effect of the pozzolanic reaction between silica and portlandite on the properties of the hydrated phases (Richardson, 2004; Brough et al., 1995; Haas and Nonat, 2015).

2. Experimental

2.1. Materials

CEM I Portland cement was obtained from Italcementi (Bergamo, Italy). Magnesium oxide (MgO) and fumed silica (SiO_2) were supplied by Sigma-Aldrich. The main characteristics of these raw materials are summarized in Table 1.

Table 1
Chemical composition (%) and physical properties of Portland cement, MgO and SiO_2.

	Portland cement	MgO	SiO_2
Chemical composition			
SiO_2	19.81		≥99
Al_2O_3	5.41		
Fe_2O_3	3.96		
CaO	66.60		
MgO	2.50	≥99	
SO_3	1.25		
Na_2O	0.11		
K_2O	0.17		
SrO	0.04		
Mn_2O_3	0.02		
P_2O_5	0.04		
TiO_2	0.09		
BET surface area (m^2/g)	1.5 ± 0.1	121 ± 5	395 ± 25
Mean particle size (μm)	20	44	5
Reactivity (s)		80	

2.2. Preparation of the samples

The composition of the investigated samples is reported in Table 2 together with the acronyms used throughout the paper. When both present, MgO and SiO_2 were mixed in a 1:1 molar ratio. All the pastes were prepared by manually mixing 4 g of solids with 8 g of milliQ water (purified by a Millipore Organex system, $R \geq 18$ MΩ cm), i.e. at a water-to-solid weight ratio (w/s) of 2, the minimal ratio needed to obtain a workable paste for the pure MgO/SiO_2 sample. Each paste was stored at 20 °C in a polyethylene bag to avoid air contact and prevent carbonation.

For DTA, FTIR, XRD, SEM, and ^{29}Si SSNMR measurements, lyophilized samples were prepared. To this aim, about 1 g of paste was withdrawn after defined periods from preparation (1, 3, 7 and/or 28 days, depending on the measurement) and freeze-dried (50 mTorr, 24 h) to stop the hydration reaction.

2.3. Methods

The reactivity of periclase was measured according to the citric acid reactivity test (Van der Merwe et al., 2004).

The BET surface area of the powders was measured by means of a Coulter SA 3100 analyser, using nitrogen as adsorptive gas.

pH measurements were conducted with a BASIC 20 CRISON pH-meter, according to the method previously described by Zhang et al. (2011). In a polyethylene flask 1 g of mixed solid and 10 g of distilled water were added. The container was sealed and constantly shaken in an orbital stirrer. At different time intervals, the solid particles were allowed to settle and the pH of the supernatant was measured.

Thermal analyses (DTA) were performed by means of a STD Q600 instrument (TA Instruments, New Castle, USA), operating from room temperature to 1000 °C at 10 °C/min in nitrogen flux.

Fourier transform infrared (FTIR) spectra were acquired with a BioRad FTS-40 spectrometer (Biorad, Cambridge, MA, USA), between 400 and 4000 cm^{-1}, with a resolution of 2 cm^{-1}, accumulating 32 scans. For the analysis, about 1 mg of each sample was homogenized with 100 mg of KBr and pressed to obtain a pellet.

X-ray diffractograms were recorded with a XRD Bruker New D8 Da Vinci instrument operating at 40 kV and 40 mA, with a Cu source (emitting radiation $\lambda = 1.54$ Å). Data were collected in the 5°–70° 2θ range, with an increment of 0.05°.

^{29}Si SSNMR spectra were recorded on a Varian InfinityPlus 400 spectrometer working at ^{1}H and ^{29}Si Larmor frequencies of 400.35 and 79.48 MHz, respectively. ^{29}Si Direct Excitation Magic Angle Spinning (DE–MAS) spectra were recorded under ^{1}H high power decoupling, using a 7.5 mm probehead, with a ^{29}Si 90° pulse duration of 6 μs and a spinning frequency of 5.5 kHz; approximately 8000 transients were accumulated. For all the samples (except MS100) a recycle delay of 10 s between two consecutive transients was used; for MS100 the recycle delay was 20 s. The ^{29}Si chemical

Table 2
Composition of the samples as wt% of Portland cement (C), MgO (M) and SiO_2 (S).

Sample	C (wt%)	M (wt%)	S (wt%)	w/s
C100	100	0	0	2
MS20C80	80	8	12	2
MS50C50	50	20	30	2
MS80C20	20	32	48	2
MS100	0	40	60	2
CS	62.5	0	37.5	2

shift scale was referred to 3 (trimethylsilyl)-1-propanesulfonic acid sodium salt as secondary reference at 1.46 ppm, and to TMS as primary one.

For the DSC experiments carried out to determine the Free Water Index (FWI), about 50 mg of each freshly mixed paste was transferred into a steel pan (diameter 7.4 mm, capacity 60 μL) and sealed with a cover equipped with a neoprene O-ring to avoid water leaking. The pan was maintained at 20 °C in a thermostatic bath. Samples were periodically analysed in a DSC Q2000 calorimeter from TA Instruments (New Castle, USA) using the following temperature program: equilibrate to −60 °C, isothermal for 4 min, ramp from −60 °C to +50 °C at 5 °C/min. The Free Water Index was, thus, determined from the integral of the melting peak of water.

3. Results and discussion

3.1. pH measurements

Fig. 1 shows the variation of pH of the supernatant solution over the different cementitious mixtures during a period of 28 days. The pH *vs.* time trends of C100 and MS20C80 were almost the same. pH slightly increased from 12.4 to 12.7 in the first day and then it remained nearly constant, as it was buffered by portlandite ($Ca(OH)_2$, $pK_a \approx 12.5$) precipitation. MS20C80 was the only mixed sample whose pH was sufficiently high to allow the precipitation of both portlandite and brucite ($pK_a \approx 10.5$). It has been recently highlighted that at pH > 9 silica is strongly ionized, thus becoming much more soluble (Jin and Al-Tabbaa, 2014) and favouring M-S-H formation. On the contrary, at pH > 10.5 the solubility of Mg^{2+} decreases (Li et al., 2014), thus hindering M-S-H formation. The latter is the case of MS20C80, as also shown by other results (vide infra). By increasing the MgO/SiO_2 content in the mixture, pH decreased and the precipitation of $Ca(OH)_2$ was hindered. MS50C50 had an initial pH of 12.4, which, after three days, decreased to 11.9, a value that favoured the precipitation of brucite. pH of MS80C20 decreased from 11.8 to 11.0 after one day and then it slightly increased in the next days reaching a final value of 11.6. pH of MS100 was ~11 immediately after mixing. It decreased in the first three days of hydration and then it stabilized at ~9, as $Mg(OH)_2$ was consumed by the reaction with silica to form M-S-H. According to the literature, this is the optimal pH to promote M-S-H formation, at least in the first month of hydration (Li et al., 2014). pH of the CS sample was 12.2 immediately after mixing, due to the initial precipitation of portlandite. Afterwards, pH strongly decreased in the first three days and then it stabilized at ~11 due to the consumption of $Ca(OH)_2$ in the pozzolanic reaction with silica (Richardson, 2004). It is worth noting that MS50C50, although having the same Portland/SiO_2 ratio as CS, showed a higher pH value (11.9). In fact, in MS50C50 SiO_2 also reacted with MgO to form M-S-H (vide infra), so that part of CaO contained in Portland remained unreacted and increased pH through the equilibrium $CaO + H_2O \longrightarrow Ca^{2+} + 2OH^-$. This effect is well known and reported in the literature for MgO formulations containing CaO impurities (Zhang et al., 2011).

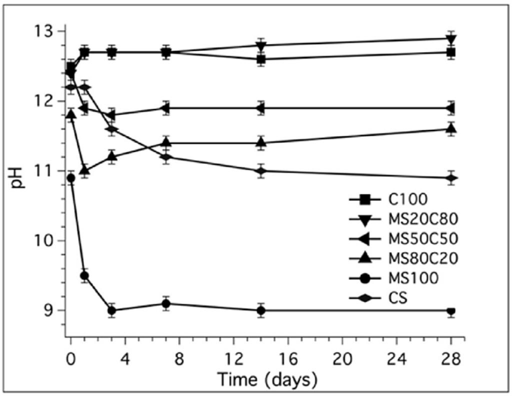

Fig. 1. pH values (±0.1) of all the investigated samples as a function of hydration time.

3.2. Thermal analyses

Fig. 2 shows DTA thermograms registered on the investigated samples after 1, 3, 7, and 28 days of hydration. In the thermograms of C100 (Fig. 2A) two endothermic signals were present: one at ~100 °C, due to the decomposition of C-S-H and other aluminate and sulphate hydrated phases, and the other at 440 °C, due to the decomposition of $Ca(OH)_2$. The intensity of both these peaks slightly increased with increasing the hydration time. The thermograms of MS20C80 (Fig. 2B) showed three endothermic peaks: one at ~100 °C, very similar to that of C100, and two at 370 °C and 440 °C, due to brucite and portlandite decomposition, respectively. These features suggest that in this sample the main hydrated phase was C-S-H, while the principal Mg-containing phase was brucite. Indeed, for this sample pH was sufficiently high to allow the precipitation of both Ca and Mg hydroxides, whose amount remained nearly constant with time. For MS100 (Fig. 2E), MS80C20 (Fig. 2D), and MS50C50 (Fig. 2C) three peaks could be observed in the thermograms: two endothermic peaks at about 100 °C and 400 °C, which correspond to the weight losses from M-S-H (possibly together with C-S-H) and $Mg(OH)_2$, respectively, and an exothermic peak between 800 and 900 °C (see also Fig. 3), associated to a solid phase transition. For MS100 the peak at ~100 °C became more intense and narrow with increasing the hydration time, indicating the progressive precipitation of M-S-H. At the same time, the intensity of the signal at ~400 °C decreased, as brucite reacted with silica to form the binder gel phase.

For MS100, the exothermic peak(s) at ~850 °C could be assigned, according to the literature, to a solid phase transition of M-S-H (Tonelli et al., 2016; Walling et al., 2015; Zhang et al., 2014). In particular, a ^{29}Si SSNMR study pointed out that, upon thermal treatment, recrystallization of “chrysotile-like” and “talc-like” subnanometric domains of M-S-H gives rise to a mixture of enstatite ($MgSiO_3$) and forsterite (Mg_2SiO_4) (Tonelli et al., 2016). The thermograms of MS80C20 were similar to those of MS100, suggesting that M-S-H mainly formed during the hydration of this mixture, although small amounts of Portland cement could influence the nanometric structure of M-S-H. In the thermograms of MS50C50, a single exothermic signal was present at ~850 °C after one day of hydration, while two broad signals at about 840 °C and 860 °C could be observed after 3 days of hydration (Fig. 3C). The observed features could be ascribed to a different nanometric structure of the M-S-H phase, but also to the recrystallization processes of C-S-H, since both hydrated phases formed in this sample, as shown in the following. In fact, it has been reported that tobermorite, constituting C-S-H, converts to beta-wollanstonite at 850–860 °C (Klimesch and Ray, 1999).

In the thermograms of CS (Fig. 2F), three peaks were present: an endothermic peak at about 100 °C, due to C-S-H weight loss, and two exothermic peaks above 800 °C, due to recrystallization events similar to those observed for MS50C50 (see Fig. 3F and C), but occurring at slightly different temperatures (~800 °C and ~860 °C). The peak due to portlandite decomposition was not observed for this sample, most probably because portlandite reacted with silica to form highly condensed C-S-H, in agreement with the pH measurements.

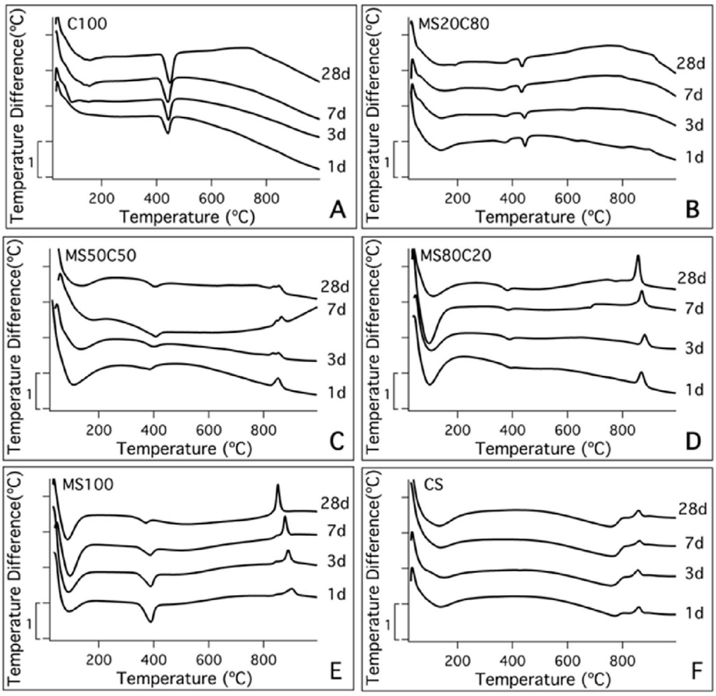

Fig. 2. DTA curves at different hydration times of samples: C100 (A), MS20C80 (B), MS50C50 (C), MS80C20 (D), MS100 (E), CS (F). Curves have been offset for the sake of clarity.

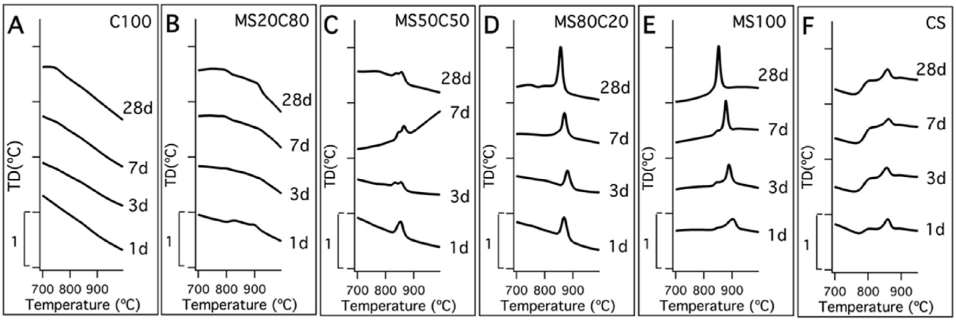

Fig. 3. Expansion of the DTA curves in Fig. 2 for samples: C100 (A), MS20C80 (B), MS50C50 (C), MS80C20 (D), MS100 (E), CS (F). Curves have been offset for the sake of clarity.

3.3. *FTIR*

Fig. 4 shows the IR spectra of the investigated samples at different hydration times. The spectra of all samples exhibited a broad band in the 3200-3600 cm^{-1} region and a narrower band at about 1640 cm^{-1}, due, respectively, to the stretching and bending of the OH groups of the binder phases. In the spectra of C100 (Fig. 4A), the $Ca(OH)_2$ characteristic peak at about 3642 cm^{-1} was present, its intensity slightly increasing with time. In the spectra of MS20C80 (Fig. 4B), the characteristic peaks of $Mg(OH)_2$ and $Ca(OH)_2$ due to O-H stretching could be hardly recognized, probably because they were overwhelmed by the broad O-H stretching band of the binder phases, present in a much larger amount. The spectra of MS50C50 (Fig. 4C) and MS80C20 (4D) showed a small peak at about 3690 cm^{-1}, attributed to $Mg(OH)_2$, the intensity of which remained approximately constant with time. For MS100, $Mg(OH)_2$ gave rise to a sharp peak at 3693 cm^{-1} (Fig. 4E), which decreased in intensity with increasing the hydration time, as brucite reacted with silica to form M-S-H.

For all the formulations many peaks, typical of Si-O vibrations, could be recognized in the 800–1300 cm^{-1} spectral range; an expansion of this region is shown in Fig. 5 for samples hydrated for 28 days. The spectrum of C100 at 1 day of hydration (Fig. 4A) resembles that of the anhydrous Portland powder (Fig. 4F). The intensity of the signal at 1110 cm^{-1}, ascribed to the stretching of SiO_4^{4-} in alite and belite, decreased with increasing the hydration time,

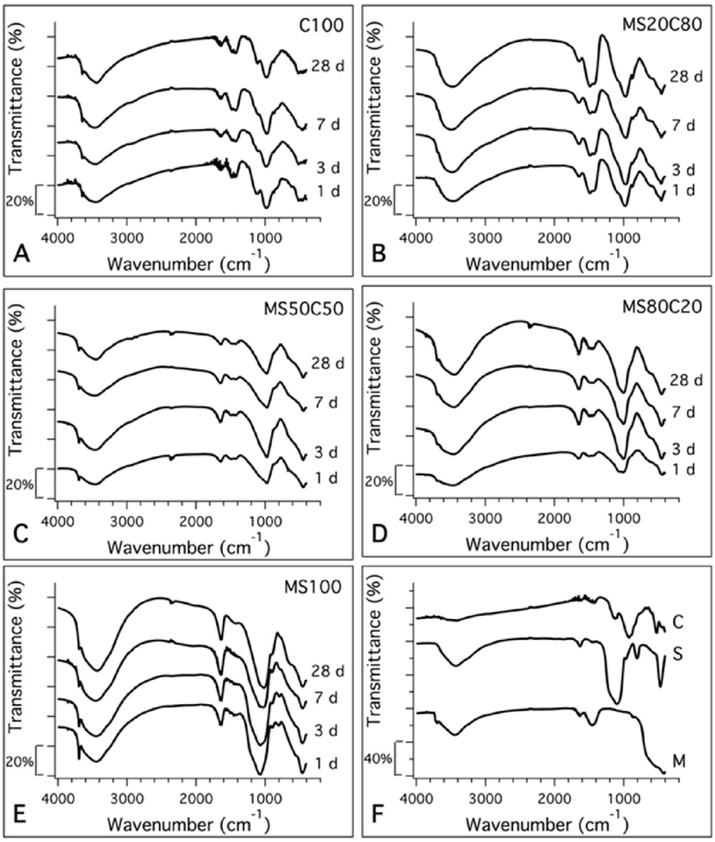

Fig. 4. FTIR spectra of C100 (A), MS20C80 (B), MS50C50 (C), MS80C20 (D), MS100 (E), and reactants (F). Portland cement, MgO, and SiO_2 spectra are indicated with labels C, M, and S, respectively. Curves have been offset for the sake of clarity.

while that of the peak at 980 cm^{-1}, due to the stretching of Q^2 SiO_4^{4-} in C-S-H, increased as a consequence of the progressive polymerization of the silicate chains. The spectra of MS20C80 were similar to those of C100 between 800 and 1300 cm^{-1} (Fig. 5), suggesting that the precipitation of C-S-H was the main reaction for this formulation. Furthermore, the spectra of MS100 and MS80C20 were very similar to each other in the same region (Fig. 5). For these samples, M-S-H was the main hydrated phase, as indicated by the presence of a band at ~1070 cm^{-1}, ascribable to Si-O vibrations, and by the decrease of the intensity of the silica peak at 800 cm^{-1} (see Fig. 4F) with increasing the hydration time. Moreover, the signals at ~1010 and 900 cm^{-1} in the spectra of MS100 and MS80C20 were in good agreement with the vibrational modes reported for talc (1020 and 890 cm^{-1}) (Lothenbach et al., 2015). MS50C50, instead, showed peculiar spectral features and, in particular, the broad band at ~1000 cm^{-1} could not be unequivocally ascribed to a specific hydrated phase.

For MS20C80 and C100, the bands in the 500-700 cm^{-1} range could not be unequivocally assigned because of the heterogeneity of the phases present. For all the samples containing MgO, a peak at 650 cm^{-1} was observed, attributed to a vibration similar to the libration of the Mg_3OH unit in magnesium phyllosilicates (Walling et al., 2015). Moreover, the peaks at about 560 and 460 cm^{-1} were assigned to MgO vibrations by comparison with the spectrum of pure MgO (Fig. 4F).

3.4. XRD

Fig. 6 shows the X-ray diffractograms of the investigated samples after 28 days of hydration. In the diffractogram of C100, the most intense peaks were due to portlandite. It was also possible to recognize the diffraction peaks of many different phases commonly present in hydrated Portland cement, such as hemicarboaluminate, monocarboaluminate, monosulphoaluminate, and ettringite. In the 29-33° range, peaks attributed to residual anhydrous phases of Portland cement were observed, together with a broad peak at 29.3° ascribed to C-S-H (Lothenbach et al., 2015). The diffractograms of MS20C80 and MS50C50 resembled that of C100. For MS50C50, the absence of intense portlandite peaks was due to its consumption, by reaction with silica, to form C-S-H, as anticipated in the previous sections. Moreover, the broad peaks expected for M-S-H at ~23°, 35° and 59° could not be easily distinguished in the diffractogram, indicating that this phase did not form in large amount. The diffractograms of both MS20C80 and MS50C50 showed an intense peak at 29.3°, typical of highly condensed C-S-H. In agreement with ^{29}Si NMR data (see next section), peaks attributable to anhydrous phases were not detected for these samples. In the diffractogram of CS, the signal at 29.3° was the most intense, indicating that the formation of highly condensed C-S-H was favoured by the presence of silica.

In the diffractograms of MS100 and MS80C20, the broad peaks

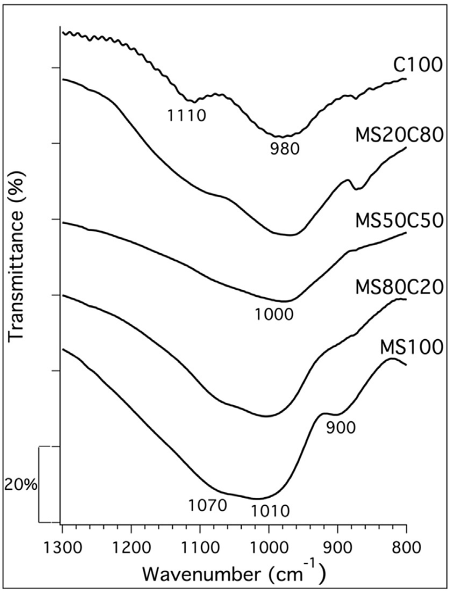

Fig. 5. Expansion of the FTIR spectra of C100, MS20C80, MS50C50, MS80C20, and MS100 at 28 days of hydration in the 800–1300 cm^{-1} range.

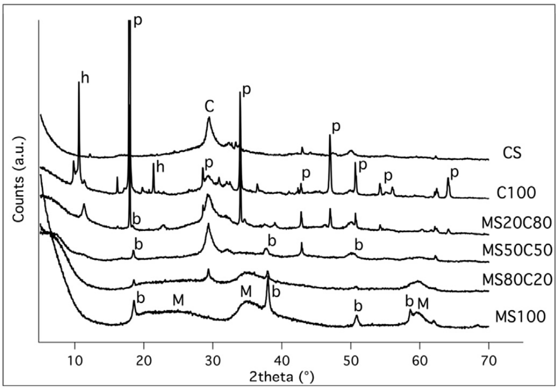

Fig. 6. XRD patterns of all the investigated samples at 28 days of hydration. The assignment of the peaks is reported in the figure using the following abbreviations: p (portlandite), C (C-S-H), h (hemicarboaluminate), b (brucite), M (MSH). Curves have been offset for the sake of clarity.

at ~23°, 35°, and 59° arose from M-S-H, which was the main hydrated phase formed in these samples (Brew and Glasser, 2004). The diffractogram of MS100 showed that brucite was the main crystalline phase, while brucite peaks were very weak in the diffractogram of MS80C20, confirming that in this sample the formation of M-S-H was favoured by the presence of Portland cement.

3.5. ^{29}Si SSNMR spectroscopy

^{29}Si DE-MAS NMR spectra of all samples after 28 days of hydration are shown in Fig. 7.

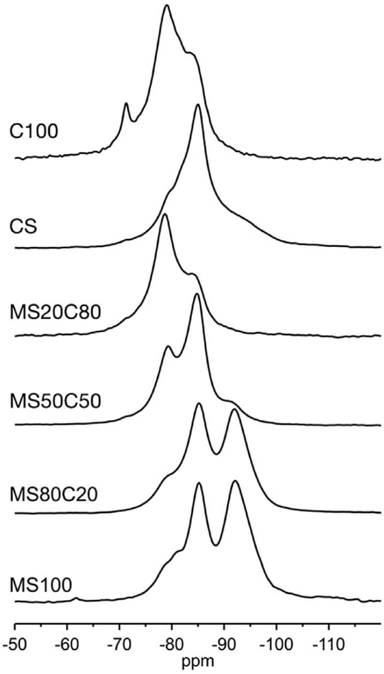

Fig. 7. ^{29}Si DE-MAS NMR spectra of the indicated samples hydrated for 28 days.

For C100, typical signals of hydrated Portland cement could be observed between −90 and −75 ppm together with small signals between −74 and −70 ppm, attributed to residual belite and alite (Andersen et al., 2004; Brough et al., 1994; Cong and Kirkpatrick, 1996; Le Saoût et al., 2006a; Rawal et al., 2010; Sun et al., 1999; Zanni et al., 1996). By contrast, typical signals of M-S-H were found in the spectrum of MS100 (Tonelli et al., 2016). By comparing the ^{29}Si DE-MAS NMR spectra of MS80C20 and MS100, we can definitely conclude that the main silicate hydrate phase formed in MS80C20 is M-S-H. On the other hand, comparison between spectra of C100 and MS20C80 strongly suggests that C-S-H was the main silicate hydrate phase formed in MS20C80, although with a slightly different condensation degree. In agreement with other findings, the spectrum of MS50C50 showed features attributed to both C-S-H and M-S-H phases. Signals typical of hydrated Portland cement were also observed in the spectrum of CS, although with different relative intensities with respect to the other C-S-H forming samples. These findings could be ascribed to a higher condensation degree of tobermorite chains in C-S-H due to the pozzolanic reaction between portlandite and silica (Brough et al., 1995; Haas and Nonat, 2015; Sun et al., 1999). An additional broad signal, centered at about −91.1 ppm, was present in the spectrum of CS, and, according to the literature (Brough et al., 1995; Cong and Kirkpatrick, 1996; Le Saoût et al., 2006b), it could be ascribed to either some species formed by silica hydration, and possibly bonded to C-S-H, or to disordered C-S-H sites cross-linking different silicate chains.

It must be pointed out that no residual silica was observed in any sample where it was used as a reactant, indicating that it was fully consumed after 28 days of hydration. Furthermore, no residual unreacted belite and alite were observed for CS, MS50C50, and MS80C20, indicating a more rapid consumption of these reactants with respect to pure Portland cement. These spectra have been analysed in more detail together with those acquired at different hydration times in order to obtain quantitative information on phase structure and hydration reaction, and are the subject of a very recent publication (Martini et al., 2017).

3.6. Hydration kinetics by the “FWI method”

The hydration kinetics of each cement formulation was followed by determining the fraction of unreacted water (Free Water Index, FWI) as a function of hydration time. As extensively reported in the literature (Damasceni et al., 2002; Ridi et al., 2003, 2011, 2012) FWI was determined from the integral of the melting peak of water, measured on heating by DSC after freezing the sample. As the reaction proceeded, water was consumed and the intensity of its melting peak decreased, as shown for example in Fig. 8A. The measured melting enthalpy ΔH_{exp} was used to extract FWI values according to the following equation:

$$FWI = \Delta H_{\exp}/\phi_w \Delta H_{theor} \quad (1)$$

where ϕ_w is the original weight fraction of water in the paste and ΔH_{theor} is the theoretical value of the melting enthalpy of water (333.4 J/g). The changes in time of the amount of “free”, still unreacted, water provide direct information on the reaction degree, allowing the hydration to be followed until completeness. The influence of a limited number of short freezing/thawing cycles on the hydration kinetics was demonstrated to be negligible (Damasceni et al., 2002). Furthermore, it has been previously shown that this method provides results in full agreement with those obtained by the isothermal calorimetry technique (Ridi et al., 2011). In addition, the FWI method has the advantage of allowing the acquisition of data until the end of the hydration process, not being limited by the evolved heat, which strongly decreases after a few days.

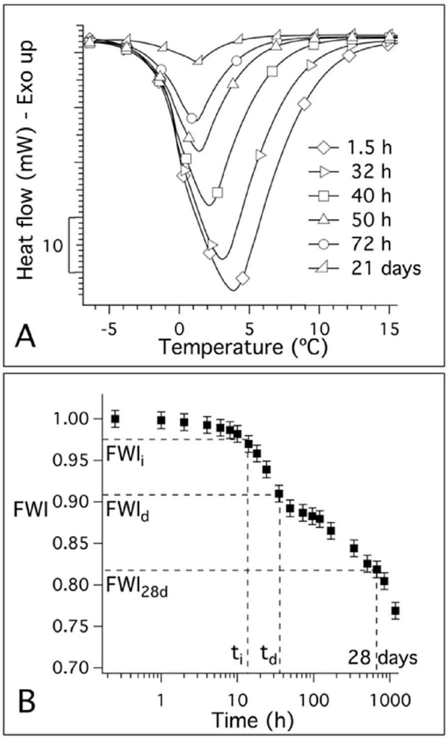

Fig. 8. Decrease with time of the melting enthalpy of water during the hydration of C100 (A) and corresponding FWI vs. hydration time curve (B).

The hydration of the samples was followed over one month and a combination of the Boundary Nucleation and Growth (BNG) model and the three-dimensional diffusional model was used to describe the curves of FWI vs. hydration time (Ridi et al., 2011). As usual for cement pastes, the kinetics showed: an initial induction period, lasting until time t_i (see Fig. 8B), during which FWI remained ~1; an acceleration period characterised by a consistent decrease of FWI as a function of time; a third stage where a significant slowing down of the hydration rate occurred. The latter period (during which the limiting rate of the process is due to the diffusion of water through the hydrated matrix to reach the anhydrous particles) starts at the discontinuity in the FWI versus time curve, marked with t_d and FWI_d in Fig. 8B, which shows the kinetics of hydration of Portland cement. Moreover, the value of FWI after 28 days of hydration (FWI_{28d} in Fig. 8B) can be used to compare the effectiveness of the hydration reaction among the different formulations.

Fig. 9 shows the FWI *vs.* time curves for the different samples investigated together with the fitting curves obtained with the combined BNGM/diffusional model. The model accurately described all the profiles and the best-fit parameters are reported in Table 3.

According to the definition given by Thomas (Thomas, 2007; Thomas et al., 2009), k_B “*describes the rate at which the surfaces become covered with hydration product*”, while k_G is the “*rate at which the pore space between the particles fills in with product*”, which is directly proportional to the growth rate. For C100, k_B could not be accurately determined by the fit, most probably because under the reaction conditions adopted (a w/s ratio of 2 is very high for Portland cement) the change of the measured melting enthalpy during the first hours of hydration was small, thus rendering the experimental data scarcely sensitive to k_B variations. On the contrary, a k_G value of 0.0024 h^{-1} was accurately determined for C100. By addition of silica (sample CS), k_G increased by two orders of magnitude ($k_G = 0.22$ h^{-1}), indicating an accelerating effect of silica on the hydration reaction.

For MS100, k_G was found to be about 0.03 h^{-1} and similar values were determined for the other systems containing MgO and SiO_2. Moreover, all these samples showed a similar rate for the formation of hydrated phases at the interface, with k_B values of the order of 0.5 h^{-1}. As a consequence, the k_B/k_G ratio resulted ~10 for all of these systems. The condition $k_B \gg k_G$ corresponds to a boundary region densely populated with nucleation sites that completely transform in the early stages of hydration (Thomas, 2007). The k_B/k_G ratio determined for the hydration of MgO was ~2, in accordance with the literature (Thomas et al., 2014). The increase of k_B/k_G by addition of SiO_2 was due to the decrease of k_G, and indicated a change in the mechanism of the hydrated product formation.

Interesting information could also be inferred from the diffusional part of the kinetics. For MS20C80, the beginning of the diffusional period (t_d) occurred earlier and FWI_d was lower than for C100. This means that the presence of MgO and SiO_2 shortened the period governed by the BNG mechanism, but the consumption of water was more efficient. An analogous effect was observed for MS80C20 with respect to MS100: t_d and FWI_d decreased, indicating that the addition of a relatively small amount of Portland cement shortened the BNG period but favoured the formation of hydrated phases. Furthermore, the lowest FWI_{28days} values were found for MS20C80 and MS80C20, indicating that in these two mixed systems the enhancement of the hydration reaction also occurred during the diffusional period. A different behaviour was observed for MS50C50: the simultaneous hydration of the same amount of

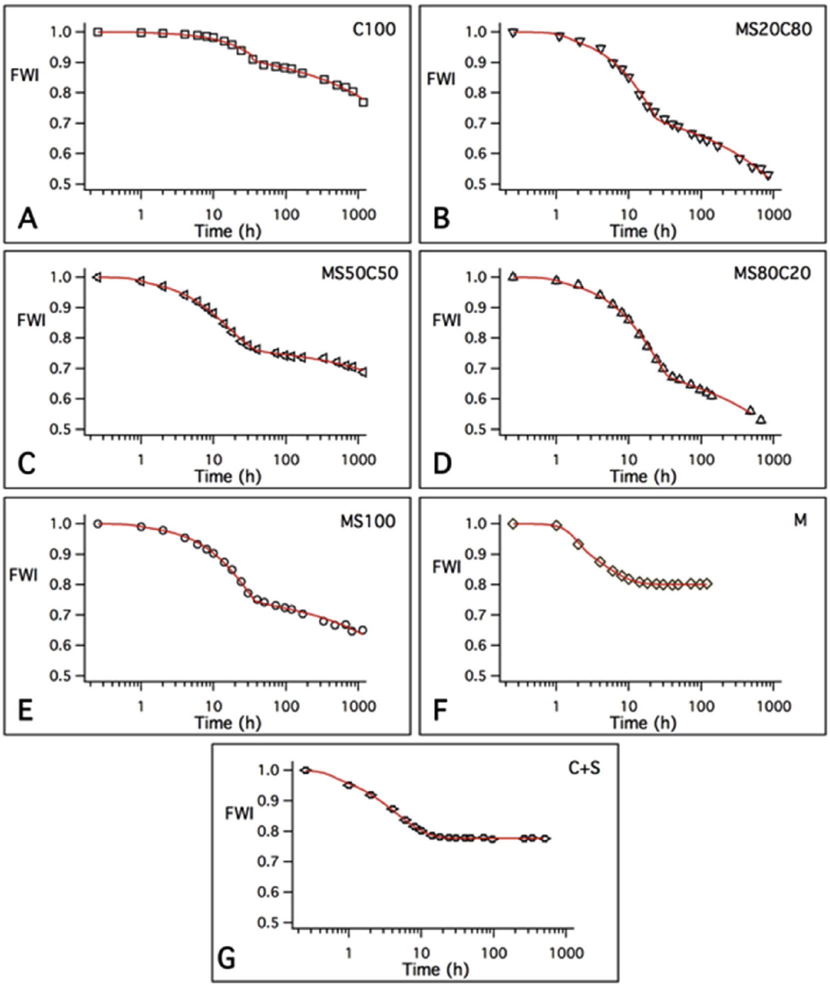

Fig. 9. Hydration kinetics of the investigated samples and MgO, reported as FWI *vs.* time. Black markers represent the experimental data and red lines are the fitting curves obtained with the BNG/diffusional model. (For interpretation of the references to colour in this figure legend, the reader is referred to the web version of this article.)

Table 3
Best-fit parameters determined from fitting the FWI *vs.* time experimental curves to the BNG/diffusional model.

	k_B (h^{-1})	k_G (h^{-1})	k_B/k_G	t_d (h)	FWI_d	$D \cdot 10^{17}$ ($m^2\ h^{-1}$)	FWI_{28days}
C100	(0.2 ± 0.5)[a]	0.0024 ± 0.0003	(83.3 ± 0.5)	34 ± 0.5	0.914 ± 0.005	7 ± 1	0.82 ± 0.01
MS20C80	0.4 ± 0.1	0.038 ± 0.008	10.2 ± 0.1	23 ± 0.5	0.725 ± 0.006	4.7 ± 0.5	0.55 ± 0.01
MS50C50	0.6 ± 0.1	0.062 ± 0.007	9.7 ± 0.1	40 ± 0.5	0.76 ± 0.07	0.19 ± 0.07	0.72 ± 0.01
MS80C20	0.5 ± 0.2	0.038 ± 0.001	13.1 ± 0.3	32 ± 0.5	0.69 ± 0.08	2.0 ± 0.4	0.53 ± 0.01
MS100	0.5 ± 0.2	0.029 ± 0.008	17.2 ± 0.2	39 ± 0.5	0.750 ± 0.005	0.49 ± 0.08	0.67 ± 0.01
MgO	0.47 ± 0.07	0.25 ± 0.03	1.9 ± 0.1	–	–	–	0.80 ± 0.01[b]
CS	1.2 ± 0.6	0.22 ± 0.02	5.5 ± 0.6	–	–	–	0.80 ± 0.01[b]

[a] Results not reliable, the error being larger than the calculated value.

[b] Extrapolated values.

Portland cement and MgO/SiO_2 did not result in a significant modification of the t_d and FWI_d values observed in MS100, while a higher FWI_{28days} value was measured.

The diffusion coefficient values obtained from the fit could not be directly compared with those usually obtained by detecting the radionuclides leaching in cementitious wasteforms. Indeed, in our case *D* represents the average diffusion coefficient of water through the hydrated matrix formed in the time interval between t_d and the end of the process. For this reason, the values here obtained can only be commented to find a relative trend among the samples. The higher values of *D* in the C100 and MS20C80 pastes had to be attributed to a w/s ratio, which is very high for Portland-rich samples, and which is responsible for the increase of capillary porosity. By contrast, the *D* value decreased with increasing the MgO/SiO_2 percentage, as the w/s used for the preparation of the pastes is more appropriated for periclase/silica formulations.

4. Conclusions

C-S-H and M-S-H have different structural properties, but it has been shown in the literature that these two gel phases can coexist, for instance, at the clay/cement interface when cement is used for radioactive waste containment. In this paper, the hydration reaction of pastes prepared by mixing different proportions of Portland cement and MgO/SiO_2 was investigated by means of a multi-technique approach. The experimental results revealed that the reactions forming C-S-H and M-S-H are influenced by the presence of MgO/SiO_2 and Portland cement, respectively, with modification of both the hydration kinetics and the composition of the hydrated phases. Moreover, the initial composition of the mixtures affects the pH *vs*. time trend, which is a fundamental parameter for the containment of radioactive wastes in clayey environments. In particular, we found that when low amounts of MgO/SiO_2 are added to Portland cement, C-S-H is the main hydrated phase. Hydration occurs faster than in pure Portland cement, probably because silica accelerates the precipitation of the hydrated phases by reacting with portlandite. Moreover, the addition of MgO/SiO_2 shortens the period kinetically controlled by the "boundary nucleation and growth" (BNG) mechanism and the consumption of water is higher, causing the precipitation of a larger amount of C-S-H. By contrast, M-S-H is the main hydration product in the MgO/SiO_2 formulations containing a minor fraction of Portland cement. Also in this case the BNG period is shortened, enhancing the formation of the hydrated phases. Moreover, M-S-H forms in large amount and with a faster kinetics than in pure MgO/SiO_2, at a higher pH value (11.8–11.5) than that previously considered as ideal.

In MS50C50, prepared from a 50:50 wt:wt MgO/SiO_2:Portland cement mixture, both hydrated phases form. In particular, due to the presence of a large amount of silica, highly condensed C-S-H precipitates, as also inferred from the comparison with the sample prepared from Portland cement and SiO_2 without MgO, and in agreement with the occurrence of the pozzolanic reaction.

Overall, the results reported in this paper show that in some specific cases it could be possible to control the formation of calcium and magnesium silicate hydrate gels and the pH of the final material by mixing appropriate amounts of MgO/SiO_2 and Portland cement powders. Therefore, by tailoring the composition of these mixtures, it could be possible to control the characteristics of the final material for predetermined applications.

Acknowledgment

This work was performed with the financial support of Ministero dell'Istruzione, Università e Ricerca scientifica MIUR (FIR2013 Project RBFR132WSM) and of Consorzio Interuniversitario per lo Sviluppo dei Sistemi a Grande Interfase, CSGI.

References

Andersen, M.D., Jakobsen, H.J., Skibsted, J., 2004. Characterization of white Portland cement hydration and the C-S-H structure in the presence of sodium aluminate by ^{27}Al and ^{29}Si MAS NMR spectroscopy. Cem. Concr. Res. 34, 857–868.

Bartier, D., Techer, I., Dauzères, A., Boulvais, P., Blanc-Valleron, M.-M., Cabrera, J., 2013. In situ investigations and reactive transport modelling of cement paste/argillite interactions in a saturated context and outside an excavated disturbed zone. Appl. Geochem. 31, 94–108.

Brew, D.R.M., Glasser, F.P., 2004. Synthesis and characterisation of magnesium silicate hydrate gels. Cem. Concr. Res. 35, 85–98.

Brough, A.R., Dobson, C.M., Richardson, I.G., Groves, G.W., 1994. Application of selective ^{29}Si isotopic enrichment to studies of the structure of calcium silicate hydrate (C-S-H) gels. J. Am. Ceram. Soc. 77, 593–596.

Brough, A.R., Dobson, C.M., Richardson, I.G., Groves, G.W., 1995. A study of the pozzolanic reaction by solid state ^{29}Si nuclear magnetic resonance using selective isotopic enrichment. J. Mater. Sci. 30, 1671–1678.

Chiang, W.-S., Ferraro, G., Fratini, E., Ridi, F., Yeh, Y.-Q., Jeng, U.S., Chen, S.-H., Baglioni, P., 2014. Multiscale structure of calcium-and magnesium-silicate-hydrate gels. J. Mater. Chem. A 2, 12991–12998.

Chiang, W.-S., Fratini, E., Ridi, F., Lim, S.-H., Yeh, Y.-Q., Baglioni, P., Choi, S.-M., Jeng, U.-S., Chen, S.-H., 2013. Microstructural changes of globules in calcium–silicate–hydrate gels with and without additives determined by small-angle neutron and X-ray scattering. J. Colloid Interface Sci. 398, 67–73.

Cong, X., Kirkpatrick, R.J., 1996. ^{29}Si MAS NMR study of the structure of calcium silicate hydrate. Adv. Cem. Based Mater. 3, 144–156.

Damasceni, A., Dei, L., Fratini, E., Ridi, F., Chen, S.-H., Baglioni, P., 2002. A novel approach based on differential scanning calorimetry applied to the study of tricalcium silicate hydration kinetics. J. Phys. Chem. B 106, 11572–11578.

Dauzères, A., Achiedo, G., Nied, D., Bernard, E., Alahrache, S., Lothenbach, B., 2016. Magnesium perturbation in low-pH concretes placed in clayey environment—solid characterizations and modeling. Cem. Concr. Res. 79, 137–150.

Dauzères, A., Le Bescop, P., Cau-Dit-Coumes, C., Brunet, F., Bourbon, X., Timonen, J., Voutilainen, M., Chomat, L., Sardini, P., 2014. On the physico-chemical evolution of low-pH and CEM I cement pastes interacting with Callovo-Oxfordian pore water under its in situ CO_2 partial pressure. Cem. Concr. Res. 58, 76–88.

Dauzères, A., Le Bescop, P., Sardini, P., Cau Dit Coumes, C., 2010. Physico-chemical investigation of clayey/cement-based materials interaction in the context of geological waste disposal: experimental approach and results. Cem. Concr. Res. 40, 1327–1340.

Fernandez, L., Alonso, C., Andrade, C., Hidalgo, A., 2008. The interaction of magnesium in hydration of C_3S and CSH formation using ^{29}Si MAS-NMR. J. Mater. Sci. 43, 5772–5783.

Gaboreau, S., Pret, D., Tinseau, E., Pellegrini, D., Stammose, D., 2011. 15 years of in situ cement–argillite interaction from Tournemire URL: characterisation of the multi-scale spatial heterogeneities of pore space evolution. Appl. Geochem. 26, 2159–2171.

García Calvo, J.L., Hidalgo, A., Alonso, C., Fernández Luco, L., 2010. Development of low-pH cementitious materials for HLRW repositories: resistance against ground waters aggression. Cem. Concr. Res. 40, 1290–1297.

Gaucher, E.C., Blanc, P., 2006. Cement/clay interactions – a review: experiments, natural analogues, and modeling. Waste Manag. 26, 776–788.

Haas, J., Nonat, A., 2015. From C–S–H to C–A–S–H: experimental study and thermodynamic modeling. Cem. Concr. Res. 68, 124–138.

Jenni, A., Mäder, U., Lerouge, C., Gaboreau, S., Schwyn, B., 2014. In situ interaction between different concretes and opalinus clay. Phys. Chem. Earth, Parts A/B/C 70–71, 71–83.

Jin, F., Al-Tabbaa, A., 2014. Strength and hydration products of reactive MgO–silica pastes. Cem. Concr. Compos. 52, 27–33.

Klimesch, D.S., Ray, A., 1999. DTA-TGA evaluations of the $CaO–Al_2O_3–SiO_2–H_2O$ system treated hydrothermally. Thermochim. Acta 334, 115–122.

Le Saoût, G., Lécolier, E., Rivereau, A., Zanni, H., 2006a. Chemical structure of cement aged at normal and elevated temperatures and pressures. Part I. Class G oilwell cement. Cem. Concr. Res. 36, 71–78.

Le Saoût, G., Lécolier, E., Rivereau, A., Zanni, H., 2006b. Chemical structure of cement aged at normal and elevated temperatures and pressures, Part II: low permeability class G oilwell cement. Cem. Concr. Res. 36, 428–433.

Li, Z., Zhang, T., Hu, J., Tang, Y., Niu, Y., Wei, J., Yu, Q., 2014. Characterization of reaction products and reaction process of $MgO–SiO_2–H_2O$ system at room temperature. Constr. Build. Mater. 61, 252–259.

Lothenbach, B., Nied, D., L'Hôpital, E., Achiedo, G., Dauzères, A., 2015. Magnesium and calcium silicate hydrates. Cem. Concr. Res. 77, 60–68.

Martini, F., Tonelli, M., Calucci, L., Geppi, M., Ridi, F., Borsacchi, S., 2017. MgO/SiO_2 and Portland cement formulations: mutual effects on hydration processes and products. Cem. Concr. Compos. Submitted.

Nied, D., Enemark-Rasmussen, K., L'Hôpital, E., Skibsted, J., Lothenbach, B., 2016. Properties of magnesium silicate hydrates (M-S-H). Cem. Concr. Res. 79, 323–332.

Norris, S., Bruno, J., Cathelineau, M., Delage, P., Fairhurst, C., Gaucher, E.C., Höhn, E.H., Kalinichev, A., Lalieux, P., Sellin, P., 2014. Clays in natural and engineered barriers for radioactive waste confinement. Geological Society of London, London.

Pytel, Z., Malolepszy, J., 2000. DTA studies of phases synthesized in the system $CaO-MgO-SiO_2-H_2O$. Silic. Ind. 65, 81–85.

Rawal, A., Smith, B.J., Athens, G.L., Edwards, C.L., Roberts, L., Gupta, V., Chmelka , B.F., 2010. Molecular silicate and aluminate species in anhydrous and hydrated cements. J. Am. Chem. Soc. 132, 7321–7337.

Richardson, I.G., 2004. Tobermorite/jennite- and tobermorite/calcium hydroxide-based models for the structure of C-S-H: applicability to hardened pastes of tricalcium silicate, β-dicalcium silicate, Portland cement, and blends of Portland cement with blast-furnace slag, metakaolin, or silica fume. Cem. Concr. Res. 34, 1733–1777.

Ridi, F., Dei, L., Fratini, E., Chen, S.-H., Baglioni, P., 2003. Hydration kinetics of tricalcium silicate in the presence of superplasticizers. J. Phys. Chem. B 107, 1056–1061.

Ridi, F., Fratini, E., Luciani, P., Winnefeld, F., Baglioni, P., 2011. Hydration kinetics of tricalcium silicate by calorimetric methods. J. Colloid Interface Sci. 364, 118–124.

Ridi, F., Fratini, E., Luciani, P., Winnefeld, F., Baglioni, P., 2012. Tricalcium silicate hydration reaction in the presence of comb-shaped superplasticizers: boundary nucleation and growth model applied to polymer-modified pastes. J. Phys. Chem. C 116, 10887–10895.

Roosz, C., Grangeon, S., Blanc, P., Montouillout, V., Lothenbach, B., Henocq, P., Giffaut, E., Vieillard, P., Gaboreau, S., 2015. Crystal structure of magnesium silicate hydrates (M-S-H): the relation with 2:1 Mg–Si phyllosilicates. Cem. Concr. Res. 73, 228–237.

Shrivastava, O.P., Komarneni, S., Breval, E., 1991. Mg^{2+} uptake by synthetic tobermorite and xonotlite. Cem. Concr. Res. 21, 83–90.

Sun, G., Brough, A.R., Young, J.F., 1999. Si NMR study of the hydration of Ca_3SiO_5 and β-Ca_2SiO_4 in the presence of silica fume. J. Am. Ceram. Soc. 82, 3225–3230.

Thomas, J.J., 2007. A new approach to modeling the nucleation and growth kinetics of tricalcium silicate hydration. J. Am. Ceram. Soc. 90, 3282–3288.

Thomas, J.J., Allen, A.J., Jennings, H.M., 2009. Hydration kinetics and microstructure development of normal and $CaCl_2$-accelerated tricalcium silicate pastes. J. Phys. Chem. C 113, 19836–19844.

Thomas, J.J., Musso, S., Prestini, I., 2014. Kinetics and activation energy of magnesium oxide hydration. J. Am. Ceram. Soc. 97, 275–282.

Tonelli, M., Martini, F., Calucci, L., Fratini, E., Geppi, M., Ridi, F., Borsacchi, S., Baglioni, P., 2016. Structural characterization of magnesium silicate hydrate: towards the design of eco-sustainable cements. Dalton Trans. 45, 3294–3304.

Van der Merwe, E.M., Strydom, C., Botha, A., 2004. Hydration of medium reactive industrial magnesium oxide with magnesium acetate. J. Therm. Anal. Calorim. 77, 49–56.

Walling, S.A., Kinoshita, H., Bernal, S.A., Collier, N.C., Provis, J.L., 2015. Structure and properties of binder gels formed in the system $Mg(OH)_2$–SiO_2–H_2O for immobilisation of Magnox sludge. Dalton Trans. 44, 8126–8137.

Zanni, H., Rassem-Bertolo, R., Masse, S., Fernandez, L., Nieto, P., Bresson, B., 1996. A spectroscopic NMR investigation of the calcium silicate hydrates present in cement and concrete. Magn. Reson. Imaging 14, 827–831.

Zhang, T., Cheeseman, C.R., Vandeperre, L.J., 2011. Development of low pH cement systems forming magnesium silicate hydrate (M-S-H). Cem. Concr. Res. 41, 439–442.

Zhang, T., Vandeperre, L.J., Cheeseman, C.R., 2012. Magnesium-silicate-hydrate cements for encapsulating problematic aluminium containing wastes. J. Sustain. Cement-Based Mater. 1, 34–45.

Zhang, T., Vandeperre, L.J., Cheeseman, C.R., 2014. Formation of magnesium silicate hydrate (M-S-H) cement pastes using sodium hexametaphosphate. Cem. Concr. Res. 65, 8–14.

Paper IV

ARTICLE IN PRESS

Microporous and Mesoporous Materials xxx (2017) 1–5

Contents lists available at ScienceDirect

Microporous and Mesoporous Materials

journal homepage: www.elsevier.com/locate/micromeso

Monitoring the hydration of MgO-based cement and its mixtures with Portland cement by ^1H NMR relaxometry

Francesca Martini [a, b], Silvia Borsacchi [b, *], Marco Geppi [a, b], Monica Tonelli [c],
Francesca Ridi [c], Lucia Calucci [b, **]

[a] Dipartimento di Chimica e Chimica Industriale, Università di Pisa, via G. Moruzzi 13, 56124 Pisa, Italy
[b] Istituto di Chimica dei Composti OrganoMetallici, Consiglio Nazionale delle Ricerche – CNR, S.S. di Pisa, via G. Moruzzi 1, 56124 Pisa, Italy
[c] Dipartimento di Chimica “Ugo Schiff” & CSGI, Università di Firenze, via della Lastruccia 3, 50019 Sesto Fiorentino (FI), Italy

ARTICLE INFO

Article history:
Received 9 December 2016
Received in revised form
28 April 2017
Accepted 17 May 2017
Available online xxx

Keywords:
Proton relaxation times
Calcium silicate hydrate
Magnesium silicate hydrate
Fumed silica
Cement hydration

ABSTRACT

The hydration process of MgO-based cement, Portland cement, and several mixtures of them was investigated for 1 month by measuring ^1H transverse relaxation times (T_2) of the different fractions of water inside pastes by means of the Carr-Purcell-Meiboom-Gill pulse sequence. The obtained T_2 distributions were exploited to get information on the kinetics of the hydration process and on the evolution of the porous structure of the calcium silicate hydrate (C-S-H) and magnesium silicate hydrate (M-S-H) binder phases as a function of time. The analysis of solid echo ^1H Free Induction Decays was employed to determine the relative amount of hydrogen-containing solid phases present in pastes at the longest hydration time.

1. Introduction

In recent years, MgO-based cements have been proposed both as potential low-CO_2 alternatives to Portland cement, the dominant form of cement used worldwide, and as low-pH cements for nuclear waste immobilization [1].

The binder phase of these cements is magnesium silicate hydrate (M-S-H), the amorphous phase that forms from the reaction of MgO with a source of silica and water. Although a significant quantity of literature exists concerning the structure and nature of the M–S–H gel [2–7], the understanding of M–S–H as a binder phase is in its infancy. In particular, questions are still open concerning the hydration of MgO/SiO_2 mixtures, even if this process is fundamental for the formation of the binder phase, ultimately determining microstructural properties such as composition, porosity, and water distribution, which in turn control the mechanical properties of cement. In recent papers, the inferior mechanical properties of MgO-based cements with respect to traditional CaO-based cements have been correlated to the different structures of the respective binder phases (i.e M-S-H and C-S-H (calcium silicate hydrate)) at the nano- and micro-metric scale [8], as well as to the different distribution of water inside them [9]. In particular, it has been shown that poly-disperse spherical globules (without an internal layered structure) packed into a fractal structure constitute M-S-H at variance with C-S-H, where, according to the Jennings model [10], colloidal disc-like globules, with a layered substructure including water, pack in flocs. Moreover, the higher compressive strength of C-S-H with respect to M-S-H has been associated to a higher amount of structural and constrained water, the latter being in turn considered as an indication of a smaller average pore size.

The hydration of cement is a very complex process in which reactants dissolve in water and hydrated phases precipitate to form gels with a porous structure that evolves in time. In the case of Portland cement, calcium silicates (alite and belite) and aluminates dissolve and C-S-H forms together with Portlandite and minor amounts of calcium-aluminate phases. In the case of MgO/SiO_2 mixtures, MgO dissolves giving rise to Mg^{2+} and OH^- ions; when a saturation concentration is reached, brucite precipitates and a moderately basic pH is established, which favors the hydration of silica with formation of silicate anions. From the reaction between

---

[*] Corresponding author.
[**] Corresponding author.
E-mail addresses: silvia.borsacchi@pi.iccom.cnr.it (S. Borsacchi), lucia.calucci@pi.iccom.cnr.it (L. Calucci).

http://dx.doi.org/10.1016/j.micromeso.2017.05.031

Please cite this article in press as: F. Martini, et al., Monitoring the hydration of MgO-based cement and its mixtures with Portland cement by ^1H NMR relaxometry, Microporous and Mesoporous Materials (2017), http://dx.doi.org/10.1016/j.micromeso.2017.05.031

silicate anions and Mg^{2+} cations M-S-H forms at the expense of brucite and silica [3].

^1H NMR relaxometry, through the non invasive measurement of transverse (T_2) and/or longitudinal (T_1) relaxation time(s) of protons directly on as prepared pastes, gives unique information on the kinetics of formation of hydrogen-containing solid phases and on the evolution of the state of water and the pore network during cement hydration [11–14]. In particular, analyses of ^1H Free Induction Decay (FID) on Portland cement pastes allowed protons in solid phases to be singled out and quantified [15–17]. Moreover, the dependence of the T_2 values of protons of water inside pores on the surface-to-volume ratio of pores and on a specific surface relaxivity has been exploited to distinguish and quantify different water populations [18–21]. Under the assumption of fast diffusion conditions and fully saturated pores [22,23], the distribution of pore sizes in the C-S-H gel and its evolution in the different stages of cement hydration have been determined [24,25].

In the present work, ^1H NMR relaxometry is employed for the first time to investigate the hydration process of MgO-based cements. To this aim, T_2 measurements were performed using the Carr-Purcell-Meiboom-Gill (CPMG) pulse sequence [26] at different times, ranging from ~0.5 h to ~1 month, during the hydration of a 1:1 mol:mol mixture of highly reactive periclase and fumed silica, either alone (MS100) or mixed with different proportions of ordinary Portland cement (MS80C20, MS50C50, and MS20C80). The hydration of the sole Portland cement (C100), carried out under the same conditions, was also investigated for comparative purposes. Moreover, ^1H FID analyses on pastes of all samples hydrated for ~1 month were exploited to highlight the presence of hydrogen-containing solid phases. The results were discussed taking into account findings on the nature and structure of the hydrated phases obtained by other techniques [27,28].

2. Experimental

^1H NMR measurements were performed at 20.7 MHz and 24 °C using a Niumag permanent magnet interfaced with a Stelar PCNMR console. The temperature was controlled within ± 0.1 °C with a Stelar VTC90 variable temperature controller. The 90° pulse duration was 3 μs. CPMG measurements [26] were carried out with an echo time (τ) of 20 μs and acquiring 120 scans. Solid echo experiments were performed with an echo delay of 14 μs and acquiring 120 scans. The recycle delay was 2 s.

For the NMR measurements, pastes prepared as described in the Supplementary material were deposited at the bottom of 5 mm NMR tubes and tightly sealed with Parafilm. Samples were stored at 24 ± 1 °C in a temperature-controlled room during hydration. Measurements were performed at different hydration times and the reproducibility of the results was tested by comparing measurements on at least two independently prepared samples.

Relaxation decay data from CPMG experiments were inverted to give T_2 distributions by the algorithm UPEN [29,30] implemented in UpenWin 1.05 software [31]. Experimental FIDs acquired on resonance using the solid echo pulse sequence were fitted to a linear combination of a Gaussian and one or two exponential functions using a non-linear least squares procedure implemented in the Mathematica [32] environment. Solid echo FIDs were used to determine the fraction of protons arising from reacted water in solid phases (given by the fractional weight of the Gaussian function) and the corresponding T_2 value. The longer exponential decay(s), ascribable to unreacted water with different degree of mobility, and more affected by magnetic field inhomogeneity, was (were) instead determined by the CPMG experiments.

3. Results

Representative examples of T_2 distributions obtained from CPMG data are shown in Fig. 1 for all samples; vertical expansions are reported in Fig. S1. When well-separated T_2 peaks are observed, trends of T_2 values at the maxima and corresponding proton populations are also reported as a function of the hydration time, t_H, in Fig. 2 and Fig. S2, respectively.

For C100, at $t_H < 6$ h two T_2 peaks centered at ~3 and 12 ms with relative weights of ~20 and 80% are observed (Fig. 1), both

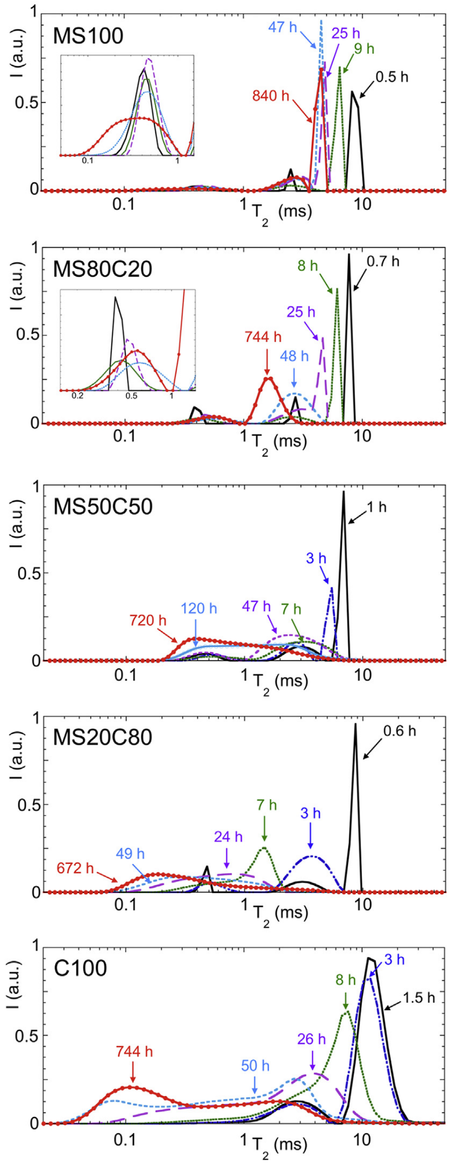

Fig. 1. Representative selection of ^1H T_2 relaxation time distributions from CPMG experiments at different hydration times. Vertical expansions of these distributions are reported in Fig. S1.

Please cite this article in press as: F. Martini, et al., Monitoring the hydration of MgO-based cement and its mixtures with Portland cement by ^1H NMR relaxometry, Microporous and Mesoporous Materials (2017), http://dx.doi.org/10.1016/j.micromeso.2017.05.031

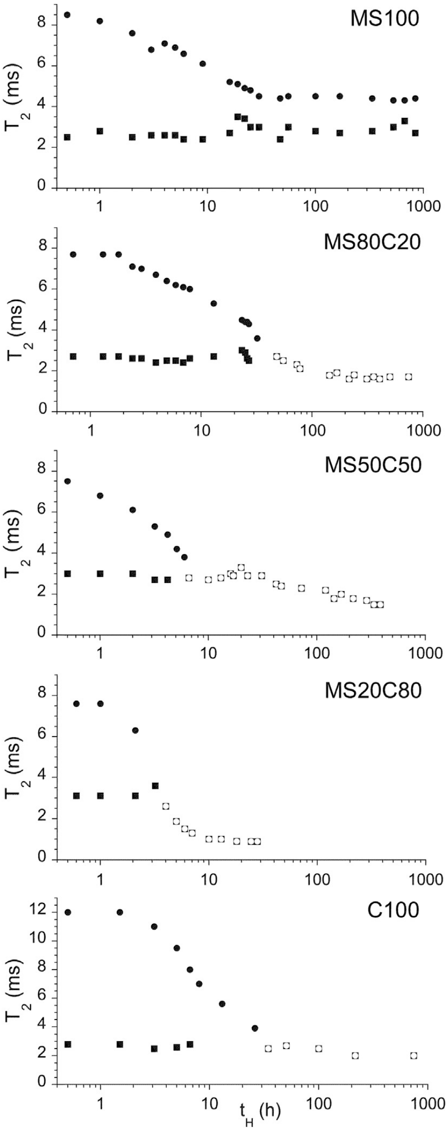

Fig. 2. Evolution of ^{1}H T_2 relaxation times from CPMG experiments as a function of hydration time. Symbols ● and ■ are for the more mobile and less mobile free water components, while symbol ⊠ is for free water at longer hydration times, becoming water in the interhydrate spaces.

ascribable to “free” water within the interstices between clinker grains [15,24]; in the following, the fractions of water associated to these peaks will be referred to as “less mobile” and “more mobile” free water, respectively. By increasing t_H, the more mobile water peak progressively broadens and shifts to shorter T_2; at $t_H = 8$ h the peak is centered at 7 ms and partially overlaps with that of less mobile water. For longer t_H values the two peaks merge in a broad one centered at ~4 ms, whose relative intensity and T_2 progressively decrease up to ~30 h (Figs. 1 and 2). Afterwards, T_2 remains approximately constant at ~2.5 ms, a value comparable with those previously ascribed to water in the spaces between C-S-H agglomerates (interhydrate water [25,36]). After one day, an additional very broad T_2 distribution shows up in the range between 0.1 and few ms, ascribable to water in C-S-H gel pores and interlayer spacings [24]. For longer t_H values, a T_2 peak centered at ~0.1 ms, due to water in C-S-H interlayer spaces, starts to be resolved, its relative intensity increasing with t_H.

For MS20C80, three peaks centered at ~0.5, 3, and 8 ms and with relative areas of 12%, 23%, and 65% are observed for $t_H < 2$ h (Figs. 1 and 2). As for C100, the two peaks at longer T_2 can be ascribed to free water [15,24]. On the other hand, the peak at the shortest T_2 can be associated to water inside powder grain agglomerations (“embedded” water [12,20,33]) and, in particular, to water embedded within fumed silica aggregates [34]. Indeed, an analogous peak is observed at early hydration times in the T_2 dispersions of all samples but C100. After ~3 h the two peaks of free water converge in a broad peak, whose maximum T_2 value and intensity decrease with increasing t_H. At the same time, the peak of embedded water broadens and, when still present, subsequently overlaps with the T_2 distribution due to water in C-S-H, which is the main hydrated phase formed in this sample (vide infra). After one day of hydration the evolution of the T_2 distribution resembles that observed for C100.

For $t_H < 4$ h, MS50C50 shows T_2 distributions analogous to those of MS20C80, whereas the T_2 distributions of the two samples are substantially different for t_H between 4 h and 5 days (Figs. 1 and 2 and Fig. S2). In the latter period a bimodal T_2 distribution is observed for MS50C50 with a peak centered at ~0.5 ms at all times and one moving from 5 to 2 ms with increasing t_H. From 5 days a broad distribution with T_2 values ranging from ~0.2 to ~10 ms is observed, a peak centered at ~0.4 ms progressively emerging with increasing t_H. In analogy with C100 and MS20C80, this distribution can be ascribed to gel pores and interlayer water in C-S-H, which is the main phase formed also for this sample (vide infra).

Samples MS100 and MS80C20 show similar T_2 distributions with three well-separated peaks for hydration times up to 1 day (see Figs. 1 and 2 and Fig. S2). In particular, at the beginning of hydration, the three peaks are centered at ~0.4, 3 and 8 ms for both samples and account for 10 (12), 10 (13), and 80 (75)% of water protons for MS100 (MS80C20). The peak at the shortest T_2 can be ascribed to embedded water, as for the previous samples, while the other peaks should be due to free water with different mobility in the spaces between powder grains. With increasing t_H, the embedded water peak broadens, but its maximum remains almost at the same T_2 value and its intensity essentially does not change (see insets of Fig. 1). The peak of less mobile free water also broadens and does not show significant changes in the T_2 maximum value, but its intensity slightly increases. On the other hand, the peak of more mobile water moves to shorter T_2 values and slightly decreases in intensity. For MS100, after ~30 h the T_2 maximum values of the three peaks remain practically constant at ~0.4, 2.8, and 4.3 ms; the only change observed consists in the broadening of the two peaks at shorter T_2. On the contrary, for MS80C20 after 1 day the two peaks of free water merge in a broad one, whose maximum T_2 progressively decreases with increasing t_H up to 6 days and then it stabilizes at ~1.7 ms. The peak at ~0.4 ms progressively broadens with increasing t_H.

After about 1 month, solid echo ^{1}H FIDs of all samples show the presence of a solid component characterized by a Gaussian decay with T_2 of 12, 19, 14, 18, and 18 μs that accounts for 24, 9, 5, 5, and 5% of protons for C100, MS20C80, MS50C50, MS80C20, and MS100, respectively.

Please cite this article in press as: F. Martini, et al., Monitoring the hydration of MgO-based cement and its mixtures with Portland cement by ^{1}H NMR relaxometry, Microporous and Mesoporous Materials (2017), http://dx.doi.org/10.1016/j.micromeso.2017.05.031

4. Discussion

Data here acquired by ^{1}H NMR relaxometry can be interpreted to get insights into the kinetics of the hydration process and the evolution of the porous structure of the hydrated phases with time, also taking into account complementary results obtained by other techniques (i.e. X-ray diffraction (XRD), thermogravimetric analysis (DTG), differential scanning calorimetry (DSC), and ^{29}Si solid state NMR) on the same samples [27,28]. As reported in Ref. [28], Free Water Index (FWI) trends obtained by DSC measurements [35] showed three steps of the hydration process: an induction period (from 30 min to few hours after mixing) with low water consumption; a "nucleation and growth" period (including the acceleration and deceleration stages), lasting until 30–40 h, during which water is rapidly consumed; a diffusional period characterized by a very low rate of water consumption. From XRD, DTG and ^{29}Si NMR data acquired on freeze-dried samples [2,27,28] we found that mainly M-S-H forms for MS80C20, while C-S-H is essentially the only phase formed for MS20C80; for MS50C50 both phases are present even if C-S-H is largely prevalent. Obviously, only M-S-H and C-S-H form in samples MS100 and C100, respectively. For all samples hydrated phases are already present after 24 h, although their formation is much faster for the mixed samples with respect to C100 and MS100, and reactants are almost completely consumed after 28 days of hydration. Brucite also forms for all MgO containing samples, while Portlandite is found only for C100 and MS20C80.

In the present work, in agreement with FWI results, the three stages of hydration above described [35] can be distinguished in the monitored period (from ~0.5 h to ~1 month) by following the evolution of the T_2 distributions as a function of t_H.

For C100 the trend of the more mobile water T_2 as a function of t_H (Fig. 2) is in agreement with those previously reported in the literature for white and ordinary Portland cements [15,20,21,25,36]. Up to ~2 h T_2 is practically constant: this corresponds to the induction period characterized by the dissolution of the calcium silicates, with slow release of calcium and hydroxide ions. The second stage, between 2 and 30 h, is characterized by a rapid decrease of the more mobile water T_2 with increasing t_H. For $t_H > 8$ h a sole T_2 peak is observed for free water centered at a value further decreasing with increasing t_H. This stage corresponds to the nucleation and growth period of cement hydration, during which C-S-H and Portlandite form; C-S-H fills the spaces between the cement grains, thus confining water in progressively smaller pores associated with shorter T_2 values. During the diffusional period ($t_H > 30$ h), the T_2 of free water stabilizes at a value of ~2 ms, typical of interhydrate water [25,36]. At the end of the deceleration period and during the diffusional one, the progressive formation of the C-S-H gel pores and interlayer spaces is indicated by the appearance of a broad T_2 distribution between 0.1 and few ms (Fig. 1).

For MS100 the progressive decrease of T_2 of the more mobile free water peak observed up to 40 h (Fig. 2), accompanied by a concomitant slight decrease of its relative proton population (Fig. S2), can be associated to the nucleation and growth period, during which water is consumed and M-S-H forms filling the interstitial spaces between the powder grains. Differently from Portland cement, the induction period seems to be quite short, since the decrease of T_2 already starts within the first hour of hydration. The progressive broadening of the peaks of less mobile free water and embedded water with increasing t_H can be due to changes of the paste microstructure associated with the formation of M-S-H. From previous studies on MS100 [7,27,28], it is known that the formation of M-S-H continues between 7 and 28 days; however, the fact that the T_2 values and the weights of the different water fractions remain practically constant after 40 h indicates that the average sizes and the relative amounts of the main pore populations do not significantly evolve.

The T_2 distributions obtained for the mixtures can be discussed in comparison with those of MS100 and C100 to highlight mutual effects of the reactants on the hydration process. In the case of MS80C20, for which M-S-H is mainly formed, the evolution of the T_2 distributions with increasing t_H is analogous to that observed for MS100 (Figs. 1 and 2), but with three noticeable differences: the induction period seems to be slightly longer; a single free water population is observed after about one day of hydration; the T_2 of free water decreases until over 100 h of hydration, suggesting a corresponding decrease of pore sizes for a longer time with respect to MS100. These differences can be at least partially ascribed to the formation of small amounts of C-S-H, as detected by XRD [27,28]. In the case of MS20C80, for which C-S-H is the main binder phase, the evolution of the T_2 dispersions with increasing t_H is similar to that observed for C100, suggesting an analogous development of the gel structure. However, the hydration kinetics is accelerated in both the induction and nucleation and growth periods, in agreement with findings from FWI measurements and structural characterizations [27,28]. This is most probably due to the presence of fumed silica, which can both act as nucleating agent for the formation of C-S-H and form additional C-S-H through the pozzolanic reaction with Portlandite [37–40]. For MS50C50 the evolution of the T_2 distributions with hydration time cannot be straightforwardly associated to that of either C100 or MS100 (Figs. 1 and 2 and Fig. S2). Indeed, the induction period is very short, as for MS100, but the hydration kinetics in the nucleation and growth period is accelerated. Moreover, differently from all the other samples, T_2 of free water remains constant and practically no evolution of the T_2 distributions is observed for a quite long period (from 6 to 30 h). On the other hand, after ~30 h, T_2 distributions resemble those observed for C100 and MS20C80, in agreement with the fact that C-S-H is the main phase formed also for this sample.

Considering that, on the basis of XRD and ^{29}Si NMR findings, in all cases reactants are almost completely consumed at 28 days of hydration, the results of ^{1}H solid echo FID analyses can be exploited to compare the amount of reacted water among the different samples. For Portland cement the fast decaying Gaussian component of the FID can be mainly ascribed to Portlandite and/or to Ettringite crystal water [15,17,24,25], with minor contributions from OH groups and bound water in C-S-H, whereas for MS100 it can be associated to OH groups of brucite and/or M-S-H. This considered, the decrease of the relative amount of protons in the solid phases observed going from C100 to MS20C80 and MS50C50 can be accounted for by the decrease of Portlandite content observed by XRD experiments, Portlandite being consumed in the pozzolanic reaction with silica. For MS100 and MS80C20, the equal contributions of solid phase protons to the FIDs are in agreement with the similar amounts of brucite and M-S-H and the absence of Portlandite in MS80C20 found by XRD measurements.

For samples hydrated for 28 days, T_2 distributions (Fig. 1 and Fig. S1) can be exploited to obtain qualitative information on the pore size distributions in the formed gels [22,23]. For C100, MS20C80 and MS50C50, a broad distribution is observed ascribable to the presence of interlayer spaces, gel pores, and interhydrate pores in the C-S-H binder phase. On the other hand, for MS100 and MS80C20 well separated and relatively narrow distributions are observed. An estimate of pore dimensions was obtained for C100 and MS100 by low temperature DSC (see Supplementary material). Pores with size in the 1–3 nm range were found for both samples, while pores with dimensions between 3 and 12 nm were also determined for MS100.

Please cite this article in press as: F. Martini, et al., Monitoring the hydration of MgO-based cement and its mixtures with Portland cement by ^{1}H NMR relaxometry, Microporous and Mesoporous Materials (2017), http://dx.doi.org/10.1016/j.micromeso.2017.05.031

5. Conclusions

Monitoring the evolution of the state of water in pastes of MgO-based cement, Portland cement, and their mixtures by ^{1}H NMR relaxometry gave important information on the kinetics of the hydration reaction and on the formation of the porous structure of the hydrated phases. In particular, we found that the hydration of MgO/SiO$_2$ has a very short induction period, although consumption of water during the nucleation and growth period is slower than for Portland cement. The presence of fumed silica accelerates the hydration of Portland cement, both in the induction and nucleation and growth stages.

The hydration kinetics is reflected into the evolution of the porous structure of the formed hydrated phases. For Portland cement and mixtures forming C-S-H as the main binder phase, a substantial change in pore size distributions occurs during the paste hardening due to the massive formation of C-S-H with water in the interlayer spaces and in gel pores. On the other hand, for MgO/SiO$_2$ and its mixture with Portland for which M-S-H forms as binder phase, a more gradual and less pronounced evolution of the porous structure is observed during hydration. In particular, for M-S-H, the formation of the gel microstructure seems to be governed by the original spaces between MgO and silica particles and within silica aggregates and agglomerates, into which water can enter promoting magnesium silicate precipitation by dissolution of the reactants and transport of ions. The final pore distribution is compatible with the globular structure of M-S-H proposed by Chiang et al. [8].

Acknowledgments

This work was supported by Ministero dell'Istruzione, Università e Ricerca scientifica - MIUR (FIR2013 Project RBFR132WSM).

Appendix A. Supplementary data

Supplementary data related to this article can be found at http://dx.doi.org/10.1016/j.micromeso.2017.05.031.

References

[1] S.A. Walling, J.L. Provis, Chem. Rev. 116 (2016) 4170–4204 and references therein.
[2] D.R.M. Brew, F.P. Glasser, Cem. Concr. Res. 35 (2005) 85–98.
[3] Z. Li, T. Zhang, J. Hu, Y. Tang, Y. Niu, J. Wei, Q. Yu, Constr. Build. Mater. 61 (2014) 252–259.
[4] C. Roosz, S. Grangeon, P. Blanc, V. Montouillot, B. Lotenbach, P. Henocq, E. Giffaut, P. Vieillard, S. Gaboreau, Cem. Concr. Res. 73 (2015) 228–237.
[5] S.A. Walling, H. Kinoshita, S.A. Bernal, N.C. Collier, J.L. Provis, Dalton Trans. 44 (2015) 8126–8137.
[6] B. Lotenbach, D. Nied, E. L'Hôpital, G. Achiedo, A. Dauzères, Cem. Concr. Res. 77 (2015) 60–68.
[7] M. Tonelli, F. Martini, L. Calucci, E. Fratini, M. Geppi, F. Ridi, S. Borsacchi, P. Baglioni, Dalton Trans. 45 (2016) 3294–3304.
[8] W.-S. Chiang, G. Ferraro, E. Fratini, F. Ridi, Y.-Q. Yeh, U.-S. Jeng, S.-H. Chen, P. Baglioni, J. Mater. Chem. A 2 (2014) 12991–12998.
[9] P. Le, E. Fratini, K. Ito, Z. Wang, E. Mamontov, P. Baglioni, S.-H. Chen, J. Colloid Interf. Sci. 469 (2016) 157–163.
[10] H.M. Jennings, Cem. Concr. Res. 38 (2008) 275–289.
[11] J.-P. Korb, Curr. Opin. Colloid Interface Sci. 14 (2009) 192–202.
[12] P.F. Faure, S. Rodts, Magn. Reson. Imaging 26 (2008) 1183–1196.
[13] V. Bortolotti, P. Fantazzini, R. Mongiorgi, S. Sauro, S. Zanna, Cem. Concr. Res. 42 (2012) 577–582.
[14] A. Valori, P.J. McDonald, K.L. Scrivener, Cem. Concr. Res. 49 (2013) 65–81.
[15] J. Greener, H. Peemoeller, C. Choi, R. Holly, E.J. Reardon, C.M. Hansson, M.M. Pintar, J. Am. Ceram. Soc. 83 (2000) 623–627.
[16] V. Bortolotti, R.J.S. Brown, P. Fantazzini, M. Mariani, Micropor. Mesopor. Mater. 178 (2013) 108–112.
[17] V. Bortolotti, L. Brizi, R.J.S. Brown, P. Fantazzini, M. Mariani, Langmuir 30 (2014) 10871–10877.
[18] P.J. McDonald, V. Rodin, A. Valori, Cem. Concr. Res. 40 (2010) 1656–1663.
[19] A.C.A. Muller, K.L. Scrivener, A.M. Gajewicz, P.J. McDonald, Micropor. Mesopor. Mater. 178 (2013) 99–103.
[20] A. Pop, C. Badea, I. Ardelean, Appl. Magn. Reson. 44 (2013) 1223–1234.
[21] M.W. Bligh, M.N. d'Eurydice, R.R. Lloyd, C.H. Arns, T.D. Waite, Cem. Concr. Res. 83 (2016) 131–139.
[22] K.R. Brownstein, C.E. Tarr, Phys. Rev. A 19 (1979) 2446–2453.
[23] W.P. Halperin, J.-Y. Jehng, Y.-Q. Song, Magn. Reson. Imaging 12 (1994) 169–173.
[24] M. Gombia, V. Bortolotti, B. De Carlo, R. Mongiorgi, S. Zanna, P. Fantazzini, J. Phys. Chem. B 114 (2010) 1767–1774.
[25] A.C.A. Muller, K.L. Scrivener, A.M. Gajewicz, P.J. McDonald, J. Phys. Chem. C 117 (2013) 403–412.
[26] S. Meiboom, D. Gill, Rev. Sci. Instrum. 29 (1958) 688–691.
[27] F. Martini, M. Tonelli, L. Calucci, M. Geppi, F. Ridi, S. Borsacchi, Cem. Concr. Res., submitted for publication.
[28] M. Tonelli, F. Martini, L. Calucci, M. Geppi, S. Borsacchi, F. Ridi, Phys. Chem. Earth, in press DOI: http://dx.doi.org/10.1016/j.pce.2017.01.011.
[29] G.C. Borgia, R.J.S. Brown, P. Fantazzini, J. Magn. Reson. 132 (1998) 65–77.
[30] G.C. Borgia, R.J.S. Brown, P. Fantazzini, J. Magn. Reson. 147 (2000) 273–285.
[31] V. Bortolotti, R.J.S. Brown, P. Fantazzini UpenWin, A Software for Inversion of Multiexponential Decay Data for Windows System ©, Alma Mater Studiorum – Università di Bologna, 2012. http://software.dicam.unibo.it/upenwin%20.
[32] Mathematica, Version 10, Wolfram Research, Inc., Champaign, IL, 2010.
[33] S. AnMing, Y. Wu, Sci. China-Tech. Sci. 53 (2010) 1471–1476.
[34] V.M. Gun'ko, I.F. Mironyuk, V.I. Zarko, E.F. Voronin, V.V. Turov, E.M. Pakhlov, E.V. Goncharuk, I.M. Nychiporuk, N.N. Vlasova, P.P. Gorbik, O.A. Mishchuk, A.A. Chuiko, T.V. Kulik, B.B. Palyanytsya, S.V. Pakhovchishin, J. Skubiszewka-Zięba, W. Janusz, A.V. Turov, R. Leboda, J. Colloid Interf. Sci. 289 (2005) 427–445.
[35] F. Ridi, E. Fratini, P. Luciani, F. Winnefeld, P. Baglioni, J. Colloid Interf. Sci. 364 (2011) 118–124.
[36] A.C.A. Muller, K.L. Scrivener, J. Skibsted, A.M. Gajewicz, P.J. McDonald, Cem. Concr. Res. 74 (2015) 116–125.
[37] G. Land, D. Stephan, J. Mater. Sci. 47 (2012) 1011–1017.
[38] L.P. Singh, S.R. Karade, S.K. Bhattacharyya, M.M. Yousuf, S. Ahalawat, Constr. Build. Mater. 47 (2013) 1069–1077.
[39] D. Kong, Y. Su, X. Du, Y. Yang, S. Wei, S.P. Shah, Constr. Build. Mater. 43 (2013) 557–562.
[40] L.P. Singh, A. Goel, S.H. Bhattacharyya, G. Mishra, Front. Struct. Civ. Eng. 10 (2016) 162–167.

Please cite this article in press as: F. Martini, et al., Monitoring the hydration of MgO-based cement and its mixtures with Portland cement by ^{1}H NMR relaxometry, Microporous and Mesoporous Materials (2017), http://dx.doi.org/10.1016/j.micromeso.2017.05.031

Monitoring the hydration of MgO-based cement and its mixtures with Portland cement by ^{1}H NMR relaxometry

Francesca Martini,[a,b] Silvia Borsacchi,[b,*] Marco Geppi,[a,b] Monica Tonelli,[c] Francesca Ridi,[c] Lucia Calucci[b,*]

[a]*Dipartimento di Chimica e Chimica Industriale, Università di Pisa, via G. Moruzzi 13, 56124 Pisa, Italy*

[b]*Istituto di Chimica dei Composti OrganoMetallici, Consiglio Nazionale delle Ricerche – CNR, S.S. di Pisa, via G. Moruzzi 1, 56124 Pisa, Italy*

[c]*Dipartimento di Chimica "Ugo Schiff" & CSGI, Università di Firenze, via della Lastruccia 3, 50019 Sesto Fiorentino (FI), Italy*

---

[*] Corresponding authors: Silvia Borsacchi, Istituto di Chimica dei Composti OrganoMetallici, Consiglio Nazionale delle Ricerche – CNR, S.S. di Pisa, via G. Moruzzi 1, 56124 Pisa, Italy. Phone: +39-0503153052, e-mail:silvia.borsacchi@pi.iccom.cnr.it; Lucia Calucci, Istituto di Chimica dei Composti OrganoMetallici, Consiglio Nazionale delle Ricerche – CNR, S.S. di Pisa, via G. Moruzzi 1, 56124 Pisa, Italy. Phone: +39-0503152517, e-mail: lucia.calucci@pi.iccom.cnr.it

Sample preparation

CEM I Portland cement was obtained from Italcementi (Bergamo, Italy); its composition is reported in Table S1. Highly reactive magnesium oxide (MgO, ≥99%, reactivity 80 s with the Van der Merwe test [1], BET surface area 121 m^2/g) and fumed silica (SiO_2, ≥99%, BET surface area 395 m^2/g) were supplied by Sigma-Aldrich.

Pastes were prepared by manually mixing 0.5 g of solid with 1 g of ultrapure water; the composition of the dry mixtures is reported in Table S2 together with the abbreviated notations used throughout the paper to indicate the samples. For MS100 and MS80C20 a high water to solid ratio (w/s = 2) was necessary to obtain workable pastes. For the sake of comparison, the same w/s ratio was used also for the other samples; in the case of Portland cement, a slurry was obtained upon mixing and water in excess was expelled from the solid during cement hardening.

Table S1. Main constituents of CEM I Portland cement.

Chemical composition (wt%)	
CaO	66.60
SiO_2	19.81
Al_2O_3	5.41
Fe_2O_3	3.96
MgO	2.50
SO_3	1.25

Table S2. Portland cement (C), MgO (M), and SiO_2 (S) content (wt%) in the dry mixtures used for preparing the pastes.

Sample	C	M	S
C100	100	0	0
MS20C80	80	8	12
MS50C50	50	20	30
MS80C20	20	32	48
MS100	0	40	60

^{1}H T_2 analysis

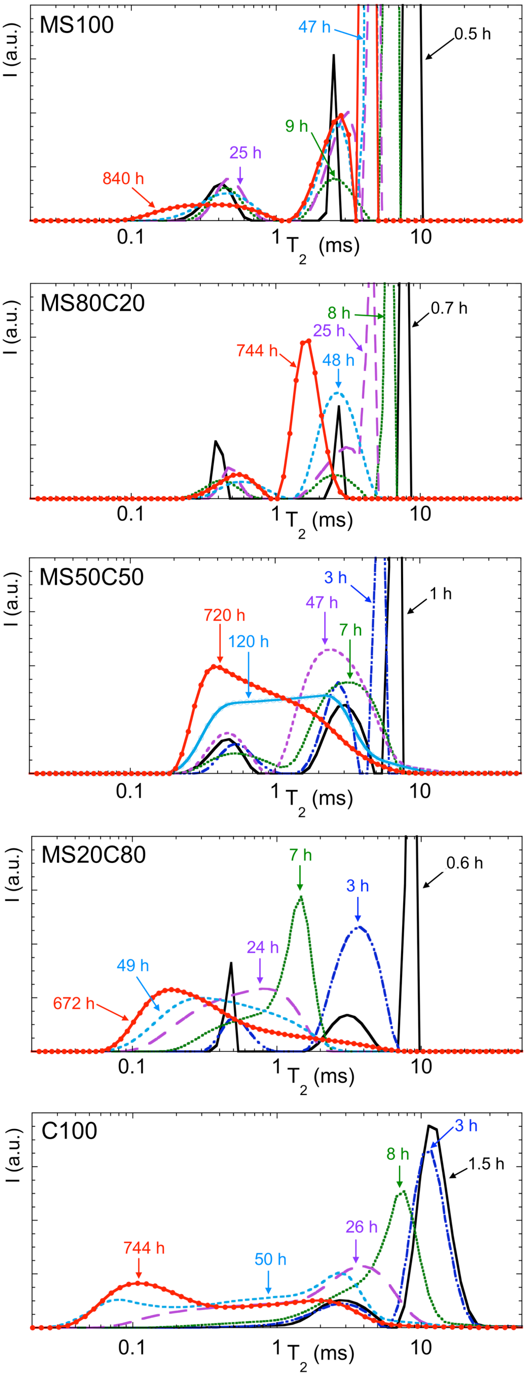

Figure S1. Vertical expansions of the ^{1}H T_2 relaxation time distributions shown in Figure 1.

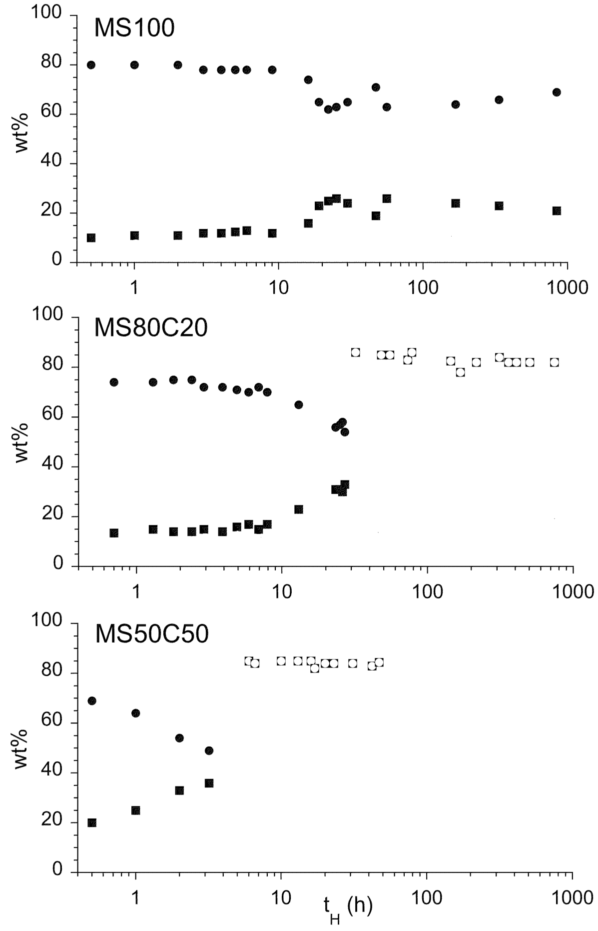

Figure S2. Populations of water protons relative to T_2 peaks obtained from the analyses of CPMG decays by the UPEN algorithm. Symbols ● and ■ are for the more mobile and less mobile free water components, respectively, while symbol □ is for free water at longer hydration times becoming water in the interhydrate spaces. The corresponding T_2 values are reported in Figure 2. For C100 and MS20C80, populations of water protons are not reported because T_2 peaks are not resolved already at short t_H values.

Low Temperature Differential Scanning Calorimetry measurements

Experimental

Low Temperature Differential Scanning Calorimetry (LT-DSC) measurements were performed by means of a Q2000 DSC, TA Instruments (New Castle, USA). MS100 and C100 pastes were prepared by manually mixing water with MgO/SiO_2 and Portland cement, respectively, with a w/s ratio of 2. After 24 hours of hydration, samples were crashed and put under water at 20 ºC, in order to saturate the porosity. Roughly 40 mg of each paste (MS100 and C100) were withdrawn after 28 days of hydration and closed in aluminum pans. The temperature program for each measurement was: ramp to -80 ºC at 0.5 ºC/min; equilibrate to 25 ºC.

Results

The cooling scan of the LT-DSC thermograms obtained for MS100 and C100 samples at 28 days of hydration are reported in Figure S3.

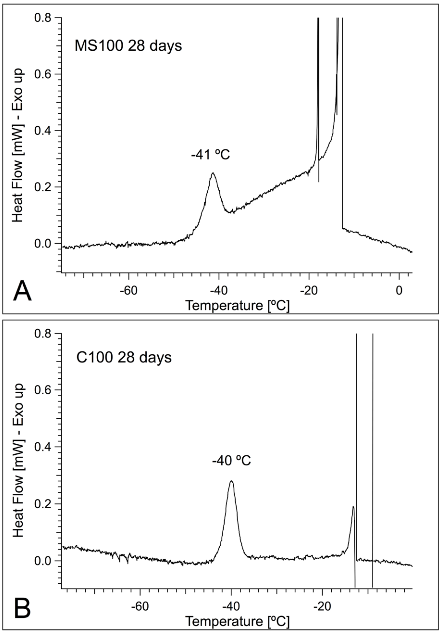

Figure S3. Cooling scans of the thermograms of the MS100 (A) and C100 (B) cement pastes at 28 days of hydration.

The results showed that, upon slow cooling, the freezing of water present in the samples occurs at sub-zero temperatures, showing well-defined peaks. A sharp peak between -10 and -20 °C is present, due to crystallization of bulk water, while water confined in nanometric pores freezes at lower temperatures [2-6]. In particular, a characteristic peak centered at ~ -40 °C can be observed in both samples; furthermore MS100 also shows another broad feature in the temperature range between -25 and -35 °C. According to the literature, these peaks are indicative of water confined in pores whose size ranges between 1-3 nm (~-40 °C) and 3-12 nm (between -25 and -35 °C) [5, 6].

Jennings Colloidal Model for C-S-H

According to the Jennings Colloidal Model [7], the porosity inside C-S-H can be classified in *capillary pores* (whose radius is larger than 12 nm, where water behaves like bulk water), *large gel pores* (LGP, approximately between 3 and 12 nm), *small gel pores* (SGP, in the range 1-3 nm) and *intra-globular pores* (IGP, < 1 nm), as sketched in Figure S4. In the IGP pores the confinement is so significant that water is not able to freeze: as a consequence no peak can be detected in DSC thermograms. On the contrary, it is reported in the literature that the features around -40 °C and in the -25 to -35 °C range account for SGP and LGP, respectively [5, 6].

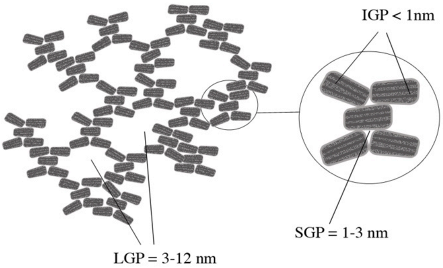

Figure S4. Schematic representation of the Jennings Colloidal Model-II (CM-II) for C-S-H microstructure. Adapted with permission from *Ridi et al., J. Phys. Chem. B 2009, 113, 3080–3087*. Copyright 2009 American Chemical Society.

References

[1] E.M. Van der Merwe, C. Strydom, A. Botha, J. Therm. Anal. Calorim. 77 (2004) 49-56.
[2] M. Brun, A. Lallemand, J.F. Quinson, C. Eyraud, Thermochim. Acta 21 (1977) 59-87.
[3] K. Ishikiriyama, M. Todoki, J. Colloid Interface Sci. 171 (1995) 103-111.
[4] M.R. Landry, Thermochim. Acta 433 (2005) 27-50.
[5] F. Ridi, E. Fratini, P. Baglioni, J. Phys. Chem. C 117, (2013) 25478-25487.
[6] F. Ridi, P. Luciani, E. Fratini, P. Baglioni, J. Phys. Chem. B 113 (2009) 3080-3087.
[7] H.M. Jennings, Cem. Concr. Res. 38 (2008) 275-289.

Paper V

LANGMUIR
Invited Feature Article
pubs.acs.org/Langmuir

Water as a Probe of the Colloidal Properties of Cement

Francesca Ridi,[†] Monica Tonelli,[†] Emiliano Fratini,*,[†] Sow-Hsin Chen,[‡] and Piero Baglioni*,[†]

[†]Department of Chemistry "Ugo Schiff" and CSGI, University of Florence, via della Lastruccia 3-Sesto Fiorentino, I-50019 Florence, Italy

[‡]Department of Nuclear Science and Engineering, Massachusetts Institute of Technology, Cambridge, Massachusetts 02139, United States

ABSTRACT: Cement is produced by mixing mineral phases based on calcium silicates and aluminates with water. The hydration reaction of the mixture leads to a synthetic material with outstanding properties that can be used as a binder for construction applications. Despite the importance of cement in society, for a long time, the chemical reactions involved in its hydration remained poorly understood as a result of the complexity of hydration processes, nanostructure, and transport phenomena. This feature article reviews the recently obtained results using water as a probe to detail the essential features in the setting process. By examining the peculiar physicochemical properties of water, fundamental information on the evolving inorganic colloid matrix can be deduced, ranging from the fractal nanostructure of the inorganic silicate framework to the transport phenomena inside the developing porosity. A similar approach can be transferred to the investigation of a plethora of other complex systems, where water plays the main role in determining the final structural and transport properties (i.e., biomaterials, hydrogels, and colloids).

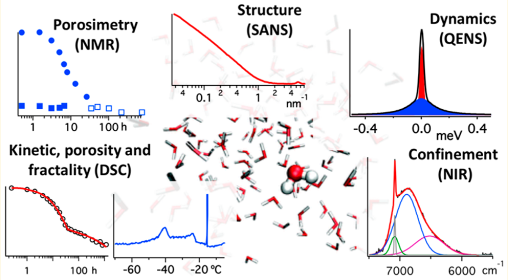

1. INTRODUCTION

The discovery of the pozzolanic reaction of volcanic materials mixed with lime and water was boasted as one of the most revolutionary innovations in history. Before the Romans, other ancient civilizations used nonhydraulic binders to build long-lasting structures such as the Great Wall in China and the Egyptian pyramids. The incredible benefits related to the addition of pozzolan to lime were the ability to set without the presence of carbon dioxide, even under water, and the impressive increase in mechanical properties. These characteristics enabled the construction of the renowned Roman aqueducts, bridges, and many other architectural structures that enormously contributed to the expansion of the Roman Empire. In modern times, three fundamental developments improved the Roman recipe for cement: the introduction of gypsum that avoids flash setting; the higher temperatures used to fire the raw materials, allowing for a more rapid setting process; and the advancement of the grinding process to increase the specific surface area available to hydration, which improves the setting process. With these changes, at the end of the XVIII century, modern Portland cement was finally formulated, and that original recipe (with few refinements) is still the most used hydraulic binder for building purposes.[1]

Cement is a complex solid that is both structurally and chemically heterogeneous. The chemical and mineralogical composition of cement formulations is variable, depending on the composition of the raw materials extracted from quarries and on the addition of extra components aimed at tuning its reactivity. With the advancement in technical knowledge, the ordinary Portland cement composition has been modified, producing several types of cements with different properties, to match specific applications. Today, a plethora of hydraulic cements are known and categorized. A summary of the most relevant is reported in Table 1. The compositions and properties of these systems are very different to cover very different applications ranging from building materials[2,3] to cement for biomedical purposes such as bone repair and orthodontics.[4] Currently, magnesium-based cements are suited for specialist applications to take advantage of their potential for CO_2 emission reduction. However, the high cost of the raw materials and the final pH not sufficiently high to passivate steel reinforcing bars limit their use and the possibility of replacing ordinary Portland cements.[3] Considering the field of cements for structural applications, magnesium silicate cement is an emerging material that finds application in the encapsulation of problematic radioactive wastes.[5−7] In addition, magnesium silicate cement is significant from a physicochemical point of view. Specifically, upon contact with water, it develops a hydrated phase (magnesium silicate hydrate, M−S−H) that is analogous to calcium silicate hydrate (C−S−H), the main binder of Portland cement. Therefore, cation substitution produces significant modifications in both the properties and structure of the hydrated phase.[8,9]

Water is one of the initial components of a cement paste and is progressively consumed during the development of the hydration products during the curing process. Therefore, the observation

Received: July 3, 2017
Revised: October 13, 2017
Published: October 16, 2017

DOI: 10.1021/acs.langmuir.7b02304

Table 1. Classification of Hydraulic Cements Based on Their Applications and Some of Their Main Hydration Reactions

construction and building applications		biomedical applications[10]	
material	main hydration reactions	material	main hydration reactions
Portland cement	$Ca_3SiO_5 + (1.3 + x)H_2O \rightarrow (CaO)_{1.7}SiO_2(H_2O)_x + 1.3Ca(OH)_2$	calcium phosphate	apatitic cements: $3\alpha\text{-}Ca_3(PO_4)_2 + H_2O \rightarrow Ca_9(PO_4)_5HPO_4OH$
	$Ca_2SiO_4 + (0.3 + x)H_2O \rightarrow (CaO)_{1.7}SiO_2(H_2O)_x + 0.3Ca(OH)_2$		brushite-based cements: $\beta\text{-}Ca_3(PO_4)_2 + Ca(H_2PO_4)_2H_2O + 7H_2O \rightarrow 4CaHPO_42H_2O$
	$2Ca_3Al_2O_6 + 12H_2O \rightarrow (CaO)_3Al_2O_3(H_2O)_6$		$\beta\text{-}Ca_3(PO_4)_2 + H_3PO_4 + 6H_2O \rightarrow 3CaHPO_42H_2O$
	$Ca_3Al_2O_6 + 3CaSO_4{\cdot}(H_2O)_2 + 26H_2O \rightarrow (CaO)_6Al_2O_3(SO_4)_3(H_2O)_{32}$		
Portland cement blends	$Ca_3SiO_5 + (1.3 + x)H_2O \rightarrow (CaO)_{1.7}SiO_2(H_2O)_x + 1.3Ca(OH)_2$	calcium sulfate	$CaSO_4{\cdot}0.5H_2O + 1.5H_2O \rightarrow CaSO_4{\cdot}2H_2O$
	$Ca_2SiO_4 + (0.3 + x)H_2O \rightarrow (CaO)_{1.7}SiO_2(H_2O)_x + 0.3Ca(OH)_2$		
	$2Ca_3Al_2O_6 + 12H_2O \rightarrow (CaO)_3Al_2O_3(H_2O)_6$		$CaSO_4 + 2H_2O \rightarrow CaSO_4{\cdot}2H_2O$
	$Ca_3Al_2O_6 + 3CaSO_4{\cdot}(H_2O)_2 + 26H_2O \rightarrow (CaO)_6Al_2O_3(SO_4)_3(H_2O)_{32}$		
magnesium phosphate cements	$2MgO + 2NH_4H_2PO_4 + 10H_2O \rightarrow 2NH_4MgPO_4\ 6H_2O$	calcium silicate	$Ca_3SiO_5 + (1.3 + x)H_2O \rightarrow (CaO)_{1.7}SiO_2(H_2O)_x + 1.3Ca(OH)_2$
magnesium silicate hydrate cements	$xMgO + yH_2O + SiO_2 \rightarrow (MgO)_x(SiO_2)(H_2O)_y$	magnesium phosphate	$2\ MgO + 2NH_4H_2PO_4 + 10H_2O \rightarrow 2NH_4MgPO_4\ 6H_2O$
			$Mg_3(PO_4)_2 + (NH_4)_2HPO_4 + 15H_2O \rightarrow 2\ MgNH_4PO_4{\cdot}6H_2O + MgHPO_4{\cdot}3H_2O$
magnesium oxychloride (Sorel) cements	$3MgO + MgCl_2 + 11H_2O \rightarrow 3\ Mg(OH)_2{\cdot}MgCl_2{\cdot}8H_2O$		
calcium sulfoaluminate cements	$(CaO)_4(Al_2O_3)_3(SO_3) + CaSO_4 + 38H_2O \rightarrow (CaO)_6Al_2O_3(SO_3)_3(H_2O)_{32} + 4Al(OH)_3$		
alkali-activated cements[10−12]	$CaO{-}SiO_2{-}MgO{-}Al_2O_3 + H_2O$ (activated with NaOH) $\rightarrow (CaO)_ySiO_2(H_2O)_x + (Mg_6Al_2CO_3(OH)_{16}{\cdot}4H_2O) + CaCO_3 +$ AFm phases		

of the physicochemical properties of water during hydration allows monitoring of the reaction kinetics and structural/dynamical features that are difficult to investigate by examining the large number of products formed during the setting process. The chemical reactions that form hydrated binding phases start with a dissolution process, followed by the nucleation and growth of hydrated phases, and continue until the rate of the reaction is limited by the diffusion of water into the growing phases. These two latter stages are responsible for the final cement properties. Furthermore, cement is an exemplary system because most of the characterization methods detailed in this feature article can be applied to study different microporous and mesoporous water-containing materials to obtain information on their properties. In the following paragraphs, we will outline the major results achieved using a multitechnique approach to monitor cement characteristics at different length and time scales using water as an in situ probe.

2. HYDRATION KINETICS

The hydration kinetics have a direct impact on the evolution of the hydrated cement microstructure, which in turn influences the mechanical properties and durability of the concrete, affecting important characteristics such as strength, elastic moduli, toughness, diffusivity, and permeability to liquids and gases.[13] The complex reactions taking place between the anhydrous phases and water can be considered to be the main cause of the setting and hardening of cement pastes, and because of their exothermic nature, the hydration process is usually monitored using calorimetry, such as heat of solution calorimetry, semiadiabatic–adiabatic calorimetry, and isothermal conduction calorimetry (IC). From an industrial point of view, IC is probably the most used technique to access the hydration kinetics in the cement research field. However, this approach presents some drawbacks because the hydration process can be followed only during the early stage of hydration. A few days after mixing, the evolved heat becomes too low to be distinguished from the instrumental baseline, which prevents the use of IC in the case of slowly curing cement formulations, such as those containing retarding agents. To overcome this limit, we proposed an alternative method based on differential scanning calorimetry (DSC),[14,15] where the evolution of unreacted water can be quantified in terms of a free or freezable water index (FWI).[14,16] In this approach, cement pastes are periodically frozen at −60 °C and then melted at a constant rate. Figure 1 shows the decrease in time of the melting peak of the free, still unreacted, water for a Portland cement paste.

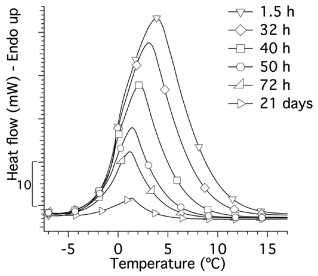

Figure 1. Evolution of the melting enthalpy of water during the hydration of a Portland cement sample (w/c = 0.4).

The ice melting peak is integrated to extract the melting enthalpy ΔH_{exp} of water and to calculate the FWI

$$\mathrm{FWI} = \frac{\Delta H_{exp}}{\phi_w \Delta H_{theor}} \qquad (1)$$

where ϕ_w is the original weight fraction of water in the paste and ΔH_{theor} is the theoretical melting enthalpy of water (333.4 J/g). In the original paper,[14] it was proven that FWI results are not affected by freeze−thaw damage expansion taking place during the DSC measurements.

Moreover, some of the authors[15] showed that hydration kinetics obtained by DSC (see, for example, Figure 2B) fully agree with those achieved from the IC technique on the very same cement paste (Figure 2A). Because DSC is based on discrete measurements, it is not limited by the evolved heat or baseline stability allowing the acquisition of data until the very end of the hydration process. Similar to IC, the DSC technique is able to capture the effect of parameters such as the water/cement ratio or temperature on the hydration kinetics.

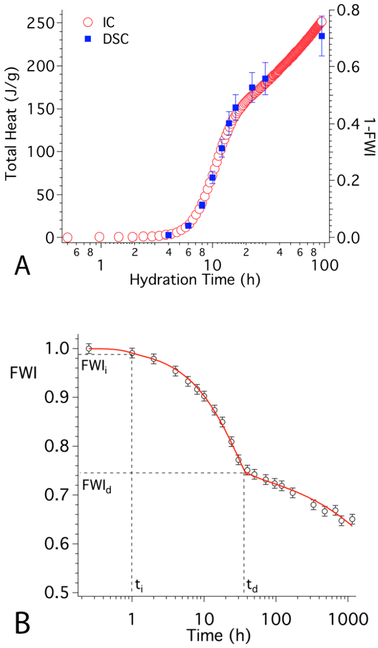

Figure 2. (A) Comparison between DSC and IC data monitoring of the hydration process of a tricalcium silicate paste ($w/c = 0.4$). Reproduced with permission from ref 15. (B) Hydration kinetics of a MgO/SiO_2 paste reported as FWI vs time. Black markers represent the experimental data; the red line represents the global fitting curves according to the BNGM + diffusional model. Adapted with permission from ref 28.

Kinetic analysis was used to obtain information on activation energies and rate constants of the developing hydrated phases. The hydration of cement powders is a complex multistage process with a well-known scheme: an initial hydration process, when the wetting of highly hygroscopic particles occurs; an induction period, when the reaction is quiescent; an acceleration period, when the nucleation and growth processes greatly increase the rate of the hydration reaction and the formation of several colloidal phases; a deceleration period; and finally, a diffusional period, where the reaction proceeds at a slower rate and the rate-limiting process is the diffusion of water through the hydrated products toward the anhydrous cores.[11,15,17,18] In past decades, the nucleation and growth stage taking place during the hydration of tricalcium silicate (C_3S) was modeled using Avrami-Erove'ev (AE) kinetic law[19−22] to extract the rate constants of the processes. In this framework, the DSC method was applied to investigate the effect of some of the most used cement additives, using the AE law for the acceleration period and a three-dimensional diffusion equation for the final part of the FWI curve.[16] More recently, some authors noted that the AE equation cannot completely explain the cement hydration process. Above all, the assumption that the probability of nucleation of the hydrating phases is the same elsewhere is not appropriate because it is commonly accepted that it occurs preferentially at the grain boundaries.[23] The boundary nucleation and growth model (BNGM) derived by Thomas overcomes this inconsistency.[24,25] This model, which was originally developed for solid-phase transformation,[26] can properly describe the process of cement hydration, even using fewer parameters than in the AE model. BNGM describes the hydration kinetics with two independent rate constants: k_B, which "describes the rate at which the surfaces become covered with hydration product" and k_G, which is the "rate at which the pore space between the particles fills in with product".[24,25] Then, the original BNGM approach developed for IC was modified to directly analyze the time evolution of FWI as accessed by the DSC protocol. In particular, an extra independent parameter was added to estimate the fraction of unreacted water, and any assumption on the hydration reaction stoichiometry was avoided. It was shown that the application of the model on kinetic profiles obtained by IC and DSC provides comparable results, which further validates the FWI approach.[15] Therefore, DSC was applied by our group to investigate the effects of particle size, temperature,[15] and additive addition[27] on the hydration reaction in cement pastes even for very long processes, such as those obtained with the so-called superplasticizing additives.

Some of the authors of this article recently proposed the application of BNGM[25] combined with a three-dimensional diffusional model to quantitatively describe the nucleation and growth processes during the hydration of the new green cements based on MgO/SiO_2 formulations.[28] Figure 2B shows the FWI vs time for the MgO/SiO_2 sample together with the best-fit curve obtained using the BNGM + diffusional combined model. The model accurately describes all three hydration periods. The curve shows the short initial induction period lasting until t_i is reached, where FWI remains ∼1; the nucleation and growth period, with a consistent decrease in FWI, which lasts up to ∼40 h; and the final diffusional period, starting at time t_d where the change in the curve slope suggests that the rate-limiting step becomes a diffusion-limited process, similar to the Portland case. These results agree with ^1H NMR relaxometry that follows the kinetics using the evolution of the transverse (T_2) spin relaxation time signal in MgO/SiO_2 pastes.[29]

The kinetics profiles associated with a curing cement paste simply detail the overall hydration reaction. During the different stages, the hydrated phases develop to yield the well-known porous structure, which is typical for cement systems. The characterization of the pore structure (i.e., total porosity, pore size distribution, and eventually specific surface area) is one of the key factors in the prediction of the final performances of cement. For example, it is known that a highly durable cement/concrete will have mostly gel pores (<5 nm) hydraulically isolated from each other.[30−32] However, accessing the porosity in detail is not trivial because of the complexity of the pore size distribution, which, in the case of a cement paste, ranges from a few nanometers to tens of micrometers, and even because many techniques require a dried sample with possible changes in the original porous structure. For these given reasons, experimental techniques that do not need a drying step (i.e., DSC, small-angle scattering, nuclear magnetic resonance, etc.) have a significant advantage with respect to all others (i.e., gas sorption, mercury intrusion, electron microscopy, etc.).

3. POROSITY AND FRACTALITY OF HYDRATING PHASES

Thermoporometry enables the characterization of a porous material, i.e., pore sizes, by analyzing the conditions of the solid−liquid phase transition of a condensate inside a porous matrix.[33] The method relies on the experimental evidence that when a pure substance is confined in nanometric cavities the equilibrium conditions of its solid, liquid, and gas phases depend on the curvature of the interface.[34] Therefore, the solidification/melting temperature of a liquid confined in a porous material changes with the size of the pores, and the energy involved in the phase transition is directly related to the pore volume, assuming that the liquid saturates all of the porosity. Furthermore, thermoporometry can also provide information on the shape of the pores by comparing the cooling and heating thermograms obtained in the temperature range from ambient to −80 °C (low-temperature differential scanning calorimetry, LTDSC).[33,35−38]

LTDSC was used to characterize the porosity of cement.[39−45] Bager and Sellevold investigated the formation of ice in mature Portland cement, evaluating the effect of different moisture contents, drying, and resaturation in the volume of large (capillary) and small pores.[39−41] Later, Bentz investigated the percolation of capillary porosity, which is of utmost importance in the transport properties and durability of cement structures.[42] More recently, our group investigated the properties of water confined in hydrating cement pastes,[43] showing that LTDSC thermograms can be fully explained considering the C−S−H microstructure, as described in Jennings' colloidal model II[46] (see next paragraph). LTDSC allows us to investigate matrixes with saturated porosity and can be used to estimate the volume of the meso/macroporosity, the depercolation threshold of capillary porosity (i.e., the separation of capillary pores due to the growth of hydrated phases or in other words the porosity whereby the volume fraction of connected pores in the cement paste decreases to zero), and the fractal dimension of hydrated cementitious samples, with results compatible with those obtained using more sophisticated techniques such as small-angle neutron or X-ray scattering. For example, an in-depth LTDSC investigation evidenced the differences in the microstructure and porosity among C_3S pastes hydrated in pure water and in the presence of organic superplasticizers (i.e., polycarboxylic backbone with grafted PEO chains) used in advanced cement formulations.[44]

The DSC heating scan, as reported in Figure 3A, shows a single hump in the −50 °C/0 °C temperature range as a direct consequence of the pore size distribution of cement microstructure spanning from the nanometer to micrometer scale. During heating, melting of the ice progressively occurs from the fractions confined in the smallest cavities to the fractions present in the largest ones, thus generating the hump. Conversely, the freezing process occurs in a discontinuous way, and the cooling scan shows specific peaks (e.g., Figure 3B). This peculiar behavior is usually attributed to the combination of homogeneous and heterogeneous freezing mechanisms. The homogeneous nucleation is an activated process where a free-energy barrier must be overcome for a critical crystallization nucleus to

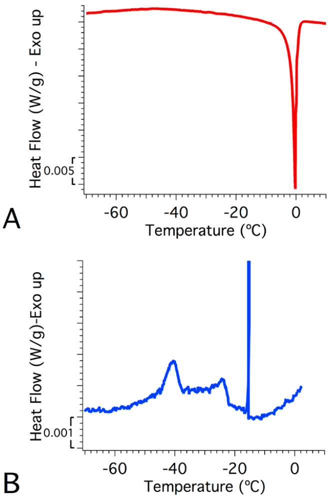

Figure 3. Heating (A) and cooling (B) scans recorded using LTDSC on a cementitious sample saturated with water. Adapted with permission from ref 44.

appear. Thus, the heterogeneous nucleation preferentially occurs because the energy required by this process is smaller. According to the molecular dynamics (MD) study on homogeneous ice nucleation,[47] at a low degree of supercooling ($-20\ °C < T < 0\ °C$), only heterogeneous nucleation is possible because of the high free energy required for the homogeneous formation of a critical nucleus (at $T \approx -15$ °C, diameter ≈ 8 nm corresponding to ∼8000 molecules). For this reason, in a saturated system, water freezes via heterogeneous nucleation even if it is confined in cavities with dimensions that are large enough to host critical nuclei isolated from the surface. Once the water in the large pores (capillary pores) is frozen, the ice remains in contact with the liquid water still present in the smaller cavities. By lowering the temperature to below −20 °C, the size of the critical cluster sensibly decreases (at $T \approx -35$ °C, diameter ≈ 3.5 nm corresponding to ∼600 molecules), and the nucleation free energy barrier decreases, making the homogeneous process likely to occur. Under these conditions, both the homogeneous and heterogeneous nucleation mechanisms become accessible at comparable rates. Then, freezing will occur in the pores whose dimensions can host a critical ice cluster that is stable at that temperature. However, the appearance of peaks in the cooling curve indicate that the process starts at the pore entrance, where the liquid water is in contact with the surrounding ice, which is a preferential site for the nucleation. The dimensional range of these freezing pores must be comparable to the size of their entrance because, for the reasons given before, the water in larger pores is already frozen at this stage, and the smaller pores cannot host a critical ice nucleus. In the case of cement pastes, the developing phases originate from three classes of nanometric porosities on top of the capillary porosity. According to Jennings' colloidal model II,[46] these are named the interlayer lamellar porosity (IGP, <1 nm), small gel pores (SGP, 1−3 nm), and large gel pores (LGP, 3−12 nm). The water inside the lamellar IGP of the primary unit cannot freeze (see paragraph on LTDSC), and thus it cannot be detected using DSC. By integrating each peak in the cooling scan (e.g., Figure 3B), the amount of water contained in different classes of pores (SGP, LGP, and capillary) can thus be obtained after considering the variation with temperature of the standard enthalpy of the fusion of ice.[48]

It is important to stress here that, in addition to pore size effects, the heterogeneous behavior of water crystallization at low T can also be partially ascribed to the different chemical environments experienced by the water molecules. Using the reactive force field MD method, Hou et al.[49] demonstrated that water molecules, which are confined in the nanopores of the C−S−H gel, show heterogeneity in the structure and dynamic behavior, respectively. Water molecules near the surface can react with the high-energy nonbridging oxygen atoms, producing Si−OH and Ca−OH (i.e., chemically bound water in the developing C−S−H phase). Water molecules that are approximately 1 nm away from the chemically bound water (i.e., close to the surface) have a higher arrangement, longer exchange time, and lower diffusion coefficient than bulk water because of both the strong H-bond with oxygen atoms in silicate chains and the ionic effect induced by the highly concentrated surface calcium ions.[49−51] Because of the strong hydrophilic effect from the C−S−H surface, more energy is needed for the surface-adsorbed water molecules to overcome the energy barrier to transform into ice crystals. This restriction is particularly pronounced for the water molecules confined in the nanometer pores. Moreover, the chemical composition of the C−S−H gel is also very important for influencing the thermodynamic behavior of gel pore water molecules.[52] Even if the pore size is the same, C−S−H with a lower Ca/Si ratio can reduce the diffusion rate of the interlamellar pore water to a greater extend because the protruded bridging tetrahedron has a higher tendency to disturb the transport channel that exists in the gel porosity.

The LTDSC method is useful for studying the porosity of samples containing water regardless of their composition. For example, Figure 4 shows two thermograms obtained from cementitious samples hydrated for 28 days whose composition is very different from the standard one (i.e., the water/solid ratio, w/c, is 2 instead of 0.4). In particular, Figure 4A shows the cooling scan of MgO/SiO_2: the shape of the curve indicates that, similar to C−S−H-containing matrixes, this sample has a fraction of water confined in large (capillary) pores where the liquid can freeze via heterogeneous nucleation, and another fraction that is confined in smaller pores gives rise to the large bump between −20 and −35 °C and to the sharp peak at −41 °C. Figure 4B shows Portland cement hydrated for the same time and with the same w/c: the thermogram shows that when the amount of water is high, only the capillary porosity remains, together with the porosity in the 1−3 nm range (SGP), which is a structural characteristic of the Portland-based samples. The significant difference existing between the two thermograms (in the region of −20 °C/−40 °C) can be further understood by considering the difference existing in the structure and the enclosed porosity of the two main hydration products (M−S−H and C−S−H), as we will discuss later in this article.

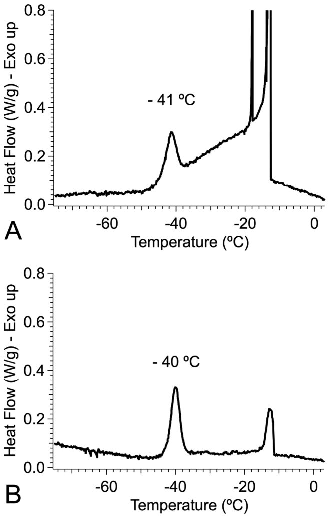

Figure 4. LTDSC cooling scans recorded on (A) MgO/SiO_2 paste and (B) Portland cement paste; both with $w/c = 2$, hydrated for 28 days and saturated with water. Adapted with permission from ref 103.

As already mentioned, the pore size distribution, $P(r)$, determines the hump in the heating part of the thermogram. Thus, in principle, it should contain information on the fractal arrangement of the cementitious matrix, which is the result of how the primary units are assembled into the volume generating the porosity of the hydrated phase. Mass and surface fractal dimensions (D_m, D_s, respectively) are usually obtained using small-angle scattering techniques, as reported in the literature for various cement pastes.[53−55] The fractal nature of porous matrixes can also be determined using DSC by relying on the fact that the melting temperature of an ice crystal confined in a pore of radius R (with $R = r - l$, where r is the radius of the pore and l is the thickness of the nonfreezable layer of water at the solid interface) is depressed by a quantity $\Delta T = T_m^0 - T_m$. Previous estimations from NMR measurements on porous glasses report a value for l of 0.5 ± 0.1 nm.[56] This is the reason that the water confined in IGP within the calcium silicate layers does not freeze, and the size of these pores is approximately 1 nm. The Gibbs−Thomson equation states that the melting temperature, T_m, and the pore radius, R, are inversely related as follows

$$T_m = T_m^0\left(\frac{1 - 2\gamma V_s}{\Delta HR}\right) \qquad (2)$$

where T_m^0 is the melting temperature of an ice crystal of infinite dimension, γ is the solid−liquid interfacial tension, ΔH is the specific melting heat, and V_s is the specific volume of the solid. Considering water (i.e., $T_m^0 = 273.15$ K, $\gamma = 40 \times 10^{-3}$ N m^{-1}, $\Delta H = 334$ J g^{-1}, and $V_s = 1.02$ cm^3 g^{-1}), eq 2 becomes

$$\Delta T = \frac{68.29}{R} \qquad (3)$$

with R in nanometers.

When a water-saturated porous sample, with a pore size distribution of $P(r)$, is heated from −80 °C to room temperature, the melting of the liquid confined in pores of progressively increasing dimensions occurs. Then, the heat flux registered by DSC is proportional to the incremental volume dV of the ice melting at a given temperature, T_m. If the experimental heating rate is slower than 2 °C/min, then the equilibrium conditions are satisfied[57] so that the detected heat flow is independent of the heating rate and its estimation is quantitative. The incremental pore volume per solid mass can be written as d$V = P(r)$ dr. To obtain dV, the heating signal should be normalized by the total pore volume V_p obtained by integrating the melting peak, scaled by the bulk water density value at 0 °C (0.9998 g/cm^3). According to the literature,[57] the heat flow, J_q, measured using DSC is related to ΔT by a scaling law consistent with the fractal nature of the systems. The porous system can be regarded as a homogeneous solid of density ρ_S, where an incremental pore volume per solid unit mass dV was used to account for the change in the bulk density of the porous sample, $\rho(r)$, as a function of the pore-filling steps.[58] Mathematically, the process is described as

$$\frac{1}{\rho(r)} = \frac{1}{\rho_S} + \int_0^r P(r)\,\mathrm{d}r \tag{4}$$

In the fractal regime, where $a \leq r \leq \xi$, $\rho(r)$ will scale with r as follows

$$\rho(r) = \rho_S (r/a)^{D_m - 3} \tag{5}$$

where a is the characteristic dimension of the smallest repeating unit and ξ is the maximum correlation length of the fractal aggregate. Combining eqs 3 and 5,

$$\mathrm{d}V = A(\Delta T)^{D_m - 3} \tag{6}$$

where A is the scaling factor.

Hence, D_m can be simply obtained from the fitting of the dV vs ΔT log−log plots (Figure 5). This procedure enabled us to investigate the effect of different superplasticizer on the fractality of C_3S pastes.[44] For example, Figure 5 shows the dV vs ΔT log−log plots,and the fitting lines from $\Delta T_\xi \cong 1$ K to $\Delta T_a \cong 10$ K, corresponding to pores with a radius of between 100 and 10 nm (eq 3). The size range explored by DSC is very close to what is usually measured in a standard small-angle scattering experiment.

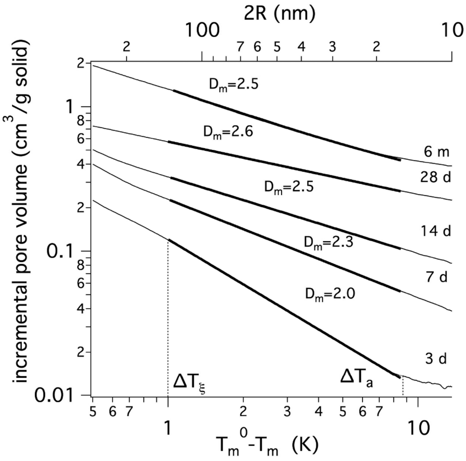

Figure 5. Incremental pore volume per solid mass as a function of the melting depression, $\Delta T = T_m{}^0 - T_m$ for a paste of C_3S/water during hydration. Reproduced with permission from ref 44.

As is reported in Figure 5, a C_3S/water paste ($w/c = 0.4$) has a fractal dimension that increases from 2.0 to 2.6 in the first 28 days of curing.[44] These results are in good agreement with previous SAXS investigations,[53] which reported D_m for a similar paste to vary from 1.9 to 2.8 in the same time interval. The same approach was also used on C_3S/water samples containing superplasticizers to highlight their effect on both C−S−H nanostructure and porosity. The D_m values for pastes cured for 1 month in the presence of superplasticizers resulted in lower values than in the C_3S/water case, indicating that the presence of superplasticizers causes the formation of a more open nanoscale structure with respect to a pristine sample.

Even if the exact nanostructure of the C−S−H gel is still an active topic of research, Jennings colloidal model CM-II[46,59] represents one of the best micro/nanoscale descriptions reconciling the colloidal nature of cement-based systems with a large amount of experimental data available in the literature. Very recently, CM-II was used as a starting point to work out a detailed mathematical equation that is able to depict the hierarchy of pore sizes giving rise to the fractal structure property of the C−S−H phase,[60] even including the internal structure of the globule.[61] In general, the scattering intensity distribution related to an assembly of anisotropic units can be written as

$$I(Q) = N\langle\overline{P(Q)}\rangle S(Q)_c + \text{bkg} \tag{7}$$

where N is a scaling constant considering the number density and the probe interaction of the globules, $\langle\overline{P(Q)}\rangle$ is the normalized intraparticle structure factor averaged over the distribution of the size and all possible orientations of the globules, $S(Q)_c$ accounts for the interglobule structure factor coming from the fractal arrangement corrected for the polydispersity of the system, Q is the scattering vector, and bkg is the background term. $\langle\overline{P(Q)}\rangle = \langle|F(Q)|^2\rangle$ takes into account the internal layered structure of the primary globules (i.e., $F(Q)$ is the particle form factor; in the case of C−S−H, it describe the scattering of the disklike unit).[60] If the size, orientation, and position of the basic units are uncorrelated, then $S(Q)_c = 1 + \beta(Q)[S(Q) - 1]$ with $\beta(Q) = |\langle F(Q)\rangle|^2/\langle|F(Q)|^2\rangle$. The interparticle structure factor for the fractal arrangement can be expressed as

$$S(Q) = 1 + \left(\frac{\xi}{R_e}\right)^{D_m}\Gamma(D_m + 1)\frac{\sin[(D_m - 1)\tan^{-1}(Q\xi)]}{(D_m - 1)[1 + (Q\xi)^2]^{[D_m - 1/2]}(Q\xi)} \tag{8}$$

where $R_e(3\bar{n}R^2L/4)^{1/3}$ is the equivalent radius (where $\bar{n}$ is average number of stacks in a disklike unit and R and L are defined in Figure 6) and D_m and ξ are the mass fractal and cutoff dimension of the aggregate, as already defined in the LTDSC section.

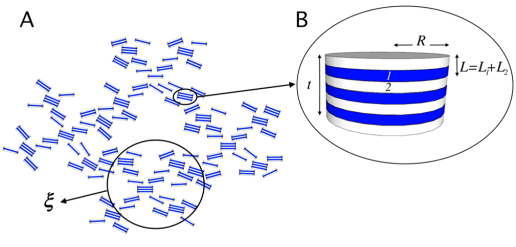

Figure 6. Interparticle (A) and intraparticle (B) structures associated with the fractal arrangement property of the disklike C−S−H units. Adapted with permission from ref 61.

This equation was used to model small-angle scattering curves (from either neutrons or X-rays) with the aim of unveiling the globule shape and size distribution as well as the fractal dimension and correlation distance characteristic of the overall arrangement in the case of the C−S−H phase. It turns out that the disklike shape of the globular unit assumed in CM-II is experimentally confirmed. This approach was used to investigate the effect of the water content[61] and of the addition of comb-shaped superplasticizers[62] on C−S−H synthetic phases.

The decrease in the water content from 30 to 10% caused the shrinkage of the lamellar space characteristic of the IGP and concurrently an increase in the mass fractal dimension from 2.58 to 2.75, which is associated with a reduction in the average globule size from 18 to 12 nm.[61] Moreover, the addition of comb-type superplasticizers resulted in an increase in the average silicate chain length of the C−S−H building block that in the end linearly translated into an increase in dimensions of the globule.[62]

Using the same approach, some of the authors were also able to reconstruct the microstructure of synthetic M−S−H, the principal binding phase in MgO-based cements. In the case of M−S−H, the globule turned out to be spherical in shape, and more importantly, when a mixed M−S−H/C−S−H system is prepared, the two distinct morphologies are still present in the sample,[8] evidencing that these hydrates are not compatible even on the nanoscale. In both cases, a fractal arrangement of the globules is retained. However, globules pack more compactly in M−S−H but in a less extended way (ξ), resulting in a greater fractal exponent than in the C−S−H case. The intrinsic shape difference between the two types of globules in C−S−H and M−S−H gels also reflects in their morphology from submicrometer to micrometer levels and more importantly can be a key parameter in understanding the different mechanical behavior of the MgO-based cements with respect to the better-performing CaO-based equivalent.

4. STATE OF THE WATER: NEAR-INFRARED SPECTROSCOPY, NIR

The confinement and interaction of water within the host system result in different types of water molecules being present in the cement paste (i.e., bulklike, surface-interacting or constrained, and structural). Near-infrared spectroscopy (NIR), which uses wavenumbers from 14 000−4000 cm^{-1}, provides information on the vibrational modes of stretching and bending of bonds where hydrogen is involved and, in particular, on the overtone and combination vibrations.[63] The absorption bands in the NIR region (and in particular the first overtone of the symmetric and antisymmetric O−H stretching mode of water at ∼7000 cm^{-1}) are excellent probes of the state of water because both the strength and geometry of O−H bonds affect the frequency of these peaks.[64−66] Moreover, because of the smaller extinction coefficients with respect to IR, the analysis of samples containing large amounts of water is feasible in the NIR region (i.e., saturation of the signal is not crucial). This characteristic enables the direct analysis of bulk cementitious samples with $w/c = 0.4$ or even higher. The NIR technique, probing thin layers of the samples, can provide information representative of the bulk properties only if the specimen is well-homogenized. According to the literature,[67] the absorption of water in the NIR region can be attributed to two different classes of O−H oscillators, the so-called weakly hydrogen bonded (WHB) and strongly hydrogen bonded (SHB) oscillators. The SHB oscillator has a broad absorption at lower wavenumbers, whereas the WHB oscillator is sharper and centered at higher wavenumbers. A significant increment of the WHB intensity is registered as a result of the increase in temperature[67] or the increase in the confinement effects due to a solid matrix.[65] The existence of two classes of hydrogen bonds in a C−S−H/H_2O system has also been validated by MD simulations[51] showing that the structural hydrogen bond (formed between silicate oxygen atoms and water molecules) has a longer lifetime than the hydrogen bond formed between neighboring water molecules. In the first case, the hydrogen bond is more persistent even if the interaction with the surface induces a change in the local water topology resulting in a reduction in the number of hydrogen bonds[68] (i.e., WHB in the previous notation).

When applied to a hydrating tricalcium silicate paste,[69] the NIR technique allowed the assessment of hydration kinetics by monitoring the decrease with time in the intensity of the 5000 cm^{-1} combination band: this trend follows the hydration profile as obtained using DSC (Figure 7A). The time evolution of the 7000 cm^{-1} overtone band accounts for the evolution of the two types of water coexisting in the matrix: the surface-interacting and the bulklike water. The quantification of these two species was possible by deconvoluting the 7000 cm^{-1} band into Gaussian components, as shown in Figure 7B. Figure 7C shows that the two Gaussian peaks are directly connected to the bulk water; the strongly hydrogen bonded (SHB, named β and γ) component decreases in time, and the α component, associated with the surface-interacting water, weakly hydrogen bonded (WHB) contribution, sensibly increases as a result of the developing surface area.

NIR spectroscopy is also particularly powerful in assessing the state of the confined water. This is possible by taking advantage of the temperature dependence of the NIR bands of water and ice. The behavior of the hexagonal ice NIR bands with temperature is well described in the literature, particularly for the determination of the temperature of icy regions on remote

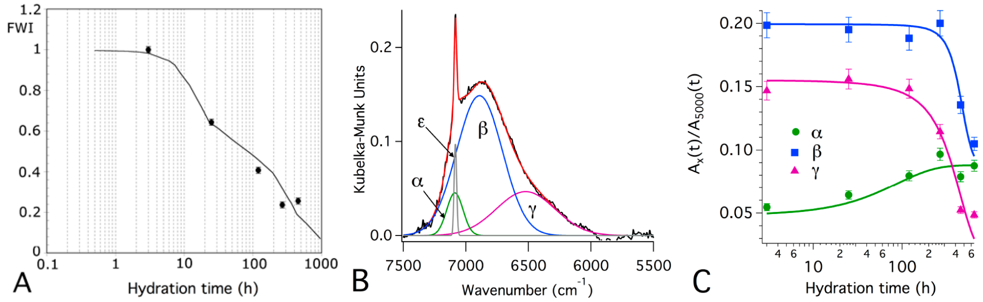

Figure 7. (A) Hydration kinetics of the C_3S + water paste, as monitored by the 5000 cm^{-1} peak area (black circles) compared to the FWI vs time curve obtained using DSC (line). (B) Deconvolution of the 7000 cm^{-1} band of the sample C_3S + water hydrated for 24 h at 20 °C: the α, β, and γ Gaussians account for the water, and the sharp ε Gaussian is linked to the OH vibrations in $Ca(OH)_2$. (C) Plot of the area vs time of the three Gaussian components describing the water contribution. Reproduced with permission from ref 69.

planets.[70,71] The NIR spectra registered in the 20/−150 °C temperature range on a hydrated sample containing bulk water ($w/c = 0.4$) appears as shown in Figure 8A:[43] a sudden change in the shape of the 7000 cm^{-1} band occurs when liquid water freezes, with a net red shift of the entire band and the appearance of a new band centered near 6080 cm^{-1}, which is commonly considered to be a fingerprint of hexagonal ice. After a week, the trend in the spectra with temperature is similar to that shown in Figure 8B: the figure clearly shows that hexagonal ice formation is inhibited, indicating that water still present in the C_3S paste solidifies in an amorphous state. This is particularly interesting when compared to the LTDSC experiments (section 3) because it indicates that water confined in the nanometric porosity of the cement matrix is not able to crystallize but solidifies in an amorphous state.

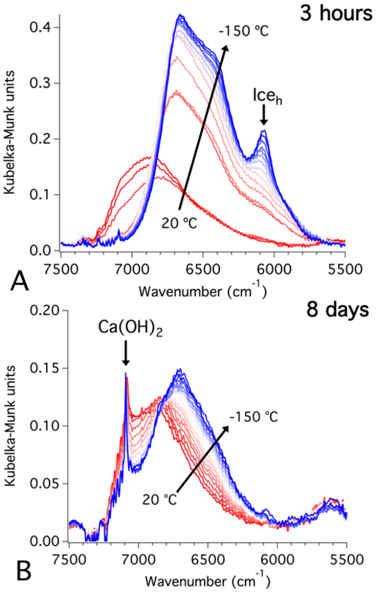

Figure 8. NIR spectra acquired from −150 to +20 °C from cement paste cured for (A) 3 h and (B) 8 days. Reproduced with permission from ref 43.

5. STATE OF THE WATER: WATER RELAXATION DYNAMICS

5.1. Quasi-Elastic Neutron Scattering. Quasi-elastic neutron scattering (QENS) is a technique especially suited for the in situ investigation of relaxation dynamics of hydrogenated species, from the picosecond to nanosecond time scale corresponding to an energy window from a few μeV to tenths of a meV.[72] In complex systems containing water, this technique allows us to characterize the actual state of the water molecules from bulk/confined to completely immobile. QENS experiments on cementitious pastes are particularly informative about water dynamics because the incoherent scattering cross section of hydrogen is 10 times larger than that of other elements constituting the cement powder (oxygen, calcium, aluminum, iron, and silicon).[21,73] Thus, the QENS signal from a cement paste is dominated by the hydrogen self-dynamics term,[74] allowing for a precise description of both the water state and the transport properties on the nanoscale. *The diffusion processes are of fundamental importance in predicting the service life (durability) of cement based systems since corrosive mechanisms involve the permeation of substances, such as aggressive ions, gases or just water, into the concrete.*[74,75]

A QENS spectrum usually contains two main contributions: an elastic and a quasi-elastic component (Figure 9A).[73,77]

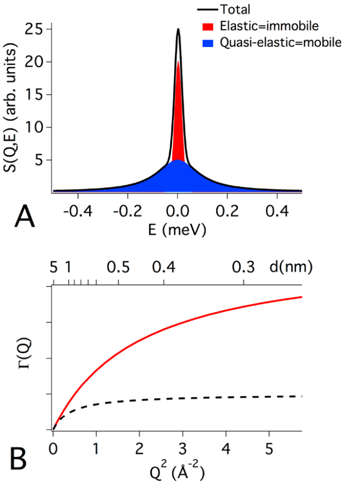

Figure 9. (A) Example of a QENS spectrum showing the two characteristic contributions: elastic and quasi-elastic, with an experimental resolution of 40 μeV. (B) Broadening of the quasi-elastic component as a function of Q^2 and the probed dimension, d. Passing from the continuous line (red) to the dashed line (black), the diffusion coefficient decreases, and the characteristic relaxation time increases. This is usually the evolution in time observed in a hydrating cement paste and reflects the conversion from bulk/capillary water into gel-confined water.

The elastic component is easily recognizable because it has the same width of resolution of the QENS spectrometer (and it is on the order of few tenths of a μeV). This component gathers all neutrons scattered elastically (i.e., no exchange in energy) by the nuclei that are immobile in the sample or, in other words, that relax with characteristic times longer than hundreds of ns (i.e., a time longer than the one associated with the resolution of the instrument). In the case of a cement paste, the immobile fraction accounts for the hydrogenated species (mainly chemically bound water) contained in the hydrated phases (CH, C−S−H, etc.). This quantity can be used to follow and detail the hydration kinetics in both the nucleation and growth stage and in the diffusional regime,[78] as already seen in the DSC case.

In the case of mobile atoms, the neutron−nuclei interaction results in an exchange of energy, and the QENS signal shows a broadening associated with the main relaxation processes of the sample (mainly water translational and rotational motions). In general, in the range of interest of a QENS investigation, $t > 0.1$ ps, the scattering equation for the mobile part can be generally written as $S(Q, E) = \exp(-\langle u^2\rangle Q^2/3) \otimes T(Q, E) \otimes R(Q, E)$, where the first term is the so-called Debye−Waller factor accounting for the mean square displacement of hydrogen in the O−H species, $T(Q, E)$ represents the contribution of the translational motion, and $R(Q, E)$ is the contribution of the rotational motion. In the case where $Q < 1$ Å^{-1}, only the translational motion is considered, which greatly simplifies the modeling of the quasi-elastic component[74,79,80] when compared to the cases where larger Q vectors are considered.[81,82] Moreover, the dependence of the broadening as a function of Q gives additional information on the type of motion (free diffusion, random jump diffusion, free diffusion in a confined geometry, etc.) allowing the calculation of the diffusion coefficient and eventually the residence times and associated jump lengths (Figure 9B). For a detailed review of the fitting models of both the mobile and immobile water fraction, the reader can refer to the literature.[83] However, current approaches tend to ignore the fact that part of the elastic signal comes from liquid water even without the presence of structural water because the Q dependence of the elastic fraction, especially at very low Q (typically $Q < 1$ Å^{-1}), contains information on the form factor of the confining volume. Very recently, to overcome this limit, a new global fitting approach has been proposed[84] where all of the QENS spectra at a given time are simultaneously modeled over a Q range covering the decay of the elastic incoherent structure factor. This novel improved analysis method can accurately extract the structural water fraction and the associated spatial information directly linked to the confinement of the matrix.

The quasi-elastic component is a key feature in disclosing the evolution of the confinement imposed by the developing C−S−H nanoporosity. Therefore, Fratini et al.[82] clearly evidenced that in the random jump diffusion approximation the average diffusion coefficient for the mobile water fraction decreases by approximately 1 order of magnitude (from 4.0×10^{-9} to 4.0×10^{-10} m^2/s) for the C_3S/H_2O model system in 2 days of curing. Not surprisingly, MD simulations for water on the surface of model C−S−H[68] resulted in an average diffusion coefficient on the order of 10^{-10} m^2/s for all surface-associated molecules, which is in agreement with our QENS investigation and with water dynamics in the ^{1}H NMR field cycling relaxation experiments.[85,86] The same decrease was evidenced by Bordallo et al.[87] by decoupling water dynamics of the capillary pores from that of the gel pores. In addition, the increase in confinement imposed by the developing inorganic matrix causes a reduction of the average jump length from 6 Å to approximately 4 Å in the first 2 days of curing.[82] Thus, the quantitative results obtained using the QENS experiment on hydrating cement pastes consist of the conversion of bulklike water (mainly contained in the capillary pores) in favor of constrained (i.e., strongly interacting with the surface, confined mainly in gel porosity) and bound water (i.e., being part of the hydration products, such as C−S−H and CH).

Recently, Bordallo et al.[88,89] disclosed very important aspects related to the hydration of cement-based systems. By following water dynamics in a 28-cured sample and in the same sample rehydrated after drying at 105 °C, they clearly found that the water reabsorbed into the dried cement paste was more mobile than the water in the pristine cured sample. This suggests that water, once reabsorbed, goes initially into capillary pores and eventually will be admitted into the gel pores only at longer times, as recently confirmed by Pinson et al. using water sorption measurements.[90] Moreover, the initial situation can also be impossible to be restored if the drying process irreversibly damaged the C−S−H nanostructure and the associated porosity.

As a matter of fact, QENS can differentiate among bound, constrained, and free water because their relaxation dynamics are quite distinct (i.e., they move differently). The advantage of this technique is twofold: it monitors the conversion of water in the hydration products and simultaneously detects the water state during the hydration of the cement paste, being able to differentiate between capillary and gel-confined water.

5.2. Porosimetry via NMR Relaxometry. The dynamics of water in a porous system can also be probed using nuclear magnetic resonance (NMR), which is noninvasive, nondestructive, and quantitative.[91] In particular, NMR relaxometry is a well-established method of characterizing pore size distributions, specific surface areas, binder phase densities, water fractions, and dynamics. This technique has been applied to calcium-based cements for decades to study the formation and characteristics of cement microstructure and to monitor the evolution of water within them. One of the main advantages of NMR experiments is that they provide highly detailed information concerning the microstructure of both crystalline and amorphous phases.[91,92]

The use of combined Carr−Purcell−Meiboom−Gill (CPMG) and quad-echo pulse sequences was recently reported in the literature as an effective method to measure and quantify all hydrogen protons in different environments such as crystalline phases, interlayer water, gel pore water, and capillary water.[91] The measurement of the transverse (T_2) and longitudinal (T_1) spin relaxation time can be used to estimate the size of the pores, to gain information on the pore network evolution during the hydration process, and to monitor the kinetics of formation of hydrogen-containing solid phases.[92−95] This technique relies on the dependence of the T_2 values of the pore water on the surface/volume ratio and on the specific surface relaxation. In the cement research field, a tool to quantitatively discriminate different populations of water has been demonstrated.[91,96−98] By assuming the fast diffusion regime,[99,100] the relationship

$$\frac{1}{T_2} \approx \frac{\varepsilon S}{V} \frac{1}{T_2^{\mathrm{surf}}} \tag{9}$$

can be applied, in which T_2 is the measured spin−spin relaxation time, T_2^{surf} is the T_2 value for water molecules adsorbed on the surface, ε is the thickness of the adsorbed water layer, and S and V are the pore surface area and volume, respectively. Under this condition, from the experimental value of T_2, it is possible to obtain information on the S/V ratio and therefore on the pore size dimensions, distribution, and evolution in different phases.[101,102]

Similarly, this approach was further used, for the first time, with MgO/SiO_2 cements to discriminate different populations of water and to correlate their evolution with the hydration kinetics.[103] T_2 measurements were performed at different times, ranging from ∼0.5 h to 1 month, during the hydration of the investigated samples. In this study, several mixtures of Portland cement and MgO/SiO_2 were investigated, and important differences were highlighted. The two binder gel phases, magnesium silicate hydrate (M−S−H) and calcium silicate hydrate (C−S−H), showed significantly different pore size distributions. In the MgO/SiO_2 sample, three peaks were present soon after mixing with water. The peak at the shortest T_2 is due to embedded water, which broadened with increasing hydration time. The other signals were assigned to free water with different mobilities in the spaces between powder grains. The so-called less-mobile water contribution broadened, and the more-mobile water moved to shorter values and decreased with time. In the Portland cement sample, two populations of free water, less mobile and more mobile, appear soon after mixing with water. In the first 6 h, two separate peaks were present, and then they merged into a single signal that decreased and shifted to shorter T_2 with increases in the hydration time to up to 30 h. After 1 day of hydration, an additional signal was observed as a result of water in the gel pores and interlayer spacing, and then, at a longer hydration time, a peak assigned to water in C−S−H interlayer spaces started to be resolved, and its relative intensity increased in the first month of hydration. Figure 10 shows the T_2 evolution vs the hydration time for the investigated MgO/SiO_2 (Figure 10A) and Portland cement (Figure 10B). When M−S−H is the binder phase, the porous structures evolve during the entire investigated period, and the final pore distribution confirms the globular structure previously proposed in the literature.[8] However, with C−S−H as the main phase, the pore size distribution dramatically changes when this binder phase precipitates, i.e., when water remains segregated in the interlayer spaces and in gel pores.

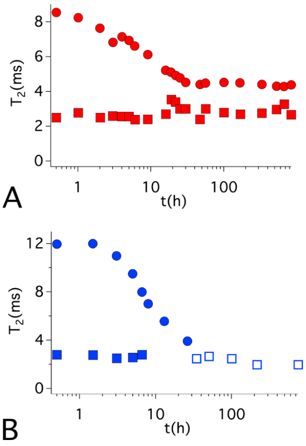

Figure 10. Evolution of hydrogen T_2 relaxation time as a function of hydration time: (A) MgO/SiO_2 and (B) Portland cement. Filled symbols (● and ■) are for the more-mobile and less-mobile free water components, and the open symbol (□) is for free water at longer hydration times, becoming water in the interhydrate spaces. Adapted with permission from ref 103.

5.3. Dielectric Relaxation. Various dielectric relaxation experiments were conducted on cement pastes and mortars. Depending on the frequency range, several relaxation processes can be followed during the hydration reaction. Typically, three components are monitored: a low relaxation occurring near 1 MHz, a medium relaxation at approximately 100 MHz, and a high relaxation in the GHz regime.[104] The main experimental evidence is that the relaxation strength of free water at high frequency (∼10 GHz) decreases rapidly as the curing time passes, which enables us to follow the hydration reaction kinetics in these types of systems. The two components observed at lower frequencies (i.e., ∼100 and 1 MHz) are usually distinctive of the reorientation of water constrained in the C−S−H phase.[105]

Cerveny et al.[106] studied the influence of the water level on the dielectric response of the synthetic C−S−H phase. Even in this case, three different relaxation processes related to water are present at room temperature. The effect of the temperature (110−260 K) was investigated as a function of the water level (6−15 wt %) to evidence the activation mechanism behind these relaxations. All three relaxations exhibited Arrhenius behavior at low water content (<10 wt %). With increasing water level, the process associated with water in small gel pores (medium frequency) shows a crossover from Arrhenius to super-Arrhenius (i.e., the motions become cooperative) as the water level reaches 10 wt % or in other words more than one monolayer is present. In the case of the water confined in large gel pores (high-frequency process), no crossover (from Arrhenius to super-Arrhenius) is present, and the super-Arrhenius behavior testifies to a cooperative relaxation for high water content. The two populations described agree with the findings reported using LT-NIR and DSC by some of the authors of the present paper.[43] More interesting, the crossover from Arrhenius to super-Arrhenius behavior was reported in the translational relaxation dynamics as obtained using QENS in C−S−H, M−S−H,[107] and various cement pastes.[108,109]

6. CONCLUDING DISCUSSION

The physicochemical properties of water can be a fundamental and unique resource to investigate complex porous matrixes. This feature article presented relevant results obtained on cement, which is a complex inorganic nanocomposite with structural characteristics (such as the pore size range and the dimension of the basic building block generating the fractal microstructure) that undoubtedly allow its allocation among the vast class of colloidal systems.[73] Furthermore, the number of innovative hydraulic cement formulations both for building and biomedical applications is going to increase, and the characterization of their kinetics and structural properties will become crucial for their improvement and formulation. The colloidal nature of cement suggests that the approach of using water as a probe can be extended to several other colloidal systems with very different chemical composition, where water plays a key role in the structure of the material (i.e., water is the main constituent). For example, in nonevolving systems with pores in the nanometer range, such as zeolites, clays, carbon nanotubes, or other inorganic matrixes, the thermal behavior evaluation of water is a method to infer their properties in terms of porosity, whereas the combination of QENS, NIR, NMR relaxometry, and dielectric relaxation allows one to study the translational, vibrational, and rotational motions of the confined liquid, thus evidencing the transport properties of the host material. However, biological molecules such as proteins, polysaccharides, and DNA always display behavior that is dictated by the presence of water as in the case of the plasticizing effect of water on the glass transition of biopolymers, and the study of water dynamics often yields precious information on their structure and activity. In addition, hydrogels can be successfully investigated by studying the properties of water, which directly regulates the transport phenomena of ions, molecules, and even gases through them.

■ AUTHOR INFORMATION

Corresponding Authors

*E-mail: emiliano.fratini@unifi.it.
*E-mail: piero.baglioni@unifi.it.

ORCID

Francesca Ridi: 0000-0002-6887-5108
Emiliano Fratini: 0000-0001-7104-6530
Sow-Hsin Chen: 0000-0001-6588-2428
Piero Baglioni: 0000-0003-1312-8700

Funding

This work was performed with the financial support of Ministero dell'Istruzione, Università e Ricerca scientifica MIUR (FIR2013 project RBFR132WSM) and of Consorzio Interuniversitario per lo Sviluppo dei Sistemi a Grande Interfase, CSGI.

Notes

The authors declare no competing financial interest.

Biographies

From left to right: Sow-Hsin Chen, Piero Baglioni, Francesca Ridi, Monica Tonelli, and Emiliano Fratini

Sow-Hsin Chen, a condensed matter physicist, is a professor emeritus in the Department of Nuclear Science and Engineering at MIT (a faculty member at MIT since 1968). His main research area is thermal neutron, synchrotron X-ray, and laser light scattering spectroscopies of soft condensed matter. His recent work mainly involves molecular dynamics of various types of confined water in deeply supercooled states under high pressure, including water in MCM-41 porous silica, in cement pastes, in carbon nanotubes, and hydration water near surfaces of proteins, DNA, and RNA. He is the author of more than 450 publications in condensed matter physics.

Piero Baglioni has been a full professor of physical chemistry in the Department of Chemistry at the University of Florence since 1994 and is an MIT affiliate. He was appointed as a visiting scientist/professor by the University of Houston, the Weizmann Institute, the Collège de France, and MIT. He is the Director of CSGI, and he is on the editorial/advisory boards of several international journals and a member of the scientific board of several national and international institutions and societies. He is the author of more than 450 publications and 25 patents in the field of colloids and interfaces and a pioneer in the application of soft matter to the conservation of cultural heritage.

Francesca Ridi is a researcher in the Department of Chemistry at the University of Florence. She received her Ph.D. in chemical sciences at the University of Florence. Her research is focused on the investigation of the physicochemical processes occurring during the hydration reaction of hydraulic cements both for construction and building materials and for bone tissue engineering applications.

Monica Tonelli received her B.S. in chemistry and M.S. in chemical sciences at the University of Florence, where she is currently a Ph.D. student in chemical sciences. Her research interests include magnesium-based cements with a focus on the use of nanotubular reinforcing fibers and phosphate-based additives. She is also working in collaboration with Italcementi SpA on the physicochemical characterization of Portland-based formulations.

Emiliano Fratini is an associate professor of physical chemistry in the Department of Chemistry of the University of Florence. His research topics include multifunctional nanocomposites, novel hydrogels and organogels, water dynamics in confining matrices, new mesoporous silica scaffolds for catalysis and actives delivery, and structural and dynamical characterization of nanomaterials and soft matter.

■ ACKNOWLEDGMENTS

Ministero dell'Istruzione, Università e Ricerca scientifica MIUR (FIR2013 project RBFR132WSM), and Consorzio Interuniversitario per lo Sviluppo dei Sistemi a Grande Interfase, CSGI are acknowledged for financial support.

■ ABBREVIATIONS

NMR, nuclear magnetic resonance; CPMG, Carr−Purcell−Meiboom−Gill; LTDSC, low-temperature differential scanning calorimetry; C_3S, tricalcium silicate; PEO, poly(ethylenoxide); DSC, differential scanning calorimetry; SGP, small gel pores; LGP, large gel pores; IGP, interlamellar gel pores; FWI, free water index; AE, Avrami-Erove'ev; BNGM, boundary nucleation and growth model; NIR, near-infrared spectroscopy; WHB, weakly hydrogen bonded; SHB, strongly hydrogen bonded; QENS, quasi-elastic neutron scattering; SANS, small-angle neutron scattering

■ REFERENCES

(1) Hewlett, P. *Lea's Chemistry of Cement and Concrete*, 4th ed.; Elsevier, 1998.

(2) Khatib, J. *Sustainability of Construction Materials*; Woodhead Publishing, 2016.

(3) Walling, S. A.; Provis, J. L. Magnesia-Based Cements: A Journey of 150 Years, and Cements for the Future? *Chem. Rev.* **2016**, *116* (7), 4170−4204.

(4) Sinitsina, O. V.; Veresov, A. G.; Putlayev, V. I.; Tretyakov, Y. D.; Ravaglioli, A.; Krajewski, A.; Mazzocchi, M. Cements for Biomedical Applications. *Mendeleev Commun.* **2004**, *14* (4), 179−180.

(5) Brew, D. R. M.; Glasser, F. P. Synthesis and Characterisation of Magnesium Silicate Hydrate Gels. *Cem. Concr. Res.* **2005**, *35* (1), 85−98.

(6) Zhang, T.; Cheeseman, C. R.; Vandeperre, L. J. Development of Low pH Cement Systems Forming Magnesium Silicate Hydrate (M-S-H). *Cem. Concr. Res.* **2011**, *41* (4), 439−442.

(7) Zhang, T.; Vandeperre, L. J.; Cheeseman, C. R. Magnesium-Silicate-Hydrate Cements for Encapsulating Problematic Aluminium Containing Wastes. *J. Sustainable Cem.-Based Mater.* **2012**, *1* (1−2), 34−45.

(8) Chiang, W.-S.; Ferraro, G.; Fratini, E.; Ridi, F.; Yeh, Y.-Q.; Jeng, U. S.; Chen, S.-H.; Baglioni, P. Multiscale Structure of Calcium-and Magnesium-Silicate-Hydrate Gels. *J. Mater. Chem. A* **2014**, *2* (32), 12991−12998.

(9) Lothenbach, B.; Nied, D.; L'Hôpital, E.; Achiedo, G.; Dauzères, A. Magnesium and Calcium Silicate Hydrates. *Cem. Concr. Res.* **2015**, *77*, 60−68.

(10) Hughes, E.; Yanni, T.; Jamshidi, P.; Grover, L. M. Inorganic Cements for Biomedical Application: Calcium Phosphate, Calcium Sulphate and Calcium Silicate. *Adv. Appl. Ceram.* **2015**, *114* (2), 65−76.

(11) Taylor, H. *Cement Chemistry*; Thomas Telford Publishing: London, 1997.

(12) Wang, S.-D.; Scrivener, K. L. Hydration Products of Alkali Activated Slag Cement. *Cem. Concr. Res.* **1995**, *25* (3), 561−571.

(13) Pane, I.; Hansen, W. Investigation of Blended Cement Hydration by Isothermal Calorimetry and Thermal Analysis. *Cem. Concr. Res.* **2005**, *35* (6), 1155−1164.

(14) Damasceni, A.; Dei, L.; Fratini, E.; Ridi, F.; Chen, S.-H.; Baglioni, P. A Novel Approach Based on Differential Scanning Calorimetry Applied to the Study of Tricalcium Silicate Hydration Kinetics. *J. Phys. Chem. B* **2002**, *106* (44), 11572−11578.

(15) Ridi, F.; Fratini, E.; Luciani, P.; Winnefeld, F.; Baglioni, P. Hydration Kinetics of Tricalcium Silicate by Calorimetric Methods. *J. Colloid Interface Sci.* **2011**, *364* (1), 118−124.

(16) Ridi, F.; Dei, L.; Fratini, E.; Chen, S.-H.; Baglioni, P. Hydration Kinetics of Tri-Calcium Silicate in the Presence of Superplasticizers. *J. Phys. Chem. B* **2003**, *107* (4), 1056−1061.

(17) Kondo, R.; Ueda, S. *Kinetics of Hydration of Cements*; Cement Association of Japan: Tokyo, 1969; Vol. *2*, pp 203−248.

(18) Jolicoeur, C.; Simard, M. Chemical Admixture-Cement Interactions: Phenomenology and Physico-Chemical Concepts. *Cem. Concr. Compos.* **1998**, *20*, 87.

(19) Brown, P. W.; Pommersheim, J.; Frohnsdorff, G. A Kinetic Model for the Hydration of Tricalcium Silicate. *Cem. Concr. Res.* **1985**, *15*, 35−41.

(20) Tarrida, M.; Madon, M.; Le Rolland, B.; Colombet, P. An in-Situ Raman Spectroscopy Study of the Hydration of Tricalcium Silicate. *Adv. Cem. Based Mater.* **1995**, *2* (1), 15−20.

(21) FitzGerald, S. A.; Neumann, D. A.; Rush, J. J.; Bentz, D. P.; Livingston, R. A. In Situ Quasi-Elastic Neutron Scattering Study of the Hydration of Tricalcium Silicate. *Chem. Mater.* **1998**, *10* (1), 397−402.

(22) Berliner, R.; Popovici, M.; Herwig, K. W.; Berliner, M.; Jennings, H. M.; Thomas, J. J. Quasielastic Neutron Scattering Study of the Effect of Water-to-Cement Ratio on the Hydration Kinetics of Tricalcium Silicate. *Cem. Concr. Res.* **1998**, *28* (2), 231−243.

(23) Garrault, S.; Behr, T.; Nonat, A. Formation of the C-S-H Layer during Early Hydration of Tricalcium Silicate Grains with Different Sizes. *J. Phys. Chem. B* **2006**, *110* (1), 270−275.

(24) Thomas, J. J. A New Approach to Modeling the Nucleation and Growth Kinetics of Tricalcium Silicate Hydration. *J. Am. Ceram. Soc.* **2007**, *90* (10), 3282−3288.

(25) Thomas, J. J.; Allen, A. J.; Jennings, H. M. Hydration Kinetics and Microstructure Development of Normal and CaCl$_2$-Accelerated Tricalcium Silicate Pastes. *J. Phys. Chem. C* **2009**, *113* (46), 19836−19844.

(26) Cahn, J. W. The Kinetics of Grain Boundary Nucleated Reactions. *Acta Metall.* **1956**, *4* (5), 449−459.

(27) Ridi, F.; Fratini, E.; Luciani, P.; Winnefeld, F.; Baglioni, P. Tricalcium Silicate Hydration Reaction in the Presence of Comb-Shaped Superplasticizers: Boundary Nucleation and Growth Model Applied to Polymer-Modified Pastes. *J. Phys. Chem. C* **2012**, *116* (20), 10887−10895.

(28) Tonelli, M.; Martini, F.; Calucci, L.; Geppi, M.; Borsacchi, S.; Ridi, F. Traditional Portland Cement and MgO-Based Cement: A Promising Combination? *Phys. Chem. Earth ABC* **2017**, *99*, 158−167.

(29) Martini, F.; Tonelli, M.; Calucci, L.; Geppi, M.; Ridi, F.; Borsacchi, S. Hydration of MgO/SiO$_2$ and Portland cement mixtures: a structural investigation of the hydrated phases by means of X-ray diffraction and Solid State NMR spectroscopy. *Cem. Concr. Res.* **2017**, *102*, 60.

(30) Bordallo, H. N.; Aldridge, L. P.; Desmedt, A. Water Dynamics in Hardened Ordinary Portland Cement Paste or Concrete: From Quasielastic Neutron Scattering. *J. Phys. Chem. B* **2006**, *110* (36), 17966−17976.

(31) Jacobsen, J.; Rodrigues, M. S.; Telling, M. T. F.; Beraldo, A. L.; Santos, S. F.; Aldridge, L. P.; Bordallo, H. N. Nano-Scale Hydrogen-Bond Network Improves the Durability of Greener Cements. *Sci. Rep.* **2013**, *3*, 2667.

(32) Bordallo, H. N.; Aldridge, L. P.; Fouquet, P.; Pardo, L. C.; Unruh, T.; Wuttke, J.; Yokaichiya, F. Hindered Water Motions in Hardened Cement Pastes Investigated over Broad Time and Length Scales. *ACS Appl. Mater. Interfaces* **2009**, *1* (10), 2154−2162.

(33) Brun, M.; Lallemand, A.; Quinson, J. F.; Eyraud, C. A New Method for the Simultaneous Determination of the Size and the Shape of Pores: The Thermoporometry. *Thermochim. Acta* **1977**, *21*, 59−87.

(34) Defay, R.; Prigogine, I.; Bellemans, A.; Everett, D. H. *Surface Tension and Adsorption*; Longmans Green: London, 1966.

(35) Landry, M. R. Thermoporometry by Differential Scanning Calorimetry: Experimental Considerations and Applications. *Thermochim. Acta* **2005**, *433* (1−2), 27−50.

(36) Ishikiriyama, K.; Todoki, M. Pore Size Distribution Measurements of Silica Gels by Means of Differential Scanning Calorimetry. *J. Colloid Interface Sci.* **1995**, *171* (1), 103−111.

(37) Ishikiriyama, K.; Todoki, M. Evaluation of Water in Silica Pores Using Differential Scanning Calorimetry. *Thermochim. Acta* **1995**, *256* (2), 213−226.

(38) Ishikiriyama, K.; Todoki, M.; Motomura, K. Pore Size Distribution (PSD) Measurements of Silica Gels by Means of Differential Scanning Calorimetry: I. Optimization for Determination of PSD. *J. Colloid Interface Sci.* **1995**, *171* (1), 92−102.

(39) Bager, D. H.; Sellevold, E. J. Ice Formation in Hardened Cement Paste, Part I — Room Temperature Cured Pastes with Variable Moisture Contents. *Cem. Concr. Res.* **1986**, *16* (5), 709−720.

(40) Bager, D. H.; Sellevold, E. J. Ice Formation in Hardened Cement Paste, Part II — Drying and Resaturation on Room Temperature Cured Pastes. *Cem. Concr. Res.* **1986**, *16* (6), 835−844.

(41) Bager, D. H.; Sellevold, E. J. Ice Formation in Hardened Cement Paste, Part III — Slow Resaturation of Room Temperature Cured Pastes. *Cem. Concr. Res.* **1987**, *17* (1), 1−11.

(42) Bentz, D. P. Capillary Porosity Depercolation/Repercolation in Hydrating Cement Pastes Via Low-Temperature Calorimetry Measurements and CEMHYD3D Modeling. *J. Am. Ceram. Soc.* **2006**, *89* (8), 2606−2611.

(43) Ridi, F.; Luciani, P.; Fratini, E.; Baglioni, P. Water Confined in Cement Pastes as a Probe of Cement Microstructure Evolution. *J. Phys. Chem. B* **2009**, *113* (10), 3080−3087.

(44) Ridi, F.; Fratini, E.; Baglioni, P. Fractal Structure Evolution during Cement Hydration by Differential Scanning Calorimetry: Effect of Organic Additives. *J. Phys. Chem. C* **2013**, *117* (48), 25478−25487.

(45) Sun, Z.; Scherer, G. W. Pore size and shape in mortar by thermoporometry. *Cem. Concr. Res.* **2010**, *40* (5), 740−751.

(46) Jennings, H. M. Refinements to Colloid Model of CSH in Cement: CM-II. *Cem. Concr. Res.* **2008**, *38* (3), 275−289.

(47) Sanz, E.; Vega, C.; Espinosa, J. R.; Caballero-Bernal, R.; Abascal, J. L. F.; Valeriani, C. Homogeneous Ice Nucleation at Moderate Supercooling from Molecular Simulation. *J. Am. Chem. Soc.* **2013**, *135* (40), 15008−15017.

(48) Hansen, E. W.; Gran, H. C.; Sellevold, E. J. Heat of Fusion and Surface Tension of Solids Confined in Porous Materials Derived from a Combined Use of NMR and Calorimetry. *J. Phys. Chem. B* **1997**, *101* (35), 7027−7032.

(49) Hou, D.; Zhao, T.; Ma, H.; Li, Z. Reactive molecular simulation on water confined in the nanopores of the calcium silicate hydrate gel: structure, reactivity, and mechanical properties. *J. Phys. Chem. C* **2015**, *119* (3), 1346−1358.

(50) Li, D. K.; Zhao, W. Y.; Hou, D. S.; Zhao, T. J. Molecular dynamics study on the chemical bound, physical adsorbed and ultra-confined water molecules in the nano-pore of calcium silicate hydrate. *Constr. Build. Mater.* **2017**, *151*, 563−574.

(51) Youssef, M.; Pellenq, R. J. M.; Yildiz, B. Glassy nature of water in an ultraconfining disordered material: the case of calcium− silicate− hydrate. *J. Am. Chem. Soc.* **2011**, *133* (8), 2499−2510.

(52) Qomi, M. J. A.; Bauchy, M.; Ulm, F. J.; Pellenq, R. J. M. Anomalous composition-dependent dynamics of nanoconfined water in the interlayer of disordered calcium-silicates. *J. Chem. Phys.* **2014**, *140* (5), 054515.

(53) Kriechbaum, M.; Degovics, G.; Tritthart, J.; Laggner, P. Fractal Structure of Portland Cement Paste during Age Hardening Analyzed by Small-Angle X-Ray Scattering. *Prog. Colloid Polym. Sci.* **1989**, *79*, 101−105.

(54) Livingston, R. A. Fractal Nucleation and Growth Model for the Hydration of Tricalcium Silicate. *Cem. Concr. Res.* **2000**, *30*, 1853−1860.

(55) Winslow, D.; Bukowski, J. M.; Young, J. F. The Fractal Arrangement of Hydrated Cement Paste. *Cem. Concr. Res.* **1995**, *25* (1), 147−156.

(56) Rault, J.; Neffati, R.; Judeinstein, P. Melting of Ice in Porous Glass: Why Water and Solvents Confined in Small Pores Do Not Crystallize? *Eur. Phys. J. B* **2003**, *36* (4), 627−637.

(57) Neffati, R.; Rault, J. Pore Size Distribution in Porous Glass: Fractal Dimension Obtained by Calorimetry. *Eur. Phys. J. B* **2001**, *21* (2), 205−210.

(58) Vollet, D.; Donatti, D.; Ruiz, A. I. Comparative Study Using Small-Angle X-Ray Scattering and Nitrogen Adsorption in the Characterization of Silica Xerogels and Aerogels. *Phys. Rev. B: Condens. Matter Mater. Phys.* **2004**, *69* (6), 64202.

(59) Jennings, H. M. A Model for the Microstructure of Calcium Silicate Hydrate in Cement Paste. *Cem. Concr. Res.* **2000**, *30* (1), 101−116.

(60) Allen, A. J.; Thomas, J. J.; Jennings, H. M. Composition and Density of Nanoscale Calcium-Silicate-Hydrate in Cement. *Nat. Mater.* **2007**, *6* (4), 311−316.

(61) Chiang, W.-S.; Fratini, E.; Baglioni, P.; Liu, D.; Chen, S.-H. Microstructure Determination of Calcium-Silicate-Hydrate Globules by Small-Angle Neutron Scattering. *J. Phys. Chem. C* **2012**, *116* (8), 5055−5061.

(62) Chiang, W.-S.; Fratini, E.; Ridi, F.; Lim, S.-H.; Yeh, Y.-Q.; Baglioni, P.; Choi, S.-M.; Jeng, U.-S.; Chen, S.-H. Microstructural Changes of Globules in Calcium−silicate−hydrate Gels with and without Additives Determined by Small-Angle Neutron and X-Ray Scattering. *J. Colloid Interface Sci.* **2013**, *398*, 67−73.

(63) Siesler, H. W. *Near-Infrared Spectroscopy: Principles, Instruments, Applications*; Wiley-VCH: Weinheim, 2002.

(64) Andaloro, G.; Chiricò, P.; Guzzio, G.; Leone, M.; Palma-Vittorelli, M. B. Thermal Behavior of the near IR Absorption of H_2O and $NaClO_4$ Aqueous Solutions. *J. Chem. Phys.* **1977**, *66* (1), 335−341.

(65) Cupane, A.; Levantino, M.; Santangelo, M. G. Near-Infrared Spectra of Water Confined in Silica Hydrogels in the Temperature Interval 365−5 K. *J. Phys. Chem. B* **2002**, *106* (43), 11323−11328.

(66) Czarnik-Matusewicz, B.; Pilorz, S.; Hawranek, J. P. Temperature-Dependent Water Structural Transitions Examined by near-IR and Mid-IR Spectra Analyzed by Multivariate Curve Resolution and Two-Dimensional Correlation Spectroscopy. *Anal. Chim. Acta* **2005**, *544* (1−2), 15−25.

(67) Angell, C. A.; Rodgers, V. Near Infrared Spectra and the Disrupted Network Model of Normal and Supercooled Water. *J. Chem. Phys.* **1984**, *80* (12), 6245−6252.

(68) Hou, D.; Li, Z.; Zhao, T.; Zhang, P. Water transport in the nano-pore of the calcium silicate phase: reactivity, structure and dynamics. *Phys. Chem. Chem. Phys.* **2015**, *17* (2), 1411−1423.

(69) Ridi, F.; Fratini, E.; Milani, S.; Baglioni, P. Near-Infrared Spectroscopy Investigation of the Water Confined in Tricalcium Silicate Pastes. *J. Phys. Chem. B* **2006**, *110* (33), 16326−16331.

(70) Grundy, W. M.; Schmitt, B. The Temperature-Dependent near-Infrared Absorption Spectrum of Hexagonal H_2O Ice. *J. Geophys. Res. Planets* **1998**, *103* (E11), 25809−25822.

(71) Grundy, W. M.; Buie, M. W.; Stansberry, J. A.; Spencer, J. R.; Schmitt, B. Near-Infrared Spectra of Icy Outer Solar System Surfaces: Remote Determination of H_2O Ice Temperatures. *Icarus* **1999**, *142* (2), 536−549.

(72) Bee, M. *Quasielastic Neutron Scattering: Principles and Applications in Solid State Chemistry, Biology and Materials Science*; Adam Hilger: Bristol, 1988.

(73) Ridi, F.; Fratini, E.; Baglioni, P. Cement: A Two Thousand Year Old Nano-Colloid. *J. Colloid Interface Sci.* **2011**, *357*, 255−264.

(74) Fratini, E.; Chen, S. H.; Baglioni, P.; Bellissent-Funel, M. C. Quasi-Elastic Neutron Scattering Study of Translational Dynamics of Hydration Water in Tricalcium Silicate. *J. Phys. Chem. B* **2002**, *106* (1), 158−166.

(75) RILEM Technical Committee TC 116-PCD; *Relations between Transport Characteristics and Durability*; Hilsdorf, H., Kropp, J., Eds.; E & FN Spon: London,1995.

(76) Mindess, S.; Young, J. F.; Darwin, D. *Concrete*, 2nd ed.; Prentice Hall: Upper Saddle River, NJ, 2003.

(77) Harris, D. H. C.; Windsor, C. G.; Lawrence, C. D. Free and Bound Water in Cement Pastes. *Mag. Concr. Res.* **1974**, *26* (87), 65−72.

(78) Del Buffa, S.; Fratini, E.; Ridi, F.; Faraone, A.; Baglioni, P. State of Water in Hydrating Tricalcium Silicate Pastes: The Effect of a Cellulose Ether. *J. Phys. Chem. C* **2016**, *120* (14), 7612−7620.

(79) Fratini, E.; Chen, S. H.; Baglioni, P.; Bellissent-Funel, M. C. Age-Dependent Dynamics of Water in Hydrated Cement Paste. *Phys. Rev. E: Stat. Phys., Plasmas, Fluids, Relat. Interdiscip. Top.* **2001**, *64* (2), 20201.

(80) Fratini, E.; Chen, S. H.; Baglioni, P. Investigation of the Temporal Evolution of Translational Dynamics of Water Molecules in Hydrated Calcium Aluminate Pastes. *J. Phys. Chem. B* **2003**, *107* (37), 10057−10062.

(81) Li, H.; Zhang, L.-L.; Yi, Z.; Fratini, E.; Baglioni, P.; Chen, S.-H. Translational and Rotational Dynamics of Water Contained in Aged Portland Cement Pastes Studied by Quasi-Elastic Neutron Scattering. *J. Colloid Interface Sci.* **2015**, *452*, 2−7.

(82) Fratini, E.; Faraone, A.; Ridi, F.; Chen, S.-H.; Baglioni, P. Hydration Water Dynamics in Tricalcium Silicate Pastes by Time-Resolved Incoherent Elastic Neutron Scattering. *J. Phys. Chem. C* **2013**, *117* (14), 7358−7364.

(83) Peterson, V. K. Studying the Hydration of Cement. In *Studying Kinetics with Neutrons: Prospects for Times-Resolved Neutron Scattering*; Springer Series in Solid-State Sciences; Springer, 2010; Vol. *161*, pp 19−75.

(84) Le, P.; Fratini, E.; Zhang, L.-L.; Ito, K.; Mamontov, E.; Baglioni, P.; Chen, S.-H. Quasi-Elastic Neutron Scattering Study of Hydration Water in Synthetic Cement: An Improved Analysis Method Based on a New Global Model. *J. Phys. Chem. C* **2017**, *121*, 12826−12833.

(85) Kalinichev, A. G.; Wang, J.; Kirkpatrick, R. J. Molecular Dynamics Modeling of the Structure, Dynamics and Energetics of Mineral−water Interfaces: Application to Cement Materials. *Cem. Concr. Res.* **2007**, *37* (3), 337−347.

(86) Korb, J.-P.; McDonald, P. J.; Monteilhet, L.; Kalinichev, A. G.; Kirkpatrick, R. J. Comparison of Proton Field-Cycling Relaxometry and Molecular Dynamics Simulations for Proton−water Surface Dynamics in Cement-Based Materials. *Cem. Concr. Res.* **2007**, *37* (3), 348−350.

(87) Bordallo, H. N.; Aldridge, L. P.; Desmedt, A. Water Dynamics in Hardened Ordinary Portland Cement Paste or Concrete: From Quasielastic Neutron Scattering. *J. Phys. Chem. B* **2006**, *110* (36), 17966−17976.

(88) Jacobsen, J.; Rodrigues, M. S.; Telling, M. T. F.; Beraldo, A. L.; Santos, S. F.; Aldridge, L. P.; Bordallo, H. N. Nano-Scale Hydrogen-Bond Network Improves the Durability of Greener Cements. *Sci. Rep.* **2013**, *3*, 2667.

(89) Bordallo, H. N.; Aldridge, L. P.; Fouquet, P.; Pardo, L. C.; Unruh, T.; Wuttke, J.; Yokaichiya, F. Hindered Water Motions in Hardened Cement Pastes Investigated over Broad Time and Length Scales. *ACS Appl. Mater. Interfaces* **2009**, *1* (10), 2154−2162.

(90) Pinson, M. B.; Masoero, E.; Bonnaud, P. A.; Manzano, H.; Ji, Q.; Yip, S.; Thomas, J. J.; Bazant, M. Z.; Van Vliet, K. J.; Jennings, H. M. Hysteresis from Multiscale Porosity: Modeling Water Sorption and Shrinkage in Cement Paste. *Phys. Rev. Appl.* **2015**, *3*, 064009.

(91) Muller, A. C. A.; Scrivener, K. L.; Gajewicz, A. M.; McDonald, P. J. Use of Bench-Top NMR to Measure the Density, Composition and Desorption Isotherm of C−S−H in Cement Paste. *Microporous Mesoporous Mater.* **2013**, *178*, 99−103.

(92) Valori, A.; McDonald, P. J.; Scrivener, K. L. The Morphology of C−S−H: Lessons from ^{1}H Nuclear Magnetic Resonance Relaxometry. *Cem. Concr. Res.* **2013**, *49*, 65−81.

(93) Faure, P. F.; Rodts, S. Proton NMR Relaxation as a Probe for Setting Cement Pastes. *Magn. Reson. Imaging* **2008**, *26* (8), 1183−1196.

(94) Korb, J.-P. NMR and Nuclear Spin Relaxation of Cement and Concrete Materials. *Curr. Opin. Colloid Interface Sci.* **2009**, *14* (3), 192−202.

(95) Bortolotti, V.; Fantazzini, P.; Mongiorgi, R.; Sauro, S.; Zanna, S. Hydration Kinetics of Cements by Time-Domain Nuclear Magnetic Resonance: Application to Portland-Cement-Derived Endodontic Pastes. *Cem. Concr. Res.* **2012**, *42* (3), 577−582.

(96) McDonald, P. J.; Rodin, V.; Valori, A. Characterisation of Intra- and Inter-C−S−H Gel Pore Water in White Cement Based on an Analysis of NMR Signal Amplitudes as a Function of Water Content. *Cem. Concr. Res.* **2010**, *40* (12), 1656−1663.

(97) Pop, A.; Badea, C.; Ardelean, I. The Effects of Different Superplasticizers and Water-to-Cement Ratios on the Hydration of

Gray Cement Using T_2-NMR. *Appl. Magn. Reson.* **2013**, *44* (10), 1223−1234.

(98) Bligh, M. W.; d'Eurydice, M. N.; Lloyd, R. R.; Arns, C. H.; Waite, T. D. Investigation of Early Hydration Dynamics and Microstructural Development in Ordinary Portland Cement Using ^{1}H NMR Relaxometry and Isothermal Calorimetry. *Cem. Concr. Res.* **2016**, *83*, 131−139.

(99) Brownstein, K. R.; Tarr, C. E. Importance of Classical Diffusion in NMR Studies of Water in Biological Cells. *Phys. Rev. A: At., Mol., Opt. Phys.* **1979**, *19* (6), 2446−2453.

(100) Halperin, W. P.; Jehng, J.-Y.; Song, Y.-Q. Application of Spin-Spin Relaxation to Measurement of Surface Area and Pore Size Distributions in a Hydrating Cement Paste. *Magn. Reson. Imaging* **1994**, *12* (2), 169−173.

(101) Gombia, M.; Bortolotti, V.; De Carlo, B.; Mongiorgi, R.; Zanna, S.; Fantazzini, P. Nanopore Structure Buildup during Endodontic Cement Hydration Studied by Time-Domain Nuclear Magnetic Resonance of Lower and Higher Mobility ^{1}H. *J. Phys. Chem. B* **2010**, *114* (5), 1767−1774.

(102) Muller, A. C. A.; Scrivener, K. L.; Gajewicz, A. M.; McDonald, P. J. Densification of C−S−H Measured by ^{1}H NMR Relaxometry. *J. Phys. Chem. C* **2013**, *117* (1), 403−412.

(103) Martini, F.; Calucci, L.; Geppi, M.; Tonelli, M.; Ridi, F.; Borsacchi, S. Monitoring the Hydration of MgO-Based Cement and Its Mixtures with Portland Cement by ^{1}H NMR Relaxometry. *Microporous Mesoporous Mater.* **2017**, doi: 10.1016/j.micromeso.2017.05.031.

(104) Hager, N. E.; Domszy, R. C. Monitoring of Cement Hydration by Broadband Time-Domain-Reflectometry Dielectric Spectroscopy. *J. Appl. Phys.* **2004**, *96* (9), 5117−5128.

(105) Miura, N.; Shinyashiki, N.; Yagihara, S.; Shiotsubo, M. Microwave Dielectric Study of Water Structure in the Hydration Process of Cement Paste. *J. Am. Ceram. Soc.* **1998**, *81* (1), 213−216.

(106) Cerveny, S.; Arrese-Igor, S.; Dolado, J. S.; Gaitero, J. J.; Alegria, A.; Colmenero, J. Effect of Hydration on the Dielectric Properties of C-S-H Gel. *J. Chem. Phys.* **2011**, *134* (3), 034509.

(107) Le, P.; Fratini, E.; Ito, K.; Wang, Z.; Mamontov, E.; Baglioni, P.; Chen, S.-H. Dynamical Behaviors of Structural, Constrained and Free Water in Calcium- and Magnesium-Silicate-Hydrate Gels. *J. Colloid Interface Sci.* **2016**, *469*, 157−163.

(108) Zhang, Y.; Lagi, M.; Fratini, E.; Baglioni, P.; Mamontov, E.; Chen, S.-H. Dynamic Susceptibility of Supercooled Water and Its Relation to the Dynamic Crossover Phenomenon. *Phys. Rev. E* **2009**, *79* (4), 40201.

(109) Li, H.; Chiang, W.-S.; Fratini, E.; Ridi, F.; Bausi, F.; Baglioni, P.; Tyagi, M.; Chen, S.-H. Dynamic Crossover in Hydration Water of Curing Cement Paste: The Effect of Superplasticizer. *J. Phys.: Condens. Matter* **2012**, *24* (6), 064108.

Ringraziamenti

Il ringraziamento piú sentito é per la mia tutrice, la Dr. Francesca Ridi, per essere stata in questi anni una figura di riferimento sia dal punto di vista scientifico che personale. Vorrei ringraziarla profondamente per la fiducia riposta nei miei confronti, oltre che per il suo fondamentale contributo scientifico e la sua disponibilitá. La sua competenza, tenacia e professionalitá sono state di esempio per me, spingendomi a dare sempre il massimo con spirito propositivo. L'esperienza positiva del mio dottorato, sia in termini di risultati accademici che di realizzazione personale, é in gran parte dovuta a lei. Grazie.

Ringrazio tutti coloro che hanno lavorato con me nel corso di questi tre anni, poiché i risultati presentati in questa tesi sono il frutto di una proficua collaborazione tra diverse persone, senza le quali la realizzazione di questo lavoro non sarebbe stata possibile. Un ringraziamento in particolare ai Prof. Marco Geppi, Dr. Lucia Calucci, Dr. Silvia Borsacchi e Dr. Francesca Martini del CNR e dell'Universitá di Pisa, e ai Prof. Marco Sebastiani e Dott. Riccardo Moscatelli dell'Universitá di Roma Tre.
Desidero ringraziare vivamente il Prof. Piero Baglioni e tutto il gruppo di ricerca CSGI di Firenze. Un ringraziamento in particolare al Prof. Massimo Bonini, per le proficue discussioni avute nel corso del mio dottorato e per la disponibilitá dimostrata in questi anni.

Faccio un sentito ringraziamento a tutti gli studenti e colleghi del gruppo di ricerca, in particolare a Paolo, Stefano, Chiara, Rita, Martina, Claudio e Annalú, per aver reso piacevole e stimolante il tempo passato dentro e fuori il laboratorio.

Grazie a tutte le persone che mi sono state vicine e a tutti gli immigrati, per il loro affetto e sostegno.

Infine, un ringraziamento speciale va ai miei genitori, alla nonna, alla famiglia Tonuffi e a Giuseppe, per aver sempre creduto in me e per avermi sempre sostenuta con entusiasmo.